01 Apr 1979

Plastic Analysis and Tests for Rigid High-rise Composite Frames

J. Hartley Daniels

Dirk P. duPlessis

Thomas Wenk

STEEL RESEARCH for construction

PLASTIC ANALYSIS AND TESTS FOR RIGID HIGH-RISE COMPOSITE FRAMES

Lehigh University

I Strength and Stiffness of Composite Beam-to-Column Connections
J. Hartley Daniels and *Dirk P. duPlessis*

II Composite Assemblage Experiments
J. Hartley Daniels and *Thomas Wenk*

Committee of Structural Steel Producers • Committee of Steel Plate Producers
american iron and steel institute
1000 16th St. N.W., Washington, D.C. 20036

BULLETIN NO. 28, APRIL 1979

FOREWARD

It is the purpose of the Steel Research for Construction Bulletins to make available to engineering designers and specifiers information covering the use of steel in construction.

The material presented in this publication reports on research and is for general information only. This information should not be used without first securing competent advise with respect to its suitability for any given application. The publication of the material contained herein is not intended as a representation or warranty on the part of American Iron and Steel Institute or of any other person named herein, that this information is suitable for any general or particular use or of freedom from infringement of any patent or patents. Anyone making use of this information assumes all liability arising from such use.

STEEL RESEARCH for construction

PLASTIC ANALYSIS AND TESTS FOR RIGID HIGH-RISE COMPOSITE FRAMES - Lehigh University

I Strength and Stiffness of Composite Beam-to-Column Connections

J. Hartley Daniels and Dirk P. duPlessis

II Composite Assemblage Experiments

J. Hartley Daniels and Thomas Wenk

American Iron and Steel Institute Bulletin

Part I

Strength and Stiffness of Composite Beam-to-Column Connections

by

J. Hartley Daniels and Dirk P. duPlessis

TABLE OF CONTENTS

ABSTRACT

Part I reports the results of an extensive three phase investigation into the behavior of composite steel-concrete beam-to-column connections. In the first phase four composite connections were subjected to concentrated positive end moments (slab in compression) to determine experimentally the effects of slab width and thickness on the maximum strength and initial stiffness of the connections and to observe the mode of failure of the connections. The maximum strength was found to be independent of slab width and proportional to slab thickness. For the widths tested the initial stiffness was found to approximate the stiffness of the transformed cross section using the full slab width. In the second phase the effects of seven primary variables on the maximum strength, initial stiffness and ductility of composite beam-to-column connections were investigated experimentally. Sixteen connections were tested under positive end moments using a partial factorial experiment design to evaluate the significance of the seven test variables. Based on a failure model developed from the failure modes observed in the Phase 1 and Phase 2 tests and using the theory of plasticity, upper and lower bounds to the maximum strength of the connections were established in the third phase. Several conclusions are drawn, the most important ones being that composite steel-concrete beam-to-column connections possess reliable strength and stiffness and sufficient rotation capacity to enable plastic design to be applied to rigid high-rise frames with composite floor systems.

1. INTRODUCTION

Prior research on rigid high-rise (unbraced) steel frames has focused on the maximum strength and drift characteristics (in-plane stiffness) of the unbraced steel frame alone.[1,2,3] However, the steel frame does not represent the complete structural system for a typical rigid high-rise steel-framed building. The structure consists of at least two systems - the rigid steel frames plus the floor system, which usually consists of formed metal decking and concrete. The two systems will interact to share the applied gravity and lateral loads. Composite action between the floor system and the steel beams is frequently used in the design for gravity loads. However composite action has not generally been used in the design for lateral or combined gravity and lateral loads, primarily due to lack of design guidelines and applicable specification provisions.

The presence of floor systems rigidly connected to the beams of unbraced steel frames has long been known to decrease the drift (increase the in-plane stiffness) of such frames. A recent experimental investigation into the behavior of an unbraced steel frame with composite precast concrete floor panels confirmed that such was the case.[4] It is therefore expected that the floor systems will also have a beneficial effect on the maximum strength of unbraced steel frames.

When an unbraced frame is subjected to lateral loads the columns apply end moments to the beams at the beam-to-column connections. If the floor system is attached to the beams with shear connectors, composite action results and the maximum strength and stiffness of the beams are increased. This increases the resistance to the applied end moments thereby increasing the maximum strength and stiffness of the beam-to-column connections and

the unbraced frame. It is therefore evident that composite beam-to-column connections can significantly modify the load-drift behavior of unbraced frames.

Reference 5 reports the first known study that was conducted to investigate the behavior of composite beam-to-column connections. Two test connections were used. One simulated typical interior connections and the other simulated typical exterior connections. It was concluded that the ultimate strength of a beam-to-column connection under positive moment (slab in compression) can be conservatively based on the strength of the steel beam plus that portion of the slab which is in contact with the column where the concrete strength is taken as 0.85 f_c'. This investigation also showed that the mode of failure involved extensive crushing of the concrete slab in front of the column at the attainment of the maximum positive moment. Of particular interest was the wedge-shaped failure surface adjacent to the column face. On the basis of this study it was recommended that additional theoretical and experimental studies be undertaken to further define the maximum strength stiffness and ductility of composite beam-to-column connections.

The investigation described in Part I continues the work reported in Ref. 5 and is conducted in three phases. The first phase is an experimental study to isolate the effects of slab width and thickness on the strength and stiffness of composite beam-to-column connections under positive end moment conditions, and to further observe the mode of failure at the column face.

The second phase consists of an experimental study designed to isolate the effects of seven additional variables on the strength and stiffness of

composite beam-to-column connections under positive end moment conditions. Sixteen connections were tested using a partial factorial experiment design. Of particular importance is the effect of the seven variables on the maximum strength, initial stiffness and the ductility of the connections. The seven test variables are 1) shrinkage gap between the column face and the concrete slab, 2) shear connector spacing near the column face, 3) concrete strength, 4) steel beam depth, 5) use of formed metal deck versus solid slabs, 6) effect of lateral beams framing into the column, and 7) repeated loads.

The third phase consists of theoretical predictions of the upper and lower bounds to the maximum strength of the connections tested in the first two phases using the theory of plasticity.

The investigation is limited to composite steel-concrete beam-to-column connections using headed steel stud shear connections between the beam and slab. The effects of thickness and yield strength of the column flanges are not investigated. The results are applicable to unbraced frames where the concrete in the floor system is in contact with the faces of the steel columns. Although the study is limited to unbraced frames the results are equally applicable to braced frames where a combination of bracing and rigid joints are used to resist lateral loads.

2. DESCRIPTION OF PHASE 1 CONNECTION TESTS

2.1 Phase 1 Test Program

The program consists of tests of four composite beam-to-column connections. The program is divided into two series. Series 1 consists of three composite beams designated B-44, B-64 and B-84. The first digit indicates the slab width in feet and the last digit the slab thickness in inches. Series 2 contains one composite beam designated B-66. A description of the Phase 1 connection tests and loading is shown in Table 1.

The effect of slab width on the ultimate strength and stiffness of the connections is investigated in Series 1. To obtain a sufficiently wide spread of data slab widths of 4 ft., 6 ft., and 8 ft. are investigated. A 4 in. thick slab is used for all the beams in Series 1. This thickness of slab is common in many steel framed high-rise buildings. The 6 ft. slab width for B-64 corresponds approximately to the AISC specified effective slab width for a 4 in. slab.[6] In Series 2 the slab thickness is increased to 6 in. The effect of slab thickness on maximum strength and stiffness is investigated by comparing the behaviors of beams B-66 and B-64.

Figure 1 shows a schematic view of the test setup. A plate is welded to the end of each beam to simulate the face of a column. This end plate is bolted to a column test fixture so that the beam and end plate constitute a rigid beam-to-column connection.

A W12x27 A572 Grade 50 steel section is used for all the test beams. The flange width-thickness ratio of this section ($b/t = 8.1$) is considerably greater than the limit ($b/t = 6.3$) specified for plastic design in Part 2 of the AISC Specification.[6] This is justified on the basis that since

the compression flange is connected to the concrete slab of each test beam local buckling will likely not occur. The choice of steel reflects the increasing trend towards the use of high strength steel in modern building construction.

All the test beams have 1/2 in. diameter stud shear connectors because of the undesirable stud welds obtained locally at the time on 3/4 in. connectors. The smallest size for which the AISC Specification lists allowable shear loads is 1/2 in. diameter.[6]

The concrete strength and end plate width shown in Table 1 were both selected to represent practical values found in many high-rise buildings. All the test beams are subjected to static loading.

2.2 Details of the Connections

2.2.1 Description

Figure 2 shows construction details of the test beams. All the beams have a slab length-to-width ratio of two. A 2 in. thickness was selected for the end plates to minimize the bending of the end plates which would occur during loading of the beams.

Figure 3 shows details of the steel beams and shear connectors. The first pair of connectors were placed a minimum distance of 2 in. from the end plate. Spacing of the connectors is uniform along a beam except for the region immediately in front of the end plate. Additional connectors are placed in this region because of the failure mode observed in the pilot tests reported in Ref. 5. Figure 4a shows the end plate of beam B-44. Figure 4b shows the connectors for beam B-44.

2.2.2 Design

In the design of the shear connectors it is important to ensure that the test beams fail by crushing of the concrete at the end plate and not by shearing of the connectors. This requires consideration of the possible increase in concrete strength due to confinement near the end plate. For this reason the concrete strength at the end plate is assumed equal to twice the unconfined compressive strength f_c'. The connectors are designed according to the AISC Specification.[6]

Two factors are considered in the design of the transverse reinforcement of the concrete slabs:

1) Gravity loads. These included the dead load of the slab cantilevering from the beam plus a 100 lb per ft live load at the edge of the slab to provide for personnel walking on the slab.

2) In-plane tensile stresses. Reference 7 describes the in-plane tensile stresses that are developed when a concentrated force is applied to the edge of a slab. To resist these stresses additional reinforcement is placed over the first half of each slab. This results in two spacings of the transverse reinforcement as shown in Fig. 5.

Longitudinal reinforcement for the slabs is selected on the following basis:

1) Minimum requirements of the ACI code for temperature reinforcement.[8]

2) Reinforcing required for floor slabs spanning about 6 to 8 ft between floor joists framing perpendicular to the frames. Such

reinforcement will run parallel to the frames.

2.2.3 Construction

The steel beams were delivered to the laboratory with all connectors and web stiffeners in position. Welding of the end plates to the steel beams was done at the laboratory using full penetration butt welds on the flanges and 1/4 in. fillet welds on the webs. Preheating of weld areas was performed before welding commenced.

An attempt was made to eliminate bond between the slab and the end plate by covering the end plate with a thin layer of grease. Care was taken to prevent grease from contacting the shear connectors.

All concreting was performed in the laboratory where strict control over the mixing and placing was possible. Special attention was paid to the vibration of the concrete near the end plates. The beams were moist cured for seven days and then allowed to cure under dry conditions until the beams were tested. Testing of the beams occurred between 28 and 40 days following pouring.

2.2.4 Instrumentation

Figure 6 shows the locations of the instrumented cross sections for each test beam. The instrumented sections designated A to F cover approximately the first half of each beam starting at the end plate. Each cross section is provided with a .001-in. dial gage to measure uplift of the slab. An electrical resistance slip gage also measured slip between the slab and the beam at each cross section, as shown in Figs. 6a and 7a.

The vertical deflection and rotation at the free end of each beam is measured with a .001-in. dial gage and a level bar rotation gage respectively. A .001-in. dial gage also records slip between the slab and the beam at the same end. A level bar rotation gage is also attached to the end plate to record rotation at that point. Slip between the end plate and the test fixture is measured with a .001-in. dial gage. A bar level is placed transversely on top of the slab at the free end of the beam to indicate twisting of the beam as shown in Fig. 6a.

Figure 6b shows the location of strain gages at gage section A on beam B-44. The layout of strain gages on the other test beams is similar. All strain gages are of the electrical resistance type. Each instrumented section has six strain gages placed on the beam web and flanges as shown. At the same cross section strain gages are also placed on the reinforcing bars and then covered with permagum and a polyethylene tube for protection against the concrete. Longitudinal and transverse bars are instrumented as can be seen in Fig. 7b.

2.2.5 Material Properties

Table 2 shows the mechanical properties of the steel beams. These were obtained by performing tensile tests on coupons cut from the control pieces left over from the rolled shapes used for the test beams. The coupons were tested in a 120 kip Tinius Olsen Universal machine at a speed of 0.025 in. per minute up to first yielding and then at 0.3 in. per minute until fracture occurred. For all coupon tests the dynamic yield stress, the static yield stress and the maximum load were recorded.

Table 3 shows the mechanical properties of the stud connectors. These were obtained by performing tensile tests on stud connectors welded to a short length of the beam flange. The stud welds were tested by welding some connectors to a short length of steel beam and bending them to a 45^{o} angle.[9] All welds proved to be satisfactory even when the connectors were bent through a 90^{o} angle.

Table 4 shows the properties of the concrete obtained by crushing standard 6 in. diameter cylinders. These cylinders were taken from concrete poured at the end plates as well as further away. Cylinders were always crushed one day before testing of the beams commenced.

2.3 Test Procedure and Loading

The end plates are bolted to a heavy column test fixture with eight 1-in. diameter A490 bolts as shown previously in Fig. 1. The six bolts below the slab are required to resist the full yield force of the steel beam. All bolts are tightened using the turn-of-nut method. Figure 8 shows beam B-66 in its test position.

The zero load position of a test beam is taken as the point at which there would theoretically be no moment at the fixed end. This corresponds to applying a small load at the free end equal to half the calculated weight of the beam. A 55 kip Amsler hydraulic jack is used to load the beam as shown in Fig. 8. Strain gages are read by a digital strain recorder. All dial gages are read manually.

Loading proceeds in small increments until the maximum load is reached. If significant twisting of the beam is observed during the initial stages

of loading, the beam is unloaded and the jack moved in the appropriate lateral direction. Lightly tensioned transverse cables attached to the corners of the slab at the free end of the beam prevents sidesway during loading. After the maximum load is reached the beam is unloaded and the loose concrete in front of the end plate removed to inspect the failure surface.

3. DESCRIPTION OF PHASE 2 CONNECTION TESTS

3.1 Phase 2 Test Program

Details of the test program are shown in Table 5. The individual tests, designated A1, A2, B1, B2, etc., were established on the basis of a two and three level partial factorial experiment design without replication to investigate the influence of seven primary variables as follows:

Primary Variables:

1. Shrinkage gap size: zero, 0.02 in.
2. Shear connector density: High, Normal, Zero
3. Nominal concrete strength (f_c'): 3 ksi, 5 ksi
4. Steel beam depth: 12 in., 16 in.
5. Slab construction: Solid, Longitudinal metal deck, Transverse metal deck
6. Transverse support (lateral beams) at the column: With, Without
7. Repeated loads

Of the seven variables that are investigated the first six are explicitly incorporated into the factorial test program as shown in Table 5. The seventh is investigated only during tests A1 and A2.

All secondary variables are treated as one-level factors as follows:

One-Level Factors

1. Steel beam-to-column connection: Fully welded
2. Shear connectors: headed steel stud connectors
3. Steel beams: A572 Grade 50
4. Reinforcement: σ_y = 40 ksi (nominal)

5. Slab thickness: 4 in.

6. Concrete: Normal weight

The 0.02 in. shrinkage gap is determined on the basis of a shrinkage strain of 0.0002 over a span length of approximately 25 ft. between columns. This gives a value of 0.06 in. or 0.03 in. at each end of the span. In an actual structure the connectors would resist shrinkage so that 0.02 in. represents a liberal size.

Normal connector spacing means that which is found in many typical buildings and is taken as 6 in. staggered based on calculations for a span length of approximately 25 ft between columns. Dense connector spacing implies connectors grouped considerably closer and zero spacing means a complete absence of connectors near the column face.

A smaller value of nominal concrete strength (3 ksi) is considered typical of that found in many buildings. A difference of 2 ksi between the two concrete strengths is considered sufficient to show the effect of concrete strength.

Because the Phase 1 test program used 12 in. deep steel beams the same depth was adopted for the Phase 2 test program. This establishes a link between the two programs with the purpose of comparing test results.

As in the Phase 1 test program a solid slab is retained for some of the tests. However, because of the popularity of formed metal deck slabs, it is necessary to also investigate the latter.

All the Phase 1 tests are performed without transverse support at the column. Since transverse support at a column is normally present in any

building it is considered appropriate to perform most of the tests in Phase 2 with transverse support.

The one-level factors were selected on the basis of the results obtained in the Phase 1 test program.

3.2 Details of the Test Beams

3.2.1 Description

Figure 9 shows a schematic view of the test setup. A 2 in. steel end plate is welded to both ends of each steel beam to simulate the column face. During a test one end plate is bolted to the column test fixture so that the test beam simulates a typical rigid composite beam-to-column building connection. After one end is tested, the test beam is turned around and the other end plate bolted to the column test fixture. In this manner only 8 beams are required to obtain 16 connection tests.

Each test beam is bolted to the column test fixture with eight 1-in. diameter A490 bolts. The six bolts below the slab are required to resist the full yield force of the steel beam. All bolts are tightened using the turn-of-nut method.

Also shown in Fig. 9 are the four ½ in. diameter transverse support hangers that provide the transverse support at the columns. These hangers are suspended from the transverse beam on top of the column test fixture and support the projections of the slab beyond the end plate.

Figure 10 shows a typical test beam. All the beams consist of a 10'8" x 4'0" x 4" solid concrete or concrete on metal deck slab attached with 3 in. long 3/4 in. diameter headed steel stud shear connectors to an 8 ft long

A572 Grade 50 steel beam. The size of the steel beam (W12x27) is the same as used for the Phase 1 tests.

Figures 11 and 12 show details of the test beams. The test corresponding to each end is also indicated. Beams A to D, G and H have a solid 4 in. concrete slab. Beam E has a 4 in. concrete slab on formed metal deck with ribs placed longitudinally to the steel beams. Beam F has a 4 in. concrete slab on formed metal deck with ribs running transverse to the steel beam. Beam H is the only beam with a W16x40 steel section.

Figure 13 shows details of the shear connector spacing. The variable connector spacing to provide the three levels of connector density is made within 15 in. of the steel plate as can be seen in the figure. This is done because the Phase 1 tests show that the spalled and crushed concrete never extended more than about 15 in. from the end plate. Outside these regions the connector spacing is determined by the total number of connectors required (see Section 3.2.2). Figures 14a and 14b show the typical normal and high density connector spacing in test beams with a solid slab. To obtain zero density no connectors are placed in the 15 in. region.

Figures 15a and 15b show details of the formed metal decking that is used on beams E and F respectively. It is anticipated that premature spalling of the surface would occur with the ribs in the transverse direction. For this reason a small area in front of the end plates is flattened to provide full depth of concrete. This is shown in Fig. 15b. Figure 15c shows details of the geometry of the metal decking.

Figures 16a and 16b show the reinforcement details for the beams with solid slabs and metal decking respectively. Bar reinforcement is used for

the solid slabs and welded wire mesh reinforcement is used for the slabs with metal deck. Both types of slab have a double layer of reinforcement around the end plates the purpose of which is explained in the next section.

3.2.2 Design

In the design of the shear connectors it is necessary to know the maximum compressive force which the end plate would exert on the slab. This force was calculated using a concrete stress of 2.57 f_c' as computed in Chapter 4. The connectors are designed according to the AISC specification.[6]

In the design of the reinforcement for the slabs all the factors mentioned in Chapter 4 with regard to the design of slabs are included. In addition, extra reinforcement is required to resist the bending moments caused by the projections of the slabs. The resultant distribution of reinforcement around the end plates is shown in Fig. 16. Because of the smaller strength of the metal deck slabs, the latter requires less reinforcement near the end plate than the solid slabs.

A 2 in. thickness was selected for the end plates because of the satisfactory performance of the same plates during the Phase 1 test program. The end plates are of A36 steel partly because of easy availability at the time of construction and partly because one of the high strength plates used in Phase 1 had delaminated.

The 8 ft length of the steel beam between the end plates was selected on the basis of the results obtained from the Phase 1 tests. An examination of the yield pattern and concrete failure surfaces in Phase 1, indicated that a length of 8 ft would be sufficient to prevent interaction between

the ends of the beam.

In the design of the hangers to simulate transverse support it was necessary to ensure that they would register sufficiently large strains, without yielding, so that the support forces could be accurately calculated. After estimating the maximum force which each hanger would carry, a maximum stress of 26 ksi is used to determine the required diameter.

3.2.3 Construction

The steel beams were delivered to the laboratory with the 2 in. end plates welded in position. Welding of the stud connectors was performed in the laboratory using standard stud welding equipment. The connectors for the beams with formed metal decking were welded to the steel beams through the decking as is standard practice.

For the beams which did not require a formed shrinkage gap at the end plate the reinforcement running perpendicularly into the end plate was welded to the plate. This is shown in Fig. 17a. It was assumed that this would prevent a large shrinkage gap at the end plate. The same was done for similar beams with mesh reinforcement.

For the beams which did require a shrinkage gap at the end plate a 0.02 in. steel plate was clamped to the end plate before casting the concrete as shown in Fig. 17b. Approximately 3 hours after casting the concrete, this steel plate was removed and the top of the gap sealed to prevent dirt from entering.

Concreting for all the beams except beam G was performed using ready mixed concrete. Since only beam G required a concrete strength of 5000

psi it was decided to mix the concrete for this beam in the laboratory where strict control over mixing was possible. The beams were moist cured for seven days and then allowed to cure under dry conditions until the beams were tested.

3.2.4 Instrumentation

Figures 18a and 18b show the locations of the electrical resistance strain gages on the concrete slab and steel section of each test beam. The locations of gage lines B and C were determined considering the following restrictions:

1) A minimum distance of at least 4 in. from the end plate is required to preclude the effect of local distortions.

2) A maximum distance of 15 in. from the end plate is required to comply with the region of variable shear connector spacing (see Section 3.2.1).

3) No strain gages can be placed directly below a shear connector on the steel beam.

Figure 19a shows the locations of electrical resistance strain gages on the transverse support hangers. This is also shown in Fig. 20a.

Figure 19b shows the locations of the Ames dial gages, electrical slip gages and rotation gages on a typical test beam. Ames dial gages were used to measure the following:

1) Deflection at the applied load position

2) Uplift of the slab from the steel beam at the test location

3) Relative vertical slip between the end plate and the test fixture

4) Horizontal deflection of the projections of the slab at the test location.

5) Closing of the shrinkage gap (if present) at the load position.

Relative horizontal slip between the slab and the beam is measured with the electrical slip gages at the test location. Level bar rotation gages measure the rotation of both steel plates and also the twisting of the test beam at the load position.

Figures 20b and 21a show the instrumentation at the test location and load position of a typical test beam.

3.2.5 Material Properties

Table 6 shows the mechanical properties of the steel beams. These were obtained by performing tensile tests on coupons cut from the control pieces left over from the rolled shapes used for the test beams. The coupons were tested in a 120 kip Tinius Olsen Universal machine at a speed of 0.025 in. per minute until fracture occurred. For all coupon tests the dynamic yield stress, the static yield stress and the maximum load were recorded.

Table 7 shows the mechanical properties of the stud connectors. These were obtained by performing tensile tests on stud connectors welded to a short length of the beam flange. Of the 5 connectors tested, one failed in the weld and the others failed by pulling out of the beam flange. The stud welds were also tested by welding some connectors to a short length of steel beam and bending them to a 45^{o} angle. All welds proved satisfactory.

Table 8 shows the properties of the concrete obtained by crushing standard 6 in. diameter cylinders. In general, three cylinders were crushed before starting each of the two tests on every beam. The average of the six tests was assumed to represent the concrete strength of both tests.

3.3 Test Procedure and Loading

The test setup is shown in Fig. 9. Load is applied through a 60 ton mechanical jack bearing against a loading yoke which fits around the end plate. A 5/8 in. diameter bar welded to the bottom of the loading yoke provides a swivel point for the head of the jack. The mechanical jack rests on a calibrated load cell which is supported on a swivel base as shown in Fig. 21b.

The zero load position of a particular test beam is taken as the point at which there would theoretically be no moment at the end plate at the test location. This requires application of a small load equal to half the calculated beam weight. At this point the transverse support hangers are snugly tightened.

Loading proceeds in small increments until the mechanical jack is out of stroke. At this stage some permanent deformation has normally already occurred. The beam is then unloaded and filler plates inserted between the swivel base and the load cell. Loading then continues until the jack again is out of stroke. Normally at this point the maximum load has already been reached. The beam is then unloaded and the loose concrete at the end plate removed to inspect the failure surface.

Figures 22a and 22b show beam C before and after test C1. Figure 23a shows beam E (with the longitudinal ribs) in test position for test E1. Figure 23b shows beam F (with transverse ribs) at the end of test F1. These figures are representative of all the beams tested.

Beams A, B, G and H had a formed shrinkage gap at one end only. In these cases the end without a shrinkage gap is tested first. This ensured that the end plate at the load position does not affect the stiffness of the beam-to-column connection being tested.

Beam A was subjected to cyclic loading. For test A1, 10 cycles from zero to approximately half the maximum load were performed. Test A2 was subjected to three series of cyclic loading as follows: 10 cycles from zero to approximately half the maximum load; 5 cycles from zero to approximately three quarters of the maximum load and 5 cycles at approximately the maximum load.

4. THEORETICAL ANALYSIS - PHASE 3

The principles of plasticity will be utilized to obtain upper and lower bounds to the maximum strength of the composite beam-to-column connections.

4.1 Assumptions

The following assumptions are made:

1. Steel and concrete obey the Tresca yield criterion.[10,11,12] Under this condition the yield stress in pure shear is one half the yield stress in simple tension or compression.
2. The stress-strain law for steel and concrete is rigid-perfectly plastic.
3. The yield stress of concrete in compression is equal to its crushing strength (f_c').
4. Adjacent to the end plate the concrete slab is in a condition between plane strain and plane stress. The steel beam is in a plane stress condition.

Theoretical predictions based on assumption 1 have been shown to agree well with test results.[12,13] In Refs. 13 and 14 assumptions 2 and 3 were shown to give good results for concrete blocks and cylinders.

4.2 Upper Bound Solution

The upper bound theorem of plasticity states that the plastic limit load of a composite connection obtained by equating the rate of external work to the rate of internal dissipation of energy for any assumed mechanism will always exceed or at best equal the maximum strength of the connection.

Figure 24 shows the assumed failure mechanism for connections without transverse support. At the maximum applied load P_u a plastic hinge is assumed to form as shown by the cross hatched regions so that the beam to the left of point C rotates as a rigid body about point C. The concrete wedge ABC having a width equal to the width of the end plate and region DCE of the web of the steel beam are assumed to yield in pure shear. This implies that angles ABC and DCE were right angles before deformation. It is further assumed that the bottom flange yields in pure tension, that the rest of the composite beam remains rigid and that point C lies at the beam-slab interface.

Figure 25 shows the assumed failure mechanism for connections with transverse support. There are two differences between Figs. 24 and 25.

1) a plastic hinge develops in the slab for connections with transverse support

2) for connections with transverse support there is also no shearing of the slab along the two vertical faces ABCF which are in line with each side of the end plate.

4.2.1 Rate of Internal Dissipation of Energy

Assuming that all displacements are small the total internal dissipation of energy for the mechanisms shown in Figs. 24 and 25 will consist of six or seven of the following eight parts:

1) Wedge ABC

Since the wedge is in a state of pure shear, the internal dissipation of energy D_1 is equal to

$$D_1 = \int_V k \dot{\gamma} \, dV \tag{1}$$

where k = yield stress in shear

$\dot{\gamma}$ = shear strain rate

V = volume of wedge ABC

By the Tresca yield criterion

$$k = 1/2 \, f_c'$$

where f_c' = unconfined compressive strength of the concrete.

The velocity v of any point along BC perpendicular to BC is given by

$$v = r \dot{\theta}$$

where r = distance from point C measured along BC

$\dot{\theta}$ = angular velocity about point C

The same velocity can be expressed as

$$v = r \dot{\gamma}$$

This gives

$$\dot{\gamma} = \dot{\theta} \tag{2}$$

Substituting the values of k and $\dot{\gamma}$ into Eq. 1 gives

$$D_1 = 1/2 \, f_c' \, \dot{\theta} \int_V dV$$

or

$$D_1 = 1/2 \, f_c' \, V \, \dot{\theta}$$

The value of V is given by

$$V = 1/2 \, t^2 \, B \, \text{cosec} \, \alpha \, \sec\alpha$$

$$= t^2 \, B \, \text{cosec} \, 2\alpha$$

where t = slab thickness

B = end plate width

α = inclination of wedge ABC (Figs. 24 and 25)

The internal dissipation D_1, then becomes

$$D_1 = \left[\frac{1}{2} f_c' \, t^2 \, B \, \text{cosec} \, 2\alpha\right] \dot{\theta} \tag{3}$$

2) Slab element ABCF

For connections without transverse support shearing occurs along the two vertical faces of element ABCF as the slab rotates about point C (Fig. 24). The internal dissipation of energy D_2 on the two faces is given by

$$D_2 = 2 \int_A k \, r_1 \, \dot{\theta} \, dA \tag{4}$$

where r_1 = radial distance from point C to element dA

A = area of ABCF

The integration is performed by dividing the area ABCF into a rectangle and a triangle and assuming that the resultant shear force on each area is located at the centroid of that area. A uniform shear stress equal to k is assumed to act on each area. Equation 4 then becomes

$$D_2 = \left[t^3 \, f_c' \left(\frac{1}{2} \cot \alpha \, \text{cosec} \, \alpha + \frac{1}{3}\sqrt{1 + \frac{1}{4} \tan^2 \alpha} \tan \alpha\right)\right] \dot{\theta} \tag{5}$$

3) Beam Web Element DCE

The web element CDE is in a state of pure shear and the internal dissipation of energy D_3 is therefore given by Eq. 1, that is

$$D_3 = \int_{V_w} k \, \dot{\gamma} \, dV_w \tag{6}$$

where V_w = volume of beam web element DCE

Denoting the yield stress of the steel beam web by f_{yw}, then

$$k = \frac{1}{2} f_{yw}$$

Using the value of $\dot{\gamma}$ as given by Eq. 2, that is $\dot{\gamma} = \dot{\theta}$, and substituting k and $\dot{\gamma}$ into Eq. 6 gives

$$D_3 = \frac{1}{2} f_{yw} \dot{\theta} \int_{V_w} dV_w$$

or

$$D_3 = \frac{1}{2} f_{yw} \dot{\theta} V_w$$

Since

$$V_w = \frac{1}{2} t_w d^2 \text{ cosec } \beta \text{ sec } \beta$$

where t_w = thickness of the web

d = total depth of the steel beam

β = inclination of element DCE (Figs. 24 and 25)

then the internal dissipation of energy D_3 then becomes

$$D_3 = \left[\frac{1}{2} f_{yw} d^2 t_w \text{ cosec } 2\beta\right] \dot{\theta} \qquad (7)$$

4) Beam Flange Element DE

Flange element DE is assumed to have yielded in simple tension. The internal dissipation of energy D_4 is therefore given by

$$D_4 = \int_{V_F} f_{yF} \dot{\epsilon} \, dV_F \qquad (8)$$

where $\dot{\epsilon}$ = axial strain rate

V_F = volume of flange element DE (Figs. 24 and 25)

f_{yF} = yield stress of the beam flange

The velocity v of point E perpendicular to CE is equal to

$$v = d\,\dot{\theta}\ \text{cosec}\ \beta$$

Its component v_E parallel to DE is equal to

$$v_E = d\,\dot{\theta}\ \text{cosec}\ \beta \sin \beta$$

or

$$v_E = d\,\dot{\theta}$$

The axial strain rate $\dot{\epsilon}$ is then given by

$$\dot{\epsilon} = \frac{d\,\dot{\theta}}{d\ \text{cosec}\ \beta\ \sec \beta}$$

or

$$\dot{\epsilon} = \frac{\dot{\theta}}{\text{cosec}\ \beta\ \sec \beta}$$

Substituting into Eq. 8 gives

$$D_4 = \frac{f_{yF}\,\dot{\theta}}{\text{cosec}\ \beta\ \sec \beta} \int_{V_F} dV_F$$

or

$$D_4 = \frac{f_{yF}\,\dot{\theta}\ d\ A_F\ \text{cosec}\ \beta\ \sec \beta}{\text{cosec}\ \beta\ \sec \beta}$$

or

$$D_4 = \left[A_F\ f_{yF}\ d\right]\dot{\theta} \tag{9}$$

where A_F = area of the beam flange.

5) Transverse Reinforcement

For connections without transverse support the transverse reinforcement in element ABCF of the slab is assumed to yield in shear where it crosses the two faces of the element. The internal dissipation of energy D_5 is given by Eq. 4, that is

$$D_5 = 2 \int_A k\ r\ \dot{\theta}\ dA \tag{10}$$

Setting f_{yr} equal to the yield stress of the reinforcement then

$$k = \frac{1}{2} f_{yr}$$

Assuming that the transverse reinforcement in the vicinity of the end plate is spread uniformly across a longitudinal area of the slab having unit length and thickness t, then the internal dissipation of energy can be obtained by the method used in 2 above for slab element ABCF. This gives

$$D_5 = \left[p_t \, t^3 \, f_{yr} \left(\frac{1}{2} \cot \alpha \, \operatorname{cosec} \alpha + \frac{1}{3} \sqrt{1 + \frac{1}{4} \tan^2 \alpha} \tan \alpha \right) \right] \dot{\theta} \qquad (11)$$

where p_t = transverse reinforcement ratio (area of transverse reinforcement divided by the above longitudinal area of slab).

6) Longitudinal Reinforcement

The longitudinal reinforcement contained within wedge ABC is assumed to yield in compression. The internal dissipation of energy D_6 is then given by Eq. 8, that is

$$D_6 = \int_V f_{yr} \dot{\epsilon} \, dV \qquad (12)$$

Ignoring the relatively small dissipation of energy associated with the bottom layer of reinforcement and assuming the longitudinal reinforcement in the vicinity of the end plate is spread uniformly across the transverse cross section of the slab, then the internal dissipation of energy can be obtained by the method used in 4 above for the beam flange element DE. This gives

$$D_6 = \left[\frac{1}{2} p_\ell \, B \, t \, f_{yr} (t - c_r) \right] \dot{\theta} \qquad (13)$$

where p_ℓ = longitudinal reinforcement ratio (ratio of total area of both layers of longitudinal reinforcement to the transverse area of the concrete slab)

c_r = concrete cover of the top layer of reinforcement.

For the composite beams tested the top and bottom longitudinal reinforcement was the same, accounting for the factor $\frac{1}{2}$ in Eq. 13. For other ratios of top to bottom reinforcement this factor should be adjusted accordingly.

7) Shear Connectors

If the head of a headed steel stud connector extends into the concrete wedge ABC, then the connector will elongate as wedge ABC yields in pure shear. Assuming that the connector yields in simple tension only, then the internal dissipation of energy D_7 is given by Eq. 8, that is

$$D_7 = \int_V f_{yc} \dot{\epsilon} \, dV \tag{14}$$

where f_{yc} = yield stress of the connectors.

Assuming that any connector within wedge ABC is uniformly strained over its full length, then the strain $\dot{\epsilon}$ for that connector is given by

$$\dot{\epsilon} = \frac{\ell_i \dot{\theta} \sin \alpha}{\ell_c}$$

where ℓ_i = distance of the bottom of the head of stud i to plane AC

ℓ_c = length of the shear connectors to bottom of head.

Substituting $\dot{\epsilon}$ into Eq. 14 and summing over all connectors within wedge ABC gives

$$D_7 = \left[A_c f_{yc} \sin \alpha \sum_{i=1}^{n} \ell_i \right] \dot{\theta} \qquad (15)$$

where A_c = area of one connector

n = total number of stud connectors that have their heads fully within the wedge ABC.

8) Plastic Hinge in Slab

For connections with transverse support a plastic hinge will develop in the lateral projections of the slab on both sides of the steel beam flange. The rate of internal dissipation of energy D_8 can be computed using the procedures given in 1 and 4 or 6 above and is closely given by

$$D_8 = A_{sr} f_{yr} \left[t - \frac{A_{sr} f_{yr}}{1.75 f_c'(W-B)} - c_r \right] \dot{\theta} \qquad (16)$$

where A_{sr} = total area of reinforcement in bottom of slab

f_{yr} = yield stress of reinforcement

t = concrete slab thickness

f_c' = unconfined compressive strength of concrete

W = slab width

B = column width

c_r = concrete cover of reinforcement.

4.2.2 Rate of External Work

The rate of external work W_e is given by

$$W_e = \left[P_u (L - t \cot \alpha) \right] \dot{\theta} \qquad (17)$$

where P_u = applied force at the free end of the beam

L = length of the beam.

4.2.3 Upper Bound Values of P and M

The upper bound value of the applied load P_u is obtained by equating the rate of external work to the total rate of internal dissipation of energy for each of the mechanisms shown in Figs. 24 and 25.

1) Connections without Transverse Support

$$P_u = \frac{D_1 + D_2 + D_3 + D_4 + D_5 + D_6 + D_7}{L - t \cot \alpha} \tag{18}$$

2) Connections with Transverse Support

$$P_u = \frac{D_1 + D_3 + D_4 + D_6 + D_7 + D_8}{L - t \cot \alpha} \tag{19}$$

For both cases above the corresponding upper bound value of the bending moment M_u at the end plate is equal to

$$M_u = P_u L \tag{20}$$

4.2.4 Minimization of the Upper Bound

As can be seen in Figs. 24 and 25 the angles α and β are related through the equation

$$d \tan \beta = t \cot \alpha \tag{21}$$

Equations 18 and 19 can therefore be minimized with respect to α for example. The minimum value of P_u can then be obtained by setting

$$\frac{dP_u}{d\alpha} = 0 \tag{22}$$

Since Eq. 22 is difficult to solve in closed form the minimum upper bound values of P_u and M_u are obtained using a computer program in which Eq. 22 is satisfied by varying α in Eqs. 18 and 19.

4.2.5 Limitations of the Upper Bound

Providing all energy dissipation is included, each different possible mechanism will result in a different correct upper bound solution. The bases for assuming the mechanisms shown in Figs. 24 and 25 are as follows:

1) The assumed mechanisms compared reasonably with observed test results

2) The assumed mechanisms could include all reasonable sources of energy dissipation

3) The assumed mechanisms are complex enough to assure a reasonable lowest upper bound and simple enough that the upper bound could be calculated with reasonable effort.

4.3 Lower Bound Solution

The lower bound theorem of plasticity states that the plastic limit load of a composite connection calculated on the basis of an assumed stress field which is internally in equilibrium and satisfies the yield criterion, will be less than or at best equal to the maximum strength of the connection. Such a stress field can be obtained using a simple equivalent truss method or using the slip-line theory.

4.3.1 Equivalent Truss Method

The equivalent truss method is developed for plain strain conditions in Ref. 15. It may be visualized that a pin jointed truss is embedded in the concrete slab as shown in Fig. 26a. This is a simple configuration and more complex trusses are developed in Ref. 15. Stresses are assigned only to the truss members so that the total load is only carried by the equivalent

truss. If the members of the truss are inclined at 60^{o} as shown in Fig. 26b then the equilibrium stress field which does not violate the yield criterion will be as shown in the figure. The bearing stress at the end plate is therefore given by

$$p = 3k \tag{23}$$

Taking $k = f_c'/2$ as before, the bearing stress p at the end plate becomes

$$p = 1.5\ f_c' \tag{24}$$

A possible stress field for the full beam section is shown in Fig. 26C.

With more complex equivalent trusses the value of p increases as shown in Ref. 15 and ultimately reaches the value of p given by Eq. 25 for the slip line theory (Art. 4.3.1). Figure 26b also shows that the horizontal truss member must resist a tensile stress of k. Since concrete cannot resist this tension it is assumed that the tensile stress is carried by suitable transverse reinforcement of the slab.

4.3.2 Slip-Line Theory

The theory of slip lines is presented in Refs. 10, 11 and 12. Slip lines indicate the directions of maximum shear at any point in a stressed material. Part of the slip-line field for a rigid frictionless plate of width B bearing on an infinite body is shown in Fig. 27a. For this classical problem which is solved in the above references the bearing stress p at the plate is shown to be equal to

$$p = (2+\pi)k = 5.14\ k \tag{25}$$

where k = yield stress in shear.

As can be seen in Fig. 27a the slab width of the test beams must be at least equal to three times the end plate width before the assumed slip-line field is valid. Since this is the case for all the test beams, the bearing capacity of the concrete immediately in front of the end plate, which is close to a plane strain condition, is given by Eq. 25. Taking $k = f_c'/2$ as before, the bearing stress p at the end plate becomes

$$p = 2.57\ f_c' \tag{26}$$

A possible stress field for the full beam section is shown in Fig. 27b. The stress p acts over a depth c and width B. In the case shown the steel beam is assumed fully yielded in tension. The value of c in Fig. 27b must be such that the stress field is in equilibrium with the externally applied bending moment and may be larger than the slab depth, resulting in compression yielding in the steel beam.

Slip-line theory is valid for plain strain conditions only.[10] The concrete above the heads of the stud shear connectors is in a state of plane stress. Below the heads the concrete is between plane stress and plane strain conditions since the connectors resist vertical expansion and the slab resists lateral expansion of the concrete near the end plate.

Reference 16 reports the results of 7.9" x 7.9" x 2" concrete specimens that were tested under biaxial compression. It is shown there that a maximum concrete stress of approximately $1.3\ f_c'$ can be attained in one direction if a compressive stress of about $0.4\ f_c'$ is present in the second direction. For the composite connections the concrete near the end plate is laterally confined by the projections of the slab, and further confined by the shear connectors and the top flange of the steel beam. The actual

stress at failure will therefore be dependent on the degree of confinement of the failure zone.

Figure 28 shows a possible lower bound stress field for connections without transverse support. Figure 29 shows a possible lower bound stress field for connections with transverse support. The only difference between Figs. 28 and 29 is the additional stress field in the projections of the slab. Since there is no lateral confinement in the projections the maximum concrete stress of 0.85 f_c' given by the AISC specification for the design of composite beams is used in these regions.[6]

5. PHASE 1 TEST RESULTS AND EVALUATION

5.1 Moment-Rotation Behavior

Figures 30 to 33 show the moment M versus rotation θ behavior for the four composite connections. Each figure also contains five theoretically predicted moment rotation curves. Curves 1 and 2 are for the W12x27 steel section alone. Curve 1 assumes no strain hardening. Curve 2 includes strain hardening with a modulus $E_{st} = 550$ ksi. The elastic slope of curves 3 and 4 is computed assuming a prismatic composite section consisting of the steel beam plus a slab width equal to the column face width. Similarly, the elastic slope of curve 5 is computed assuming a prismatic composite section consisting of the steel beam plus a slab width equal to the full slab width of the test beam. The elastic slopes include the effects of flexural and shear distortions and assume rigid shear connections. Flexural stresses were assumed to be distributed uniformly with respect to slab width.

The horizontal portion of curve 5 in Figs. 30 to 33 is determined using the failure mechanism of Fig. 24. The horizontal portions of curves 4 and 3 are obtained using the lower bound stress fields of Figs. 27 and 28 respectively.

Specific developments which occurred during the loading procedure are also indicated in Figs. 30 to 33. These are:

Point A: increase in elastic stiffness observed. This is due to the closing of a small shrinkage gap between the end plate and the concrete slab at small load.

Point B: observed point of initiation of general yielding in the bottom flange.

Point C: vertical cracking of the end of the slab on both sides of the end plate observed.

Point D: spalling of the top of the concrete slab adjacent to the end plate.

Point E: the maximum moment. At this point spalling and crushing of the concrete extends over a width slightly larger than the width of the end plate and to a distance of about 12 in. in front of the end plate in each test beam. Longitudinal cracks also occur in the bottom of the slab parallel to and on each side of the beam flange to a distance of about 12 in. from the end plate.

Upon reaching the maximum moment it is possible to continue deflecting the beams with only a small loss of load as shown in the figures. The exception is connection B-44 which failed by delamination in the end plate material at the maximum moment as shown in Fig. 34. A typical yield pattern in the steel beam near the end plate is shown in Fig. 35.

Figure 33 shows that for beam B-66 cracking of the slab and spalling of the concrete occurred simultaneously resulting in a sudden change in the moment-rotation curve. Examination revealed that a local failure of the top of the concrete slab in front of the end plate occurred. The concrete cover over the stud connectors was 2 in. for this beam rather than 1 in. for the other beams. Loading was continued and eventually the concrete crushed in a pattern typical of the other beams. However, it is expected that, had the local failure not occurred, the test curve would have proceeded approximately along the dashed line in Fig. 33, where the maximum moment would fall between curves 4 and 5 as is the case for Beams B-44 and B-84.

Figure 36 shows the typical spalling which occurs in front of the end plate (Point D in Figs. 30 to 33). Figure 37 shows the local failure which occurred in B-66 (Points C and D in Fig. 33).

5.2 Concrete Failure Surface

Figures 38 to 41 show the failure surfaces of the concrete slabs adjacent to the end plates. The surfaces are all dish-shaped, just exposing the top reinforcement and the shear connectors. The length of the failure surfaces measured from the end plates varies from 10 to 13 in. for beams B-44, B-64 and B-84, and 14 in. for B-66.

After removing all loose concrete from the failure zone as shown in the figures, a rigid wedge of concrete was exposed. This wedge was in contact with the end plate and sloped downward toward the beam flange. The wedge of concrete is clearly visible in Figs. 39b, 40, 41a and 41b. This is the wedge ACF shown in Figs. 24 and 25. It is assumed that since the wedge appears to be solid and uncracked it does not participate in the failure mechanism.

5.3 Slab-Beam Separation

At the maximum moment the dial gage nearest to the end plate measuring separation between the slab and the steel beam showed a rapidly increasing reading. The reading indicated that the slab at that point was moving downwards or shearing relative to the steel beam. Shearing of the slab coincided with the formation of the longitudinal cracks along the bottom of the slab (Article 5.1), and is clearly shown in Fig. 40. The final positions of the slabs relative to the steel beams are plotted in Fig. 42.

This figure shows that at the end plates all the slabs exhibited a comparatively large shear relative to the steel beams.

The region of shearing motion observed in the test results is shown by region ABCF of Fig. 24, and is accounted for in the theoretical analysis of Chapter 4 for connections without transverse support.

5.4 Strain and Stress Distributions

Figure 43 shows the strain distributions in the test beams at gage section A (see Fig. 6a) before spalling and at maximum moment. All strains are measured on the steel reinforcement and steel beam section. The strain in the concrete at the level of the reinforcement is assumed to be equal to the reinforcement strain. The yield strain ϵ_y and the strain-hardening strain ϵ_{st} of the steel beams were obtained from the tensile coupon tests.

Figure 44 shows the stress distributions in the best beams obtained from the strain distributions of Fig. 43. The modulus of elasticity E_c for the concrete is computed using the ACI formula, in lieu of a measured value.[8] The modulus of elasticity E_s of the steel is taken as 29,400 ksi. The dashed lines indicate the stress distributions just before the concrete had spalled in front the end plates. At this stage the original slab depth is still effective in resisting the applied end moment. The solid lines in Fig. 44 indicate the stress distributions at the maximum moment. At this point, the concrete has spalled completely so that only the portion of the slabs below the failure surfaces can be considered effective. In general this is the portion of the slab below the stud heads. The two sets of stress distributions indicate that when spalling of the concrete starts there is a redistribution of stress in the cross section.

To obtain an estimate of the stresses existing in the test beams at the end plates, the strains at all the gage sections of each beam are plotted and then projected to the end plate. The final result is shown in Fig. 45 where the strain distributions at the end plates at maximum moment are shown. At this section considerable strain hardening has already occurred as can be seen in the figure. Also, the method used to obtain the strains predicts approximately the same maximum strain in the tension flanges of all the test beams.

Figure 46 shows the computed stress distributions based on the strain distributions shown in Fig. 45. The maximum stress in the concrete has been arbitrarily limited to 2.57 f_c'. The dashed lines in Fig. 46 indicate the size of the rectangular stress block assuming full yielding of the steel beam and a maximum stress of 2.57 f_c' at the end plate (Art. 4.3).

5.5 Slip between Beam and Slab

Figure 47 shows the relative slip between the slab and beam at gage section A for B-44, B-64 and B-66. The slip pattern corresponds closely to that which is reported in Ref. 5.

The points A in Fig. 47 correspond to the points A of the moment-rotation curves in Figs. 30 to 33. Initially the slab moves towards the end plate as signified by the negative sign. The magnitude of this movement probably depends on the size of the shrinkage gap between the slab and the end plate. At point A the slab contacts the end plate and either remains stationary or starts to move in the opposite direction. This reverse movement is relatively small until close to the maximum moment when a large movement occurs.

The large slip near the maximum moment is probably a function of the number of shear connectors and the slab thickness. A thicker slab will transfer a higher shear force to the shear connectors than a thinner slab. Since all the test beams have approximately the same number of shear connectors, it can be expected that beam B-66 will exhibit a greater slip near the maximum moment. This is clearly shown in Fig. 47.

5.6 Evaluation of Test Results

Tables 9 and 10 show the upper and lower bound moment capacities of the four composite connections based on the analyses presented in Chapter 4. Except for the lower bound predictions based on an equivalent truss, these values are also shown on Figs. 30 to 33.

Comparing the moment-rotation curves of Figs. 30 to 33 the following is observed:

1) The initial slope of each test curve, except for part OA, is close to that of curves 3 or 4 and can well be approximated by the slope of curve 4. This implies that there is little difference between the stiffness of the test beams and the stiffness of a similar beam where the end moment is applied over the full width of the slab.

2) Beams B-44, B-64 and B-84 have approximately the same maximum end moments indicating that for the test beams the moment capacity of the cross section at the end plate is essentially independent of the slab width.

3) The variation of maximum end moments for beams B-44, B-64 and B-84 agrees with the variation in concrete strengths reported in Table 4 indicating that the moment capacity of the cross section at the

end plate is proportional to the concrete strength.

4) Comparison of the maximum end moments of B-64 and B-66 shows that an increase in slab thickness results in an increase in the ultimate strength of the cross section. However, whereas the slab thickness increases 50 percent (from 4 in. to 6 in.) the ultimate strength increases only about 25 percent (assuming that the ultimate strength of B-66 is given by the dashed line in Fig. 33).

5) The premature failure observed in B-66 indicates that the depth of concrete cover over the shear connectors (depth of concrete in a plane stress condition) has an adverse effect on the maximum moment capacity.

6) The lower bound moment capacity based on a stress at the end plate of $p = 2.57\ f_c'$ (Art. 4.3) closely predicts the maximum moments reached in B-44 and B-84, and slightly overestimates the capacity of B-64. Due to the local failure in B-66 the moment capacity falls somewhat short of that predicted by the above stress level. This implies that it may be unrealistic to assume complete plane strain conditions near the end plate.

The stress distributions of Figs. 44 and 46 were used to check for horizontal force and moment equilibrium. An estimate of the effective slab width at gage section A is obtained assuming that the stresses in the slab spread out at a 45^{o} angle from the end plate, resulting in an effective slab width of 26 in.

Tables 11, 12 and 13 compare the computed and test moments at gage section A and at the end plate. The agreement obtained in Tables 11 and 12 is satisfactory. The results in Table 13 indicate that the effective width

at gage section A is a little wider than 26 in. providing that the strains measured on the slab reinforcement are accurate after spalling of the slab has occurred.

5.7 Conclusions

The following conclusions are based on the results of the Phase 1 tests and a comparison of the test results with predictions presented in Chapter 4.

1) For the widths tested the initial stiffness of a composite connection can be approximated assuming a prismatic beam consisting of the steel beam and the full slab width.

2) The maximum strength of a composite connection is independent of the slab width, and depends mainly on the end plate width, slab thickness, concrete strength, yield strength of steel, and degree of confinement of the concrete in the failure zone.

3) Concrete cover over the shear connectors is an important parameter affecting the performance of the composite connections. The results indicate that the cover should be minimized for maximum strength.

4) The maximum strength of the composite connections can be effectively bounded by the predictions of the theory of plasticity.

5) A good but in some cases unconservative estimate of the maximum strength of composite connections can be based on slip line theory using a stress at the end plate equal to $2.57\ f_c'$. A more reliable lower bound might be obtained using $1.30\ f_c'$.

A further investigation of the variables affecting the maximum strength and stiffness of composite beam-to-column connections is presented in Chapters 6 and 7.

6. PHASE 2 TEST RESULTS

6.1 Moment-Rotation Behavior

Figures 48 to 55 show the moment-rotation behavior of all the composite connection tests. The moment M at the column face is nondimensionalized with respect to the plastic moment M_p of the steel section. The chord rotation θ is also nondimensionalized with respect to the theoretical plastic hinge rotation θ_p of the steel beam, assuming a shape factor of 1 ($\theta_p = M_p L/3EI$).

Each figure contains four theoretically predicted moment-rotation curves. Curves 1 and 2 are for the W12x27 or W16x40 steel section alone. Curve 1 assumes no strain hardening. Curve 2 includes strain hardening with a strain hardening modulus E_{st} = 550 ksi. The elastic slope of curve 3 is computed assuming a prismatic composite section consisting of the steel beam plus a slab width equal to the column face width. Similarly the elastic slope of curve 4 is computed assuming a prismatic composite section consisting of the steel beam plus a slab width of the test beam. The elastic slopes include the effects of flexural and shear distortions and assume rigid shear connections. Flexural stresses were assumed to be distributed uniformly with respect to slab width.

The horizontal portion of curve 4 in Figs. 48 to 55 was determined using the failure mechanisms of Figs. 24 and 25. The horizontal portion of curve 3 was obtained using the lower bound stress fields of Figs. 28 and 29 with $p = 1.30\ f_c'$.

Specific developments which occurred during the loading procedure are also indicated in Figs. 48 to 55. These are:

Point A: cracking of the slab first observed

Point B: observed point of initiation of general yielding in the bottom flange

Point C: spalling of the concrete slab adjacent to the end plate

Point D: the maximum moment

Point E: normal termination of a test. This occurred when unloading was evident due to concrete crushing or when very large rotations had been reached

Point F: termination of the test due to spreading of the crack in the tension flange of the steel beam

Point Y: first observed yielding in a small localized region in the tension flange directly below the cope hole in the web. Necking occurred almost simultaneously with the yielding. This was also the region where cracking of the flange finally occurred.

Figures 49 and 50 show the results obtained when the cracked bottom flanges of tests B2 and C1 were repaired with small flange plates welded to the steel beam. The flange plate of test B2 was considerably larger than that of test C1 causing the significant increase in moment capacity and flexural stiffness as can be seen in Fig. 49. The flange plate was added to test B2 after complete cracking of the tension flange had occurred. For test C1 the flange plate was added after partial cracking was observed.

6.2 Failure Surfaces

Figures 56 and 57 show typical failure surfaces in the concrete slab at the column face at the end of testing. The crushing and spalling of the concrete exposed the metal decking of beams E and F as shown in Fig. 57. This implies that at the end of the test the composite section for these beams in the vicinity of the column face was essentially that of the steel beam alone.

Figure 58 shows the yielding and cracking patterns for tests G1 and F2. For test G1 the steel beam yielded mainly in tension as can be seen in Fig. 58a. Figure 58b shows that compression yielding occurred in the upper part of the steel beam of test F2. Local buckling of the compression flange of test F2 also can be seen. It can be further observed that the local buckling and the concrete rib that had failed are both located near the end of the flattened region of the metal deck (Art. 3.2.1).

6.3 Description of Tension Flange Cracking

Figure 59 shows two different kinds of cracking in the heat affected zone of the tension flange. For the connections with a W12x27 steel section the cracking initiated below the cope hole in the web and slowly spread outwards as shown in Fig. 59a. This figure also shows the yielding that occurred in the vicinity of the crack. Considerable necking was also visible.

Figure 59b shows the cracking that occurred in both tests with the W16x40 steel section (test H1 and H2). The cracking occurred suddenly, with a loud report, and completely severed the flanges. The cracks displayed a brittle surface with no significant necking or yielding.

6.4 Forces in the Transverse Support Hangers

Figures 60 and 61 show the forces that developed in the transverse support hangers of test C2 and E1, respectively. The tension forces are plotted against the nondimensionalized moment M/M_p at the column face. Points A, B and C in Figs. 60 and 61 correspond to the same points in Figs. 48 and 55. It is evident from Figs. 60 and 61 that the two interior bars carry essentially the total load.

Also plotted in these figures is the ratio M_s/M versus M/M_p where M_s is the moment applied at the end plate by all four transverse support hangers and M is the total applied moment at the end plate. The ratio M_s/M always remains quite small. It initially decreases but later increases rapidly when spalling of the concrete begins at the steel plate.

6.5 Slip between Slab and Steel Beam

Figure 62 shows the relative slip between the slab and the steel beam at gage section B (Fig. 18) for test beams A and B. Positive and negative values of slip imply movements of the concrete slab away and towards the end plate respectively. Tests A1 and B1 were without shrinkage gaps, while tests A2 and B2 were with shrinkage gaps. Points A, B and C in Fig. 62 correspond to the same points in Figs. 48 to 55. It is evident that the effect of a shrinkage gap is to cause a large negative slip relative to that caused by a beam with no shrinkage gap.

7. EVALUATION OF PHASE 2 TEST RESULTS

7.1 Parameters

The effect of each of the seven test variables listed in Chapter 3 will be investigated in the light of the following three parameters:

1) Maximum Strength Ratio: the maximum value of the M/M_p ratio as obtained from the moment-rotation curves in Figs. 48 to 55.

2) Initial Stiffness: the initial slope of the moment-rotation curves in Figs. 48 to 55 computed between the start and the end of the first load increment.

3) Ductility Factor: the definition of ductility given in Ref. 17 will be used. Ductility is defined there as the ability of a structure to undergo increasing deformation beyond the initial yield deformation while still sustaining load. Consider the typical moment-rotation curve in Fig. 63. Point B is the initial yield rotation "a" and point D is the peak rotation "b". A measure of ductility is the ductility factor defined by[17]

$$\text{Ductility factor} = \frac{\text{Peak rotation}}{\text{Yield rotation}} = \frac{b}{a} \qquad (27)$$

Table 14 presents the maximum strength ratio, initial slope and ductility factor for each of the tests. The lowest values of maximum strength (1.54-1.61) corespond to tests E1, E2, F1 and F2 which had the formed metal deck slabs. The highest value (1.87) corresponds to test G1 which had a solid slab and the highest concrete strength as can be seen from Table 8. It is significant to note in Fig. 54 that test G2 had a comparatively early flange rupture. This fact should be considered when noting the maximum strength ratio for test G2.

The formed shrinkage gap in tests A2, B2, D1, D2, G2 and H2 were not all exactly the same size because of the method of constructing the gaps. In addition those tests which did not require formed shrinkage gaps were observed to have a small natural shrinkage gap between the steel plate and the slab. This was especially noticeable with beams E and F probably because the smaller amount of reinforcement in the metal deck slabs was insufficient to prevent shrinkage. The above factors must be considered when comparing initial stiffnesses in Table 14. Other factors which may have had small influences on the initial stiffness are the amount of concrete that was destroyed during testing of the other end of the beam and whether or not a formed shrinkage gap was present at the other end.

The minimum ductility factor achieved was 4.4 for test G2. This value may have been affected by the comparatively early flange rupture as was mentioned earlier.

In Tables 15 to 21 the effects of the 7 test variables listed in Chapter 3 are investigated. In each of these tables "increase" implies an increase of the value of the parameter (maximum strength ratio, initial stiffness or ductility factor) corresponding to the test listed in Column 1 over that of the test listed in Column 2. The percentage increase or decrease is calculated on the basis of the value associated with the test in Column 2.

7.2 Effect of a Shrinkage Gap

Referring to Table 5 it can be seen that the only difference between tests A1 and A2, B1 and B2, G1 and G2 and H1 and H2 was the presence of a formed shrinkage gap. The results of these tests therefore will enable

the effect of a shrinkage gap to be isolated.

1) Maximum Strength Ratio

In Table 15 the variation in maximum strength ratio between the tests with and without formed shrinkage gaps are shown. The large decrease in M_{max}/M_p between tests G1 and G2 is probably due to the relatively early cracking of the bottom flange of test G2 (Section 7.1). This decrease is therefore unreliable and should be ignored. The average change in maximum strength ratio (ignoring test G2) is a decrease of 1.0 percent. Such a small change indicates that a shrinkage gap has a negligible effect on the maximum strength of a composite beam-to-column connection.

This result can be explained with the aid of Fig. 64a which shows the column in contact with the slab after the shrinkage gap has closed. Because of the inclination of the beam the concrete in contact with the column is in a three dimensional state of stress. It is known that under such a state of stress concrete strength increases greatly. Therefore, even though the lower part of the slab may still be separated from the column face the increased strength of the concrete in the upper part is sufficient for the connection to reach nearly the same strength as in the case without a shrinkage gap.

2) Initial Stiffness

Table 15 shows that there is a large decrease in the initial stiffness when a shrinkage gap is present. This can be explained with the aid of Fig. 64b. While the slab is still separated from the column face the length of noncomposite action is the distance from the column face to the first row of connectors. Because this noncomposite action occurs in a region

of maximum bending moment it results in a substantial decrease in initial stiffness.

3) Ductility Factor

Table 15 shows that there is a definite decrease in the ductility factor when a shrinkage gap is present. This decrease can be attributed to several reasons, as follows:

a) The decrease in initial stiffness mentioned earlier causes yielding to occur at a greater rotation. This can be seen in Figs. 52, 54 and 55. The value of the yield rotation "a" in Fig. 63 is therefore larger, leading to a decrease in the ductility factor.

b) The greater concrete strength under a three-dimensional state of stress near the column face may result in the connection reaching its maximum strength more rapidly after the shrinkage gap closes. This could be the reason why tests A2 and B2 reached their maximum strength at a smaller rotation than tests A1 and B1 respectively (Figs. 48 and 49). This causes the peak rotation "b" in Fig. 63 to be smaller leading also to a decrease in the ductility factor.

7.3 Effect of Connector Density

Comparing tests C1 and C2, D1 and D2, E1 and E2, F1 and F2 in Table 5 shows that the only variable in these tests is connector density. The results of these tests will therefore indicate the effect of connector density.

1) Maximum Strength Ratio

Table 16 shows that there is no definite trend in the variation of maximum strength between the pertinent tests. In addition the actual values of percentage decrease or increase are comparatively small. This result can be explained as follows. The connectors in the immediate vicinity of the column contribute little to the total transfer of shear between slab and beam. Their density in front of the column is therefore not expected to influence the maximum strength of the connections as long as there are sufficient connectors along the beam to develop the maximum concrete force or the yield force of the steel beam whichever is less.

2) Initial Stiffness

Table 16 indicates a small reduction in initial stiffness with a decrease in connector density. The largest reduction occurred between tests E1 and E2. When E1 was tested the opposite end (E2) had not yet been tested. Upon testing E2 very little concrete was present at E1 as can be seen in Fig. 57a. This could have contributed to the decrease in initial stiffness of test E2.

The average decrease in initial stiffness is comparatively small and does not indicate a definite trend. It should therefore be concluded that connector density at the column does not significantly affect the initial stiffness of a composite connection. The initial stiffness is more dependent on the total number of connectors provided along the length of the beam.

3) Ductility Factor

Table 16 shows that there is an increase in the ductility factor with a decrease in connector density at the column. This increase is contrary

to what was expected. It has been found that the ductility of reinforced concrete increases with an increase in the number of stirrups.[18,19] It was therefore expected that an increase in connector density should lead to an increase in ductility.

The connectors close to the column are largely responsible for resisting uplift of the slab when lateral support at the column is present. Increasing the connector density in this region would therefore decrease uplift and consequently increase the curvature of the slab as shown in Figs. 65a and 65b. The increased curvature causes a higher compressive stress in the upper part of the slab for the same applied load. This could result in an earlier attainment of the maximum strength ratio (tests E1 and F1 versus E2 and F2) with a consequent decrease in the ductility factor as was explained in Section 7.2.

It is therefore concluded that an increase in connector density at the column could lead to a decrease in the ductility factor.

7.4 Effect of Concrete Strength

Table 5 shows that the effect of concrete strength can be determined by comparing tests G1 and G2 with C1 and D1 respectively. Because it was shown in Section 7.3 that connector density does not affect either maximum strength ratio or initial stiffness, tests G1 and G2 can also be compared with A1, A2, C2 and D2. However, the comparatively early flange cracking of G2 (Section 7.1) makes comparisons with this test unreliable and, therefore, only the results of test G1 will be used.

1) Maximum Strength Ratio

Table 17 shows that an increase in concrete strength leads to an increase in maximum strength ratio as can be expected. This is because, as the concrete strength increases, the contribution of the slab to the maximum strength of the connection increases. However, whereas there was nearly a 50 to 70 percent increase in concrete strength (see Table 8) the average increase in maximum strength ratio was only 8.7 percent as shown in Table 17.

2) Initial Stiffness

Table 17 shows a small increase in initial stiffness with an increase in concrete strength. The modulus of elasticity of concrete is proportional to its compressive strength and an increase in the latter, therefore, increases the moment of inertia of the cross section causing an increase in initial stiffness. Again the increase in initial stiffness (3.6%) is small in comparison with the increase in concrete strength (50%).

3) Ductility Factor

As shown in Table 17 there is a definite decrease of the ductility factor with an increase in concrete strength. This may be due to the following reasons:

a) An increased concrete strength may cause the connections to attain their maximum strength more rapidly and therefore decrease the peak rotation "b" in Fig. 63. This can clearly be seen when the peak rotation of test G1 is compared with those of tests A1, C1 and C2. The ductility factor will therefore be smaller.

b) Increasing the concrete strength raises the neutral axis which retards initial yielding of the bottom flange. This would increase the initial yield rotation "a" in Fig. 63 and therefore decrease the ductility factor.

7.5 Effect of Steel Beam Depth

A comparison of tests H1 and H2 with C1 and D1 in Table 5 shows that these tests differed only in the size of the steel beam. There was, however, also a difference in concrete strength as shown in Table 8 which should be considered when comparing test results. Since it was shown in Section 7.3 that connector density does not affect either the maximum strength ratio or the initial stiffness tests H1 and H2 can also be compared with A1, A2, C2 and D2.

1) Maximum Strength Ratio

Table 18 shows a consistent decrease in maximum strength ratio with an increase in beam depth. Increasing the beam depth increases the contributions of the steel beam to the maximum strength of the connection thereby decreasing the maximum strength ratio.

2) Initial Stiffness

Table 18 indicates that the initial stiffness is decreased when the beam depth increases. The reason for this result may be the following. Because of the greater beam size the shear connectors of beam H transmitted a much greater shear force than those of beams A, C and D. Since all these beams had practically the same total number of shear connectors as can be seen in Fig. 13 the connector slip in test H1 and H2 was greater than that

in tests A1, A2, C1, C2, D1 and D2. This would have caused a decrease in the initial stiffness of H1 and H2.

3) Ductility Factor

Table 18 shows that there is a small average increase in the ductility factor with an increase in beam depth. There is however no definite trend and it should be concluded that beam depth has a negligible effect on the ductility of a composite beam-to-column connection.

7.6 Effect of Formed Metal Deck Slabs

Tests E1, E2, F1 and F2 differed from tests A1, C1 and C2 in the following way:

a) metal deck slabs versus solid slabs (Table 5)

b) arrangement of connectors near the steel plates (Fig. 13)

c) concrete strengths (Table 8)

d) small changes in yield strength of the steel beam (Table 6).

The small differences in yield strength can be ignored. Knowing the effects of connector density and concrete strength from Section 7.3 and 7.4 the above named tests can be compared to determined the effect of metal deck slabs.

1) Maximum Strength Ratio

Tables 19 and 20 show that the maximum strength ratio decreases when metal deck slabs are used. This can be expected because of the lesser amount of concrete in metal deck slabs. The tables also show that the decrease in maximum strength ratio is approximately the same regardless of the direction of the ribs. However, had it not been for the flattened

transverse ribs at the steel plate (Fig. 15b) tests F1 and F2 may have exhibited a greater decrease in maximum strength ratio.

2) Initial Stiffness

There is a substantial decrease in initial stiffness when formed metal deck slabs are used as can be seen in Tables 19 and 20. Part of this decrease is due to the lesser amount of concrete in the metal deck slabs. The major reason however for the significant decrease in initial stiffness is probably the presence of natural shrinkage gaps in tests E1 and F1 as was mentioned in Section 7.1. Had this not been the case the decreases in initial stiffness would probably not have been as large.

The tables also show that the orientation of the ribs did not play a significant role in decreasing the initial stiffness. This is most likely due to the proximity of the concrete in the ribs to the neutral axis of the composite beam.

3) Ductility Factor

Tables 19 and 20 show that there is a decrease in the ductility factor when formed metal deck slabs are used. The reason for this is probably twofold:

a) The concrete at the column is less confined because of the absence of concrete between the ribs and is therefore less ductile.[18,19] This may decrease the ductility factor.

b) Figures 48, 50, 52 and 53 show that the peak rotations of tests E1, F1 and F2 are smaller than those of A1, C1 and C2. The ductility factor which is proportional to the peak rotation (Section 7.1) would therefore also be smaller.

Tables 19 and 20 also indicate a greater decrease in the ductility factor with transverse ribs than with longitudinal ribs. Figures 52 and 53 show that the peak rotations of tests F1 and F2 were smaller than that of test E2. This could have caused the additional decrease in ductility factor for tests F1 and F2.

7.7 Effect of Lateral Support at the Column

The effect of lateral beams can be determined by comparing tests B1 and B2 with C1 and D1 as shown in Table 5. Because of the differences in concrete strength as shown in Table 8 the above comparison would yield inaccurate results. Since it was shown in Section 7.3 that connector density does not influence maximum strength ratio or initial stiffness a better comparison would be between tests B1 and A1 and B2 and A2.

1) Maximum Strength Ratio

Table 21 shows a small increase in maximum strength ratio in the presence of lateral support. The lateral support forces the projections (the portions of the slab on the sides of the column) into bending thereby increasing the moment resistance of the connection. The increase in maximum strength ratio is most likely a function of the slab width, amount of reinforcement and yield stress of the reinforcement.

2) Initial Stiffness

Lateral support at the column increases the initial stiffness of the connection as shown in Table 21. As a result of the action of the lateral support as explained above the moment of inertia of the composite section at the column is increased by that of the projections. This results

in an increase in the initial stiffness of the connection. The increase in initial stiffness is again a function of the slab width.

3) Ductility Factor

Table 21 shows a small decrease in the ductility factor in the presence of lateral support. There is however no definite trend and because the decrease is relatively small it is concluded that lateral support at the column has no significant effect on the ductility factor.

7.8 Effect of Repeated Loads

The effect of repeated loads was investigated during the execution of tests A1 and A2 (Section 3.1). Since no significant changes were observed it can be concluded that repeated loads have no appreciable effect on either maximum strength ratio, initial stiffness or ductility factor.

7.9 Correlation with Theoretical Analysis

Table 22 summarizes the test results of this experimental study.

Table 23 shows a correlation of the maximum strength ratio with the upper and lower bound values. Except for test G2 all the test values exceeded or at least equalled the lower bound values. The reason for test G2 not reaching the lower bound is due to the comparatively early flange cracking (Section 7.1). It can therefore be concluded that the lower bound stress fields of Fig. 28 or 29 are reliable lower bounds.

Table 23 also shows that none of the test values exceeded the upper bounds. The maximum strength ratios were thus effectively bounded by the upper and lower bounds obtained from Chapter 4.

Table 24 shows a theoretical breakdown of the internal dissipation of energy in the upper bound mechanism (Section 4.1) as obtained for each of the tests. The values in column 7 represent the contribution by the shear connectors. Since these values constitute a comparatively small part of the total internal dissipation the shear connectors do not significantly affect the maximum strength of the connections. This observation supports the conclusion reached in Section 7.3.

A survey of Figs. 48 to 55 shows that the initial stiffness of the connections without a shrinkage gap is well approximated by that of curve 3. The initial stiffness of the connections with a shrinkage gap lies between that of curves 1 and 3. Frame behavior in the presence of shrinkage gaps has been investigated in Ref. 20.

7.10 Application to Analysis and Design of Unbraced Frames with Composite Beams

7.10.1 Maximum Strength

Table 25 shows the ratio of maximum strength over the lower bound value ($p = 1.3\ f_c'$) for all the Phase 1 and Phase 2 tests. The lower bound values were obtained from the stress field of Fig. 29. It is therefore concluded that Fig. 29 (and Fig. 28) provides a reliable lower bound for the maximum strength of a composite beam-to-column connection under positive moment.

Figure 66 shows a plan view of a two-bay unbraced frame with composite beams. At the leeward side of the columns (slab in compression) the stress field of Fig. 29 applied using $1.30\ f_c'$ for the concrete in contact with the columns. At some distance L_t from the columns the maximum strength of the

composite section can be determined using 0.85 f_c' for the concrete.[6] Within this transition length (L_t) the concrete strength on which maximum strength calculations should be based varies from 1.30 f_c' to 0.85 f_c'. The transition length has been investigated in Ref. 20, and is further discussed in Part II of this paper, and in Ref. 23.

7.10.2 Initial Stiffness

An extensive study has been conducted in Ref. 20 to determine what uniform stiffness should be assigned to the composite beams so that the unbraced frame with these beams will have the same stiffness as with the full panel width floors.

7.10.3 Ductility

Table 14 shows that the minimum ductility factor achieved was 4.6 (ignoring G2). Reference 17 indicates that for buildings in earthquake areas a ductility factor between 4 and 6 is recommended. It can therefore be concluded that from this point of view all the connections exhibited adequate ductility.

In plastic design of steel structures rotation capacity is defined as the angular rotation which a given cross-sectional shape can accept at the plastic moment value without prior local failure.[21,22] Rotation capacity is indicated in Fig. 67. Assuming that this definition also applies to composite connections and taking the plastic moment M_p as the lower bound value (curve 3 in Figs. 48 to 55) then the rotation capacity of each test is as shown in Table 26. It has been found that in many unbraced steel frames the required rotation capacity is of the order of the deflection

index at maximum load.[2] Assuming a typical deflection index of less than 0.02 at maximum load it can be seen that all the tests except G2 had adequate rotation capacity.

It is therefore concluded that plastic design can be applied to unbraced frames with composite beams.

8. SUMMARY AND CONCLUSIONS

8.1 Summary

Part I describes a three-phase investigation into the behavior of composite steel-concrete beam-to-column connections for rigid high-rise composite frames.

The first phase which continues the work of Ref. 5 is an experimental study to isolate the effects of slab width and thickness on the strength of composite connections under positive end moment conditions and to further observe the mode of failure at the column face. Four composite beams were designed and tested.

Three of the composite beams had varying slab widths and constant slab thickness. The fourth had an increased slab thickness. The ratio of slab length to slab width was constant. All four beams had the same high strength steel section and approximately the same number of steel stud shear connectors.

One end of each composite beam was bolted to a rigid column test fixture to simulate a rigid composite beam-to-column connection. A hydraulic jack applied an upward force at the free end of the beam subjecting the concrete in front of the simulated column to compression. Loading was applied until the maximum moment was reached. At that stage the concrete in front of the column face was crushing. The beam continued to deflect with little loss of moment. After unloading the loose concrete at the column face was removed to inspect the concrete failure surface.

Strain and stress distributions in the test beams were plotted, showing that a redistribution of stress occurred in the slab as soon as

crushing of the concrete commenced at the column face. An estimate of the stress distribution existing at the end plate at maximum moment was obtained for each beam by projecting the measured strains to the end plate. Moment versus rotation curves were plotted for each test, and compared with theoretical predictions performed in the third phase.

The second phase consisted of an experimental study designed to isolate the effects of seven additional variables on the strength and stiffness of composite beam-to-column connections under positive end moment conditions. These variables were 1) a shrinkage gap between the column face and the concrete slab; 2) shear connector spacing near the column face; 3) concrete strength; 4) steel beam depth; 5) formed metal deck slabs; 6) lateral beams framing into the column and 7) repeated loads. Of particular importance was the effect of the test variables on the maximum strength, initial stiffness and ductility of the connections.

The test program comprised a two and three level partial factorial experiment design without replication. Sixteen tests were performed to investigate the seven primary variables. All secondary variables such as the yield strength of the steel beams, the slab thickness and type of shear connectors were treated as one level factors.

The experimental program consisted of testing eight composite steel-concrete beams. Each beam was bolted to a rigid column test fixture to form a cantilever. With the aid of a mechanical jack an upward load was applied at the free end of the beam. This caused compression in the concrete at the column end of the beam thus simulating the leeward side of a composite beam-to-column connection. Loading of the connection continued until either the deflection became too large or the bottom flange of the

steel beam cracked. The beam was then turned around and the other end bolted to the column test fixture. In this manner eight beams were used to obtain sixteen tests. The maximum strengths achieved were compared with theoretical predictions performed in the third phase.

In the third phase of the investigation upper and lower bounds to the maximum strength of a composite beam-to-column connection were obtained using the theory of plasticity. For the upper bound a failure mechanism was assumed and the total internal dissipation of energyminimized. For the lower bound value a statically admissible stress field was assumed at the column face. All the test values of the maximum strength lay between the upper and lower bound values.

8.2 Conclusions

The following conclusions are based on the theoretical and experimental investigations reported herein:

1) For the widths tested the initial stiffness of a composite connection can be approximated on the basis of a prismatic beam consisting of the steel beam and the full slab width.

2) The ultimate strength of a composite connection is independent of the slab width.

3) The depth of concrete cover over the shear connectors near the column face is an important parameter affecting the performance of composite connections.

4) The ultimate strength of a composite connection can be effectively bounded by using the upper and lower bounds obtained from the theory of plasticity.

5) A reliable lower bound to the maximum moment capacity of a composite connection can be obtained by using a rectangular stress block of width equal to the column face width and a concrete stress of 1.30 times the unconfined compressive strength f_c'.

6) The maximum strength of a composite connection using solid slab construction can exceed the maximum strength of the bare steel connection by 64 to 87%.

7) A shrinkage gap between the column face and concrete slab causes a significant decrease in the initial stiffness of a connection but has no effect on the maximum strength. Ductility is slightly decreased.

8) Connector density at the column face has no appreciable effect on either maximum strength or initial stiffness of a connection. Increasing the connector density may reduce the ductility of the connection.

9) Increased concrete strength results in an increase in maximum strength and initial stiffness of a connection but may reduce the ductility.

10) Increasing the size of the steel beam increases the maximum strength and initial stiffness but has no appreciable effect on ductility of a composite connection.

11) The maximum strength of a composite beam-to-column connection using formed metal deck slab construction can exceed the maximum strength of the bare steel connection by 54 to 61%.

12) Lateral beams framing into the column increases the maximum strength and initial stiffness of a composite beam-to-column

connection but has no appreciable effect on ductility.

13) Repeated service loads have no significant effect on either maximum strength, initial stiffness or ductility of a connection.

14) Composite beam-to-column connections possess adequate rotation capacity to enable plastic design to be applied to unbraced high-rise frames with composite steel-concrete floor systems.

9. ACKNOWLEDGMENTS

The investigation described herein was conducted at Fritz Engineering Laboratory, Lehigh University, Bethlehem, Pa. Dr. Lynn S. Beedle is Director of the Laboratory and Dr. David A. VanHorn is Chairman of the Department of Civil Engineering.

The authors wish to thank the Committee of Structural Steel Producers and the Committee of Steel Plate Producers of the American Iron and Steel Institute for sponsoring this research. The contribution of the AISI Task Force on Project 173 consisting of Dr. W. C. Hansell as Project Supervisor, Professor E. H. Gaylord, and Messrs. A. C. Hauswald, H. S. Lew and W. A. Milek, Jr. is gratefully acknowledged.

The authors gratefully acknowledge the assistance given by Mr. Ken Harpel, Laboratory Superintendant, and his staff in preparing the test setups. The manuscript was carefully typed by Ms. Shirley Matlock and Ms. Mary Snyder and the figures were prepared by Mr. John Gera and Ms. Sharon Balogh.

10. NOMENCLATURE

A = area (general); area of element ABCF (Fig. 24)

A_f = area of beam flange

A_c = area of stud shear connector

A_{sr} = total area of reinforcement in bottom of slab

A_s = total area of steel beam

B = width of end plate

D = internal dissipation of energy

E = Young's modulus

H = lateral load on a frame

I = moment of inertia

L = length of test beam

L_t = transition length

M = end moment of test beam

M_p = plastic moment of steel beam

M_s = total moment at the steel plate applied by transverse support hangers

P = applied vertical force at free end of test beam; column force

V = volume

V_w = volume of beam web element DCE (Fig. 24)

W = gravity load on a frame

W_e = rate of external work

c_r = concrete cover of the reinforcement

d = total depth of the steel beam

f_c' = cylinder compressive strength of concrete

f_y = average yield stress of steel beam

f_{yc} = yield stress of shear connectors

f_{yF} = yield stress of steel beam flange

f_{yr} = yield stress of reinforcement

f_{yw} = yield stress of steel beam web

k = yield stress in shear

ℓ_i = distance of head of stud connector i to plane AC (Fig. 24)

ℓ_c = length of the shear connectors

n = number of connectors in wedge ABC (Fig. 24)

p = bearing capacity of concrete at end plate

p_t = transverse reinforcement ratio (ratio of transverse reinforcement to the longitudinal area of the concrete slab)

p_ℓ = longitudinal reinforcement ratio (ratio of area of longitudinal reinforcement to the transverse area of the concrete slab)

r = radial distance

t = slab thickness

t_w = thickness of beam web

α = angle

β = angle

$\dot{\gamma}$ = shear strain rate

ε_y = yield strain

ε_{st} = strain at strain hardening

$\dot{\varepsilon}$ = axial strain rate

$\dot{\vartheta}$ = angular velocity

ϑ_p = rotation corresponding to plastic moment of steel beam

11. TABLES

COMPOSITE BEAM	B-44	B-64	B-84	B-66
SLAB WIDTH	4 ft.	6 ft.	8 ft.	6 ft.
SLAB THICKNESS		4 in.		6 in.
CONCRETE STRENGTH	3.0 ksi			
STEEL BEAM SIZE	W12x27 A572 Grade 50			
CONNECTOR SIZE	1/2 in. dia.			
END PLATE WIDTH	18 in.			
LOADING	STATIC			

Table 1 Description of the Phase 1 Connection Tests and Loading

SECTION	NO. OF TESTS	DYNAMIC YIELD POINT (KSI)	STATIC YIELD STRESS (KSI)	TENSILE STRENGTH (KSI)
		MEAN	MEAN	MEAN
FLANGE	4	59.3	57.4	83.0
WEB	2	61.1	58.5	83.5

Table 2 Mechanical Properties of Steel Beams

LENGTH (in.)	DIAMETER (in.)	NO. OF TESTS	TENSILE STRENGTH (ksi)	% ELONGATION
			MEAN	MEAN
3	1/2	2	82.3	9
4	1/2	4	78.3	10

Table 3 Mechanical Properties of Stud Connectors

BEAM	COMPRESSIVE STRENGTH AT END PLATE		AVERAGE COMPRESSIVE STRENGTH		AVERAGE MODULUS OF ELASTICITY
	No. of Tests	f'_c ksi	No. of Tests	f'_c ksi	$57\sqrt{f'_c}$ ksi
		MEAN		MEAN	MEAN
B-44	4	3.18	8	3.44	3340
B-64	4	3.32	12	3.06	3160
B-84	4	2.50	10	2.59	2900
B-66	3	3.06	10	2.81	3030

Table 4 Properties of Concrete

		SERIES 1			SERIES 2					
		W12x27 f'_c=3ksi			W12x27 f'_c=3ksi					
		4" Solid Slab			4" Longitudinal Metal Deck			4" Transverse Metal Deck		
	Gap Size (in)	Connector Density			Connector Density			Connector Density		
		High	Normal	Zero	High	Normal	Zero	High	Normal	Zero
With Transverse Support Hangers	0	C1	A1	C2	E1	E2		F1	F2	
	0.02	D1	A2	D2						
Without Transverse Support Hangers	0	B1								
	0.02	B2								

		SERIES 3			SERIES 4		
		W12x27 f'_c=5ksi			W16x40 f'_c=3ksi		
		4" Solid Slab			4" Solid Slab		
	Gap Size (in)	Connector Density			Connector Denisty		
		High	Normal	Zero	High	Normal	Zero
With Transverse Support Hangers	0	G1			H1		
	0.02	G2			H2		
Without Transverse Support Hangers	0						
	0.02						

Note: All values of f'_c shown are nominal values.

Table 5 Details of the Phase 2 Connection Test Program

SHAPE	BEAM NUMBER	PART	DYNAMIC YIELD STRESS (KSI)		STATIC YIELD STRESS (KSI)		TENSILE STRENGTH (KSI)	
			TEST	AVERAGE	TEST	AVERAGE	TEST	AVERAGE
W12x27	A B C D	FLANGE	57.4 57.6 56.7 57.5	57.3	55.2 55.6 54.3 55.0	55.0	77.8 77.8 77.0 77.8	77.6
		WEB	59.8 61.2	60.5	57.9 59.4	58.7	82.3 82.8	82.5
	E F G	FLANGE	56.4 56.4 56.6 56.8	56.5	54.9 54.3 53.7 54.0	54.2	77.7 77.2 77.0 77.0	77.2
		WEB	58.0 58.1	58.1	55.8 55.4	55.6	78.6 79.7	79.2
W16x40	H	FLANGE	57.4 57.2 57.0 57.5	57.3	55.3 54.8 55.1 54.6	55.0	82.4 83.0 82.4 83.2	82.8
		WEB	58.6 60.7	59.7	56.6	56.6	81.3 81.7	81.5

Table 6 Mechanical Properties of Steel Beams

LENGTH (in)	DIAMETER (in)	TENSILE STRENGTH (KSI)		PERCENTAGE ELONGATION	
		TEST	AVERAGE	TEST	AVERAGE
3	3/4	67.5 68.8 74.5 66.8 70.4	69.5	----	----

Table 7 Mechanical Properties of Stud Connectors

BEAM NUMBER	COMPRESSIVE STRENGTH (KSI)		SLUMP (IN)	AVERAGE MODULUS OF ELASTICITY (KSI)
	TEST	AVERAGE		$57\sqrt{f'_c}$
A1, A2	3.45 3.34	3.40	4½	3330
B1, B2	3.57 3.53	3.55	4½	3400
C1, C2	4.44 4.54 4.44 4.40 4.62 4.51	4.49	6¼	3820
D1, D2	4.52 4.67 4.51 4.47 4.60 4.59	4.56	—	3850
E1, E2	4.05 4.19 4.26 4.08 4.25 4.32	4.19	—	3690
F1, F2	4.11 4.30 4.37 4.20 4.15 4.08	4.20	—	3700
G1, G2	6.26 6.08 6.13 6.14 6.28 6.03	6.15	—	4480
H1, H2	3.70 3.84 3.59 3.77 3.77 3.77	3.74	—	3480

Table 8 Properties of the Concrete

BEAM	α	P_u (kip)	M_u (kip-ft.)	LENGTH AB (FIG. 24) (in.)
B-44	36^o	46.25	354.5	8.4
B-64	34^o	29.93	349.2	8.6
B-84	32^o	20.90	327.5	8.9
B-64	44^o	37.38	436.1	12.0

Table 9 Upper Bound Values

BEAM	M_L SLIP LINE (kip-ft.)		M_L EQUIV. TRUSS (kip-ft.)
	$2.57\ f'_c$	$1.3\ f'_c$	
B-44	332	248	294
B-64	336	250	296
B-84	310	287	283
B-66	412	305	412

Table 10 Lower Bound Values

BEAM NO.	TEST MOMENT K.FT.	PERCENT OF MAXIMUM MOMENT	COMPUTED FROM FIG. 44 K.FT.	RATIO OF TEST TO COMPUTED MOMENT
B-44	301	92	283	1.06
B-64	273	85	281	0.97
B-84	291	94	267	1.09
B-66	332	93	297	1.12

Table 11 Moments at Gage Section a Before Spalling of the Concrete

BEAM NO.	TEST MOMENT K.FT.	PERCENT OF MAXIMUM MOMENT	MOMENT COMPUTED FROM FIG. 44 K.FT.	RATIO OF TEST TO COMPUTED MOMENT
B-44	314	100	276	1.14
B-64	322	100	271	1.19
B-84	313	100	264	1.18
B-66	357	100	309	1.16

Table 12 Moments at Gage Section A at Maximum Moment

BEAM NO.	TEST MOMENT K.FT.	PERCENT OF MAXIMUM MOMENT	MOMENT COMPUTED FROM FIG. 44 K.FT.	RATIO OF TEST TO COMPUTED MOMENT
B-44	329	100	320	1.03
B-64	331	100	321	1.03
B-84	320	100	309	1.04
B-66	364	100	388	0.94

Table 13 Maximum Moment at the End Plate

TEST NUMBER	MAXIMUM STRENGTH RATIO M_{MAX}/M_p	INITIAL SLOPE	DUCTILITY FACTOR
A1	1.73	1.80	7.8
A2	1.68	1.25	5.6
B1	1.64	1.73	7.5
B2	1.65	1.23	6.4
C1	1.72	1.67	4.8
C2	1.71	1.69	5.0
D1	1.75	1.27	5.9
D2	1.79	1.21	6.3
E1	1.59	1.47	4.6
E2	1.54	1.27	5.7
F1	1.57	1.30	4.6
F2	1.61	1.31	4.8
G1	1.87	1.78	4.7
G2	(1.65)	1.45	(4.4)
H1	1.68	1.67	6.4
H2	1.67	1.00	5.6

Table 14 Maximum Strength, Initial Slope and Ductility Factors

EFFECT OF A SHRINKAGE GAP							
TESTS (WITH SHRINKAGE GAP)	TESTS (WITHOUT SHRINKAGE GAP)	MAXIMUM STRENGTH RATIO M_{MAX}/M_p		INITIAL STIFFNESS		DUCTILITY FACTOR	
1	2	INCREASE %	DECREASE %	INCREASE %	DECREASE %	INCREASE %	DECREASE %
A2	A1		2.8		30.5		28.2
B2	B1	0.6			28.9		14.7
G2	G1		(11.8)		18.5		(6.4)
H2	H1		0.7		40.0		12.5
AVERAGE			1.0		29.5		18.5

Table 15 Effect of a Shrinkage Gap

EFFECT OF CONNECTOR DENSITY							
TESTS (LESS DENSE SPACING)	TESTS (DENSER SPACING)	MAXIMUM STRENGTH RATIO M_{MAX}/M_p		INITIAL STIFFNESS		DUCTILITY FACTOR	
1	2	INCREASE %	DECREASE %	INCREASE %	DECREASE %	INCREASE %	DECREASE %
C2	C1		0.6	1.2		4.2	
D2	D1	2.3			4.7	6.8	
E2	E1		3.1		13.6	24.0	
F2	F1	2.5		0.8		4.3	
AVERAGE		0.3			4.1	9.8	

Table 16 Effect of Connector Density

EFFECT OF CONCRETE STRENGTH							
TESTS (HIGH CONCRETE STRENGTH)	TESTS (NORMAL CONCRETE STRENGTH	MAXIMUM STRENGTH RATIO		INITIAL STIFFNESS		DUCTILITY FACTOR	
		INCREASE %	DECREASE %	INCREASE %	DECREASE %	INCREASE %	DECREASE %
1	2						
G1	A1	8.1			1.1		39.1
G1	C1	8.7		6.6			2.1
G1	C2	9.3		5.3			6.0
AVERAGE		8.7		3.6			15.9

Table 17 Effect of Concrete Strength

EFFECT OF STEEL BEAM DEPTH							
TESTS (LARGER BEAM DEPTH)	TESTS (SMALLER BEAM DEPTH)	MAXIMUM STRENGTH RATIO		INITIAL STIFFNESS		DUCTILITY FACTOR	
		INCREASE %	DECREASE %	INCREASE %	DECREASE %	INCREASE %	DECREASE %
1	2						
H1	A1		2.9		7.2		18.0
H1	C1		2.3		0.0	33.3	
H1	C2		1.8		1.2	38.0	
H2	A2		0.6		20.0		0.0
H2	D1		4.6		21.3		5.1
H2	D2		6.7		17.4		11.1
AVERAGE			3.1		11.2	4.5	

Table 18 Effect of Steel Beam Depth

EFFECT OF METAL DECK SLABS: LONGITUDINAL RIBS							
TESTS (WITH METAL DECK SLABS)	TESTS (WITH SOLID SLABS)	MAXIMUM STRENGTH RATIO		INITIAL STIFFNESS		DUCTILITY FACTOR	
		INCREASE %	DECREASE %	INCREASE %	DECREASE %	INCREASE %	DECREASE %
1	2						
E1	A1		8.1		18.3		41.0
E1	C1		7.6		12.0		4.2
E1	C2		7.0		13.0		8.0
E2	A1		11.0		29.4		26.9
E2	C1		10.5		24.0	18.7	
E2	C2		9.9		24.9	14.0	
AVERAGE			9.0		20.3		7.9

Table 19 Effect of Metal Deck Slabs with Longitudinal Ribs

EFFECT OF METAL DECK SLABS: TRANSVERSE RIBS							
TESTS (WITH METAL DECK SLABS)	TESTS (WITH SOLID SLABS	MAXIMUM STRENGTH RATIO		INITIAL STIFFNESS		DUCTILITY FACTOR	
		INCREASE %	DECREASE %	INCREASE %	DECREASE %	INCREASE %	DECREASE %
1	2						
F1	A1		9.3		27.8		41.0
F1	C1		8.7		22.2		4.2
F1	C2		8.2		23.1		8.0
F2	A1		6.9		27.2		38.5
F2	C1		6.4		21.5		0.0
F2	C2		5.9		22.5		4.0
AVERAGE			7.6		24.1		15.9

Table 20 Effect of Metal Deck Slabs with Transverse Ribs

EFFECT OF LATERAL SUPPORT AT THE COLUMN							
TESTS (WITH LATERAL SUPPORT)	TESTS (NO LATERAL SUPPORT)	MAXIMUM STRENGTH RATIO		INITIAL STIFFNESS		DUCTILITY FACTOR	
		INCREASE %	DECREASE %	INCREASE %	DECREASE %	INCREASE %	DECREASE %
1	2						
A1	B1	5.5		4.0		4.0	
A2	B2	1.8		1.6			12.5
AVERAGE		3.7		2.8			4.3

Table 21 Effect of Lateral Support at the Column

TEST VARIABLE	MAXIMUM STRENGTH RATIO		INITIAL STIFFNESS		DUCTILITY FACTOR	
	INCREASE %	DECREASE %	INCREASE %	DECREASE %	INCREASE %	DECREASE %
SHRINKAGE GAP		1.0		29.5		18.5
INCREASED CONNECTOR DENSITY	0.3			4.1	9.8	
INCREASED CONCRETE STRENGTH	8.7		3.6			15.9
INCREASED BEAM DEPTH	3.1			11.2	4.5	
METAL DECK (LONGITUDINAL RIBS)		9.0		20.3		7.9
METAL DECK (TRANSVERSE RIBS)		7.6		24.1		15.9
LATERAL SUPPORT	3.7		2.8			4.3
REPEATED LOADS	0.0		0.0		0.0	

Table 22 Summary of Test Results

TEST NO	MAXIMUM STRENGTH RATIO M_{MAX}/M_P			RATIO OF UPPER BOUND TO TEST	RATIO OF TEST TO LOWER BOUND
	TEST	UPPER BOUND	LOWER BOUND		
A1	1.73	2.03	1.53	1.17	1.13
A2	1.68	2.03	1.53	1.21	1.10
B1	1.64	2.13	1.54	1.30	1.07
B2	1.65	2.13	1.54	1.29	1.07
C1	1.72	2.22	1.61	1.29	1.07
C2	1.71	2.07	1.61	1.21	1.06
D1	1.75	2.22	1.61	1.27	1.09
D2	1.79	2.08	1.61	1.16	1.11
E1	1.59	1.81	1.48	1.14	1.07
E2	1.54	1.80	1.48	1.17	1.04
F1	1.57	1.80	1.48	1.15	1.06
F2	1.61	1.80	1.48	1.12	1.09
G1	1.87	2.18	1.72	1.16	1.09
G2	(1.65)	2.18	1.72	(1.32)	(0.96)
H1	1.68	1.91	1.67	1.14	1.01
H2	1.65	1.91	1.67	1.15	1.00

Table 23 Correlation of Theoretical and Test Values of Maximum Strength Ratio

TEST NO	INTERNAL DISSIPATION OF ENERGY (Kip in)								
	1	2	3	4	5	6	7	8	TOTAL
A1	377	0	1070	1710	232	147	35	365	3936
A2	377	0	1070	1710	232	147	35	365	3936
B1	351	300	1283	1710	159	147	257	0	4207
B2	351	300	1283	1710	159	147	257	0	4207
C1	453	0	1222	1710	172	147	290	383	4377
C2	465	0	1167	1710	188	147	0	383	4060
D1	451	0	1283	1710	159	147	257	384	4391
D2	472	0	1167	1710	188	147	0	384	4068
E1	464	0	1070	1710	67	45	24	131	3511
E2	464	0	1070	1710	67	45	4	131	3491
F1	466	0	1070	1710	67	45	10	131	3499
F2	466	0	1070	1710	67	45	4	131	3493
G1	637	0	1105	1685	188	147	13	399	4174
G2	637	0	1105	1685	188	147	13	399	4174
H1	456	0	2568	3099	301	147	19	372	6962
H2	456	0	2568	3099	301	147	19	372	6962

Column 1: DISSIPATION IN SLAB - SHEAR DEFORMATION
2: DISSIPATION IN SLAB - SHEARING OF SIDES
3: DISSIPATION IN BEAM WEB
4: DISSIPATION IN BEAM FLANGE
5: DISSIPATION IN TRANSVERSE REINFORCEMENT
6: DISSIPATION IN LONGITUDINAL REINFORCEMENT
7: DISSIPATION IN SHEAR CONNECTORS
8: DISSIPATION IN SLAB IN BENDING

Table 24 Break-down of the Internal Dissipation in the Upper Bound Mechanism

TEST NO	TEST SET-UP (Span in inches)	W (in)	T (in)	BEAM SIZE	$\frac{M_{max}}{M_{Lower\ Bound}}$ 0 0.5 1.0
B-44	96	48	4 Solid	W12x27	
B-64	144	72	4 "	W12x27	
B-84	192	96	4 "	W12x27	
B-66	144	72	6 "	W12x27	
A1	97	48	4 "	W12x27	
A2	97	48	4 "	W12x27	
B1	97	48	4 "	W12x27	
B2	97	48	4 "	W12x27	
C1	97	48	4 "	W12x27	
C2	97	48	4 "	W12x27	
D1	97	48	4 "	W12x27	
D2	97	48	4 "	W12x27	
E1	97	48	4 Rib	W12x27	
E2	97	48	4 "	W12x27	
F1	97	48	4 "	W12x27	
F2	97	48	4 "	W12x27	
G1	97	48	4 Solid	W12x27	
G2	97	48	4 "	W12x27	
H1	97	48	4 "	W16x40	
H2	97	48	4 "	W16x40	

W = SLAB WIDTH

T = SLAB THICKNESS

Table 25 Comparisons of Phase 1 and Phase 2 Test Results with Lower Bound Predictions Based on $p = 1.3\ f'_c$

TEST NO	ROTATION CAPACITY (Radians)
A1	.042
A2	.040
B1	.042
B2	.034
C1	.028
C2	.037
D1	.050
D2	.048
E1	.027
E2	.040
F1	.022
F2	.022
G1	.037
G2	(.000)
H1	.038
H2	.050

Table 26 Rotation Capacity of each test

12. FIGURES

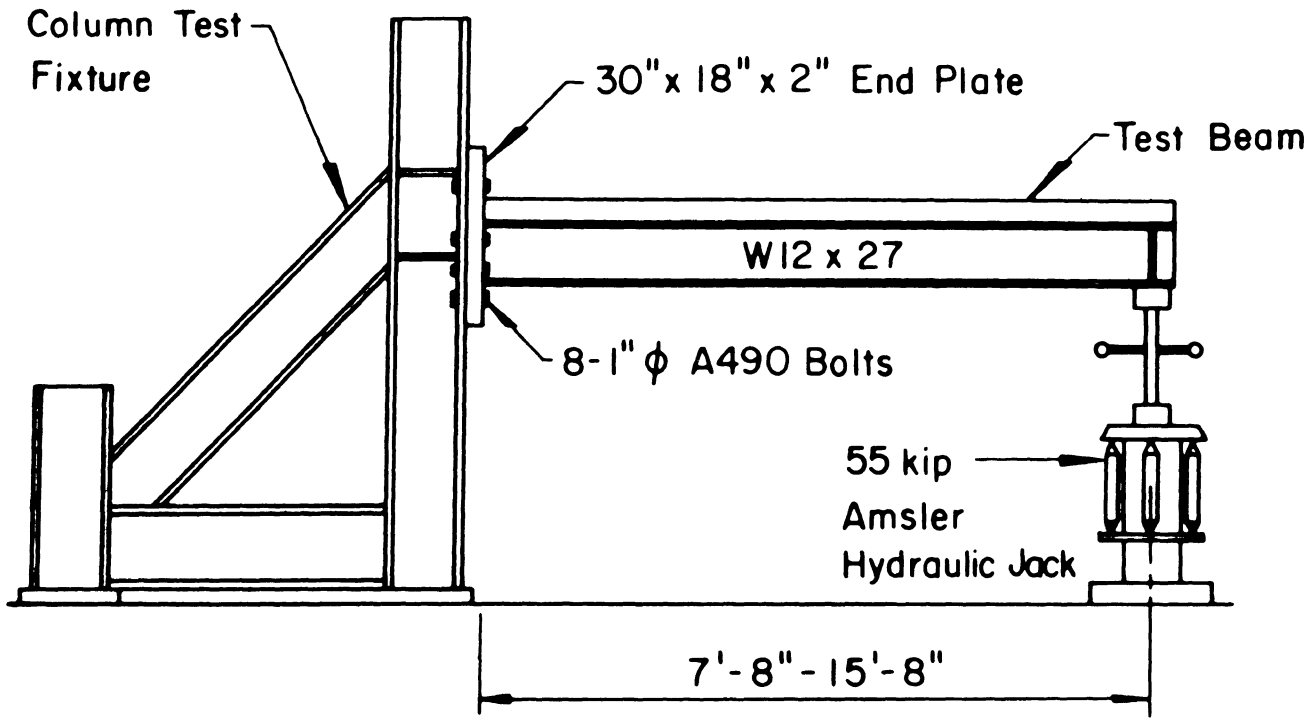

Fig. 1 Typical Test Setup

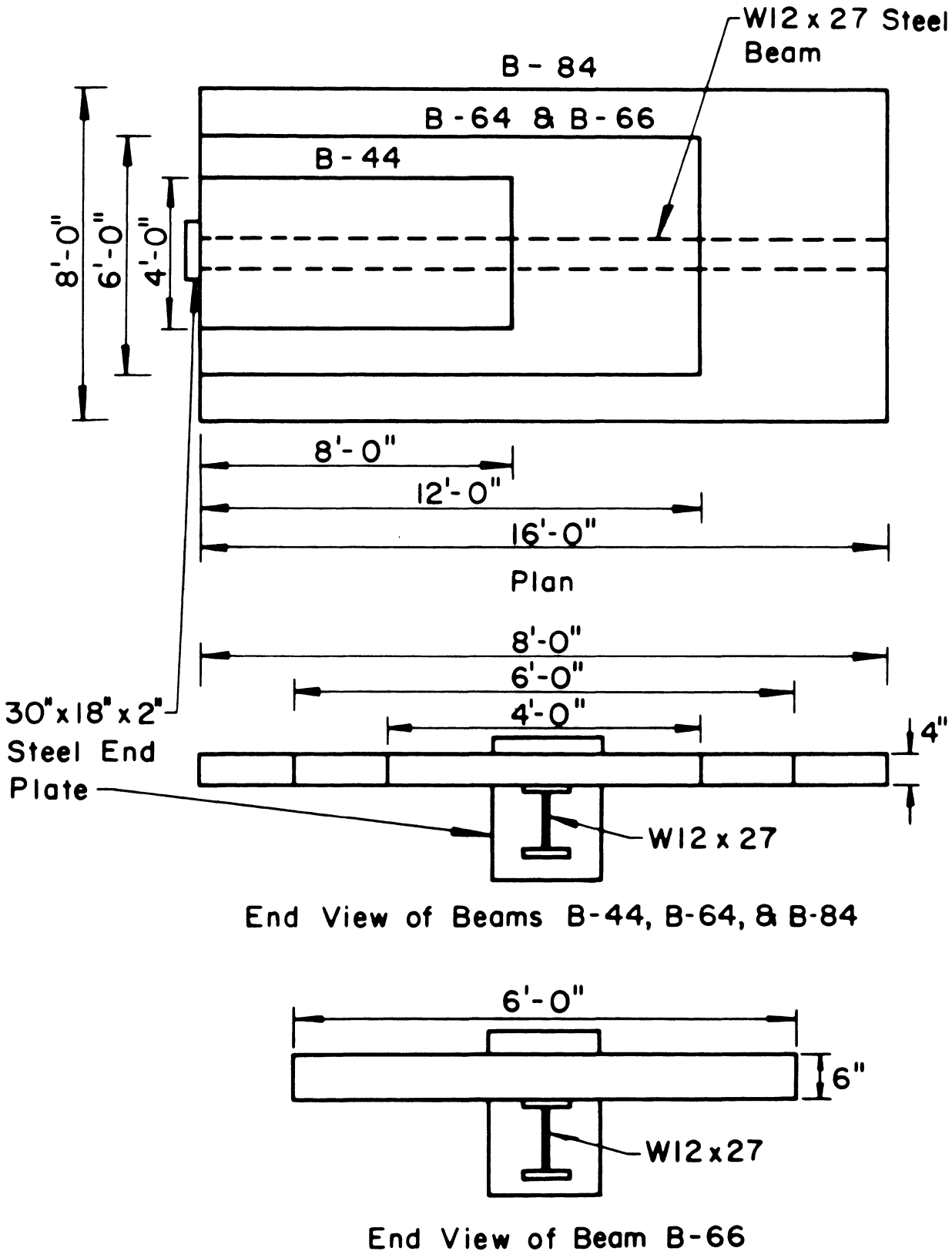

Fig. 2 Construction Details of the Test Beams

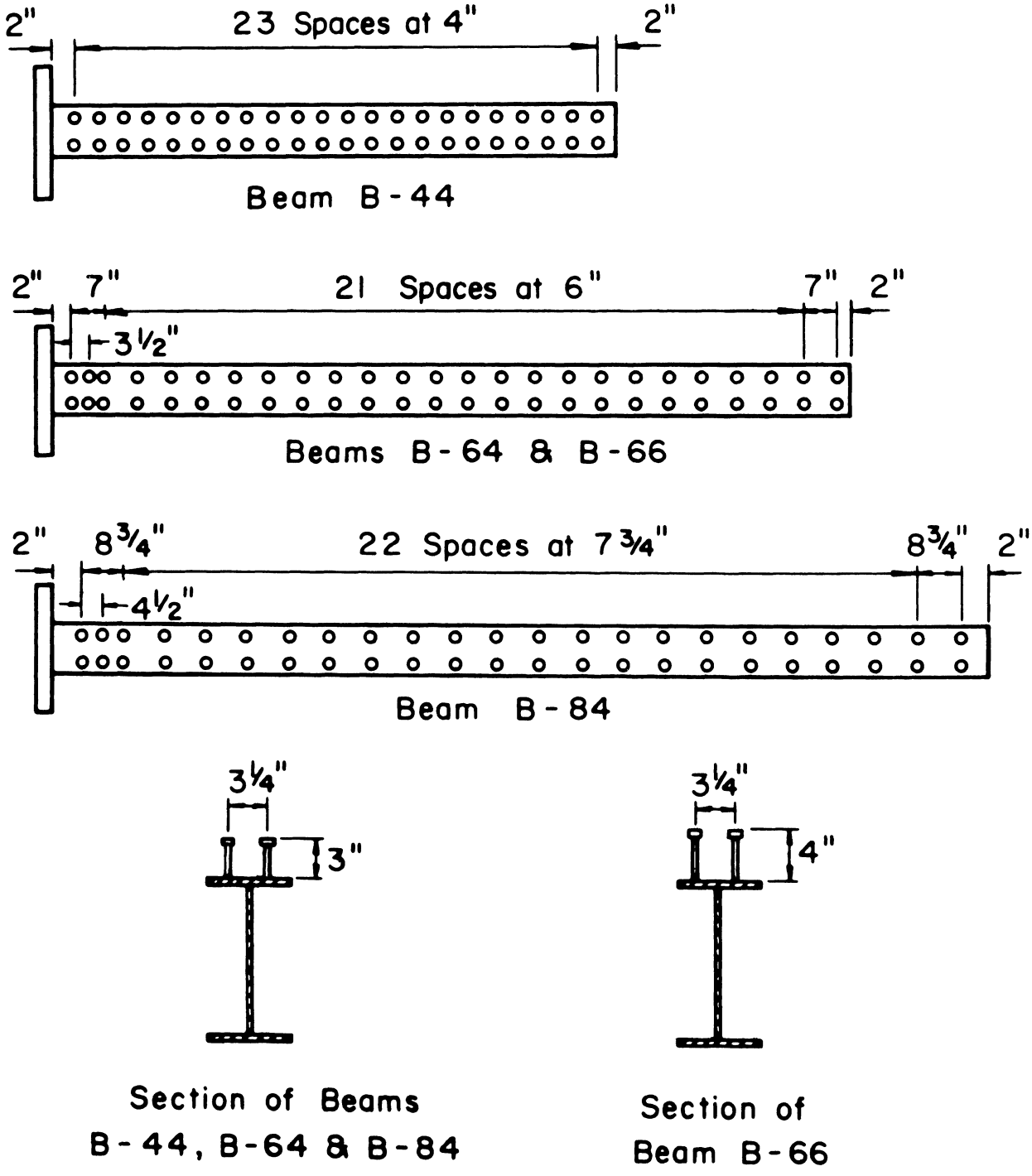

Fig. 3 Details of Steel Beams and Shear Connectors

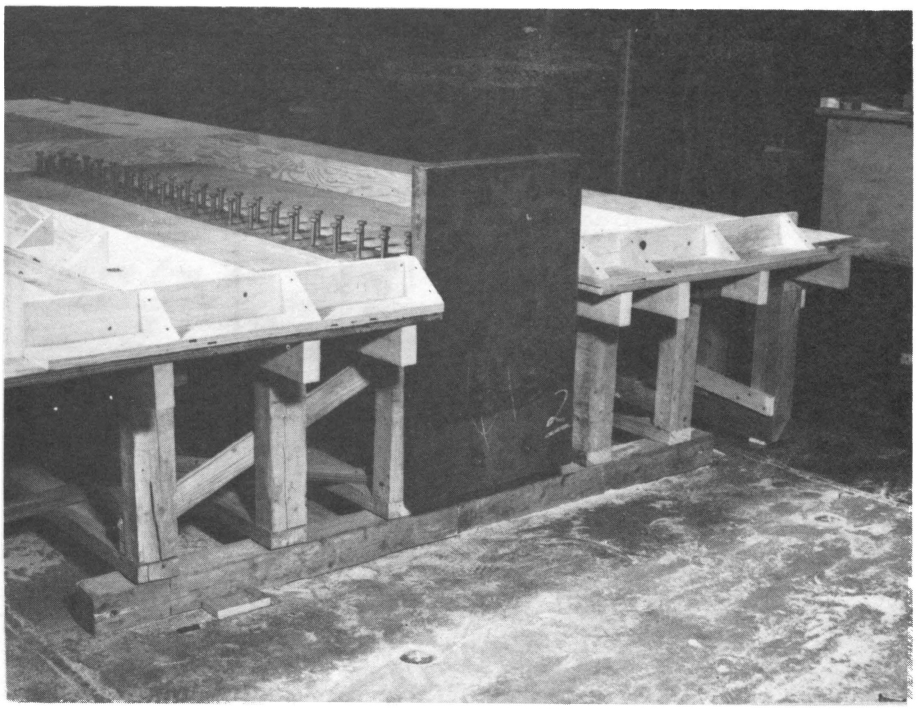

Fig. 4a B-44: View of End Plate

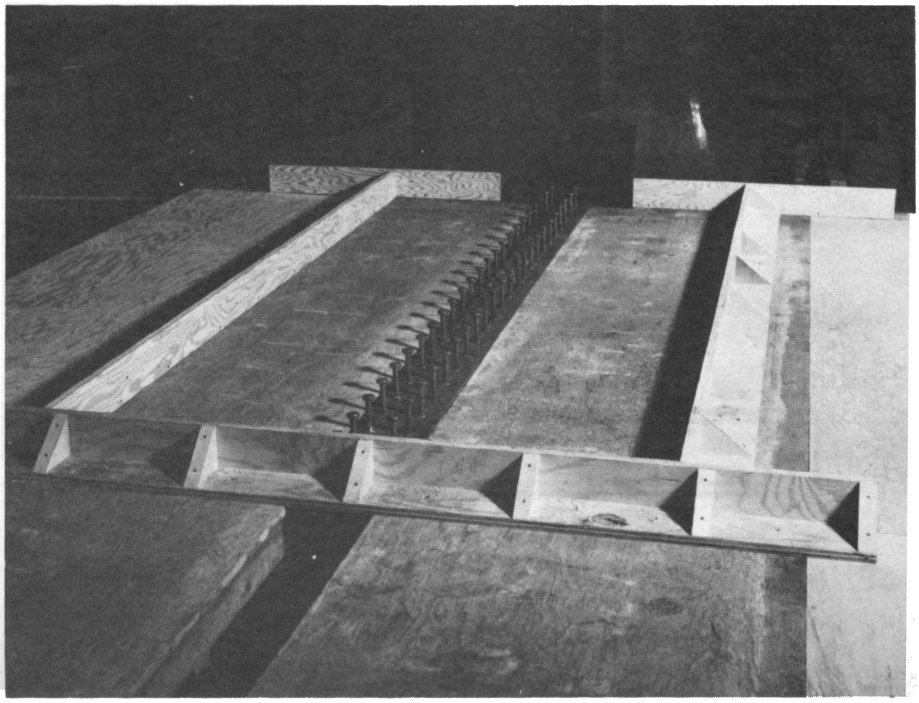

Fig. 4b B-44: Connectors

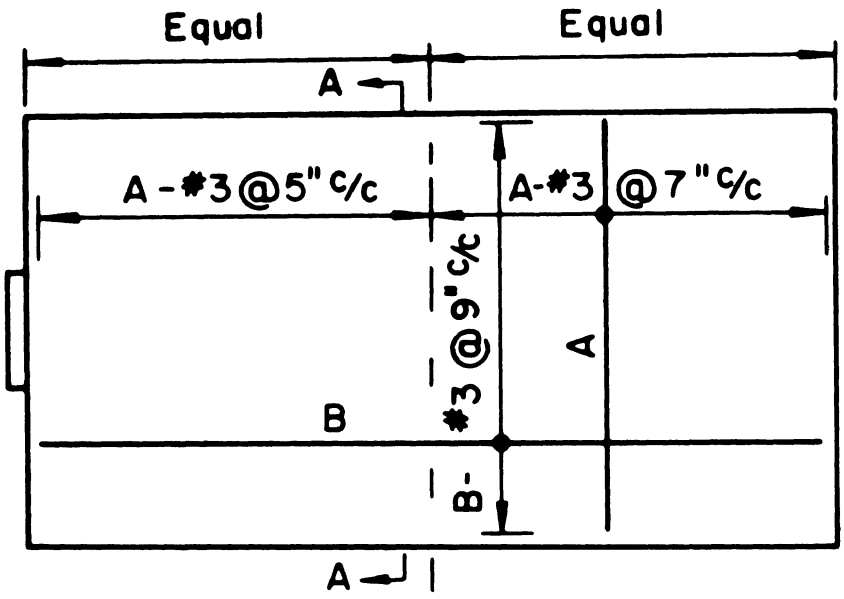

Typical Detail for B-44, B-64 & B-84

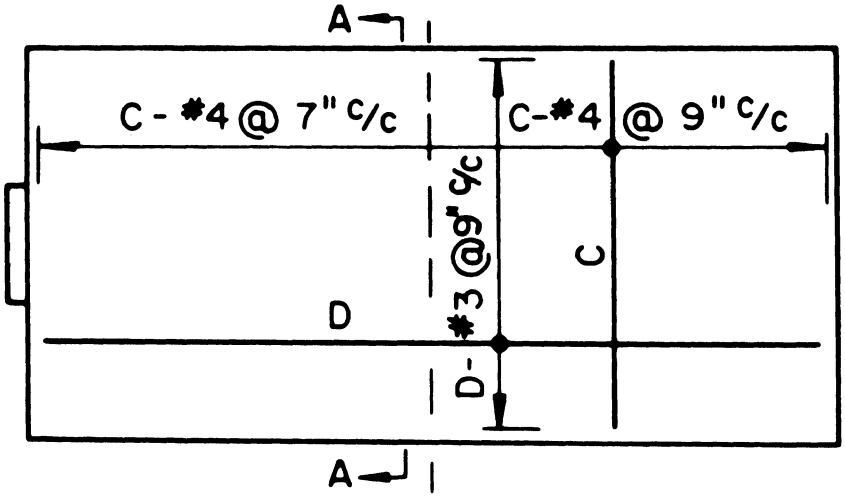

Detail for B-66

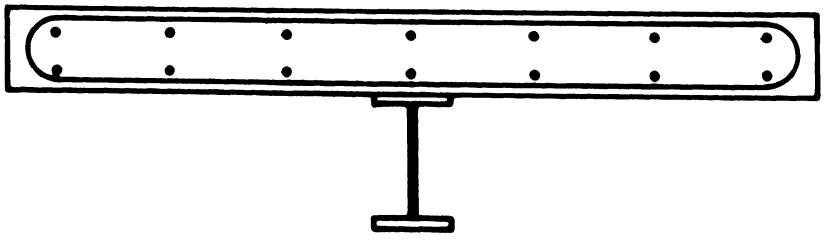

Section A-A

Fig. 5 Slab Reinforcing Details

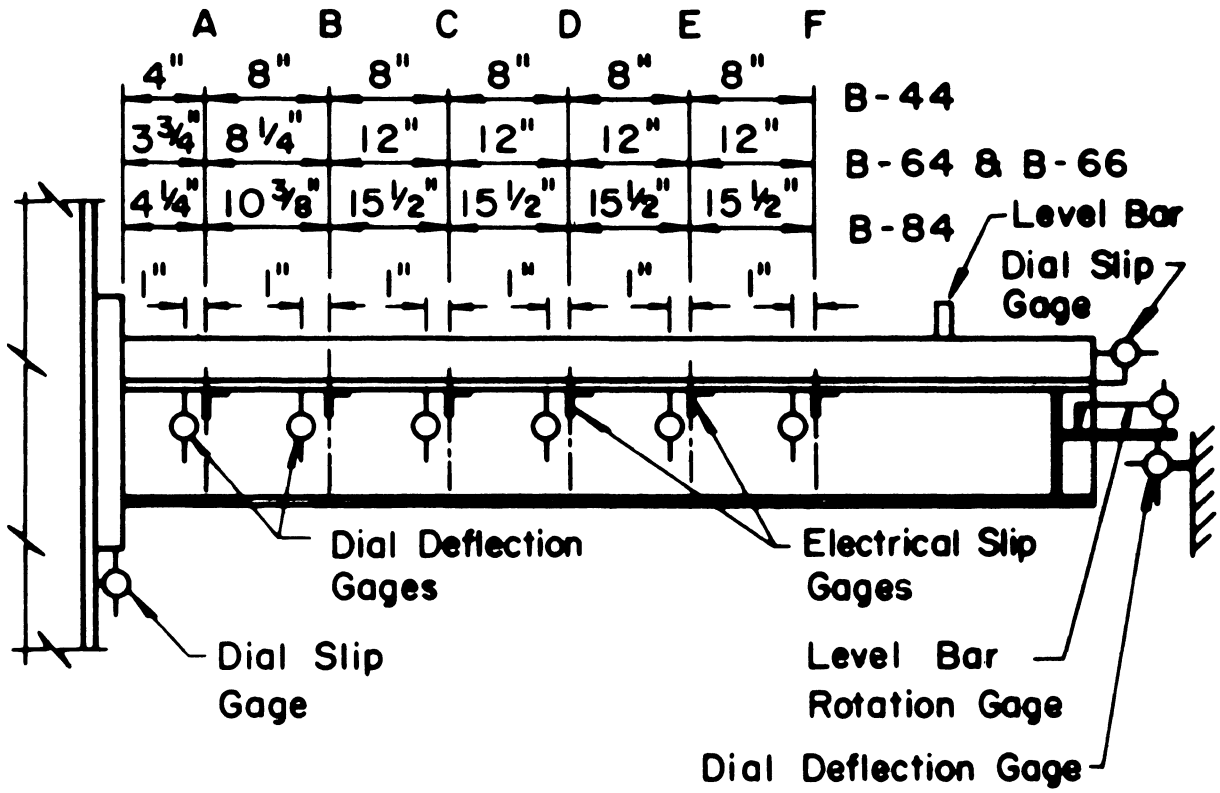

(a) Locations of Instrumented Cross Sections

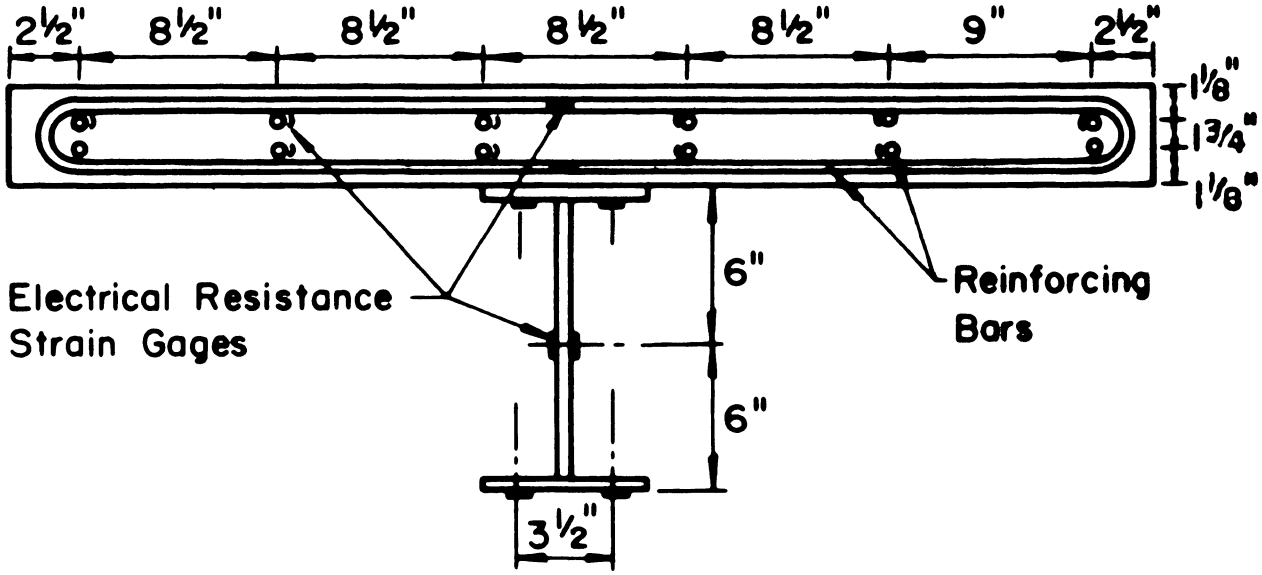

(b) Location of Strain Gages at Gage Section A on Beam B-44

Fig. 6 Instrumentation Details

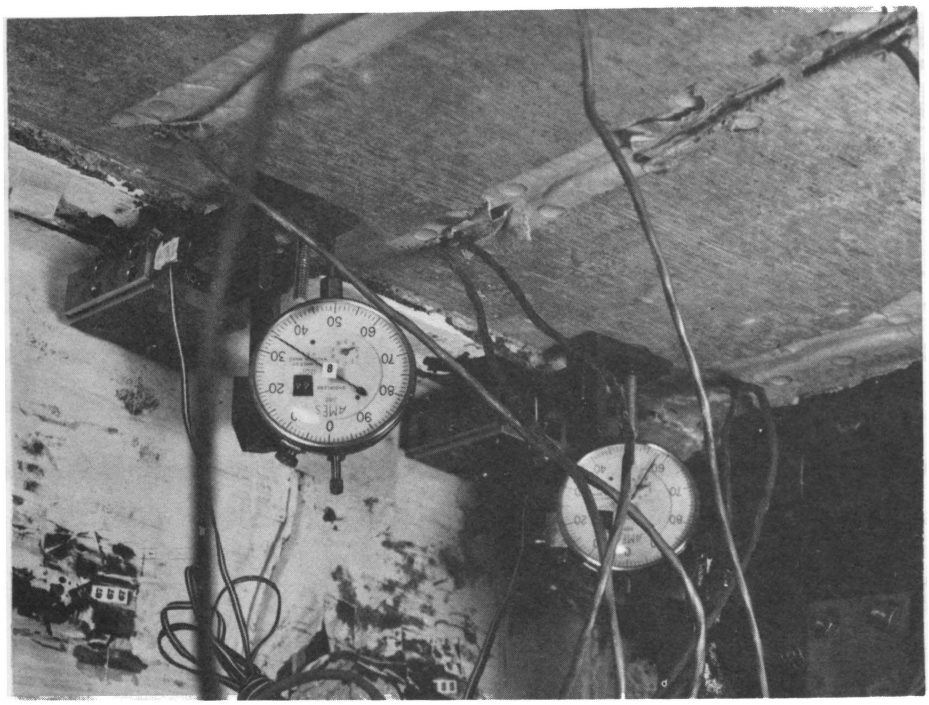

Fig. 7a Close-Up of Slip and Deflection Gages

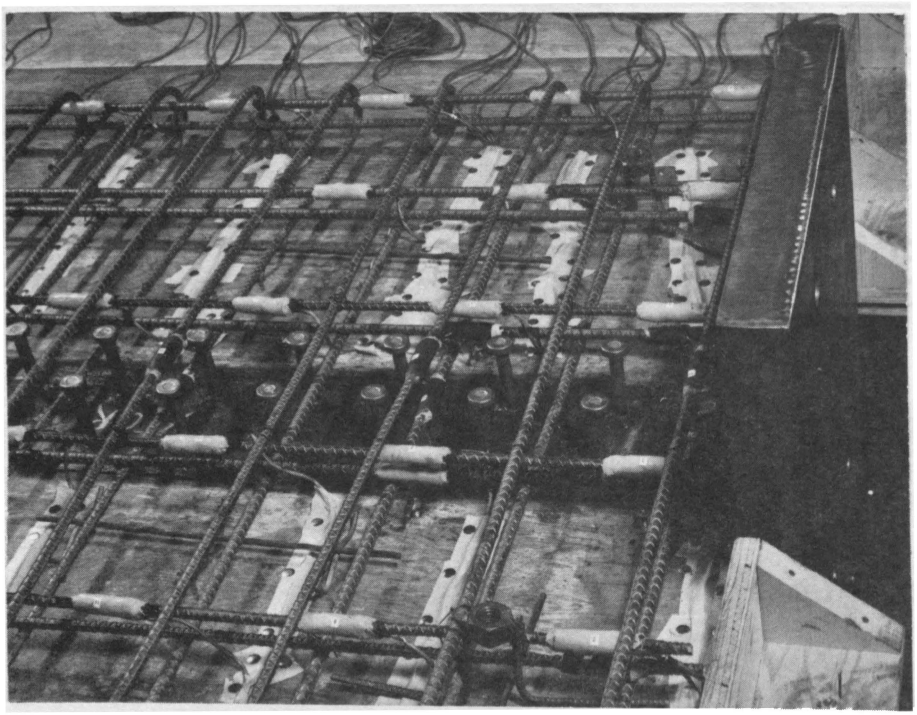

Fig. 7b View of Strain Gages on Reinforcement

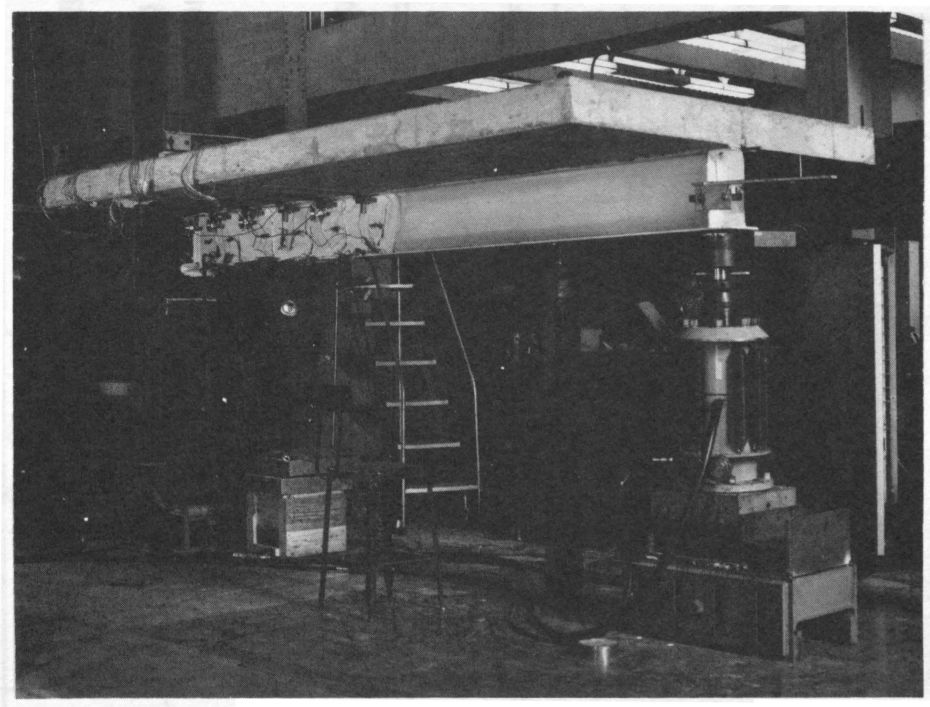

Fig. 8 B-66 in Test Position

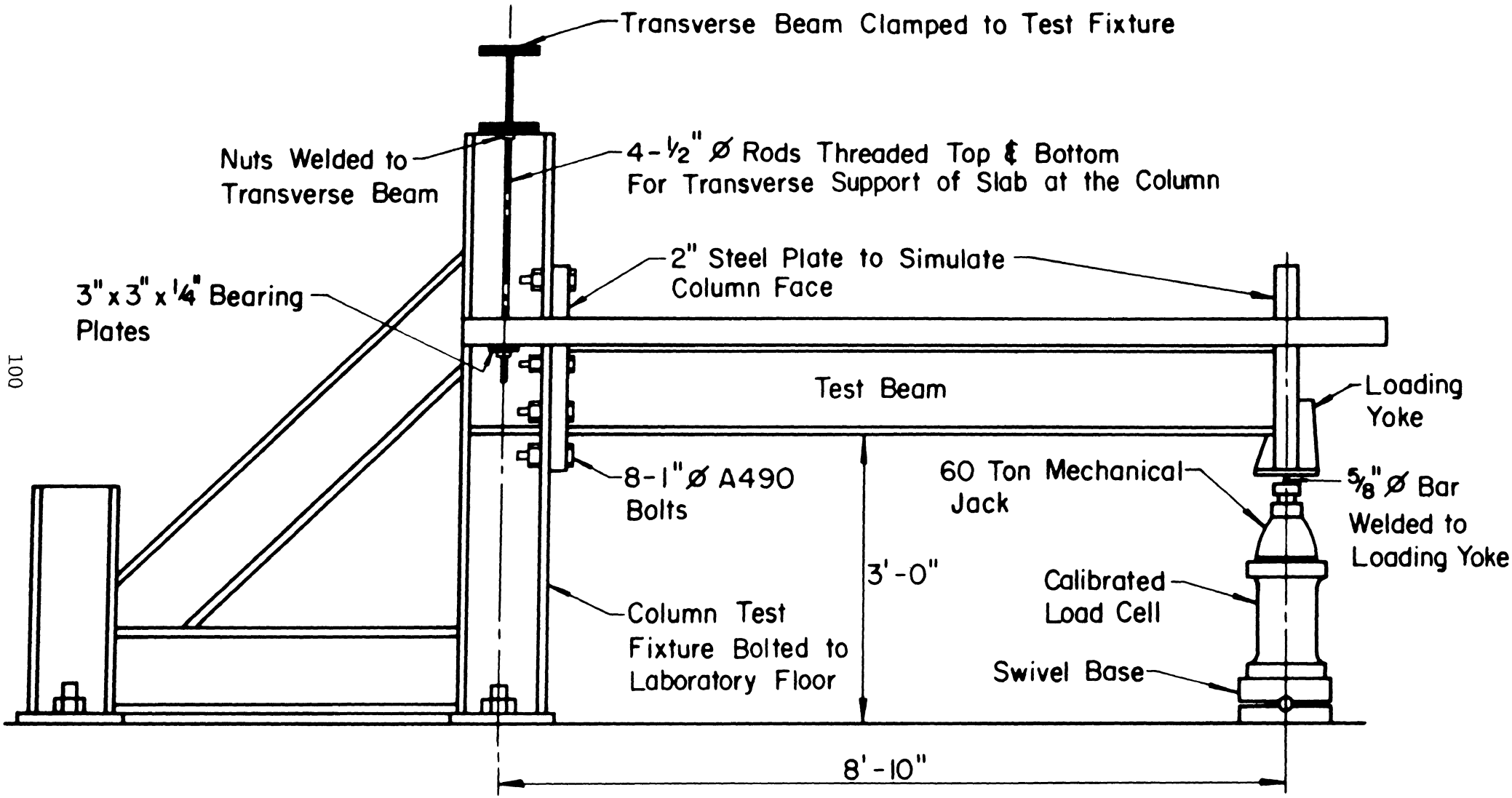

Fig. 9 Schematic View of Test Setup

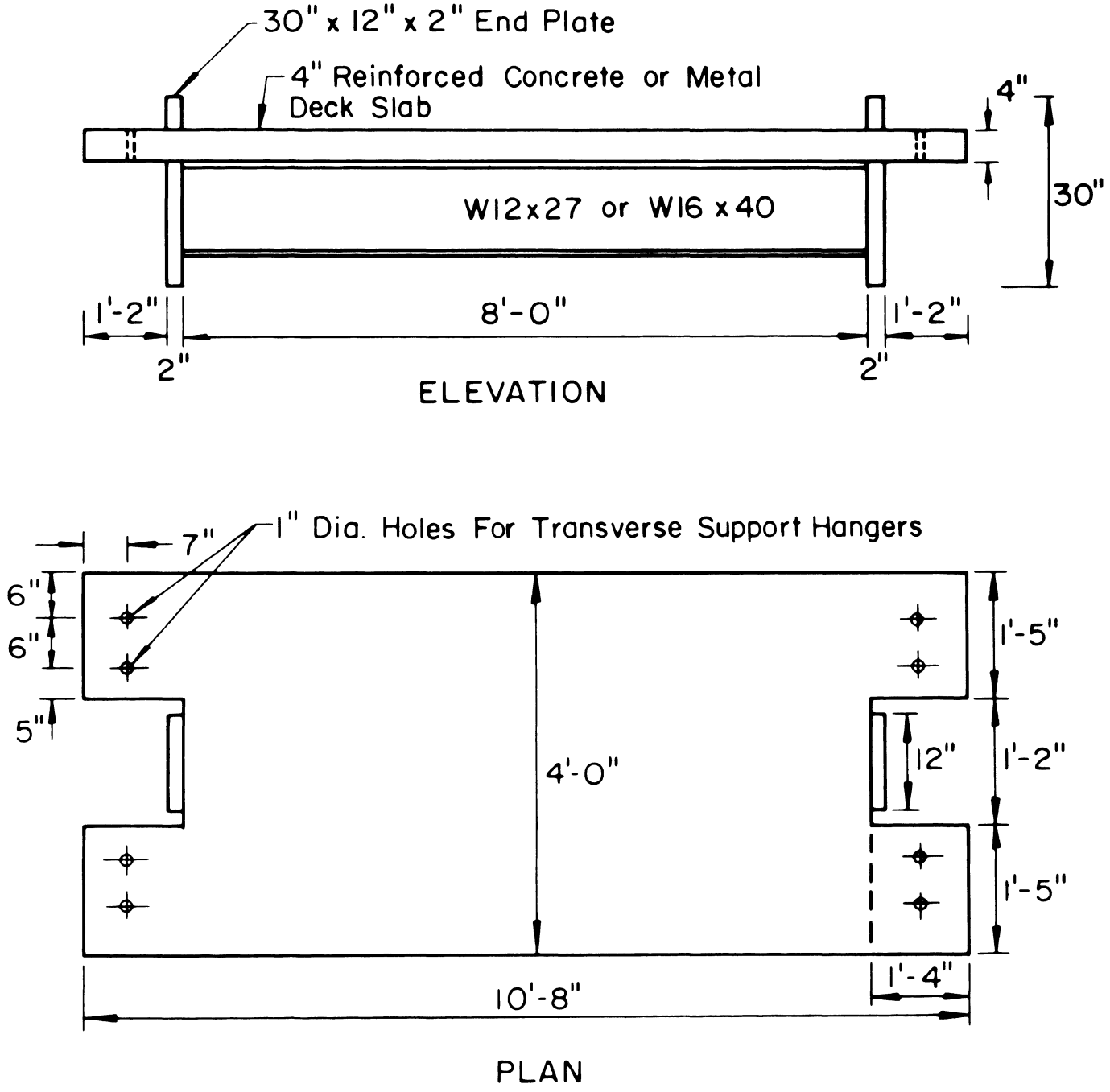

Fig. 10 Typical Test Beam

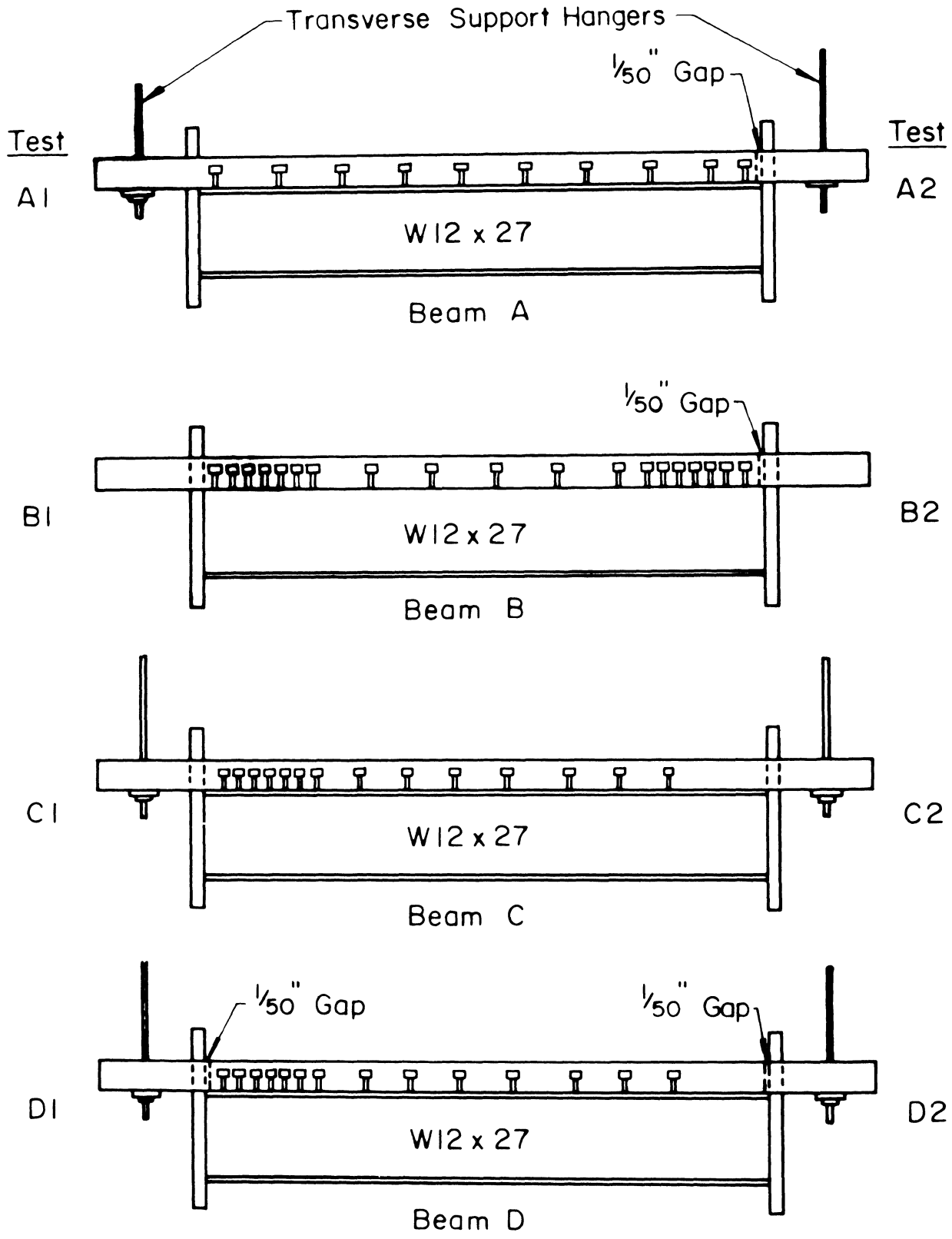

Fig. 11 Detail of Test Beams A, B, C and D

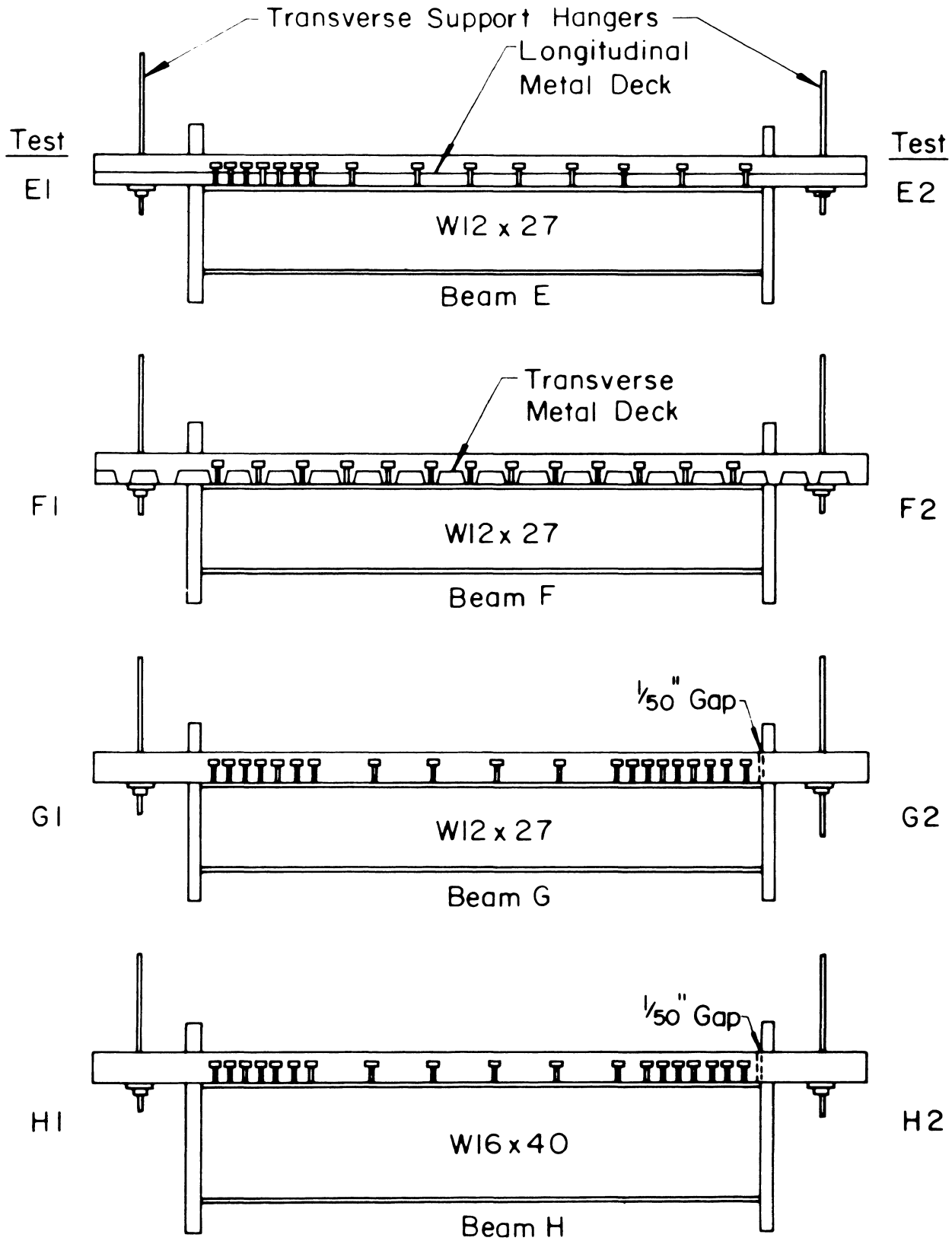

Fig. 12 Detail of Test Beams E, F, G and H

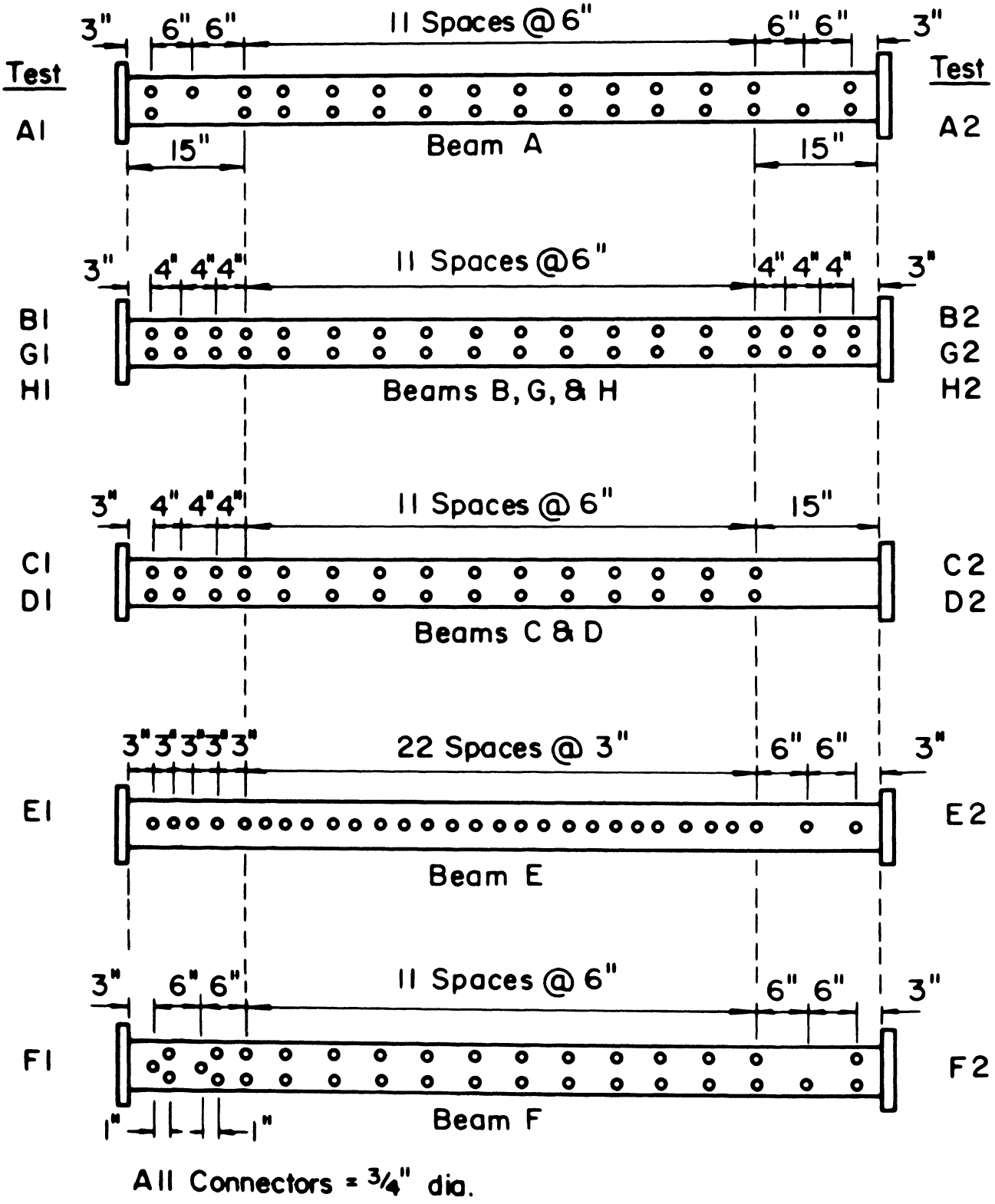

Fig. 13 Details of Connector Spacing

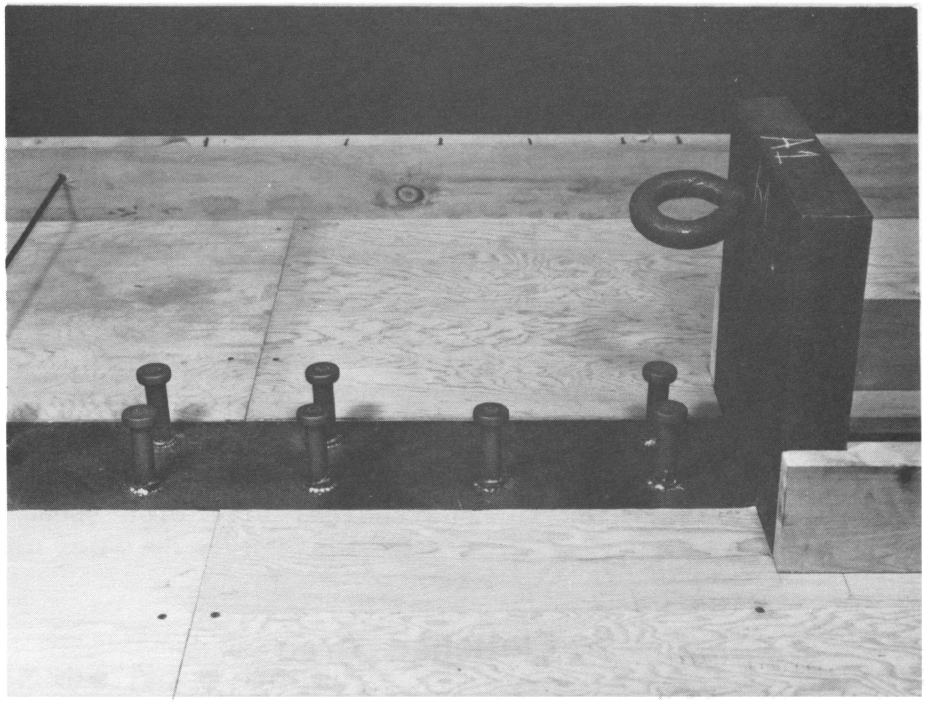

Fig. 14a Typical Normal Density Connector Spacing

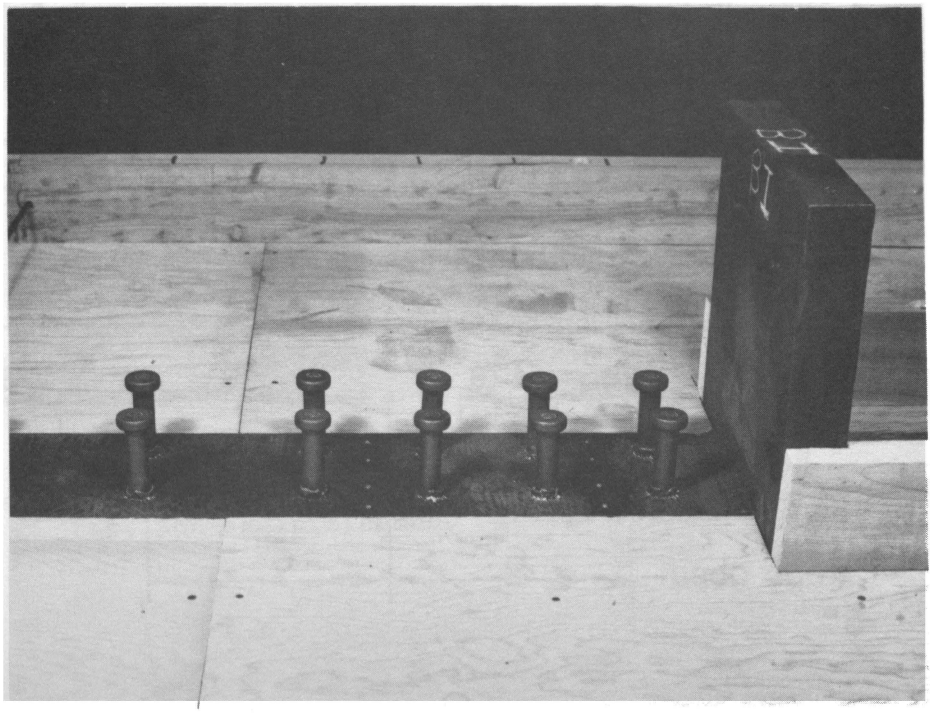

Fig. 14b Typical High Density Connector Spacing

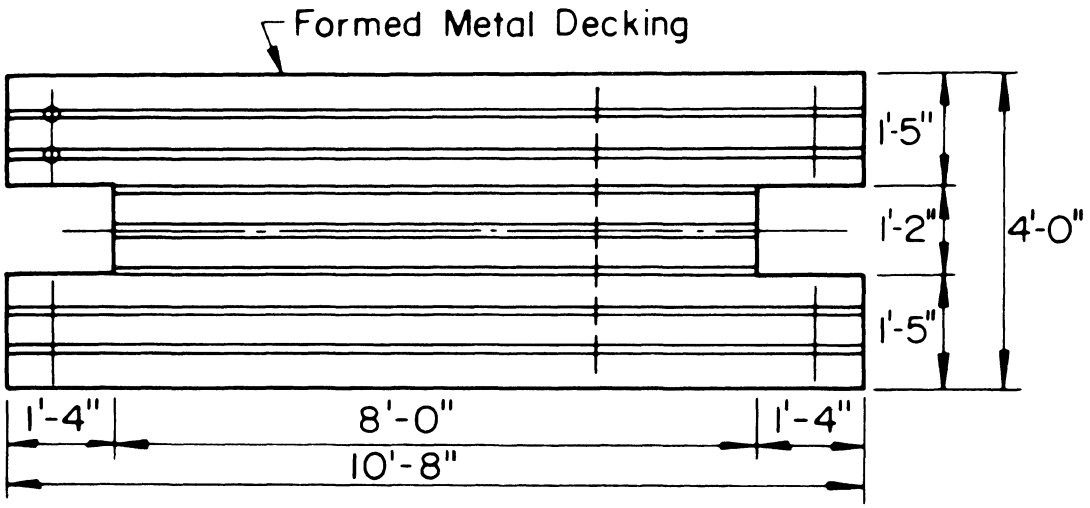

Fig. 15a Ribs in Longitudinal Direction (Beam E)

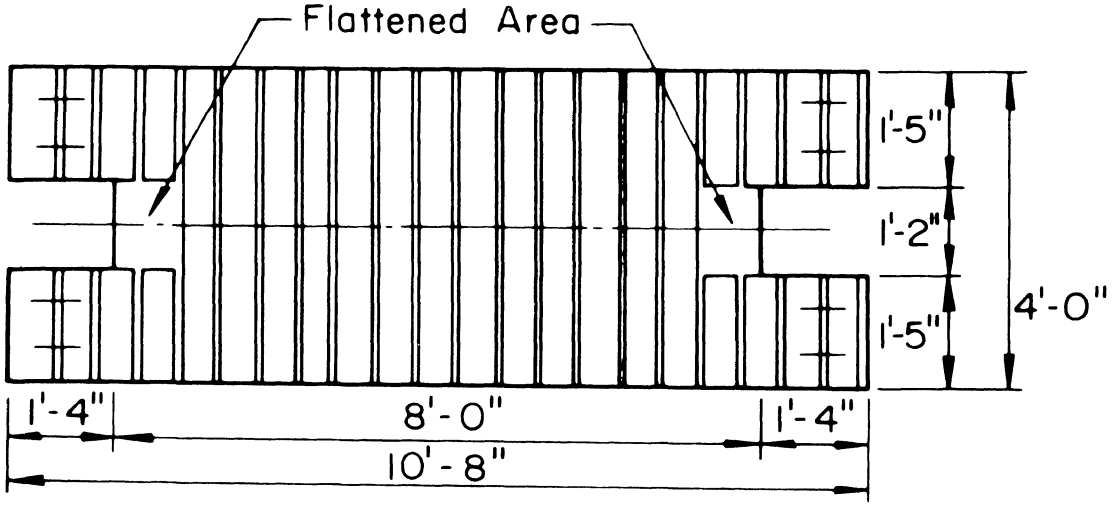

Fig. 15b Ribs in Transverse Direction (Beam F)

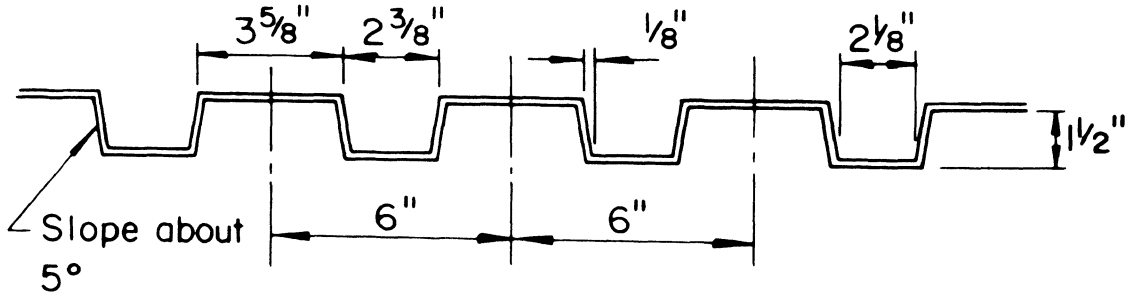

Fig. 15c Detail of Metal Decking (Gage 20)

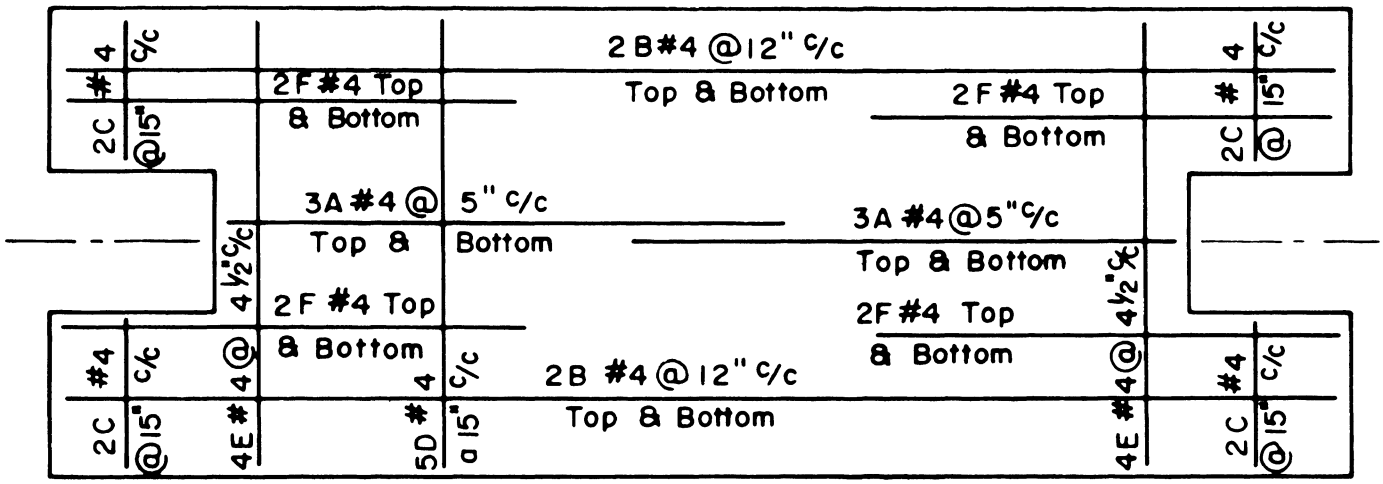

Fig. 16a Reinforcement Details for Beams A, B, C, D, G and H

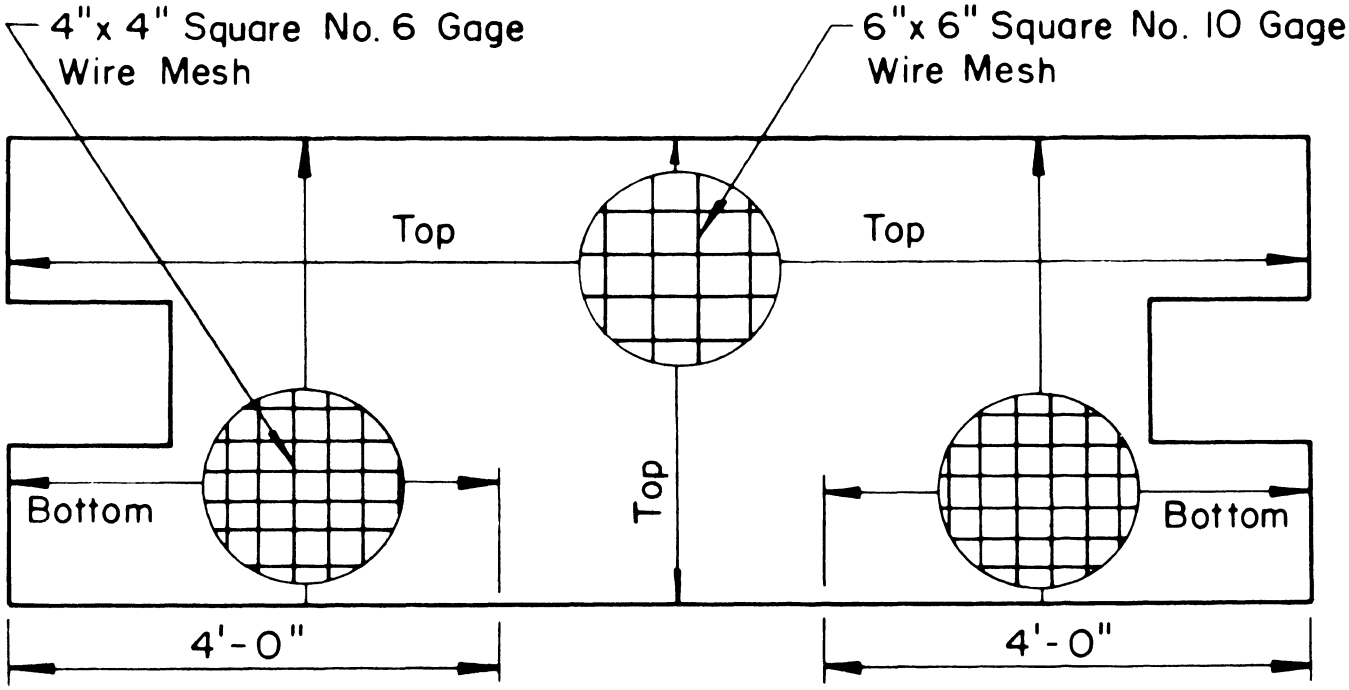

Fig. 16b Reinforcement Details for Beams E and F

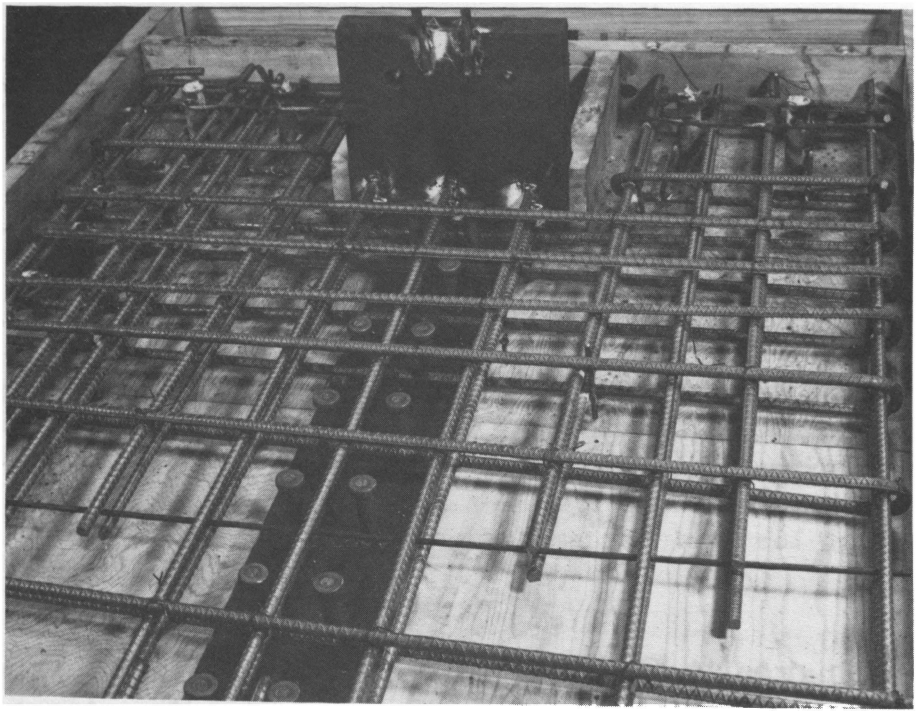

Fig. 17a Reinforcement Detail for Beam with No Shrinkage Gap

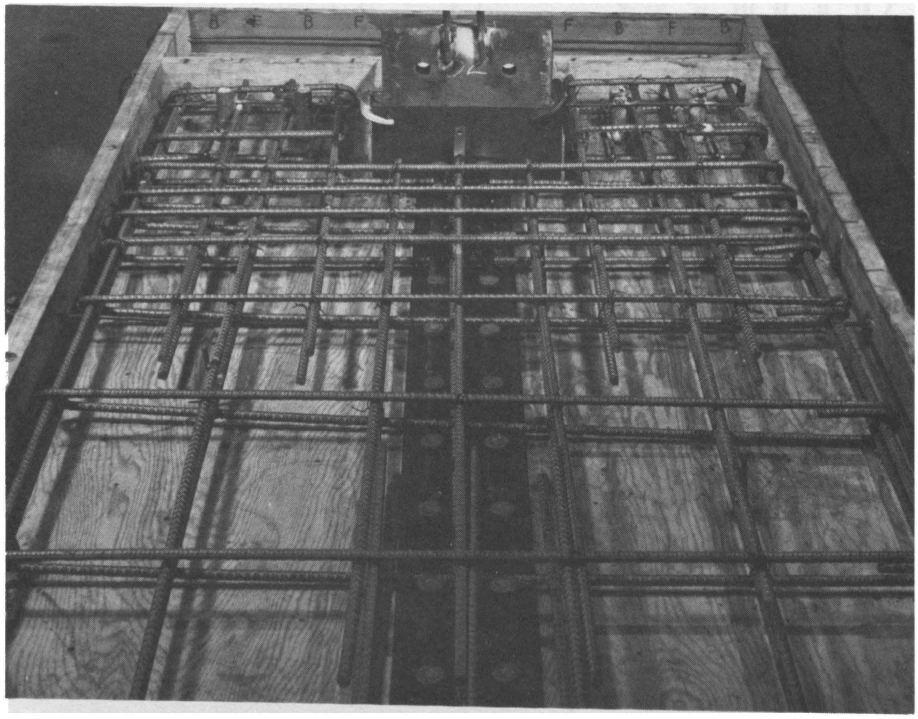

Fig. 17b Reinforcement Detail for Beam with Shrinkage Gap

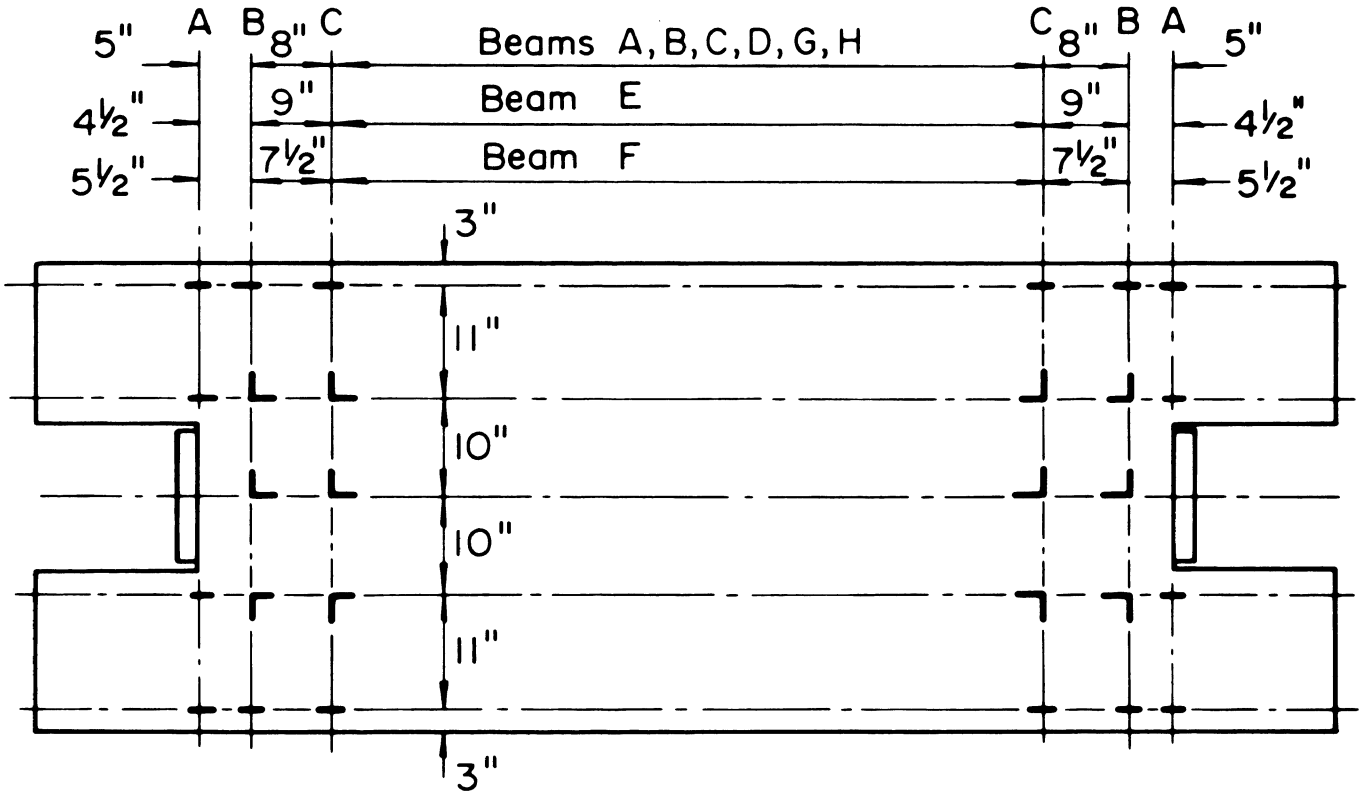

Fig. 18a Location of Electrical Resistance Strain Gages on Concrete Slab

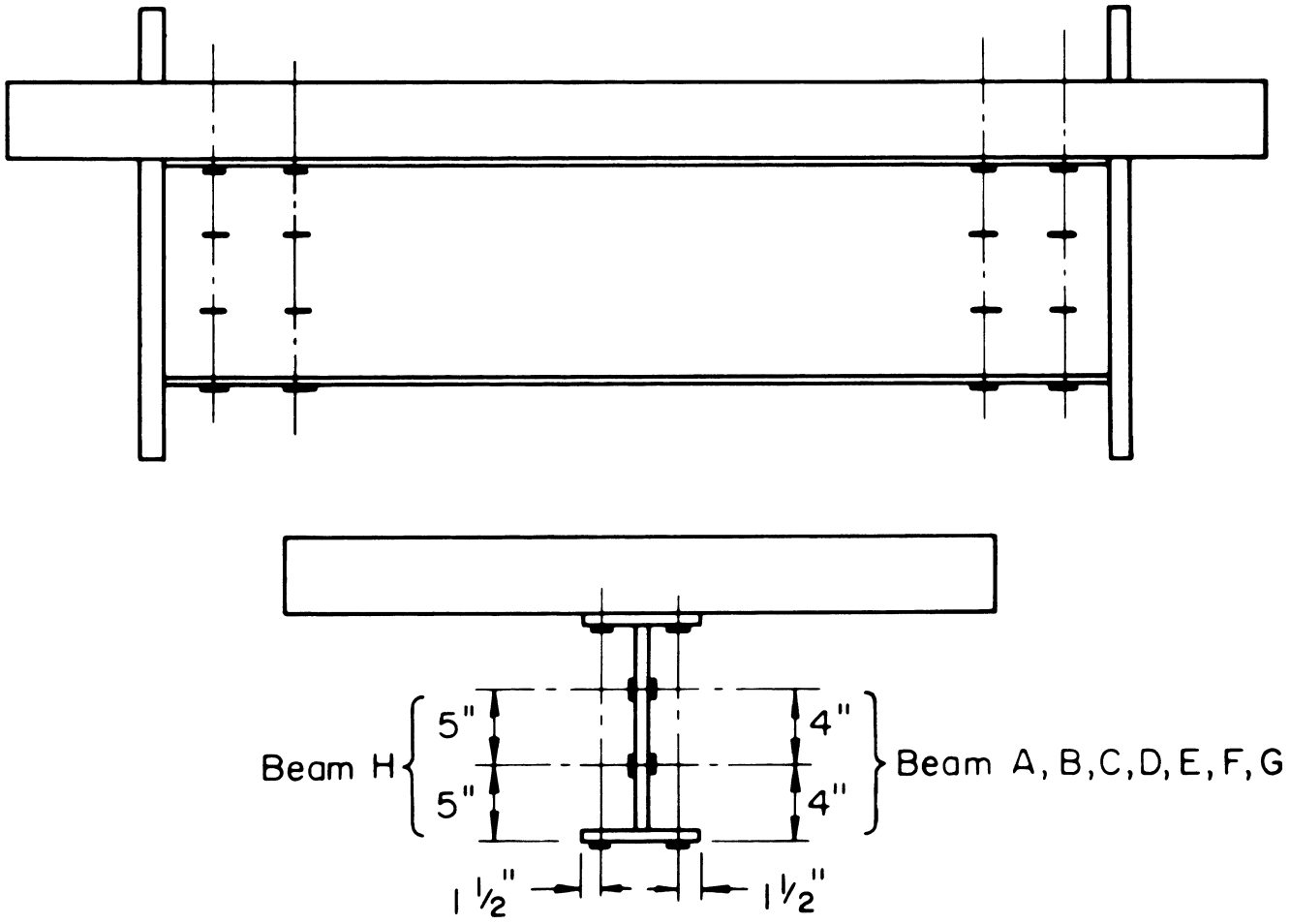

Fig. 18b Strain Gages on Steel Beam

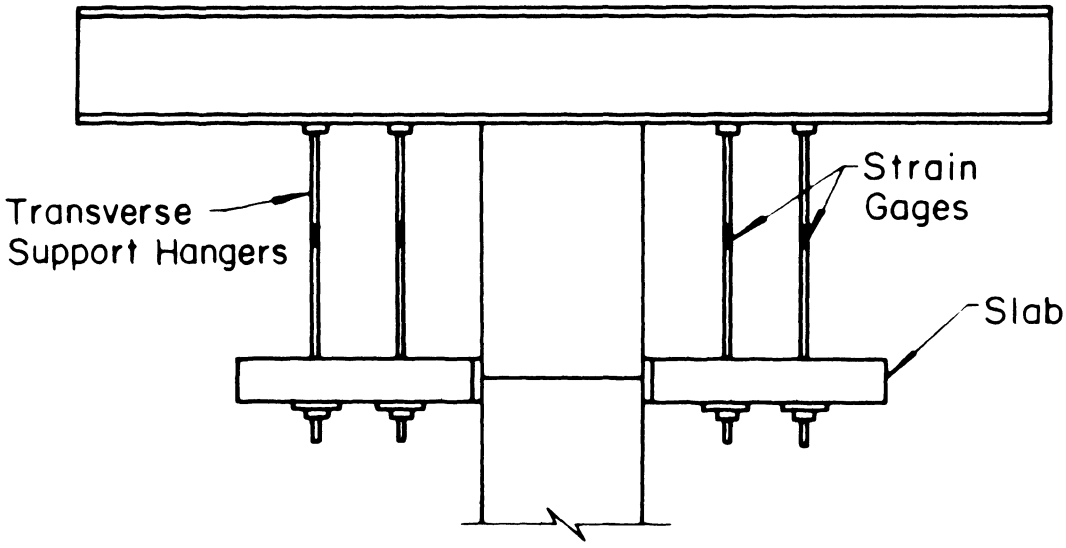

Fig. 19a Strain Gages on Transverse Support Hangers

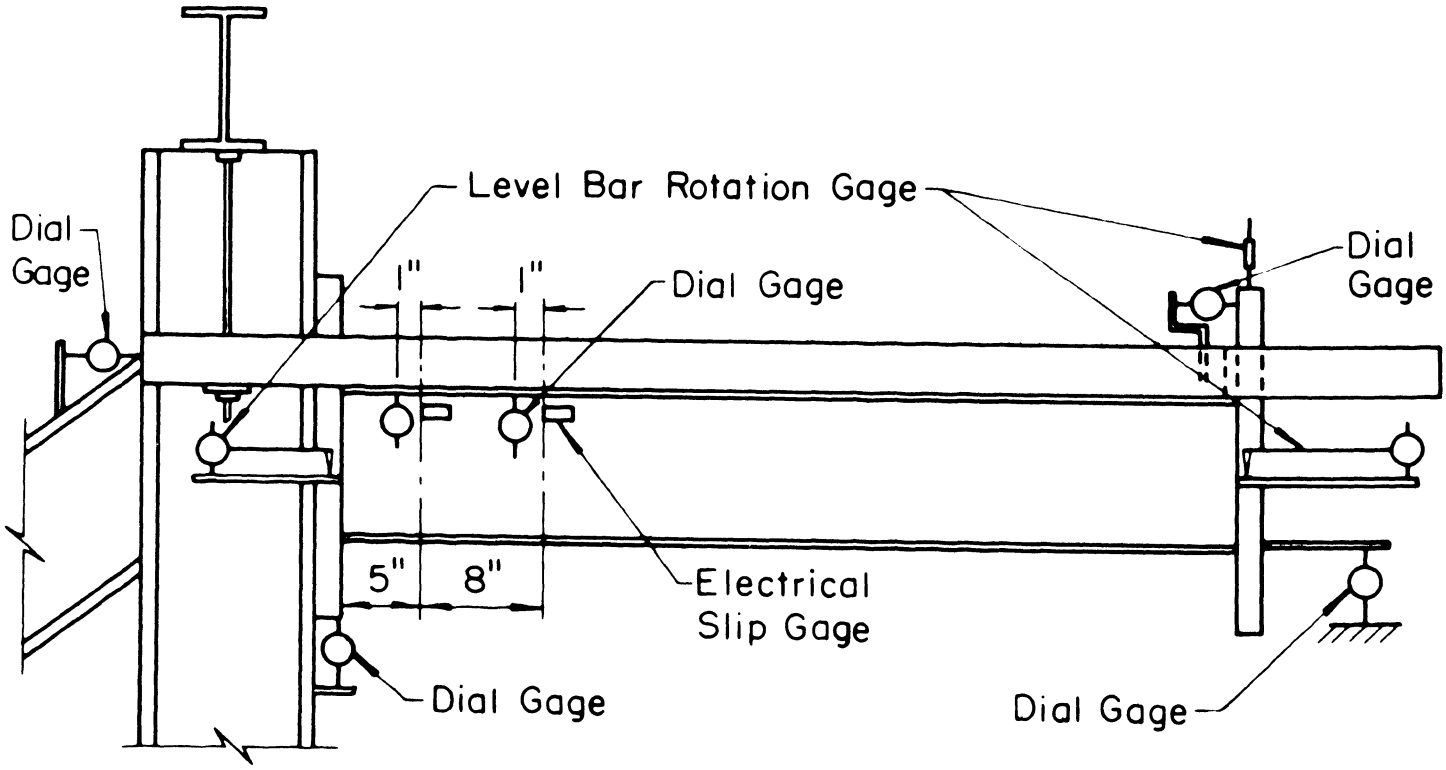

Fig. 19b Location of Ames Dial Gages, Electrical Slip Gages and Rotation Gages

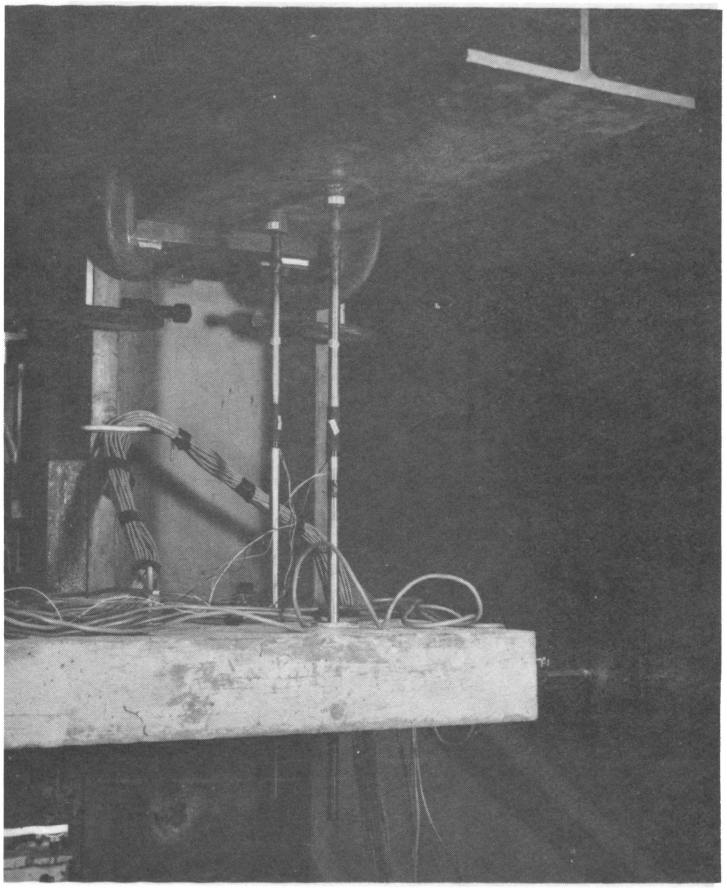

Fig. 20a Detail of Transverse Support Hangers at Test Location

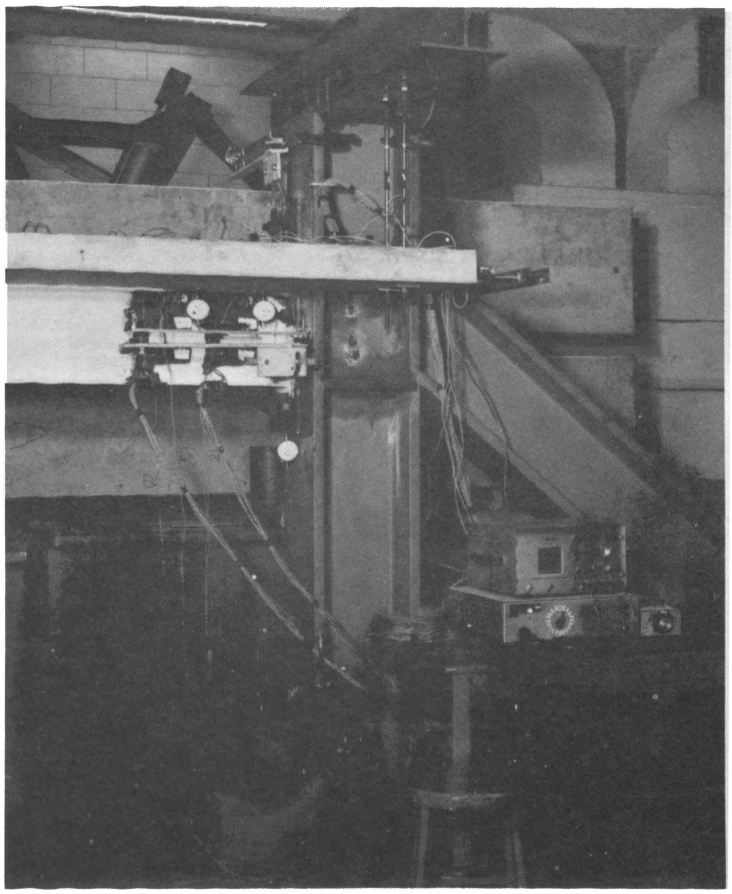

Fig. 20b Instrumentation at the Test Location

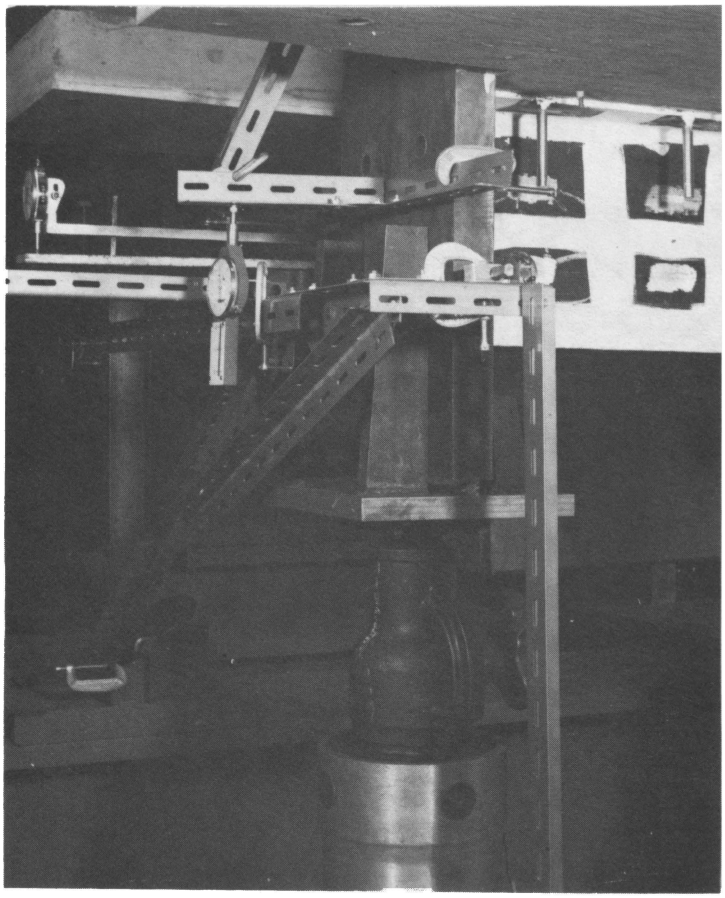

Fig. 21a Instrumentation at the Load Position

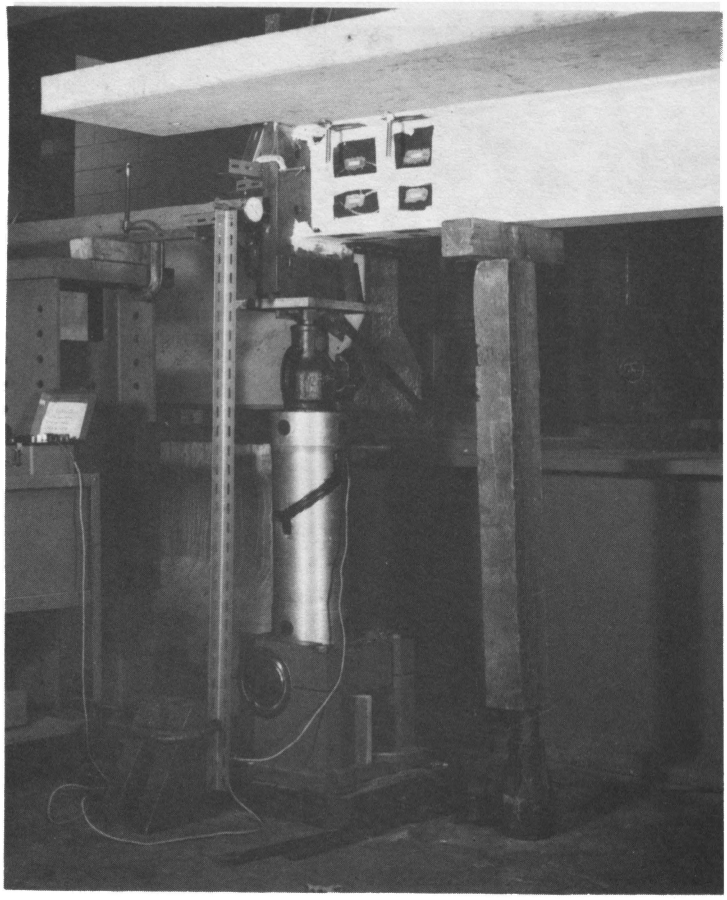

Fig. 21b Method of Loading

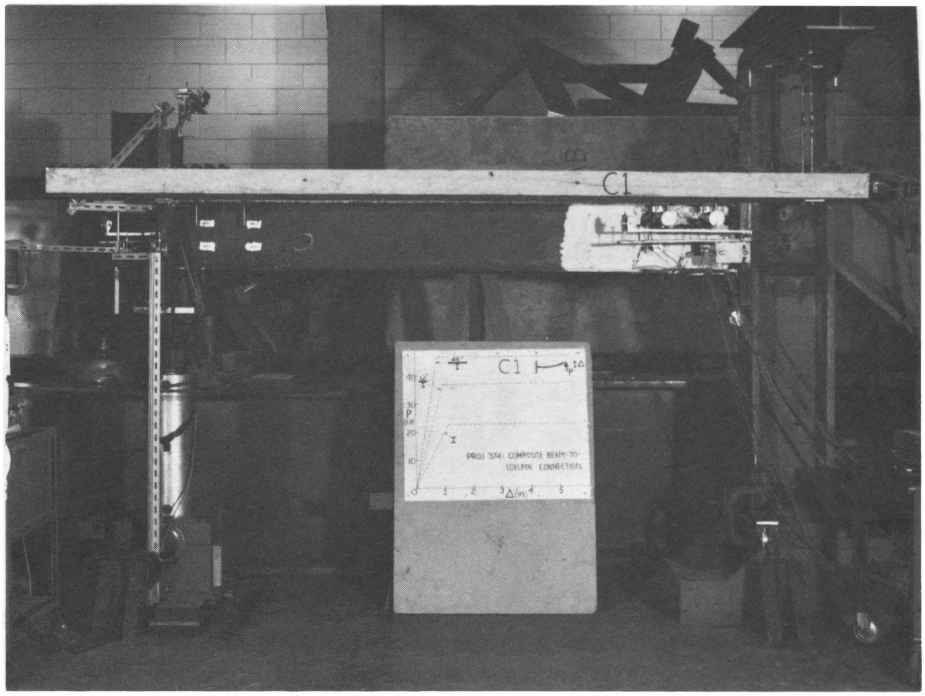

Fig. 22a View of Beam C before Test C1

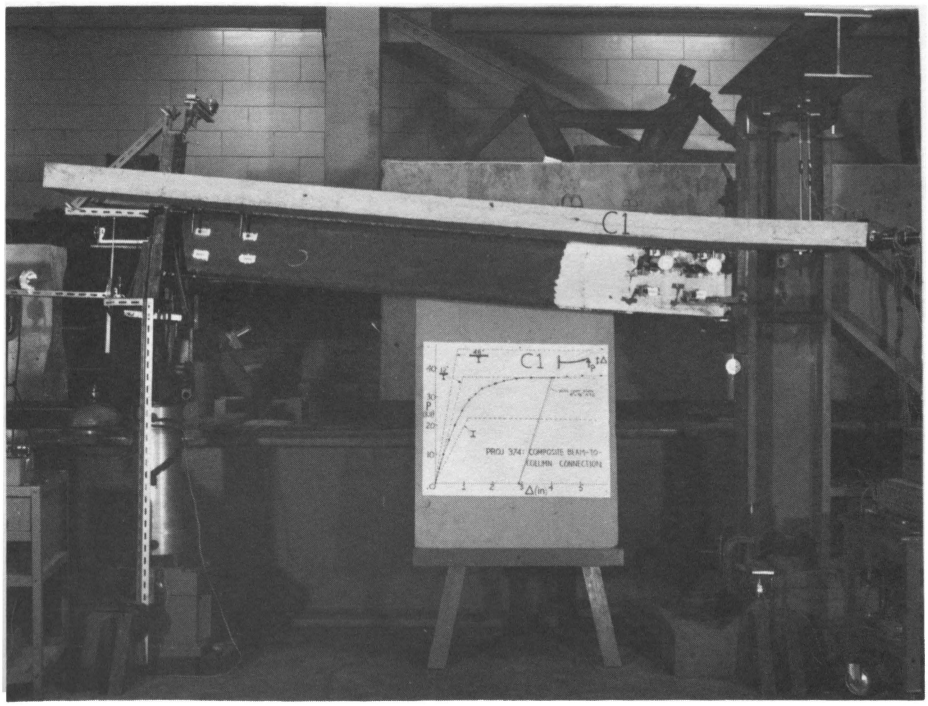

Fig. 22b View of Beam C after Test C1

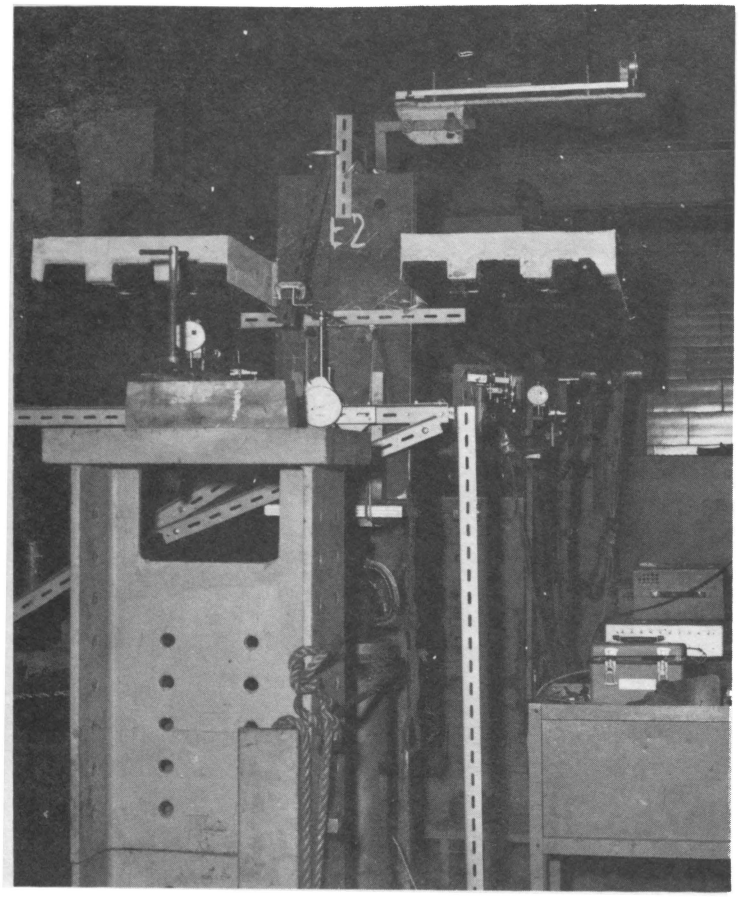

Fig. 23a Beam E in Position for Test E1

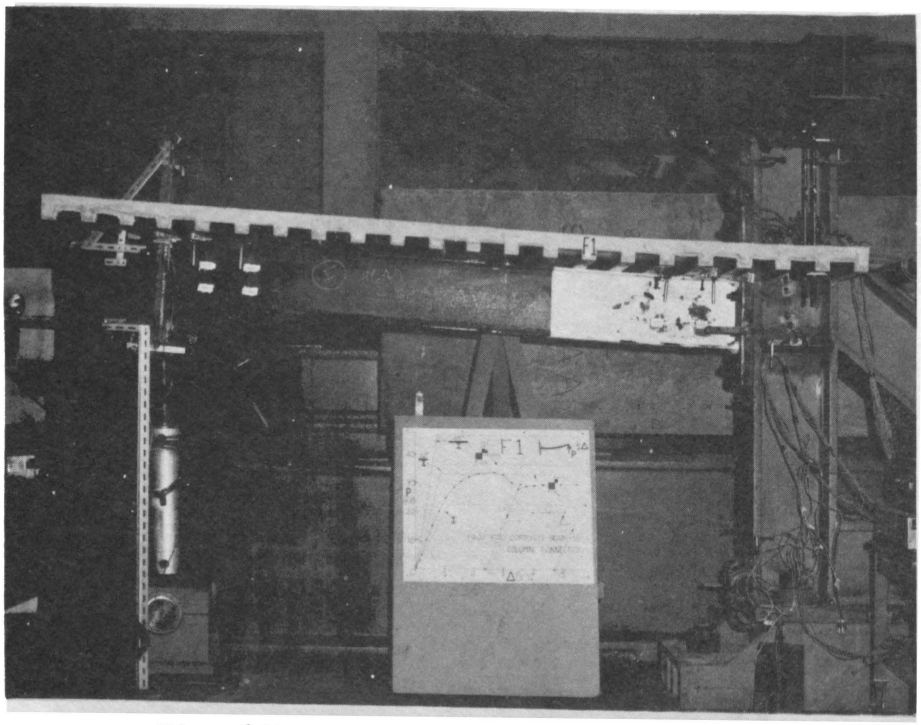

Fig. 23b Beam F at End of Test F1

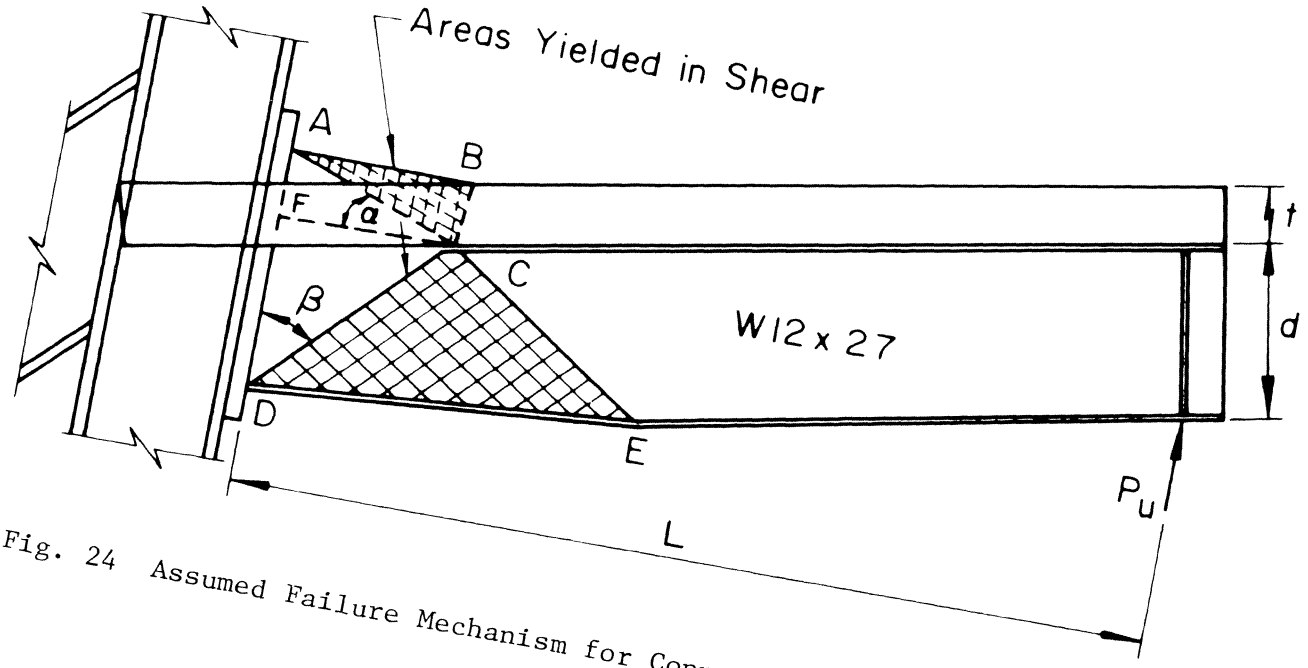

Fig. 24 Assumed Failure Mechanism for Connections without Transverse Support

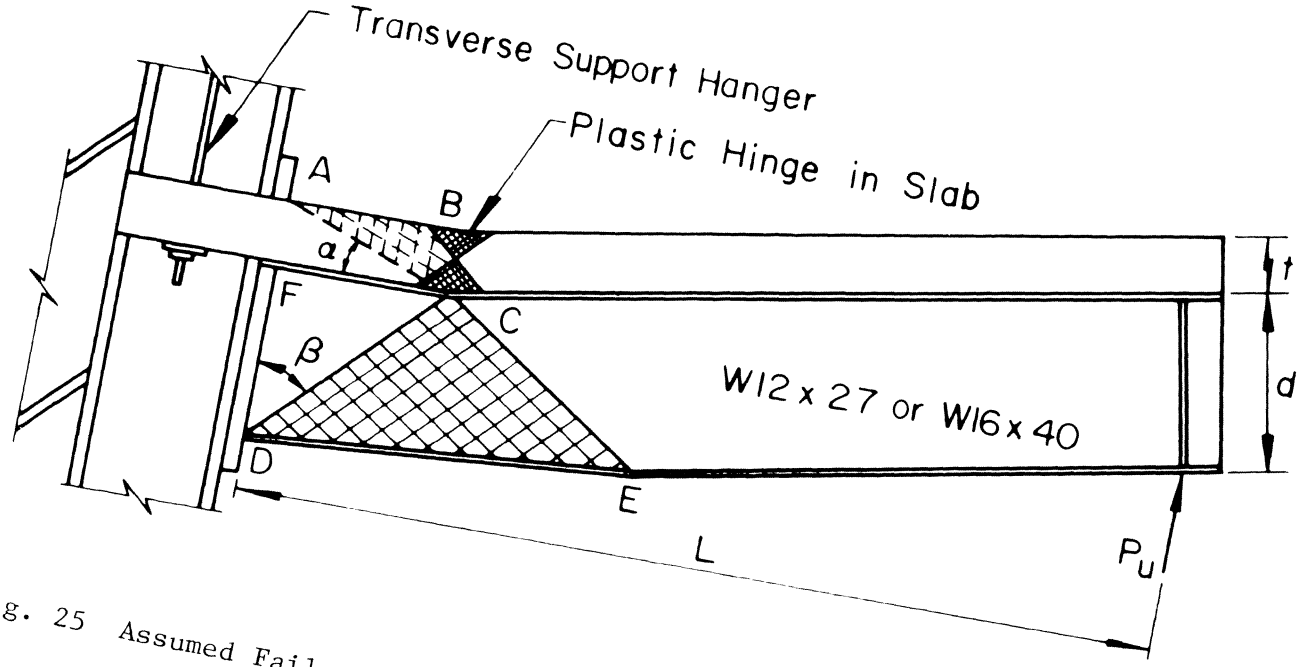

Fig. 25 Assumed Failure Mechanism for Connections with Transverse Support

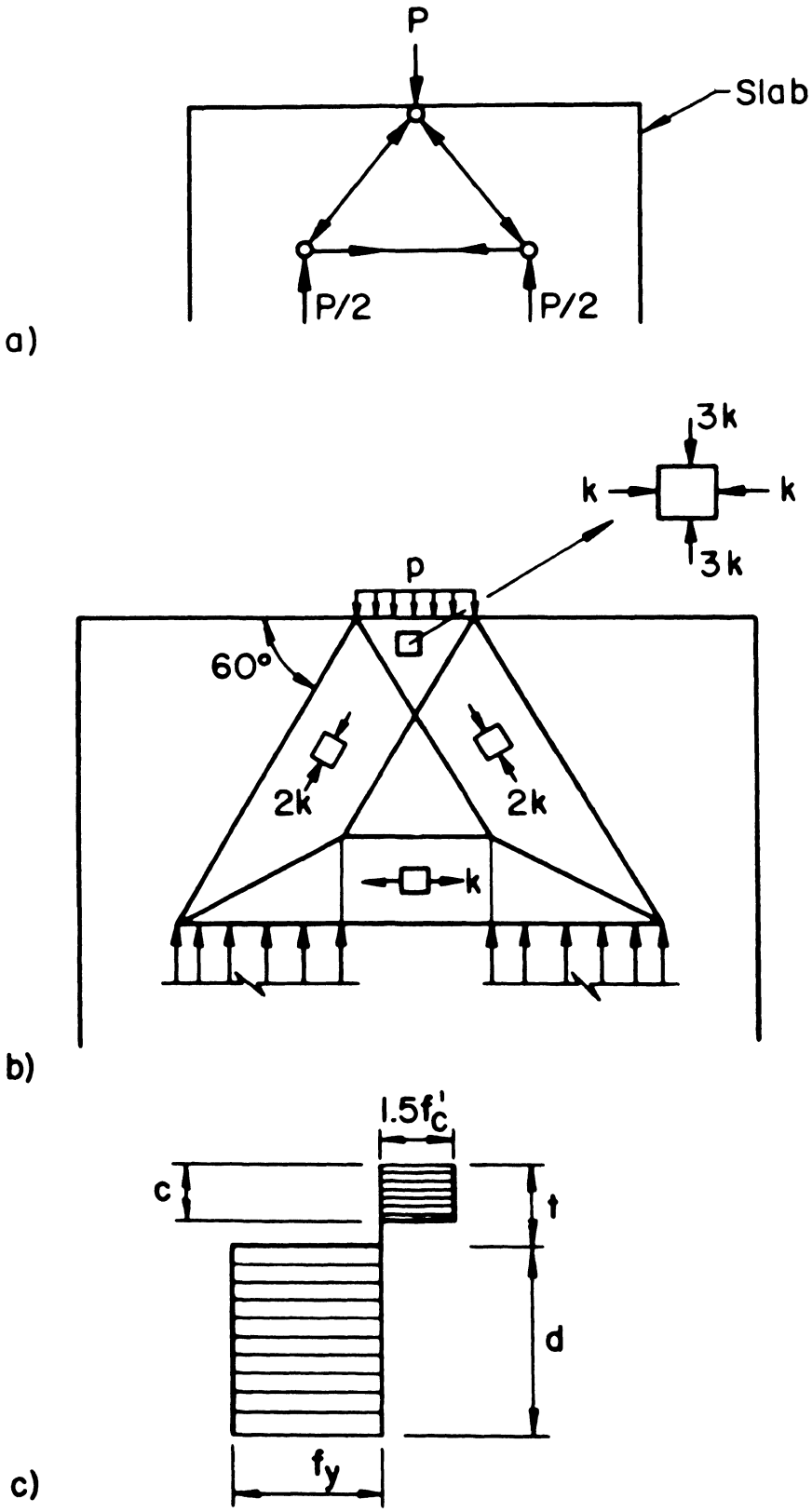

Fig. 26 Equivalent Truss and Stress Field

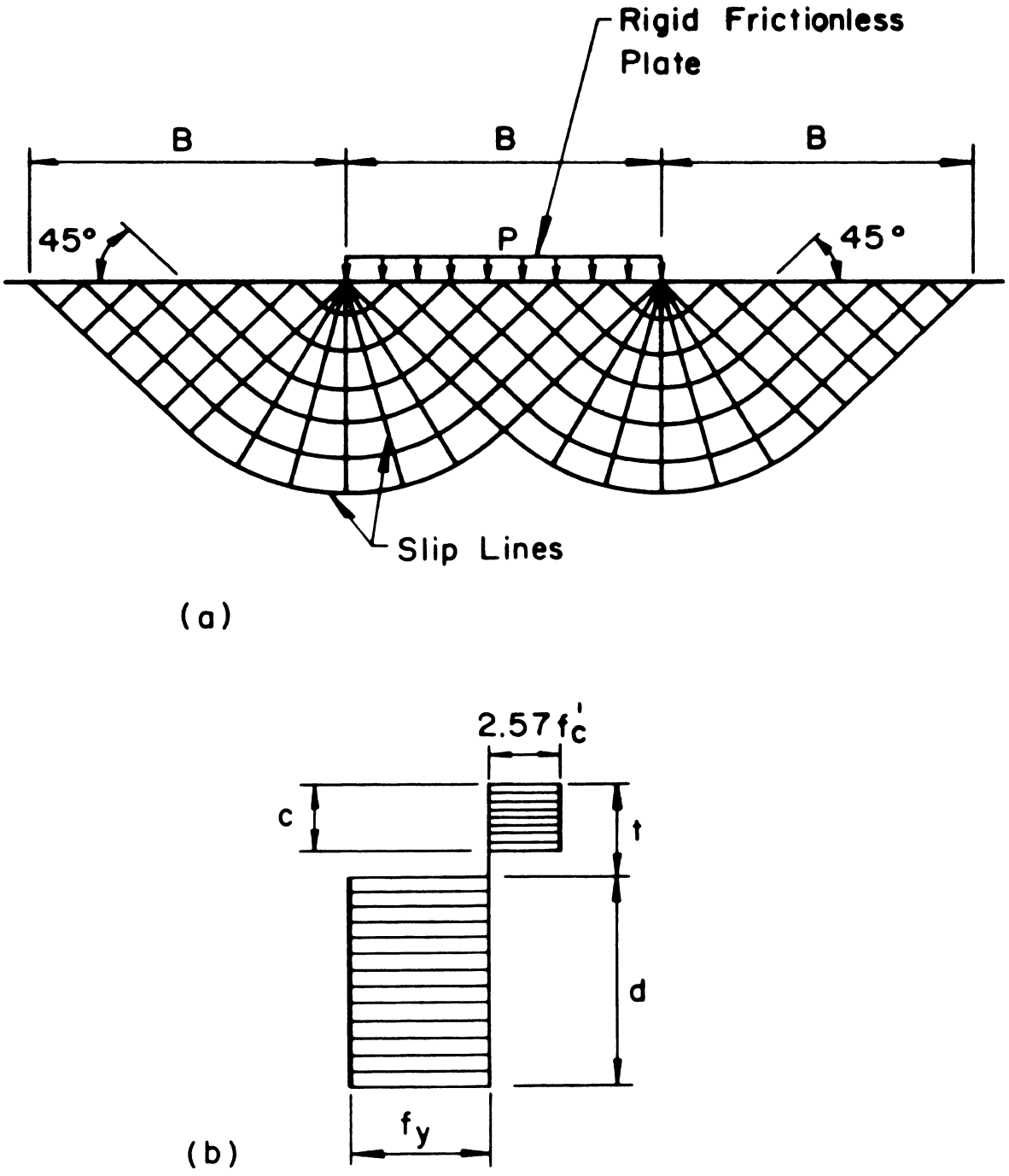

Fig. 27 Slip-Line and Stress Field

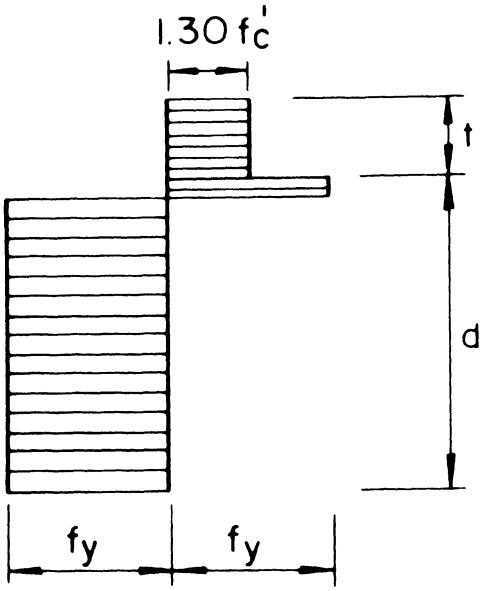

Fig. 28 Lower Bound Stress Field for Connections without Transverse Support

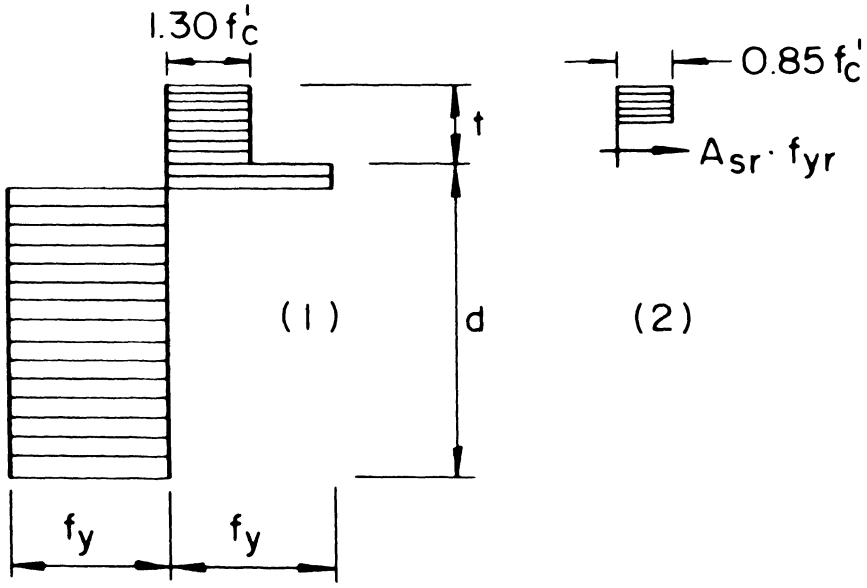

Fig. 29 Lower Bound Stress Field for Connections with Transverse Support

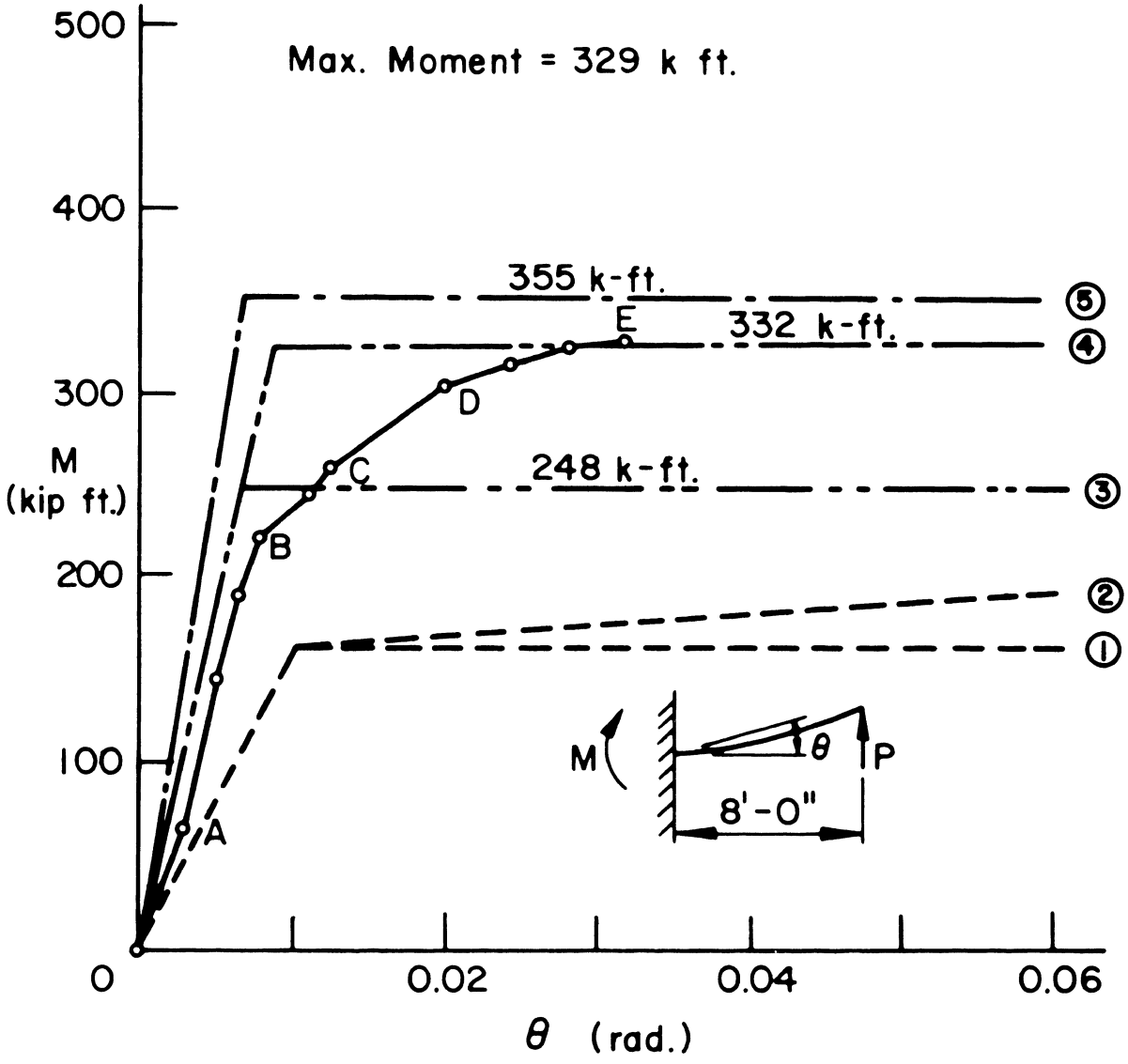

Fig. 30 B-44: Moment-Rotation Curves

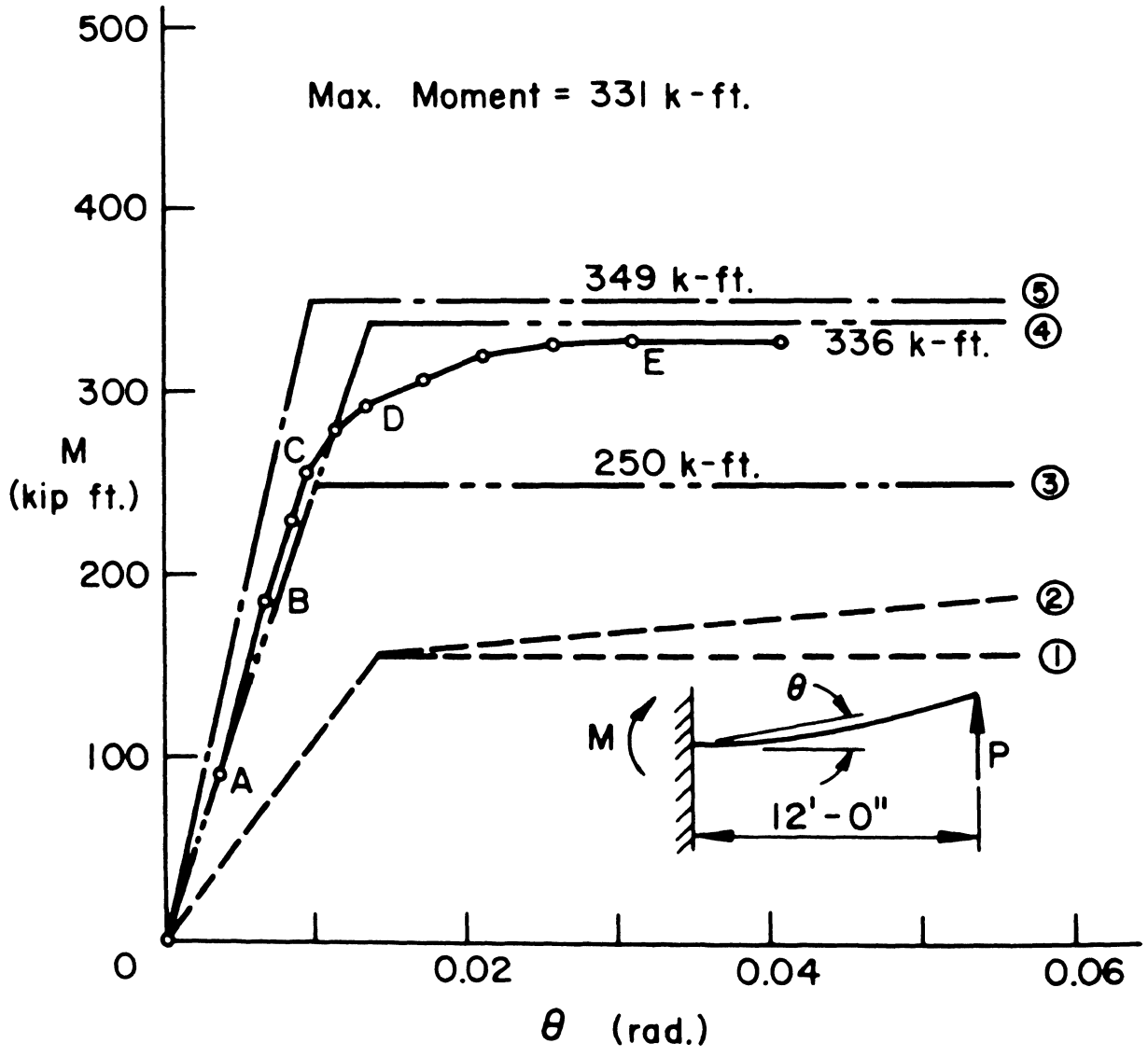

Fig. 31 B-64: Moment-Rotation Curves

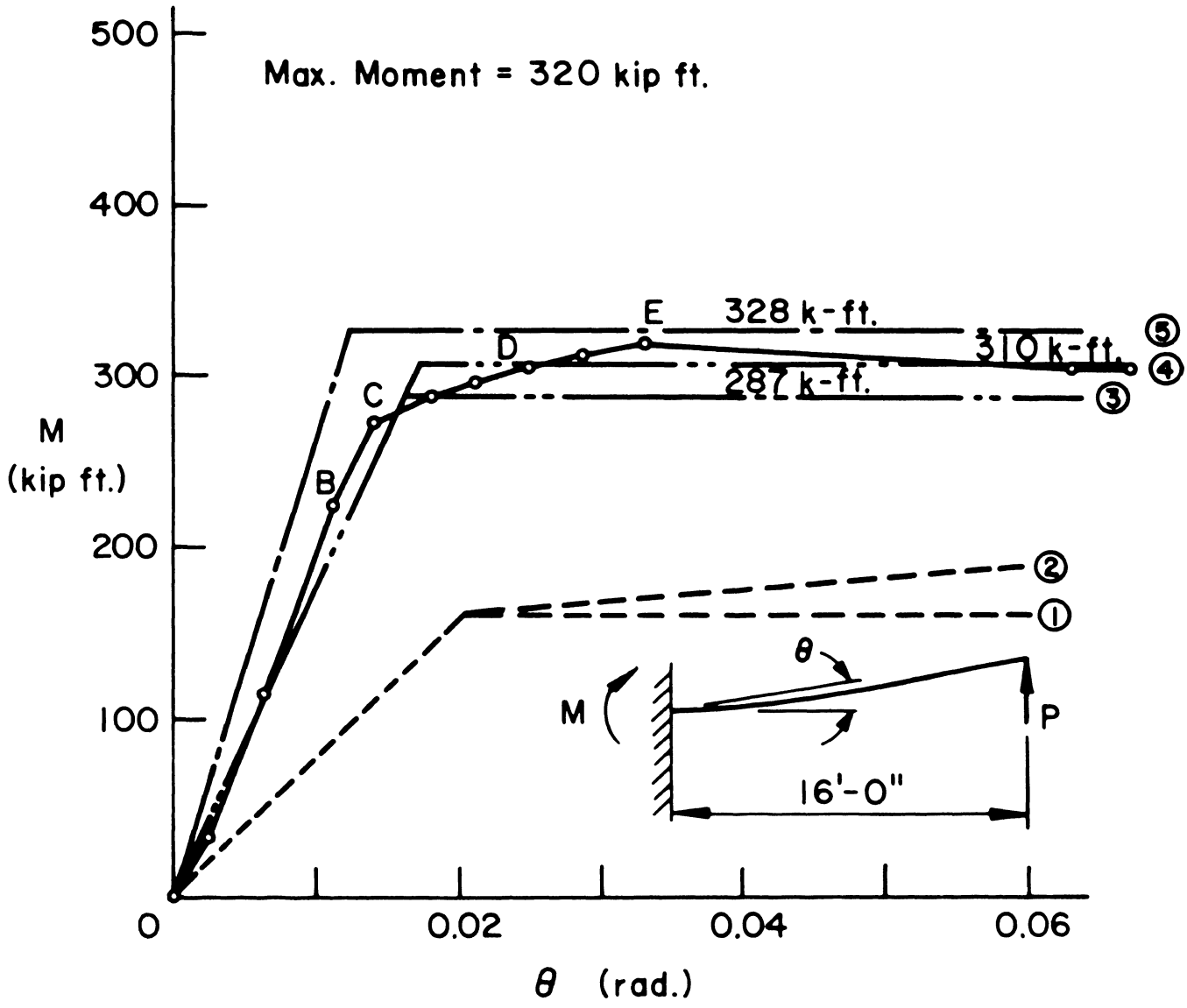

Fig. 32 B-84: Moment-Rotation Curves

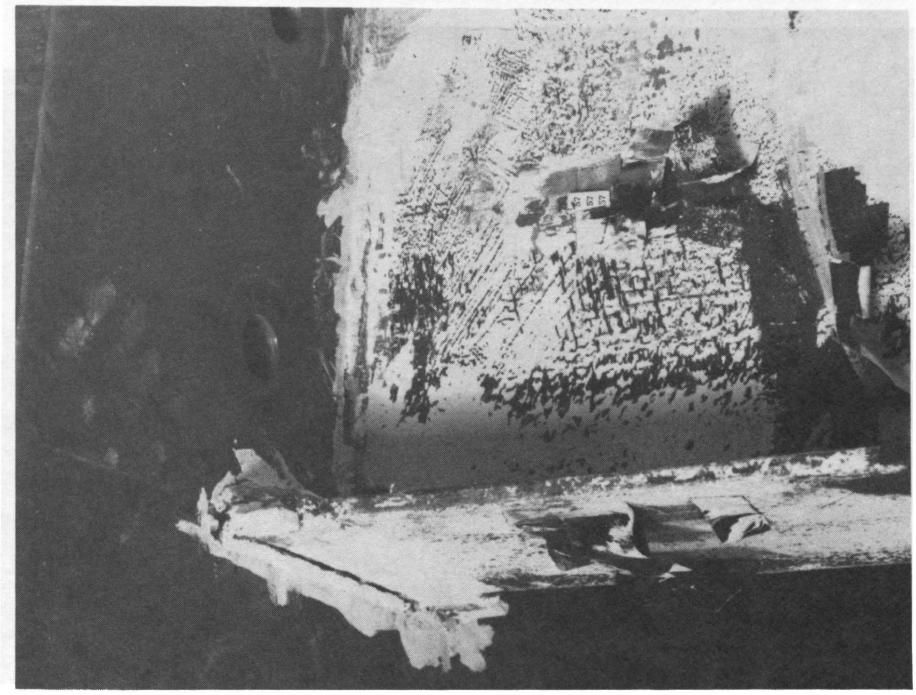

Fig. 34 B-44: Delamination

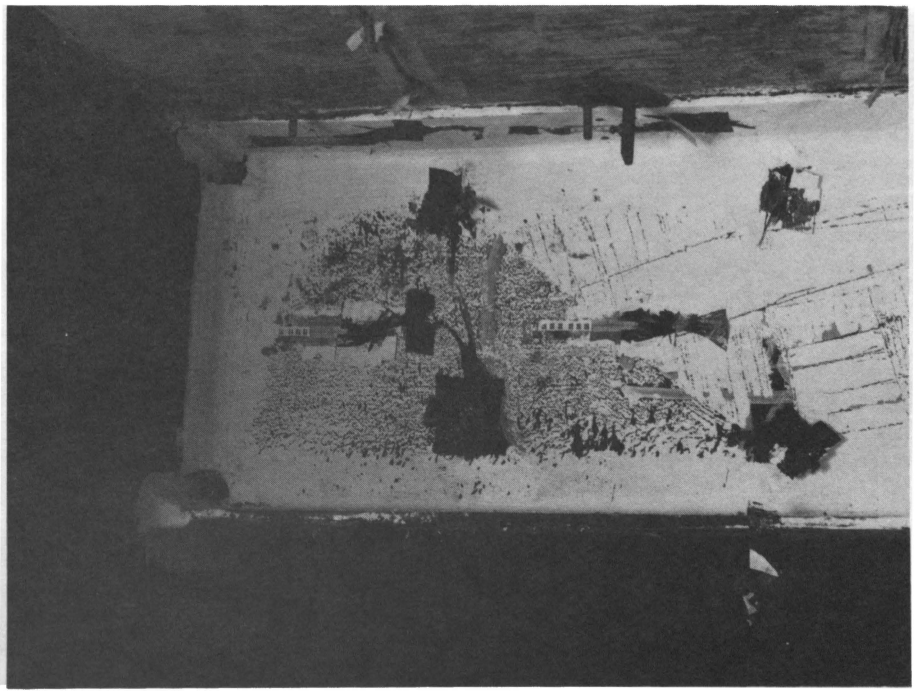

Fig. 35 Typical Yield Pattern

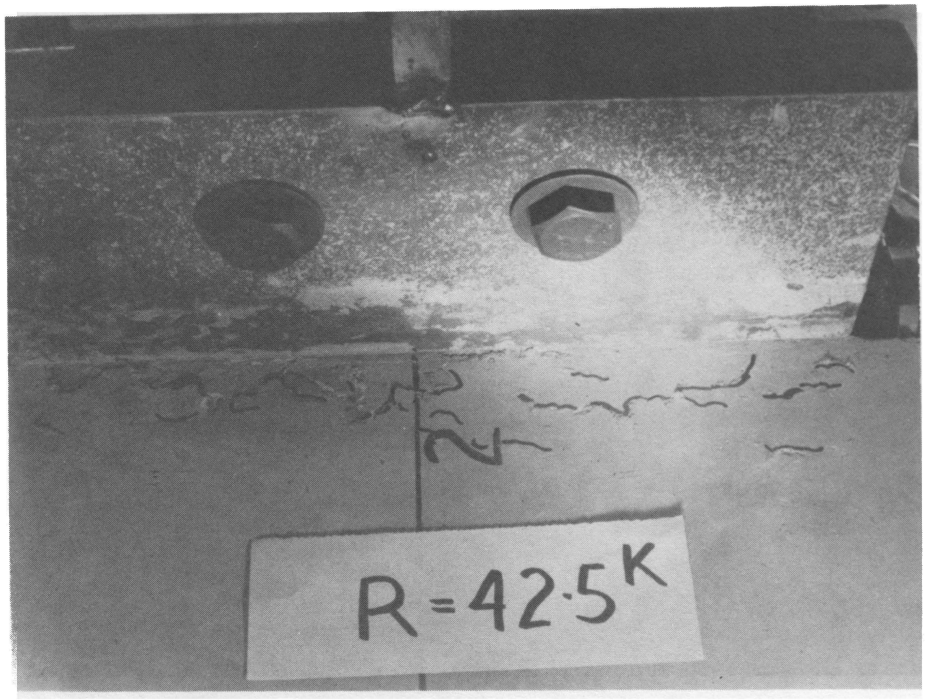

Fig. 36 B-44: Spalling at End Plate

Fig. 37 B-66: Local Failure at End Plate

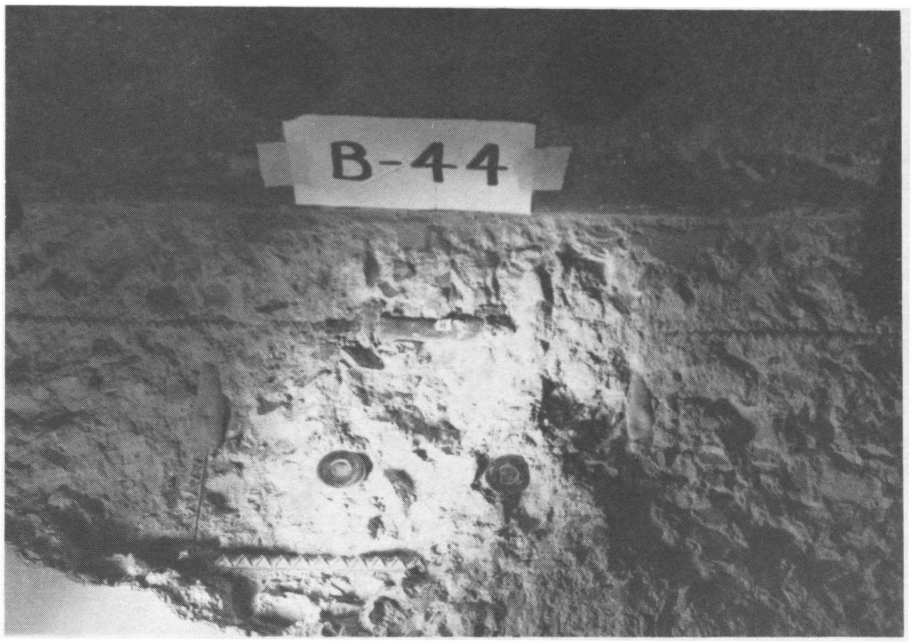

Fig. 38a B-44: Plan View of Failure Surface

Fig. 38b B-44: End View of Failure Surface

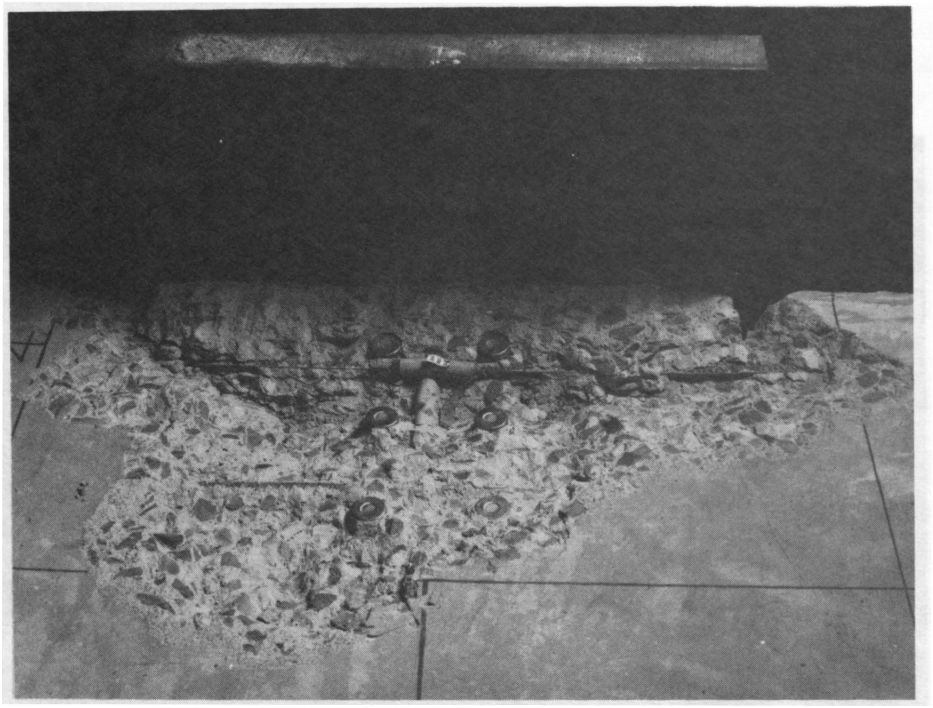

Fig. 39a B-64: Failure Surface

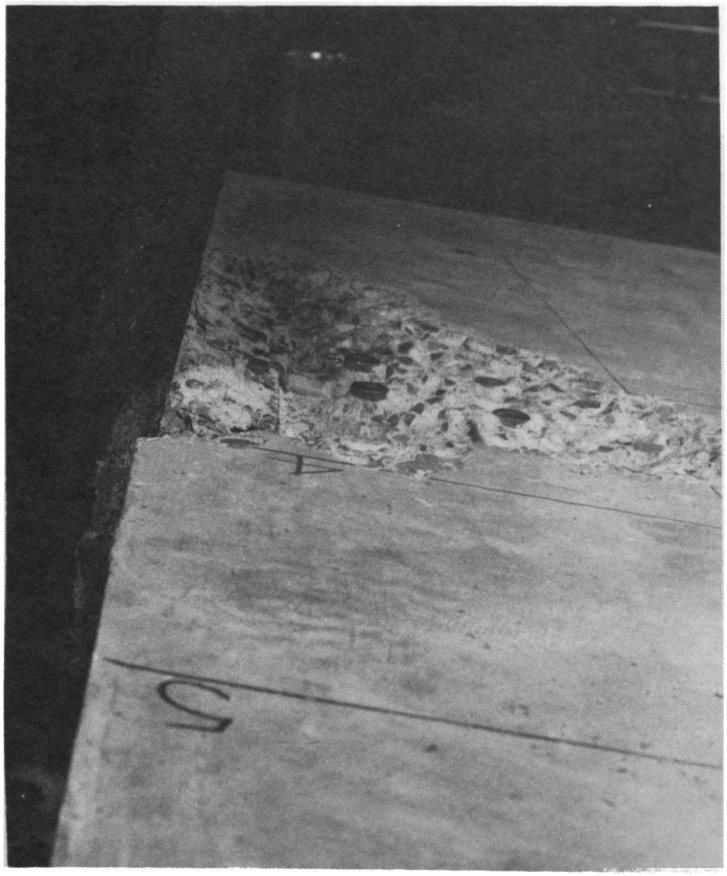

Fig. 39b B-64: Side View of Failure Surface

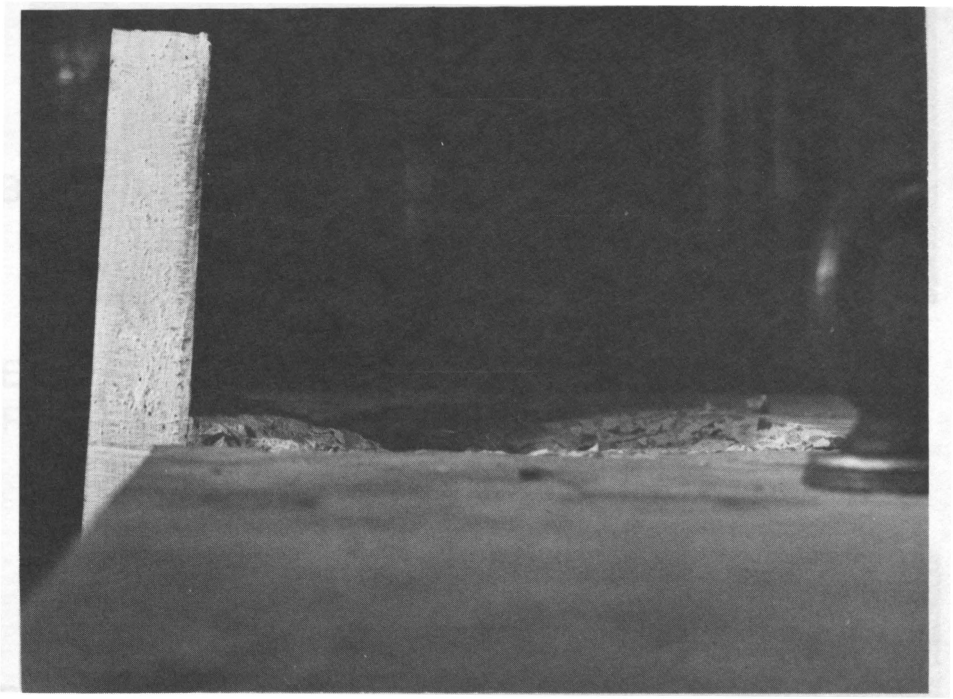

Fig. 40 B-84: Side View of Failure Surface

Fig. 41a B-66: Failure Surface

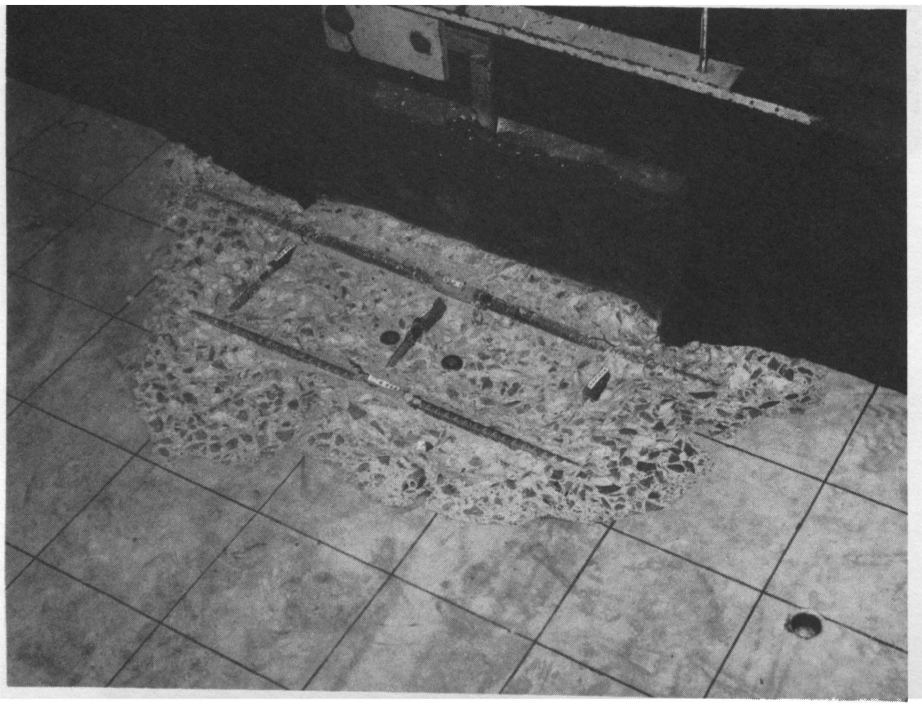

Fig. 41b B-66: Plan View of Failure Surface

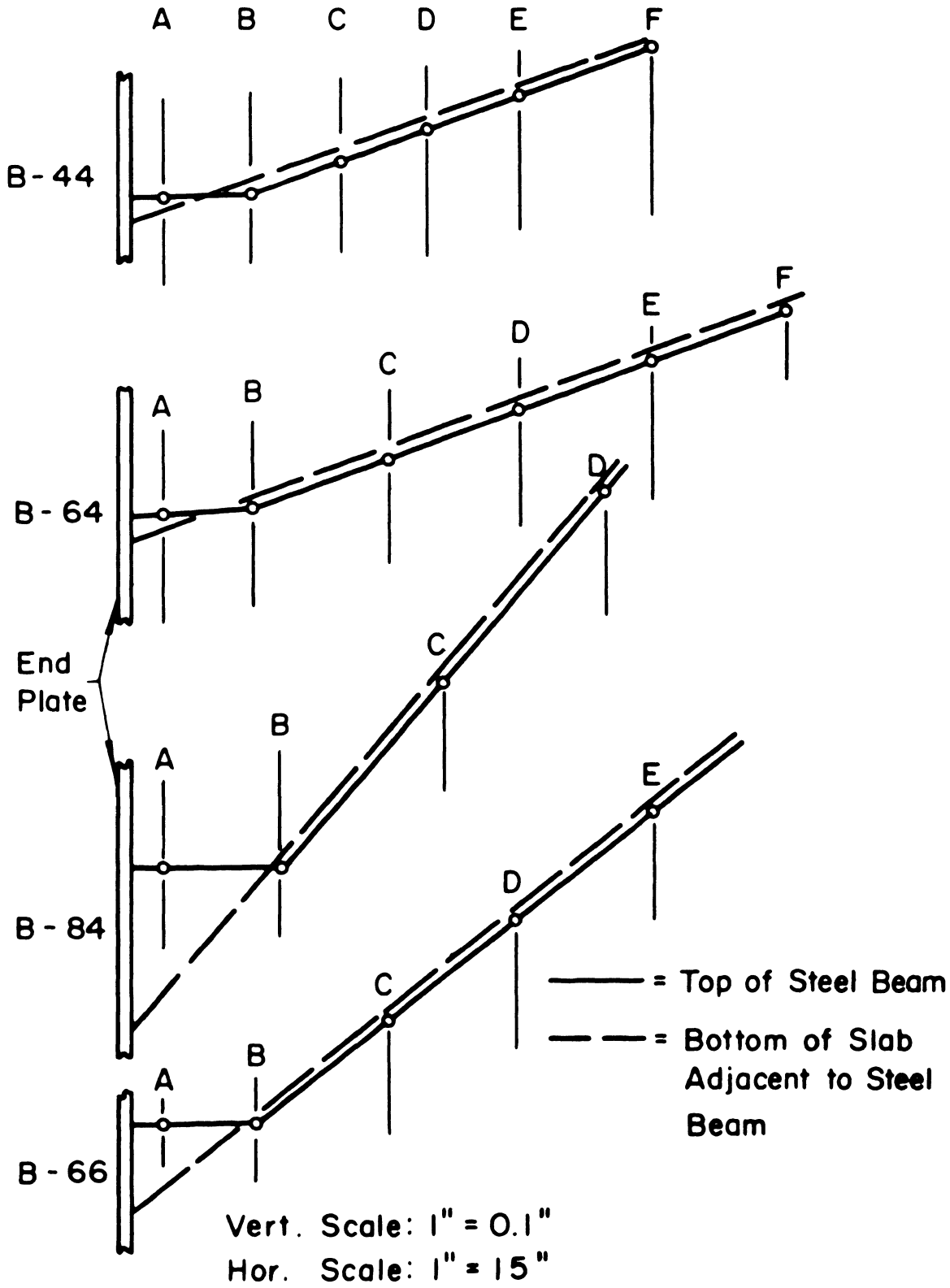

Fig. 42 Vertical Movement of Slab Relative to Steel Beam

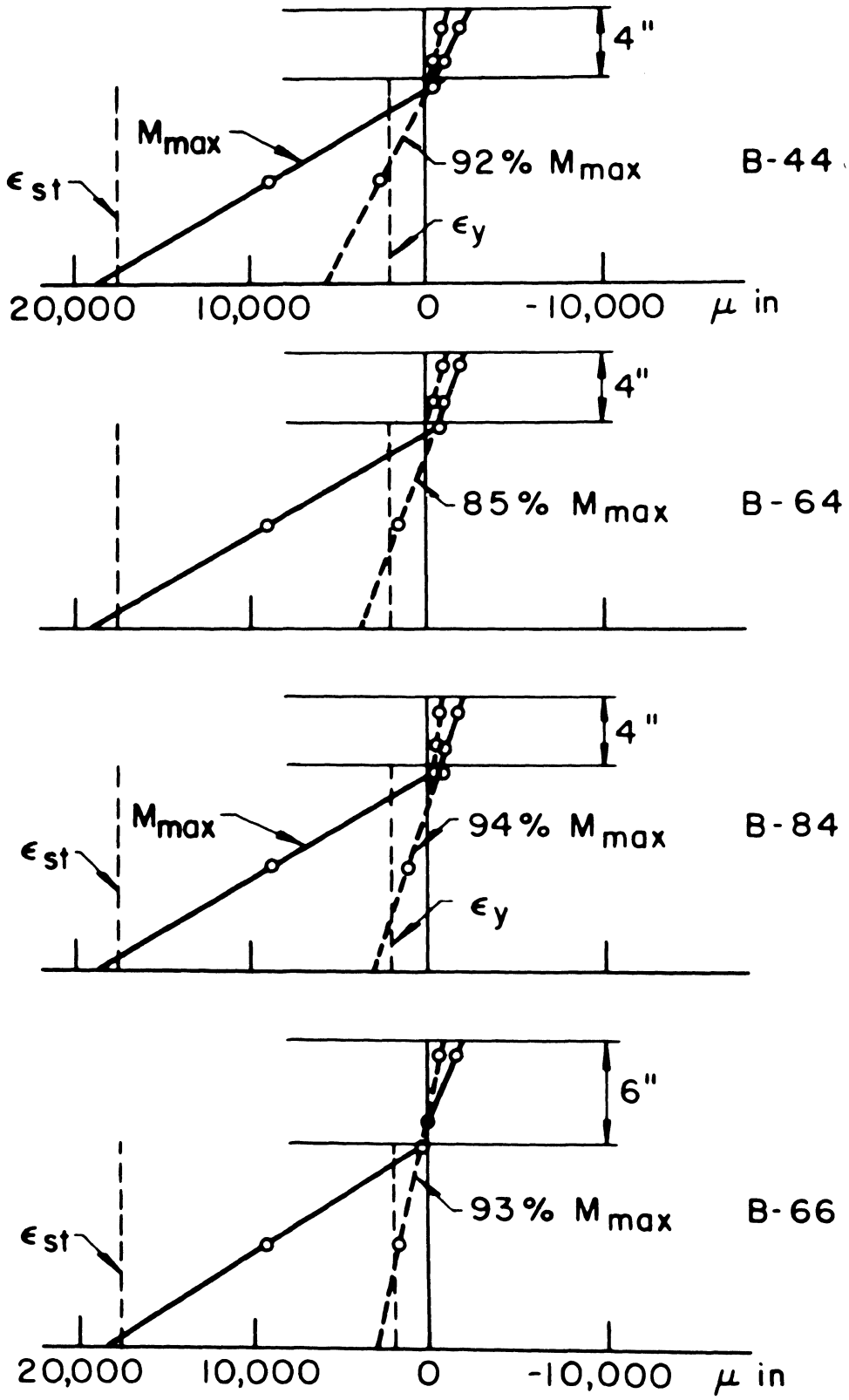

Fig. 43 Strain Distribution at Gage Section A before Spalling and at Maximum Moment

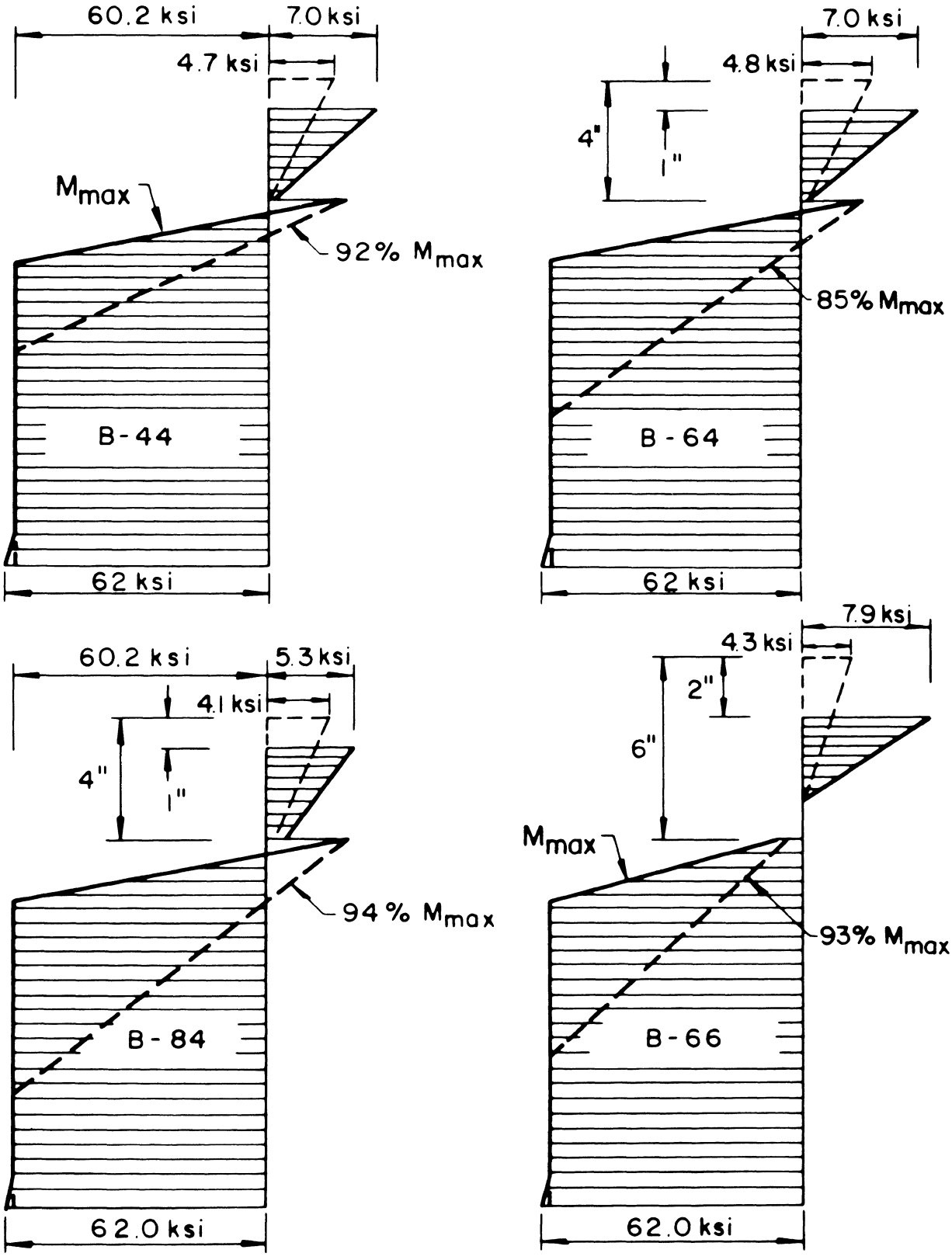

Fig. 44 Stress Distributions at Gage Section A before Spalling and at Maximum Moment

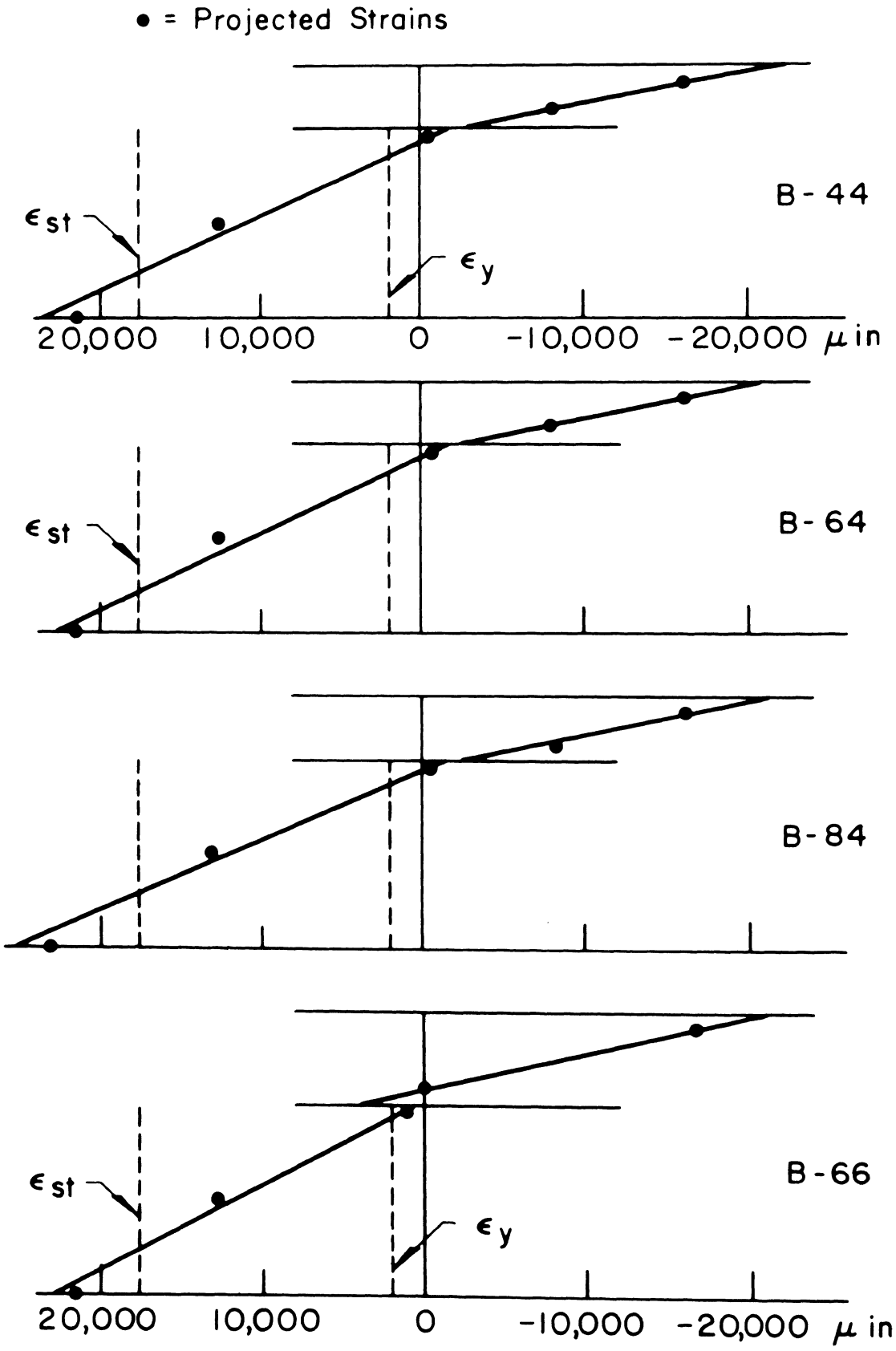

Fig. 45 Strain Distributions at End Plate at Maximum Moment

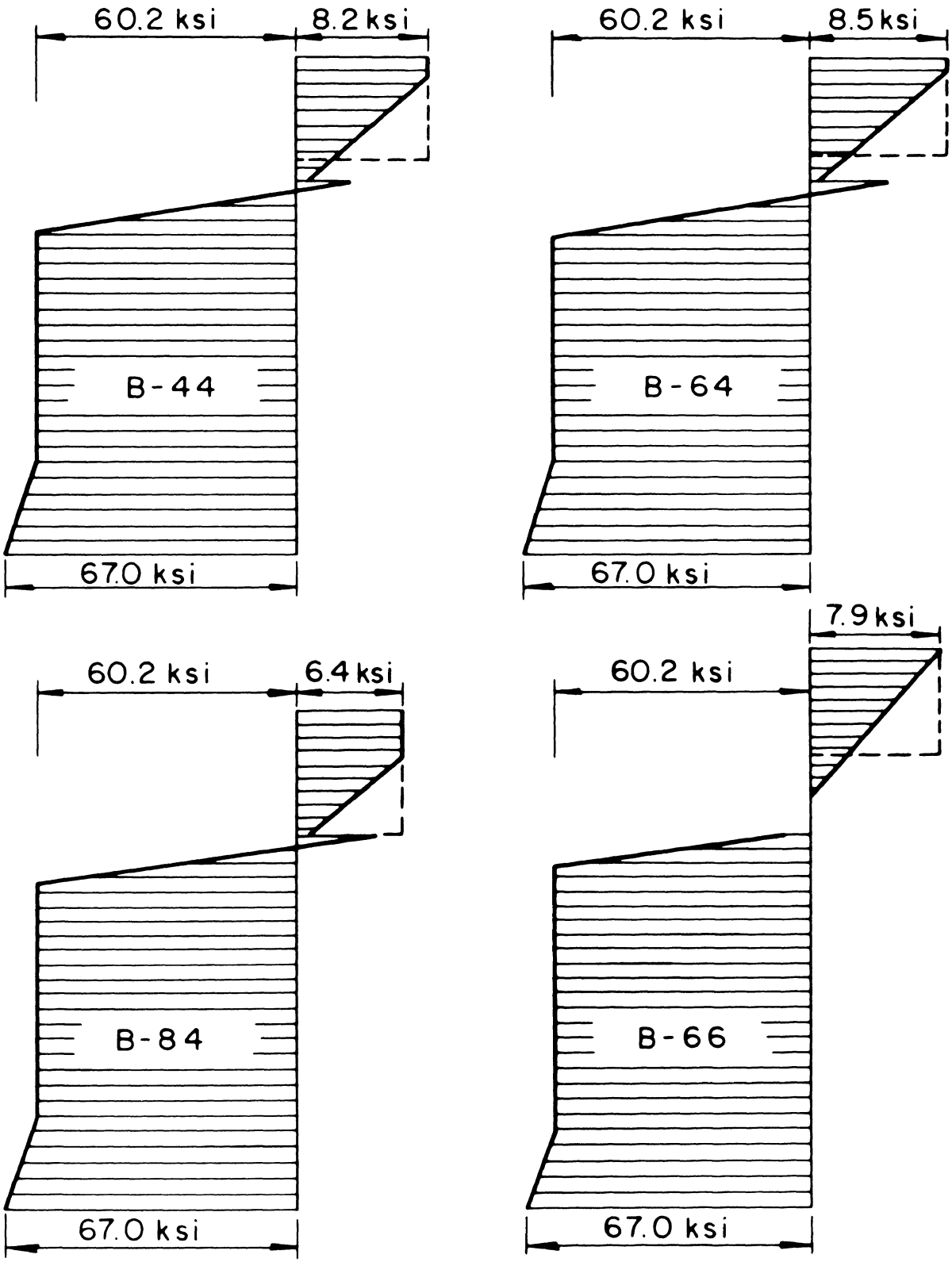

Fig. 46 Stress Distributions at End Plate at Maximum Moment

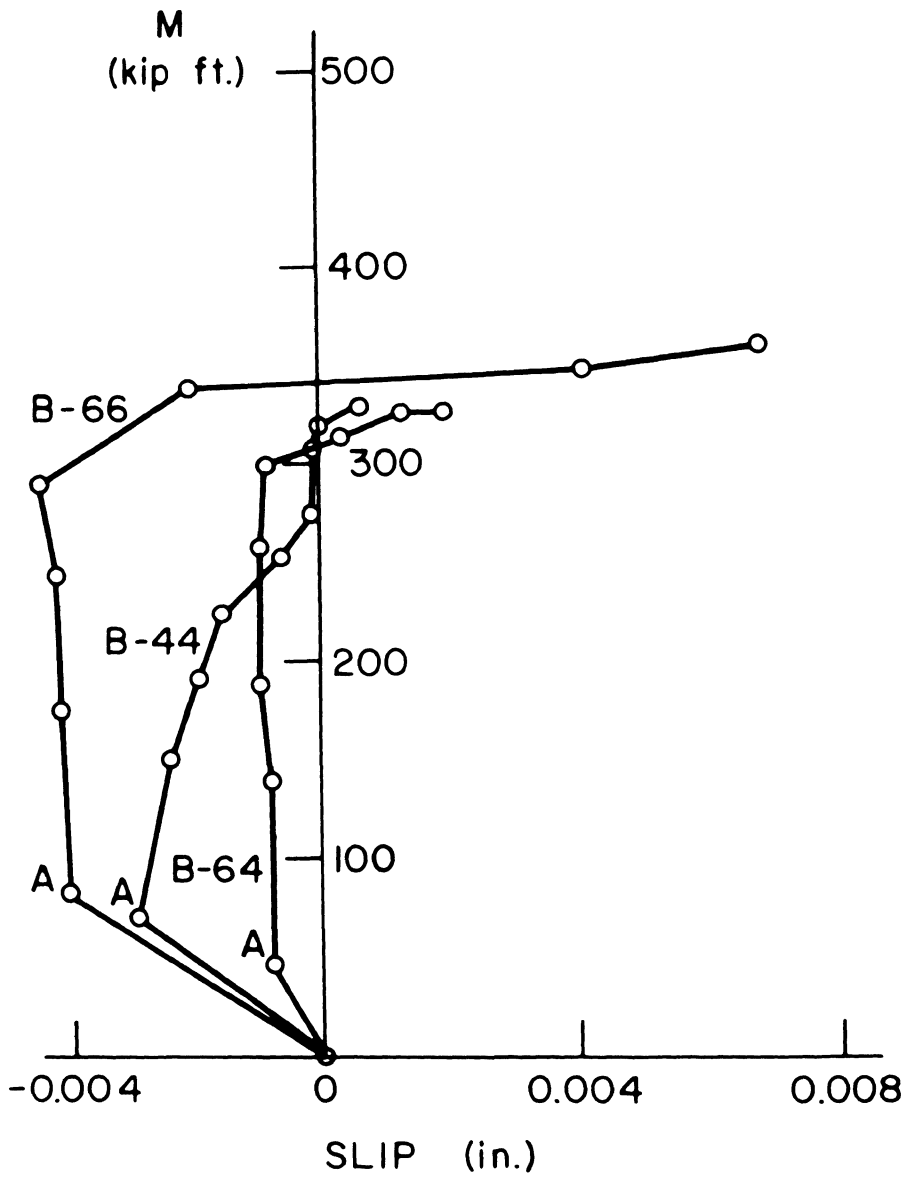

Fig. 47 Relative Slip between Slab and Beam at Gage Section A

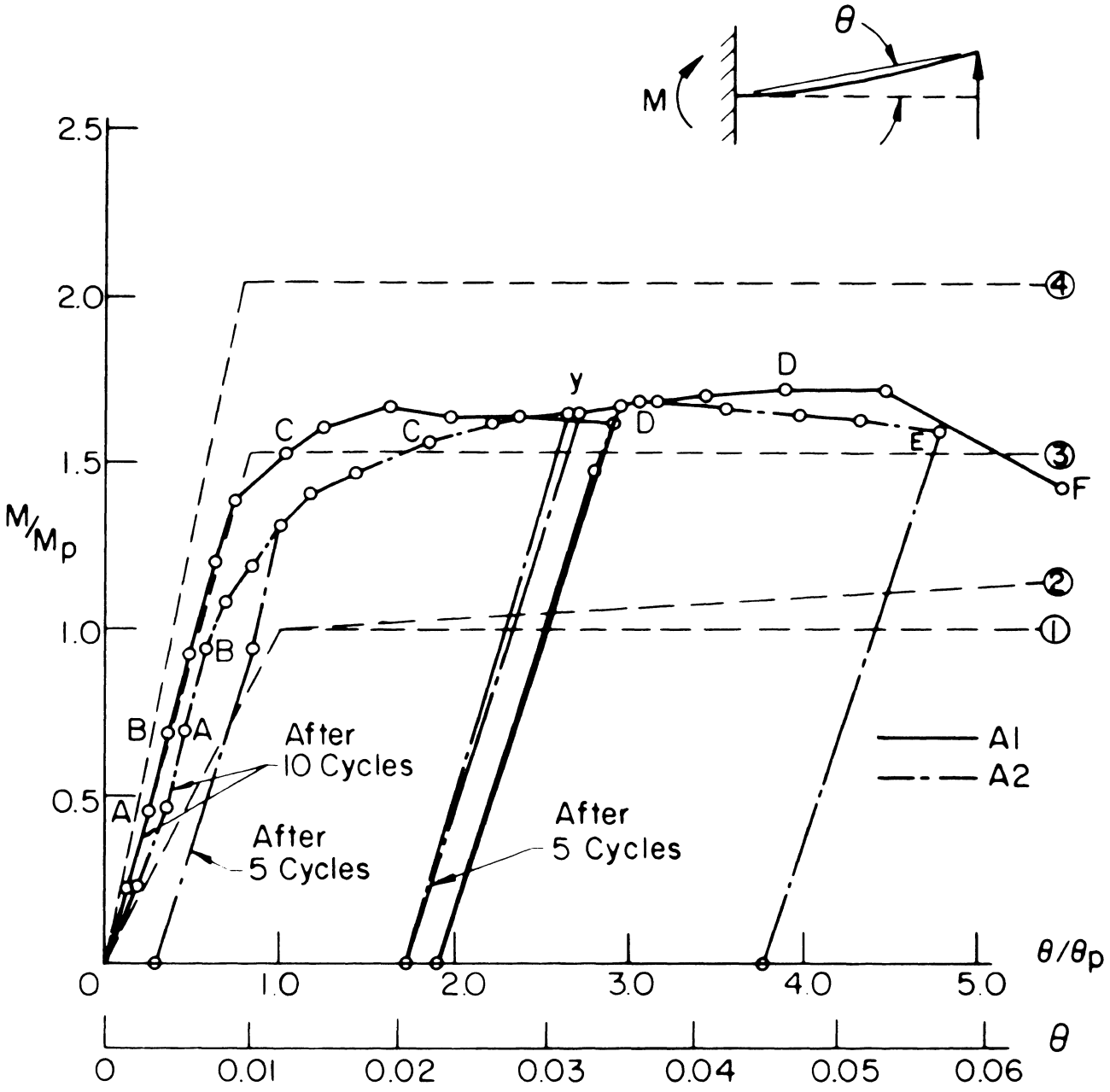

Fig. 48 Moment-Rotation Behavior: Tests A1 and A2

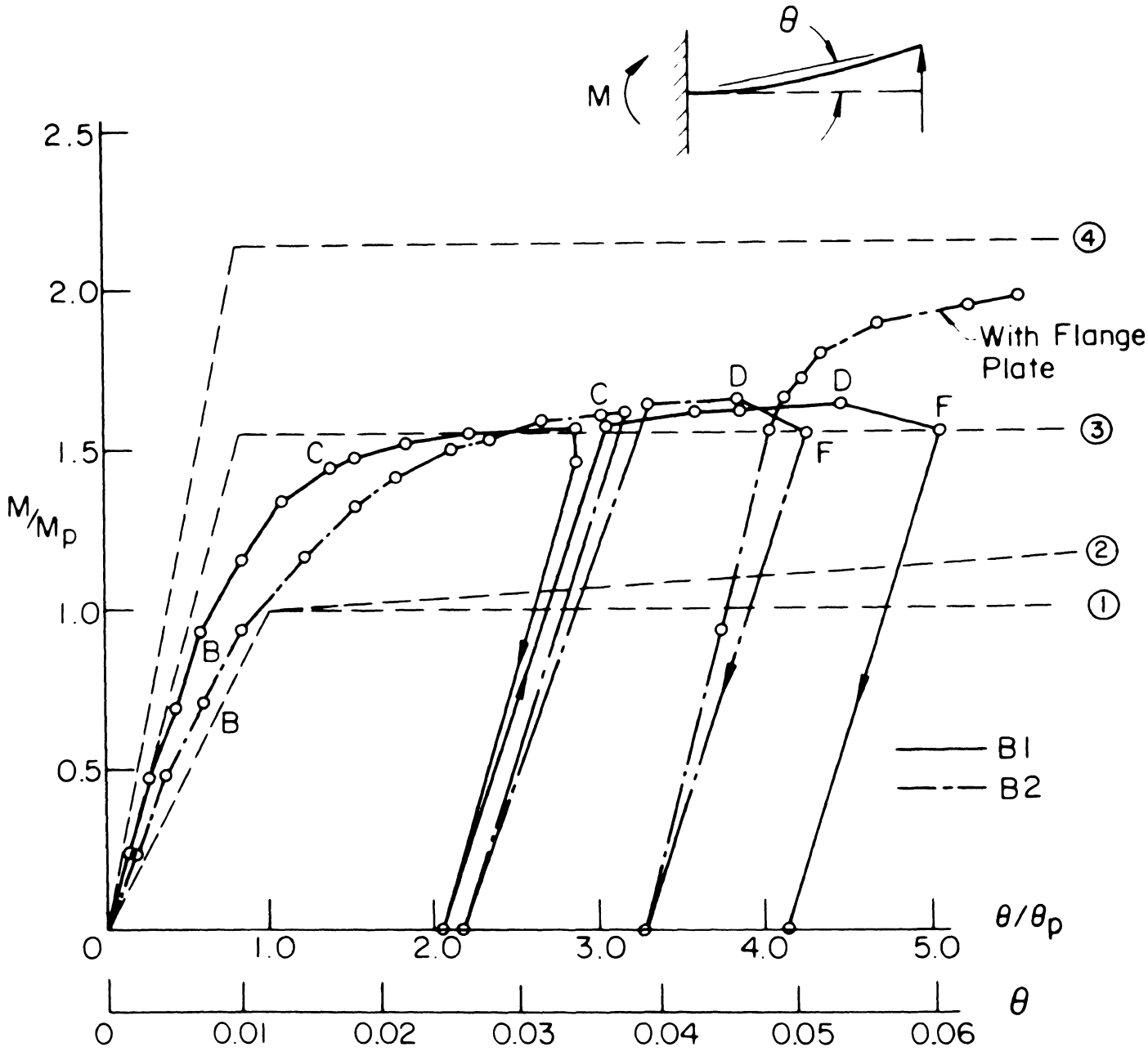

Fig. 49 Moment-Rotation Behavior: Tests B1 and B2

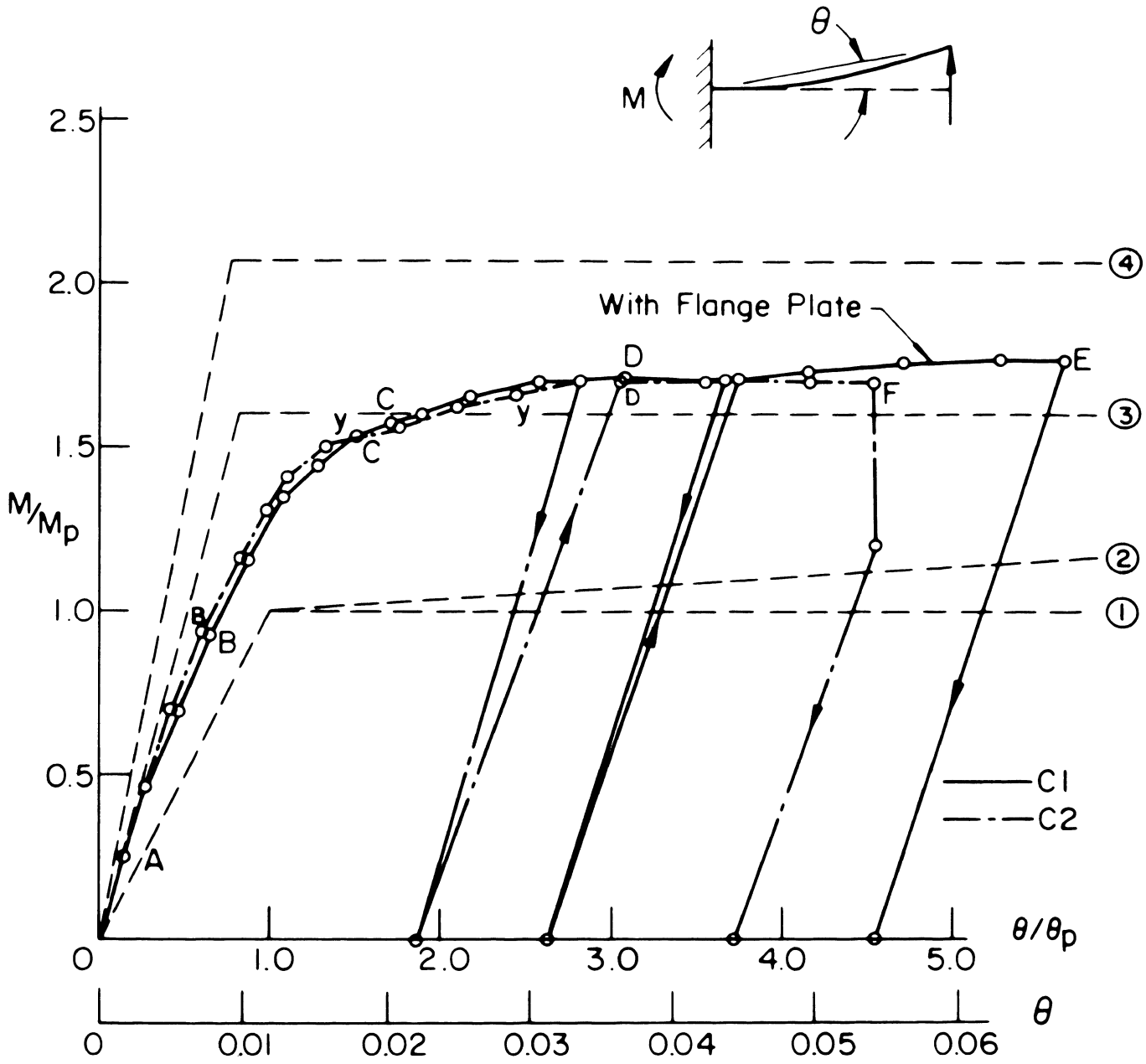

Fig. 50 Moment-Rotation Behavior: Tests C1 and C2

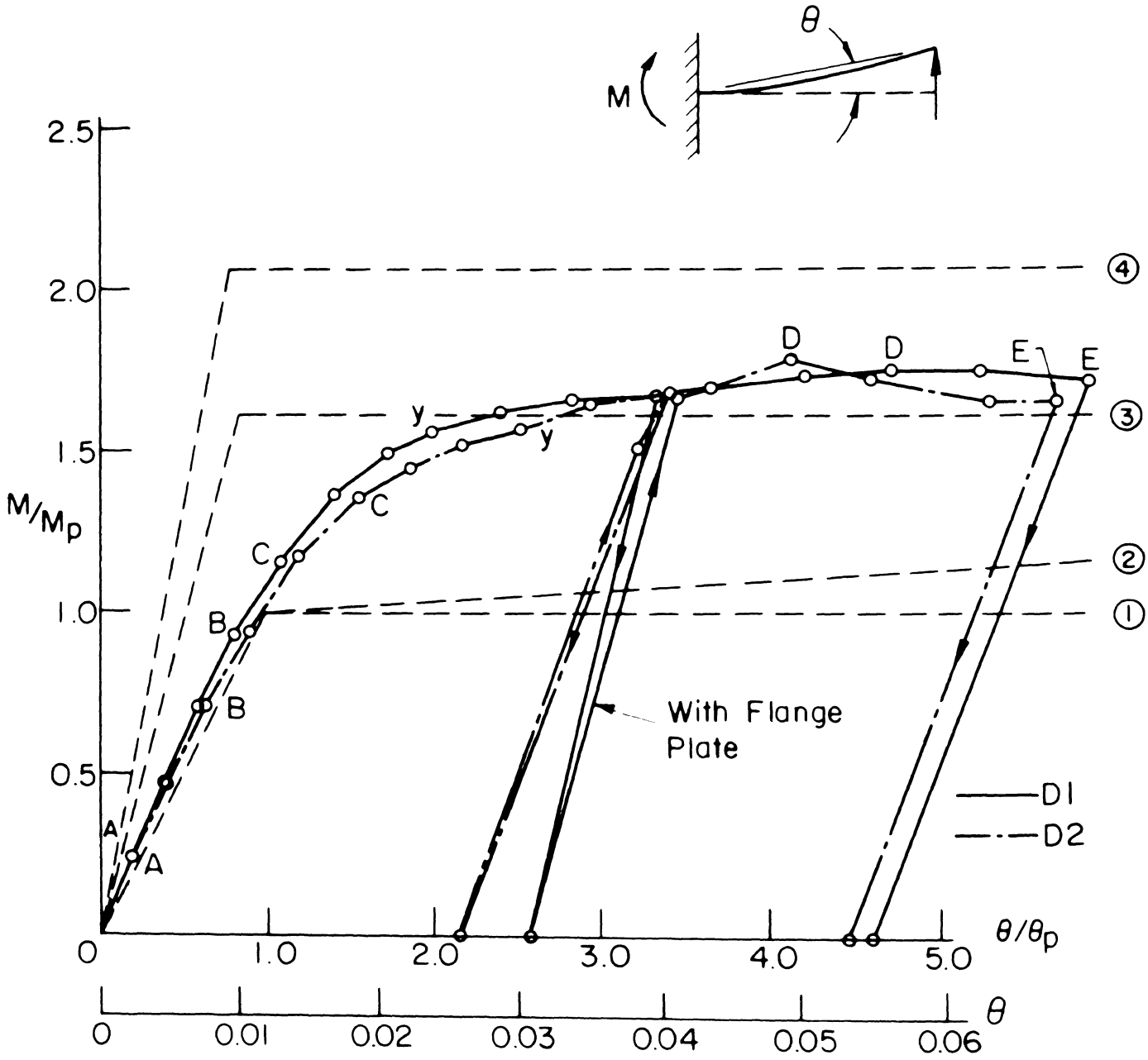

Fig. 51 Moment-Rotation Behavior: Tests D1 and D2

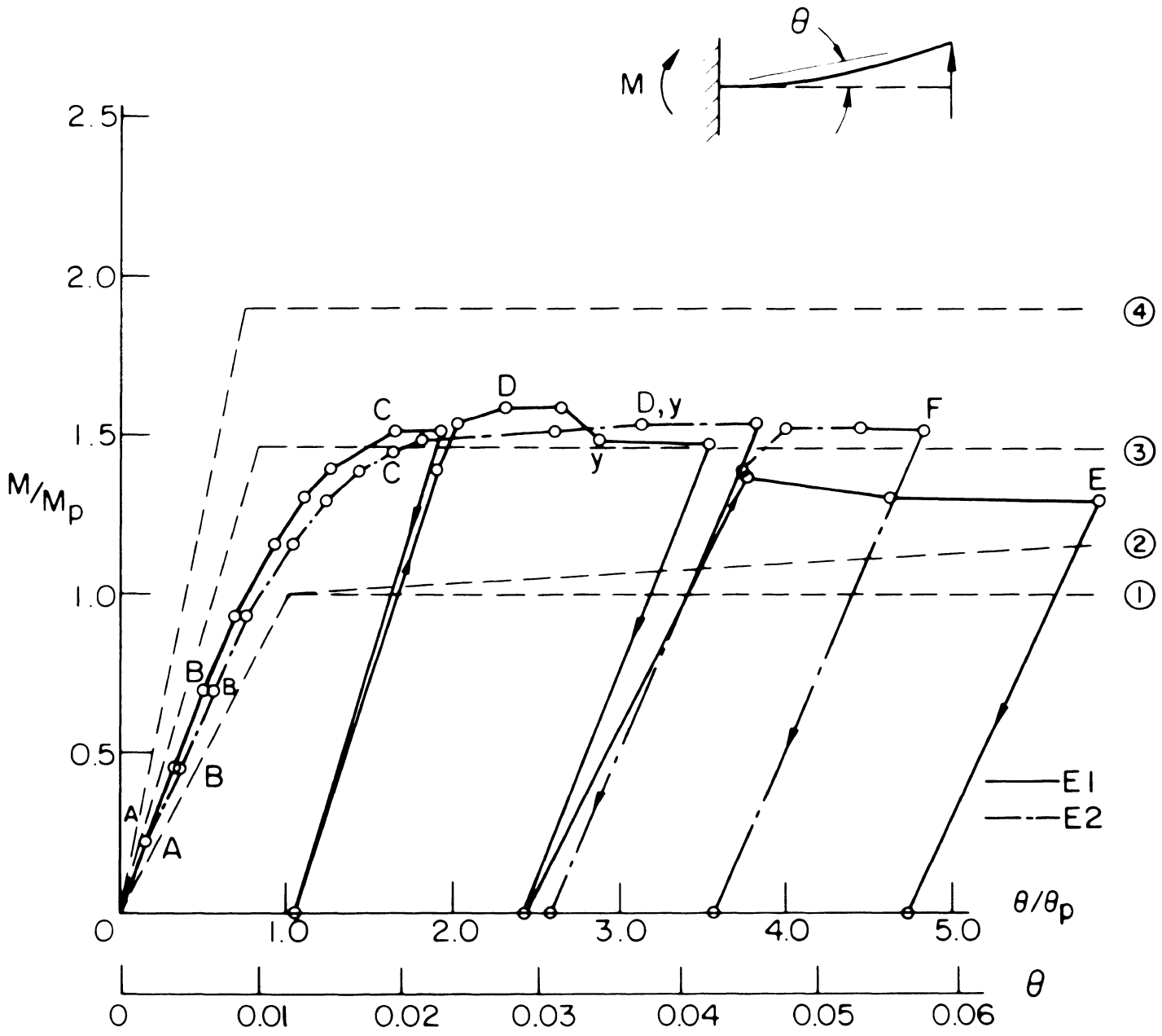

Fig. 52 Moment-Rotation Behavior: Tests E1 and E2

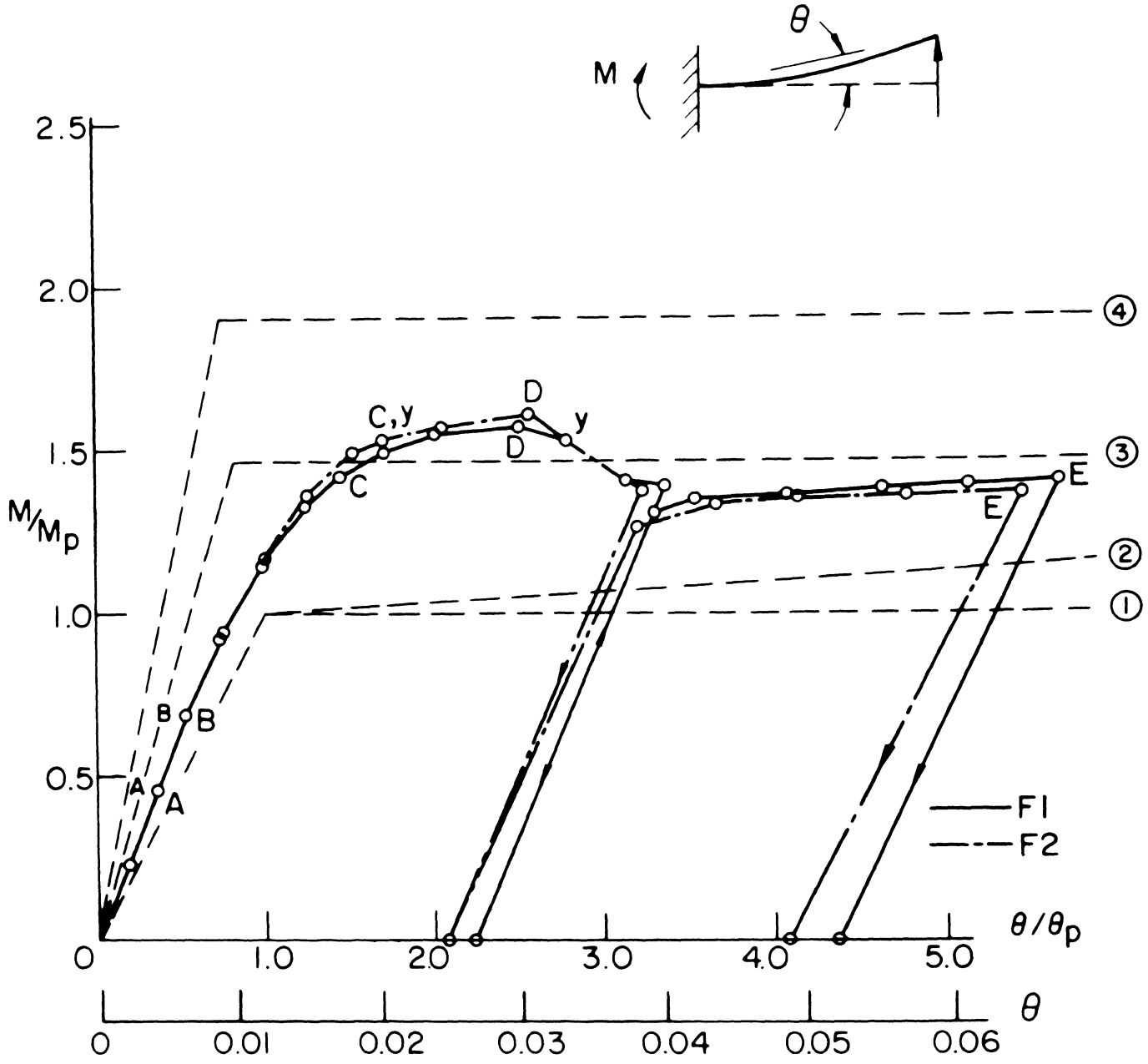

Fig. 53 Moment-Rotation Behavior: Tests F1 and F2

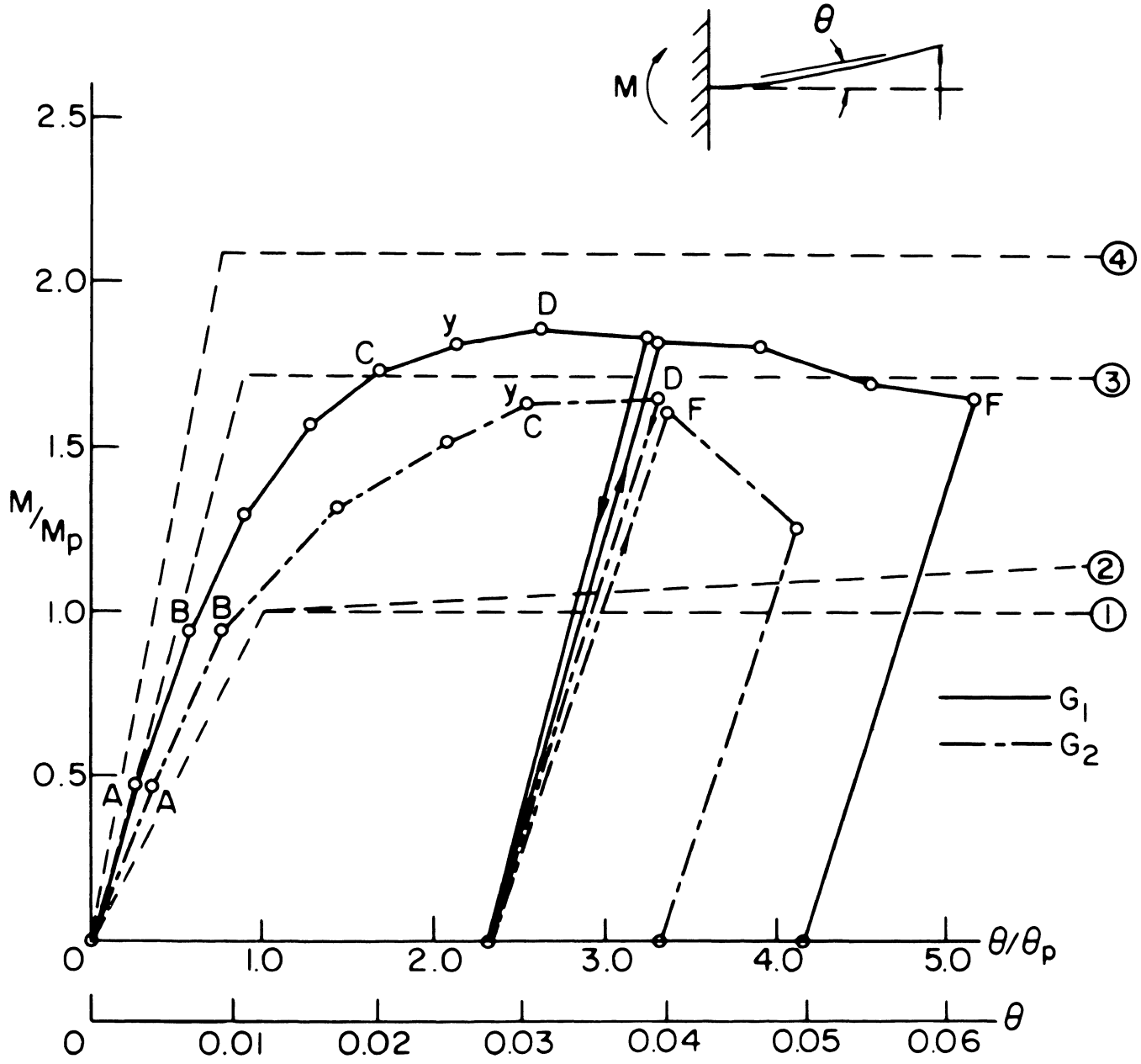

Fig. 54 Moment-Rotation Behavior: Tests G1 and G2

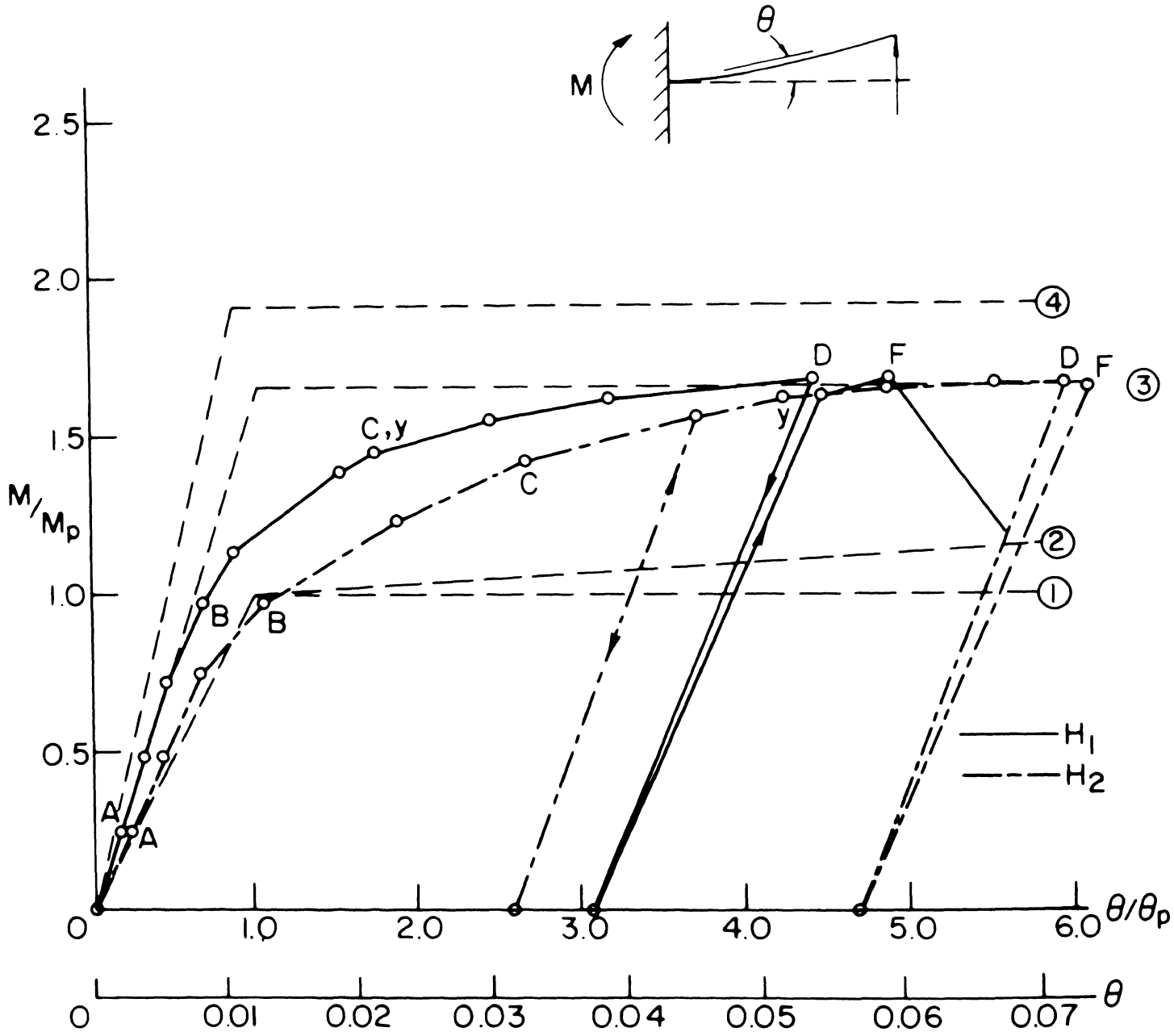

Fig. 55 Moment-Rotation Behavior: Tests H1 and H2

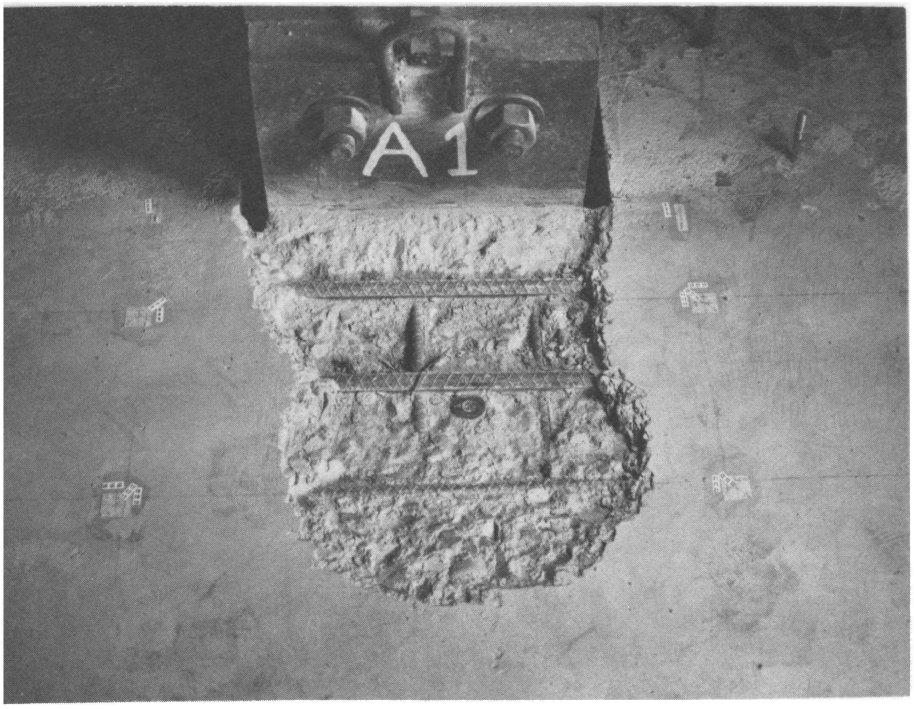

Fig. 56a Failure Surface of Test A1

Fig. 56b Failure Surface of Test C2

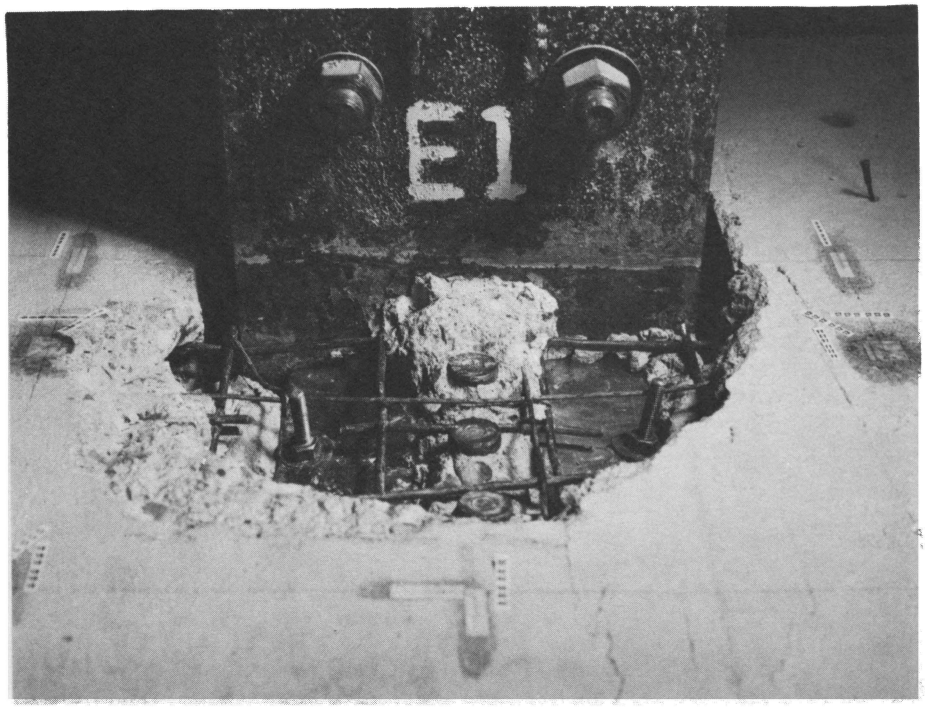

Fig. 57a Failure Surface of Test E1

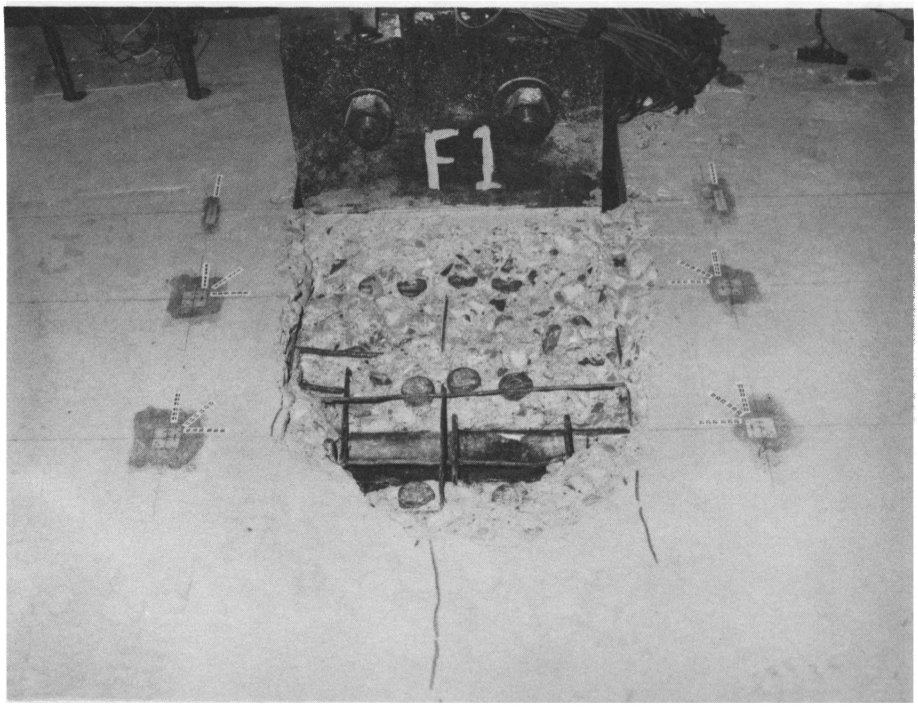

Fig. 57b Failure Surface of Test F1

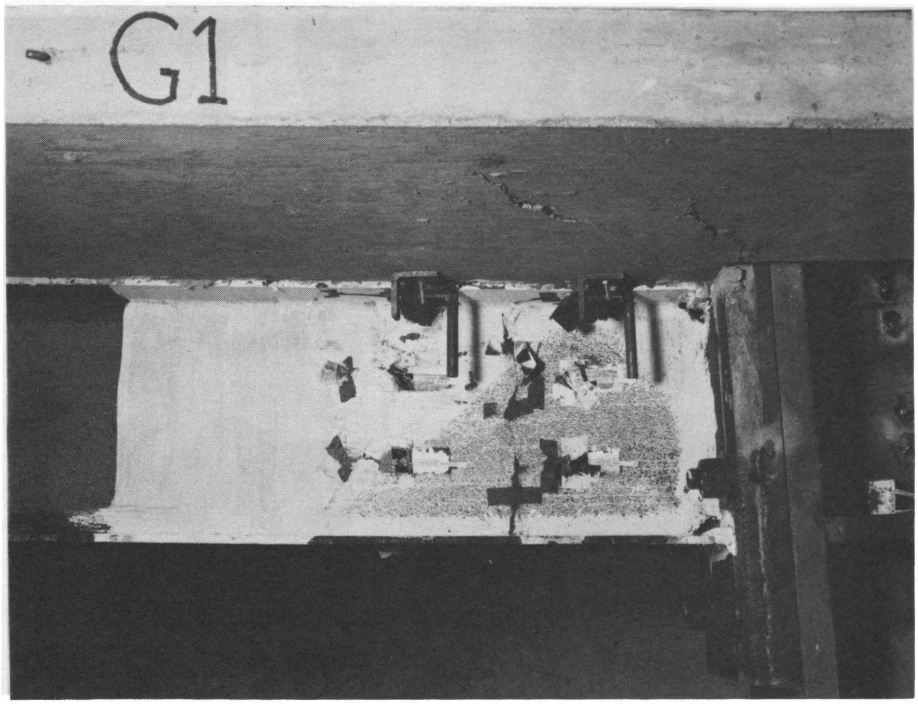

Fig. 58a Yield Pattern and Cracking of the Slab of Test G1

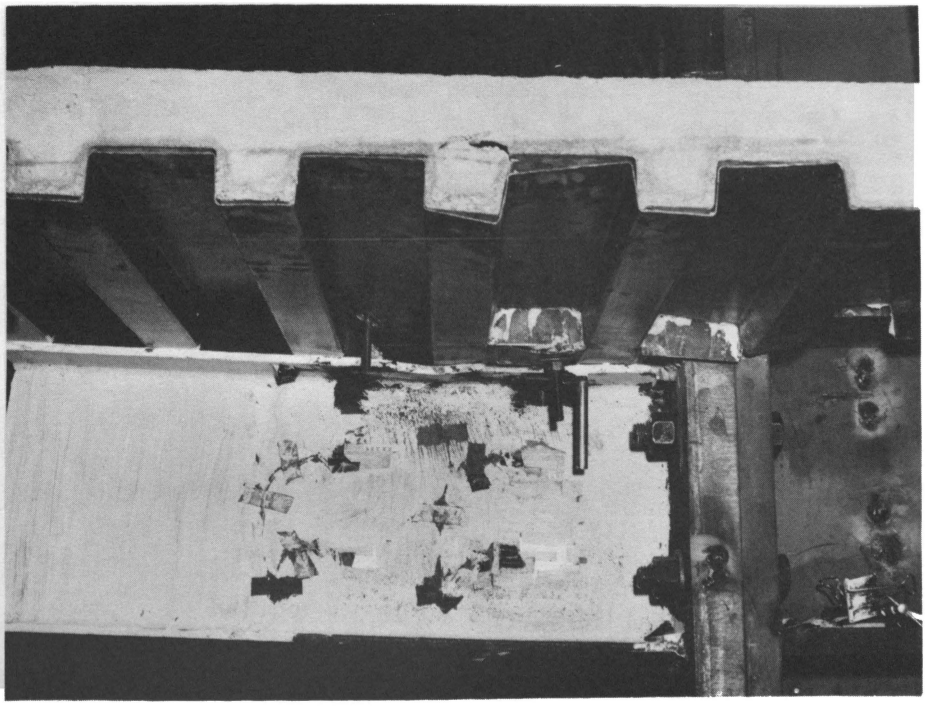

Fig. 58b Shearing of the Ribs and Local Buckling of the Top Flange of Test F2

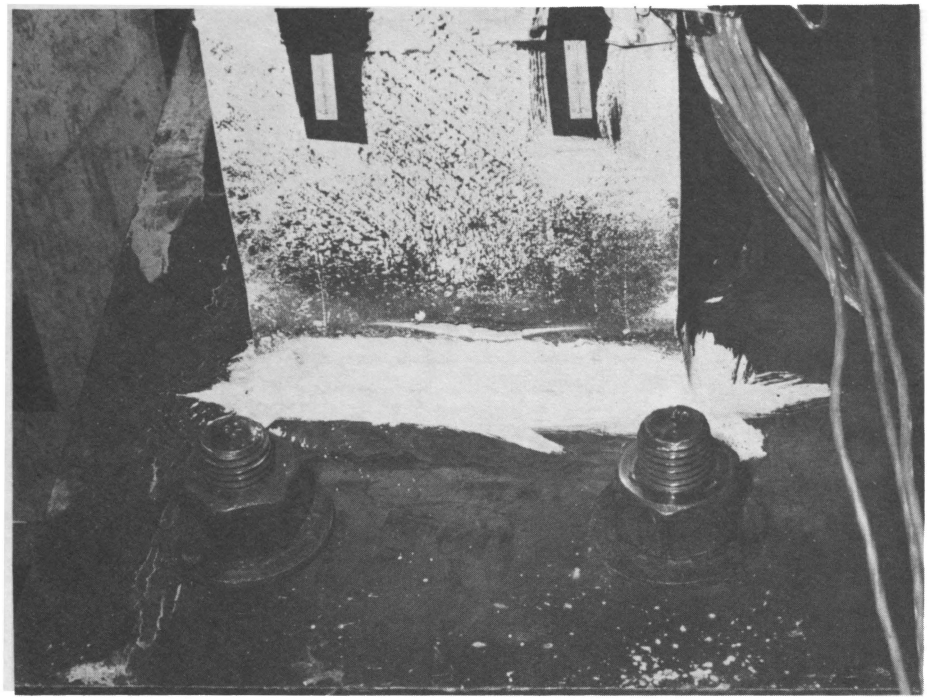

Fig. 59a Cracking of the Tension Flange of Test G1

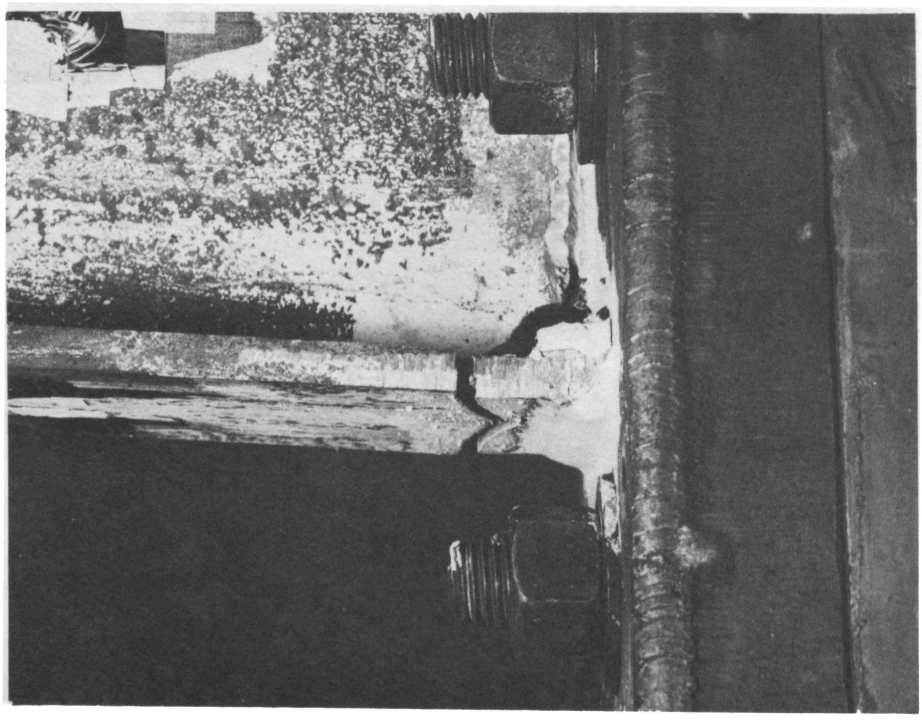

Fig. 59b Cracking of the Tension Flange of Test H1

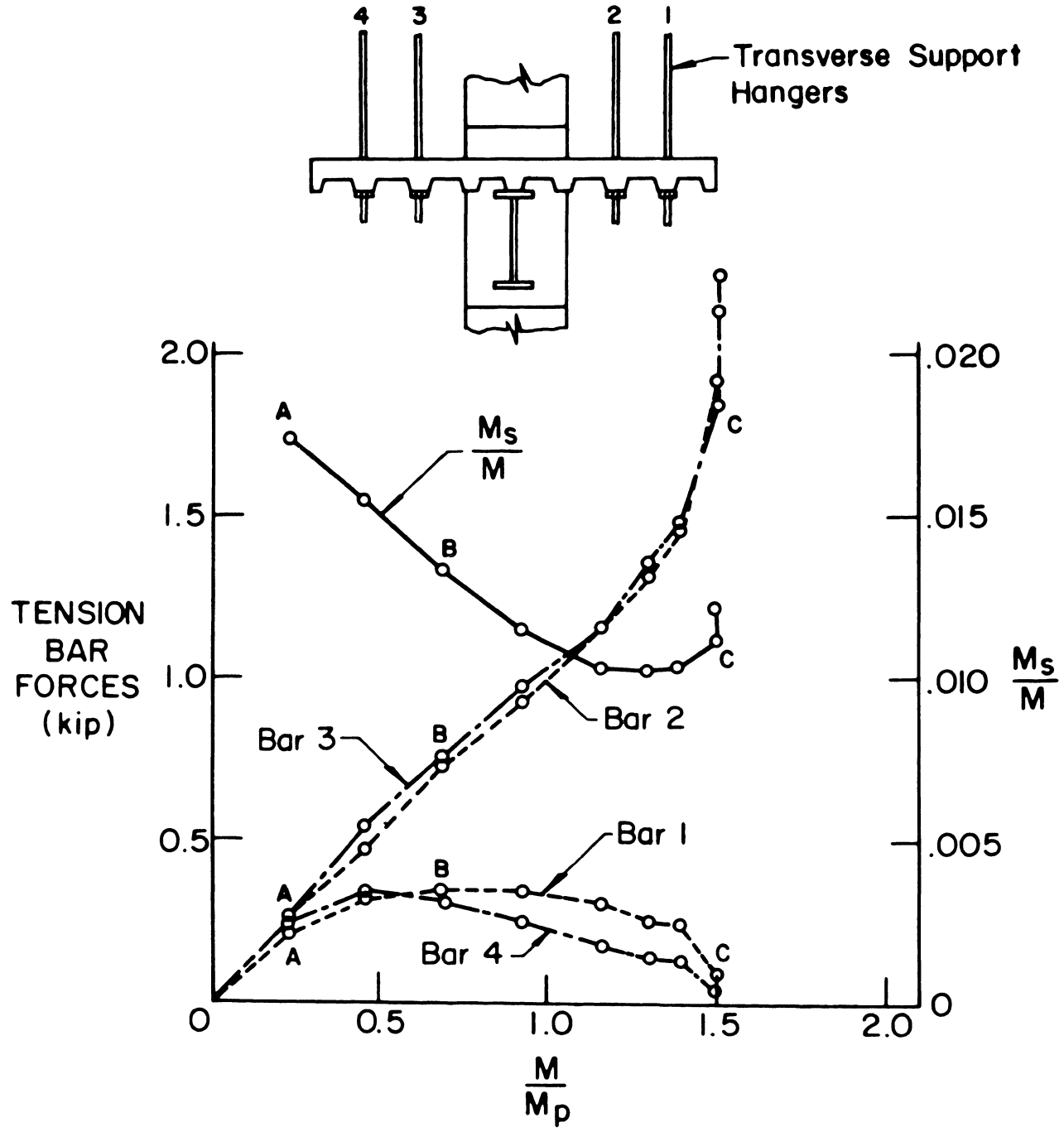

Fig. 61 Forces in Transverse Support Hangers of Test E1

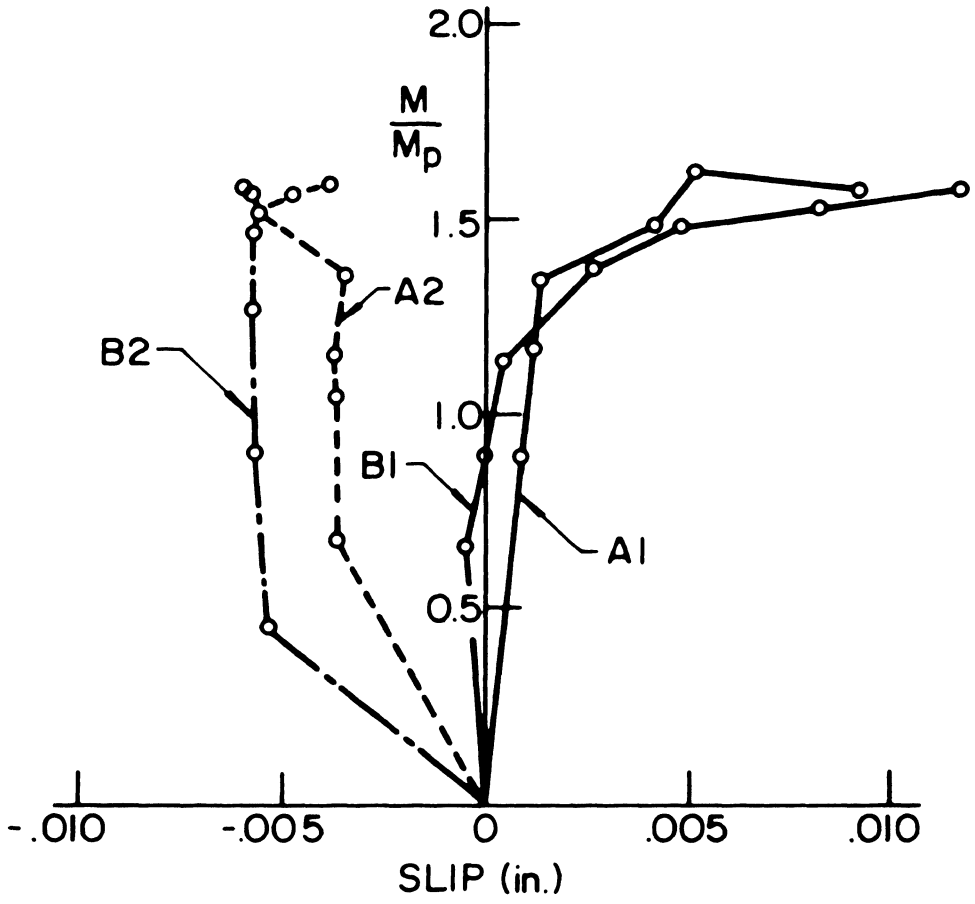

Fig. 62 Relative Slip between Slab and Steel Beam at Gage Section B

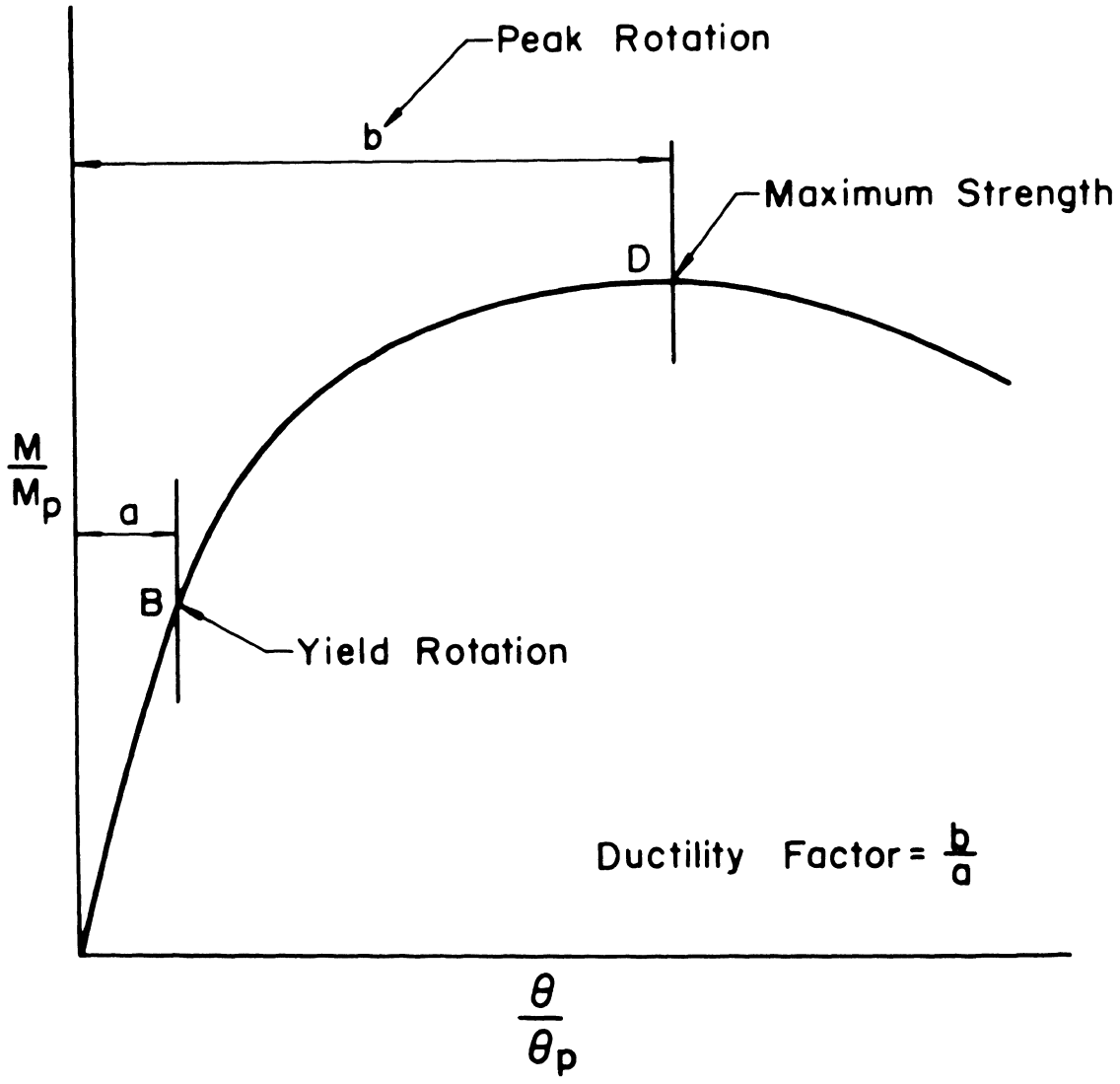

Fig. 63 Typical Moment-Rotation Curve and Definition of Ductility Factor

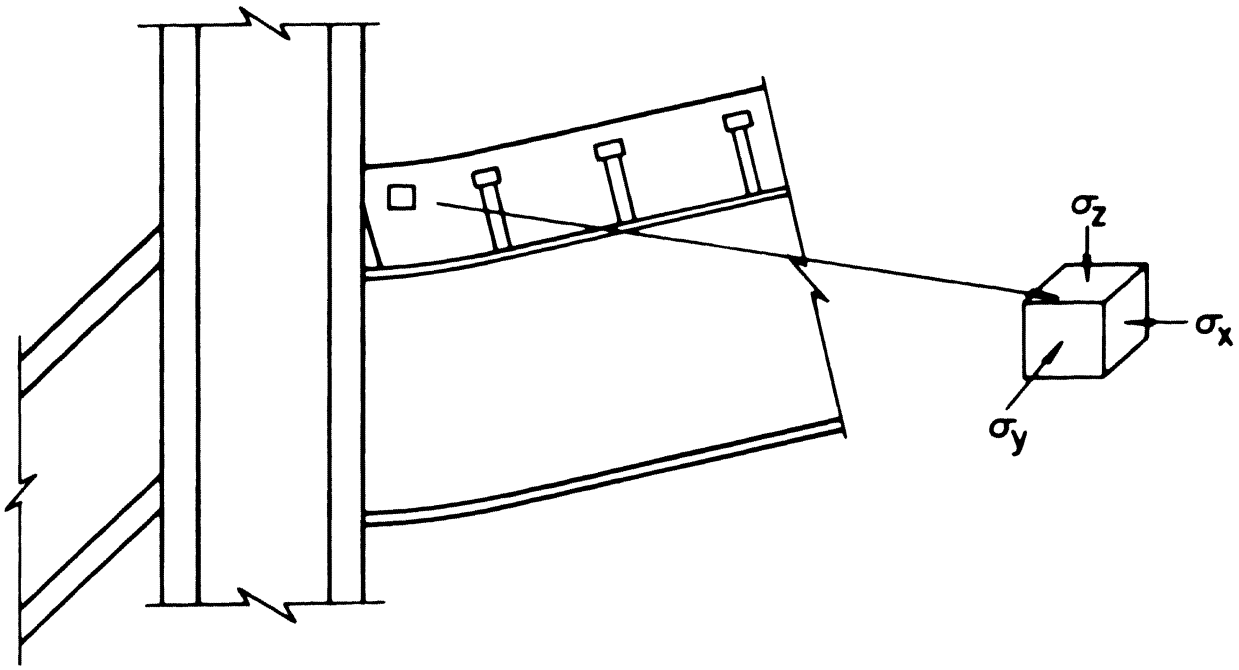

Fig. 64a Three Dimensional State of Stress in the Presence of a Shrinkage Gap

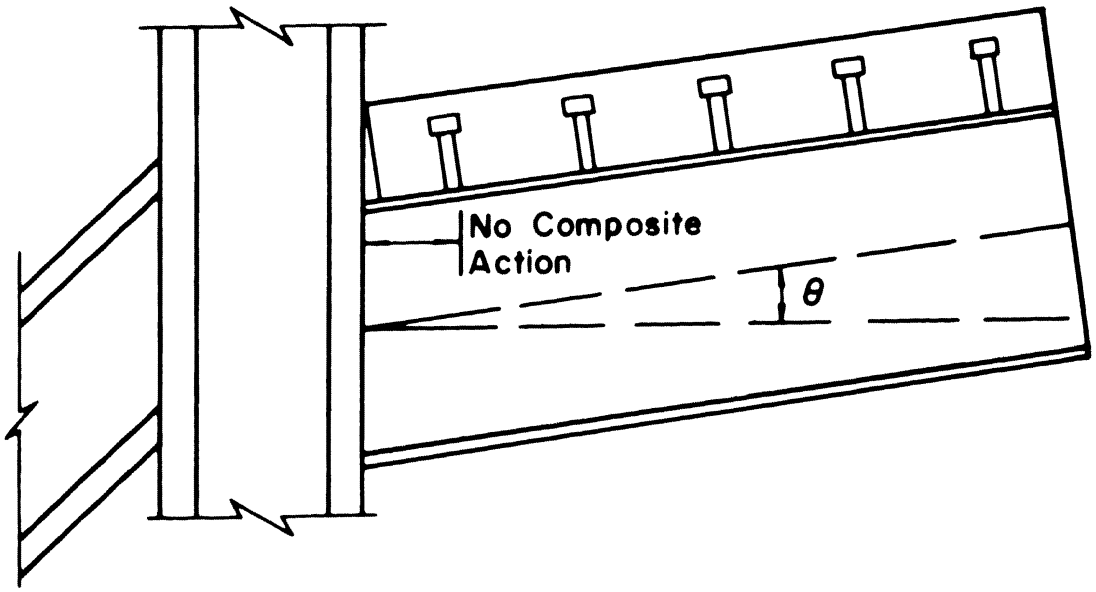

Fig. 64b Rotation Required to Close Shrinkage Gap

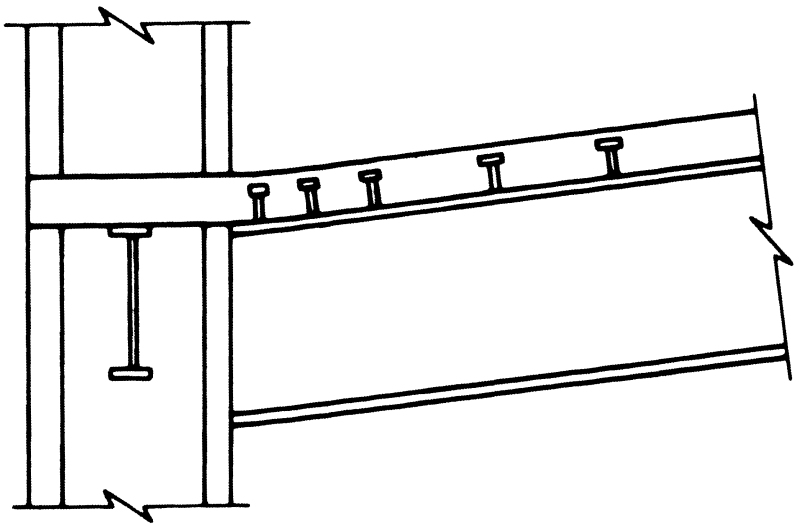

Fig. 65a Dense Connector Spacing at Column

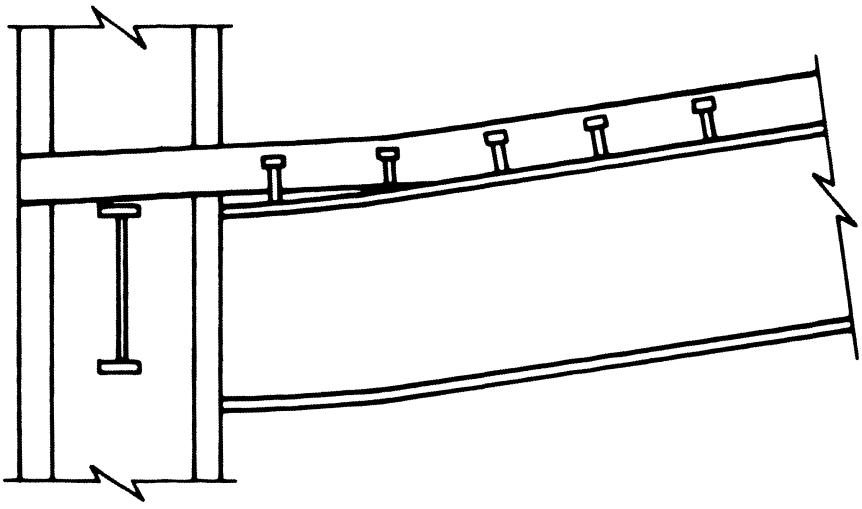

Fig. 65b Normal Connector Spacing at Column

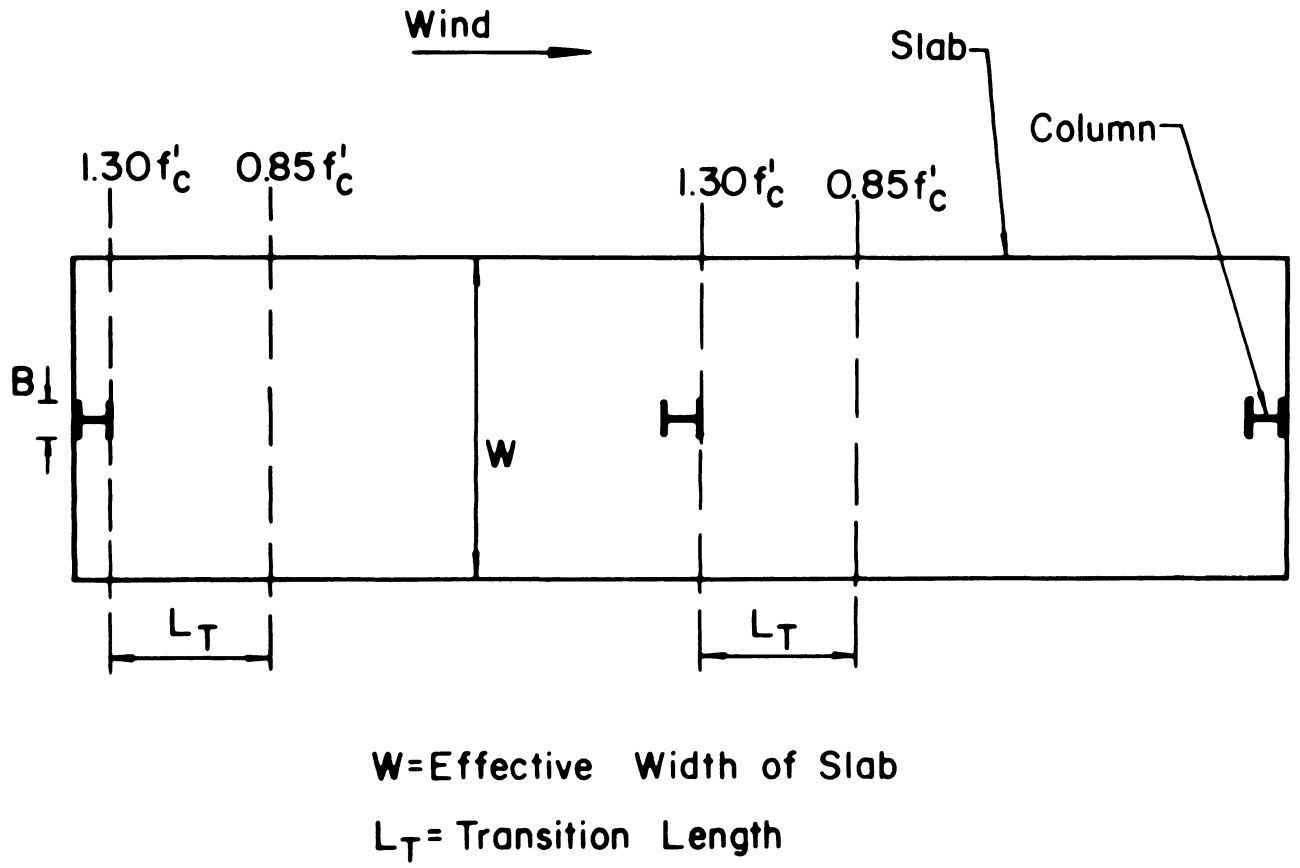

Fig. 66 Plan of Unbraced Frame with Composite Beams

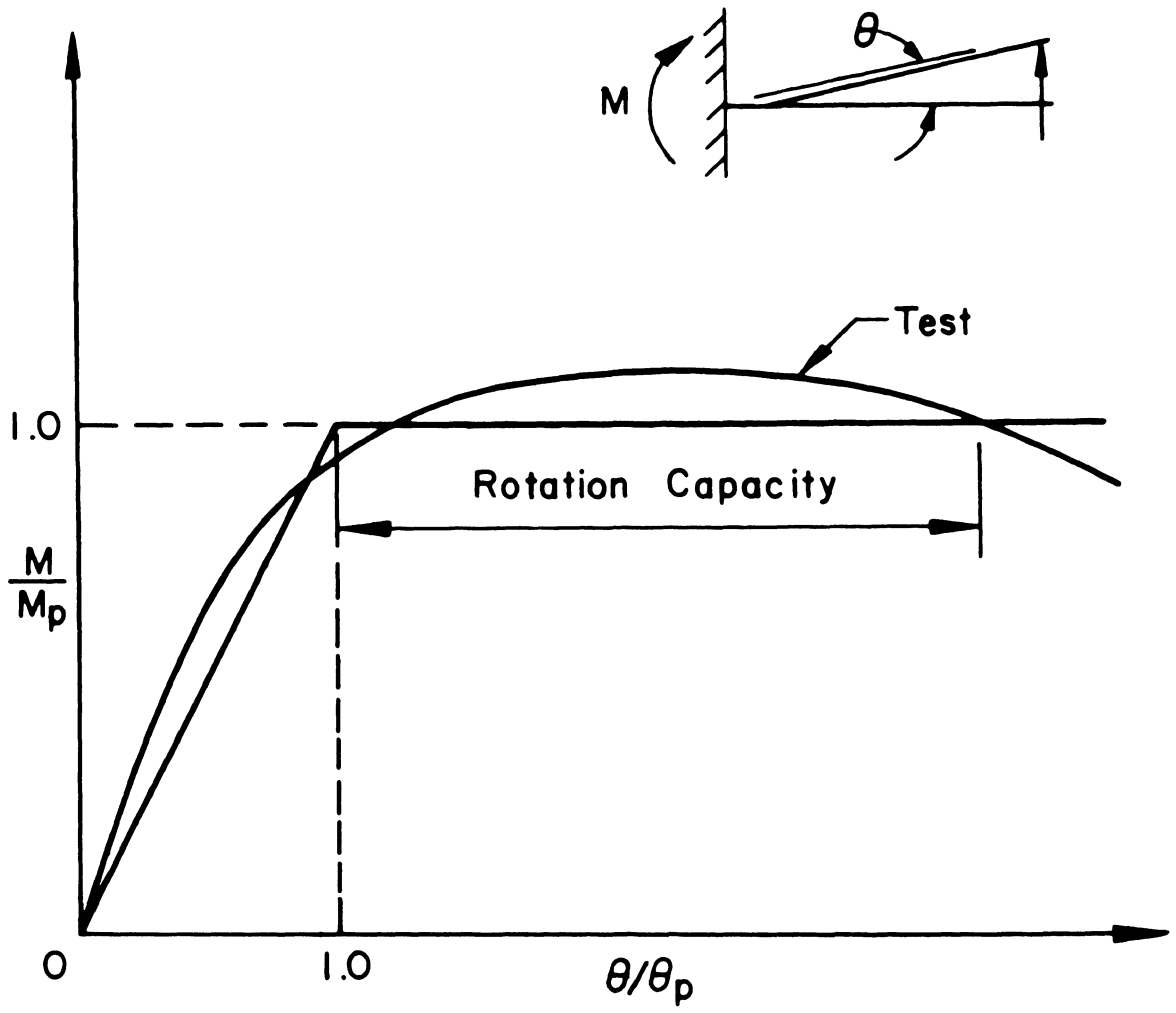

Fig. 67 Definition of Rotation Capacity

13. REFERENCES

1. Daniels, J. H. and Lu, Le-Wu
   PLASTIC SUBASSEMBLAGE ANALYSIS FOR UNBRACED FRAMES, Journal of the Structural Division, Proceedings, ASCE, Vol. 98, No. ST8, August 1972.

2. Lehigh University
   PLASTIC SUBASSEMBLAGE ANALYSIS AND TESTS FOR RIGID HIGH-RISE STEEL FRAMES, AISI Bulletin No. 23, March 1973.

3. Lu, L-W., Ozer, E., Daniels, J. H., Okten, O. S. and Morino, S.
   STRENGTH AND DRIFT CHARACTERISTICS OF STEEL FRAMES, Journal of the Structural Division, Proceedings, ASCE, Vol. 103, No. ST11, November 1977.

4. El-Dakhakhni, W. M. and Daniels, J. H.
   FRAME-FLOOR-WALL SYSTEM INTERACTION IN BUILDINGS, Fritz Engineering Laboratory Report No. 376.2, Lehigh University, Bethlehem, Pa., April 1973.

5. Daniels, J. H., Kroll, G. D., and Fisher, J. W.
   BEHAVIOR OF COMPOSITE BEAM-TO-COLUMN JOINTS, Journal of the Structural Division, Proceedings, ASCE, Vol. 96, No. ST3, March 1970.

6. AISC
   SPECIFICATION FOR THE DESIGN, FABRICATION AND ERECTION OF STRUCTURAL STEEL FOR BUILDINGS, February 1969.

7. Leonhardt, F.
   PRESTRESSED CONCRETE - DESIGN AND CONSTRUCTION, Wilhelm Ernst and Sohn, Berlin, 1964.

8. ACI
   BUILDING CODE REQUIREMENTS FOR REINFORCED CONCRETE (ACI 318-71).

9. AWS
   Supplement to AWS D1.0-66, CODE FOR WELDING IN BUILDING CONSTRUCTION, 1968.

10. Hill, R.
    THE MATHEMATICAL THEORY OF PLASTICITY, Oxford University Press, 1950.

11. Calladine, C. K.
    ENGINEERING PLASTICITY, Pergamon Press, 1969.

12. Mendelson, A.
    PLASTICITY: THEORY AND APPLICATION, MacMillan, 1968.

13. Chen, W. F.
    EXTENSIBILITY OF CONCRETE AND THEOREMS OF LIMIT ANALYSIS, Journal of the Engineering Mechanics Division, Proceedings, ASCE, No. EM3, June 1970.

14. Chen, W. F. and Drucker, D. C.
BEARING CAPACITY OF CONCRETE BLOCKS OR ROCK, Journal of the Engineering Mechanics Division, Proceedings, ASCE, No. EM4, August 1969.

15. Drucker, D. C. and Chen, W. F.
ON THE USE OF SIMPLE DISCONTINUOUS FIELDS TO BOUND LIMIT LOADS, Engineering Plasticity, Cambridge University Press, 1968.

16. Kupfer, H., Hilsdorf, H. K. and Rusch, H.
BEHAVIOR OF CONCRETE UNDER BIAXIAL STRESSES, ACI Journal, Vol. 66, p. 656, August 1969.

17. RESPONSE OF BUILDINGS TO LATERAL FORCES
ACI Journal, Vol. 68, p. 81, February 1971.

18. Sargin, M., Ghosh, S. K. and Handa, V. K.
EFFECTS OF LATERAL REINFORCEMENT UPON THE STRENGTH AND DEFORMATION PROPERTIES OF CONCRETE, Magazine of Concrete Research, Vol. 23,No. 75-76, p. 99, June-September 1971.

19. Iyengar, K. T. S. R., Desayi, P. and Reddy, C. N.
STRESS-STRAIN CHARACTERISTICS OF CONCRETE CONFINED IN STEEL BINDERS, Magazine of Concrete Research, Vol. 22, No. 72, p. 173, September 1970.

20. duPlessis, D. P.
ANALYSIS OF UNBRACED FRAMES WITH COMPOSITE FLOORS, Dissertation presented to the Department of Civil Engineering, Lehigh University, Bethlehem, Pa., in partial fulfillment of the requirements for the degree of Doctor of Philosophy, 1974.

21. Beedle, L. S.
PLASTIC DESIGN OF STEEL FRAMES, John Wiley and Sons, Inc., 1958.

22. ASCE Manual 41
PLASTIC DESIGN IN STEEL, A Guide and Commentary, 1971.

23. Schaffhausen, R. J.,
COMPOSITE MULTI-STORY RIGID FRAMES UNDER GRAVITY AND LATERAL LOADS, A Thesis presented to the Graduate School, The University of Alabama, Birmingham, in partial fulfillment of the requirements for the degree of Master of Science, 1976.

Part II

COMPOSITE ASSEMBLAGE EXPERIMENTS

J. Hartley Daniels and Thomas Wenk

TABLE OF CONTENTS

ABSTRACT

Part II summarizes a study to determine the ultimate strength and drift behavior of composite steel-concrete assemblages. The composite assemblages simulate the behavior of a story in an unbraced multistory frame. The study is based on tests of two full-scale composite assemblages. One assemblage had a solid slab, the other a slab with formed steel deck. Each assemblage consisted of three steel columns and two composite steel concrete beams forming two equal bays of 4.57 m (180 in.) and a story height of 3.05 m (120 in.). A36 steel and normal weight concrete were used. In each test the gravity loads applied to the beams were maintained constant as drift increments were given to the assemblage. The assemblages were designed so that plastic hinges would form in the composite beams.

The load-drift behavior of both assemblages was predicted by an elastic-plastic frame analysis. The initial stiffness was obtained by a finite element analysis which included the effect of slab cracking, the flexibility of the shear connection and a gap between the slab and the leeward column flange. The plastic moment of the composite beam-to-column connection was determined by using a concrete compressive stress of 1.3 f_c' over the column flange width. The experimental load-drift behavior of both composite assemblages was in good agreement with the predicted behavior.

The test results showed an increase in stiffness of the composite assemblages of about 50% and an increase in ultimate strength up to 70% compared with a steel assemblage.

1. INTRODUCTION

1.1 Background

It is common practice in the design of multistory frames for the floor system to participate in resisting gravity loads by composite action between the steel beam and the concrete slab. Wind loads, however, are still carried by the steel frame alone. Taking into account the composite action of the floor slabs in urbraced multistory frames would mean that higher strength and lower drift were possible. Conversely, composite frames would require less steel than steel frames.

An experimental pilot study showed that considerable increase in strength and stiffness existed at a composite beam-to-column connection [1]. In Part I a detailed parametric study of composite beam-to-column connections under positive end moments was described. The study included twenty connection tests. The ultimate strength of the connection tests could be closely predicted by a lower bound analysis based on the theory of plasticity. The connection tests also indicated that more than adequate ductility was available to include composite frames into plastic design. An investigation of composite connections with concrete encased columns subjected to negative moments was reported in Ref. 2.

For the preliminary plastic design of unbraced multistory steel frames the sway subassemblage method was developed[3]. The method was then experimentally confirmed in AISI Project 150 by tests of two full scale one-story steel assemblages under combined gravity and wind

loads[3,4]. In Ref. 5 the sway subassemblage method was extended to include composite frames. An analytical method to obtain complete second-order load-drift curves of unbraced composite frames was developed. As a continuing step in this research program on unbraced frames two composite one-story assemblages comparable to the steel assemblages of AISI Project 150 were tested under gravity and wind load in order to experimentally verify the method of analysis developed in Ref. 5. This part presents the results of this experimental investigation.

1.2 Scope and Objectives

The experimental part of the investigation consists of tests to ultimate strength of two composite one-story assemblages. The test variable is the type of composite slab. The other characteristics are the same for both assemblages.

The investigation also includes a theoretical analysis of the drift and ultimate strength behavior of composite assemblages. The drift analysis is an extension of the finite element analysis of Ref. 5 to include formed steel deck slabs. It also includes the effect of cracking of the concrete slab, flexible shear connection and shrinkage gaps at the column flanges. The ultimate strength analysis is based on the investigation reported in Part I. The objective is to verify the applicability of this method of analysis to predict the behavior of composite assemblages and to demonstrate the increased strength and stiffness of composite frames.

The study is limited to composite assemblages with symmetric slabs and static loading. The assemblages have steel column and steel beams with a concrete slab. Headed stud shear connectors are used for the shear connection.

1.3 Plan of Treatment

The test program includes a composite steel-concrete assemblage with a solid concrete slab and one with a concrete slab on formed steel deck with the ribs running transverse to the steel beam. The composite assemblages are designed so that plastic hinges form in the composite beams thus simulating the behavior of a story in the lower part of an unbraced multistory frame.

The steel frame of one assemblage is tested in its elastic range before pouring the concrete slab. Both composite assemblages are then tested to ultimate strength under gravity and wind loads. Gravity loads are applied to the beams and maintained constant during testing. The lateral drift is gradually incremented to beyond the ultimate load. The increase in initial stiffness due to composite action is obtained by comparison of the results from the steel frame alone and the composite assemblage tests.

To determine the increase in strength due to composite action a reliable ultimate strength prediction of the steel frame alone has to be obtained. A simple beam test is performed to determined the plastic moment capacity of the beams of the steel frame. Based on this result

the ultimate strength of the steel frame alone is accurately predicted, and compared to the composite assemblage test results.

The theoretical analysis developed in this study is applied to predict the load-drift behavior of the two composite assemblages. Experimental results are then compared with the predicted values.

2. DESCRIPTION OF ASSEMBLAGES

2.1 General

Composite assemblages CA-1 and CA-2 consist of three steel columns and two steel-concrete composite beams forming two equal bays of 4.57 m (180 in.) and a story height of 3.05 m (120 in.) as shown in Figs. 1 and 2. The column shapes are W8x28 for the exterior columns and W8x48 for the center column. The two composite beams consist of a W10x19 steel beam and a 2.03 (80 in.) wide reinforced concrete slab. All steel sections are oriented for strong axis bending and are A36 steel.

The two assemblages differ in the type of slab. Composite assemblage CA-1 has a 89 mm (3½ in.) thick solid slab as shown in Fig. 3. One row of 64x16 mm (2½ x 5/8 in.) headed stud shear connectors spaced at 153 mm (6 in.) is used for the shear connection. Composite assemblage CA-2 has a 102 mm (4 in.) thick slab on a 64 mm (1½ in.) formed steel deck with the ribs running transverse to the axis of the beam as shown in Fig. 4. Inland Ryerson type S steel deck was selected which is one of the standard types in commercial use. One row of 76x19 mm (3 x 3/4 in.) headed stud shear connectors spaced at 153 mm (6 in.) is used for the shear connection. This corresponds to one connector in every rib of the deck. Figure 5 shows a detailed view of the leeward side of the beam-to-column connections of CA-2. A small area of the deck in front of the leeward column flange was cut out to provide full depth of concrete. The required dimensions of this area were studied in Part I.

The slab reinforcement of CA-1 consists of a top and a bottom layer while CA-2 has only a top layer. The top reinforcement of CA-1 and CA-2 is shown in Fig. 6; the bottom reinforcement of CA-1 is shown in Fig. 7. Table 1 summarizes the characteristics of composite assemblages CA-1 and CA-2.

2.2 Design

Since the ultimate strength behavior of the composite beams of the assemblages is one of the main objectives of this investigation the beam and column sizes had to be selected so that plastic hinges would form in the composite beams. This means that relatively strong columns were required which remain elastic up to ultimate load. This kind of plastic hinge pattern would be found in the lower stories of an unbraced multistory frame. A composite assemblage with expected plastic hinge locations in the columns, simulating a story near the top of a multistory frame, was not considered because its ultimate strength would not differ from a steel assemblage[3].

In order to facilitate some comparison of results and the use of the same test equipment the story and bay dimensions of the steel assemblages of AISI Project 150 were maintained[4]. Unlike the tests of AISI Project 150 gravity loads were applied only to the beams and not to the columns. Column axial loads were not included in this investigation for the following reasons: 1) the resulting test setup and loading procedure are greatly simplified, 2) the composite beam behavior is the same regardless of whether the beam moments are due to a combination of lateral load plus PΔ moments or to lateral load moments

alone, 3) as column axial loads increase, the ultimate lateral load and thus the accuracy of measurement is reduced, and 4) in Ref. 4, it was found that the distribution of the gravity loads to the columns has a significant effect on the load drift behavior of an assemblage only if plastic hinges occur in the columns.

Figure 8 shows the statical system of CA-1 and CA-2 together with the applied loads and the expected plastic hinge locations. Figure 9 shows the moment diagrams at the predicted ultimate load and the plastic moment envelopes of assemblage CA-1 and CA-2. The plastic moment envelopes were calculated based on the assumptions discussed in Chapter 7. The column moments at ultimate load do not exceed about 75% of the plastic moment. Both assemblages are designed to have nearly the same ultimate load.

The longitudinal slab reinforcement was selected so that the plastic hinge on the windward side of the center column (plastic hinge location 2 in Fig. 8) would form at a higher lateral load than the plastic hinge at the leeward exterior column (plastic hinge location 1).

The transverse slab reinforcement was spaced closer on the leeward side of the columns (Fig. 6). The concentrated compressive force acting on the slab at the leeward column flange causes transverse tension stresses. The design recommendations given in Ref. 6 for the similar case of an anchor force of a prestressing cable were applied to determine the transverse reinforcement.

The shear connectors were designed for full composite action to ensure that the full plastic moments of the composite sections could be developed and to avoid a premature shear failure. The negative moment region on the windward side of the center column required the closest connector spacing. This spacing was used over the full length of the beams. For assemblage CA-1 with a solid slab the connector capacity given in the AISC Specifications was used[7]. For assemblage CA-2 with a formed steel deck slab the connector capacity given by AISC was reduced as recommended in Ref. 8.

The slab detail in front of the leeward column flanges of CA-2 (Fig. 5) was designed as recommended in Part I. Premature spalling of the concrete was anticipated with the ribs in the transverse direction. For this reason the full slab thickness was provided for a short distance in front of the column flange. The length of this zone was taken as twice the slab thickness based on the failure mechanism discussed in Part I.

2.3 Fabrication and Construction

The steel members were fabricated by the Bethlehem Contracting Company in Bath, Pennsylvania. The beams were delivered to the laboratory with the connectors welded in position. The connectors of the beams with formed steel deck were welded through the deck as is standard practice.

First the three columns were placed on their pinned supports and temporarily attached to the supporting frame. Then the beams and top

struts were lightly bolted to the columns. Schematic views of the test setup are shown in Figs. 10 and 11. Each column and beam was aligned in the correct position with a plumb line and a carpenter's level and all bolts tightened. Figure 12 shows the steel frame of CA-2 aligned and ready for welding. After completion of the alignment the beams were welded to the columns.

In the case of CA-1 the slab formwork was now constructed. The formwork was supported on the beams of the assemblage and on the surrounding framework. After the rebars were laid out the slab was poured using a ready-mixed concrete as shown in Fig. 13. The formwork was stripped after the 7 day concrete cylinder tests showed that the concrete had obtained sufficient strength. Then assemblage CA-1 was instrumented and, with the connection of the loading jacks, assemblage CA-1 was ready for the composite assemblage test.

After welding of assemblage CA-2 the steel members were instrumented and the loading jacks connected for the initial steel assemblage test. Following the steel assemblage test a formwork to support the edges of the steel deck was constructed in the zero drift position of the assemblage. Then the rebars were laid out and the slab poured as was done for CA-1. After stripping of the formwork only the slab had to be instrumented in preparation for the composite assemblage test.

3. PROPERTIES OF ASSEMBLAGES

3.1 Tensile Coupon Tests

Table 2 shows the mechanical properties of the W10x19 A36 steel beam determined by standard tensile tests. The coupons were machined from an additional section coming from the same heat of steel as the beams for the two assemblages. A total of 7 coupons were taken: 3 from the web and 2 from each flange. No tensile coupon tests were performed on the column shapes. Since the columns remained in the elastic range during the assemblage tests, it was not necessary to determine their complete stress-strain relationship.

3.2 Cross Section Properties of Steel Shapes

The cross section dimensions of each shape were measured at different locations along the length of the members. Table 3 shows the average cross section properties of each shape together with the corresponding handbook values.

3.3 Plastic Moment Capacity of W10x19 Beam

A 3.66 m (144 in.) long W10x19 beam coming from the same heat of steel as the beams of the assemblages was tested in simple bending to determine its plastic moment capacity. The test setup is shown in Fig. 14. The beam was laterally braced to prevent lateral buckling. The experimental load-deflection curve and two elastic-plastic prediction curves are plotted in Fig. 15. Prediction 1) is based on handbook cross section properties and the nominal yield strength σ_y = 250

MPa (36 ksi). Prediction 2) is based on the measured cross section properties and the yield strength obtained from the tensile coupon tests. The experimental load-deflection behavior is in good agreement with prediction 2) which corresponds to an increase of the plastic moment of 12% with respect to the nominal value. The experimental value of the plastic moment M_p = 98.9 kNm (815 kip-in.) was used to predict the ultimate strength of the steel frame of the assemblages CA-1 and CA-2.

3.4 Slab Reinforcement

The slab reinforcement of both assemblages consisted of #3 rebars. The results of two rebar tension tests are reported in Table 4. The nominal value of the yield strength was 276 MPa (40 ksi).

3.5 Slab Concrete

A normal weight ready-mix concrete with a specified 28 day compressive strength f_c' of 21 MPa (3000 psi) was used for both assemblages. The maximum grain size of the aggregates was limited to 8 mm (½ in.). The concrete properties were checked by standard 152 mm (6 in.) diameter cylinder tests. Eight cylinders were cast at the same time as the slab of each assemblage. The concrete properties of CA-1 are given in Table 5; those of CA-2 are given in Table 6.

The cylinders used to determine the compressive strength were tested according to ASTM C39. Two cylinders were tested after 7 days to check the strength prior to stripping the formwork. Four cylinders were tested at 28 days which coincided with the test day of each

composite assemblages. Two of them were moist cured, the other two were cured on the test floor under the same conditions as the slabs of the assemblages. The results showed nearly no influence of the curing conditions on the compressive strength.

The concrete tensile strength was obtained from splitting cylinder tests as described in ASTM C496.

4. INSTRUMENTATION AND TEST PROCEDURE

4.1 Instrumentation

The instrumentation used in the tests provided data to calculate the applied loads, determine deformations and to calculate the internal stress resultants of the assemblages.

Figure 16 shows the instrumentation of the steel frames. Four electrical resistance strain gages, 12 mm (0.48 in.) long, were used at each instrumented cross section, two on each flange. Five cross sections were gaged on each beam and each column was gaged above and below the beam-to-column connection. The instrumented beam cross sections were placed between stud connectors to minimize the influence of the concentrated connector force on the strain readings.

Scales were used to measure the west column drift and the beam deflection as shown in Fig. 17. Horizontal deflection readings were taken with a transit, veritcal deflections with a level. Dial gages were used to measure the horizontal movements of the column bases at pin level. The rotations of the three beam-to-column connection were measured with rotation gages.

Calibrated load cells were used to measure all applied loads. The two top struts were gaged with a full bridge hookup and calibrated before mounting between the column tops. Figure 18 shows one strut in a Fritz Laboratory testing machine during calibration. In addition to their role as structural connecting elements, the struts also serve as load cells to determine the lateral load distribution over the three columns of the assemblages.

Figures 19 and 20 show the location of the strain gages on the concrete slab. Three cross sections in the positive moment regions on the leeward side of the columns were gaged with 25 mm (1 in.) rosettes and linear gages. An effort was made not to place the slab gaged directly above rebars of the top reinforcing layer.

The longitudinal top rebars were gaged in the negative moment region adjacent to the center column (Fig. 19). Foil gages, 13 mm (½ in.) long, protected with a shrinkable plastic tubing were used as shown in Fig. 21.

4.2 Test Setup

The overall view of the test setup used for the two assemblage tests is shown in Figs. 22 and 23. The test assemblage is shown in white. The darker members are part of the supporting frame and the testing equipment.

Vertical beam loads were applied approximately at the quarter points of each beam through a spreader beam which was attached at its midpoint to a gravity load simulator as shown in Fig. 24 [9]. Tension dynamometers (load cells) were used to connect the spreader beam to the test specimen and also to measure the applied loads.

Horizontal load was applied by a hydraulic jack attached to the supporting frame and connected by a load cell to the top of the east column as shown in Fig. 25. The column tops were connected together by a pinned strut designed to maintain a nearly constant distance

between the three column tops. The column bases were supported on pin bearings.

A specially designed lateral bracing prevented lateral movement of the test specimen but did not restrain any in-plane movement[9]. Each column was braced at the top and at beam level. No lateral bracing was needed for the top flange of the beam since the concrete slab served as bracing. The bottom flange of the beams had to be braced in the negative moment region on the windward side of the columns to prevent lateral buckling (Fig. 10).

4.3 Test Procedure

Assemblage CA-2 was tested first. The test program was divided into the following two phases:

1. Initial Steel Assemblage Test

Before pouring the concrete slab the steel frame of CA-2 was tested to determine its elastic drift behavior. Half the gravity loads were applied first; then the lateral load was gradually increased to a maximum which was determined so that the resulting bending moment did not exceed 80% of the elastic moment capacity of any cross section of the assemblage.

2. Composite Assemblage Test

Twenty-eight days after pouring the concrete slab composite assemblage CA-2 was tested to ultimate strength. First a lateral load of 45 kN (10 kips) was applied in two load steps; then the full gravity loads were applied. This load sequence was used to ensure that the

struts did not buckle. From this stage the lateral load was gradually incremented. At each increment the gravity loads were adjusted to their specified constant value before strain and deflection readings were taken. When yielding was evident in the assemblage the readings were taken after a waiting period of about 20-30 minutes in order to allow the yielding process to stop. Once the lateral load came close to the predicted ultimate load drift increments instead of load increments were applied until the jack ran out of stroke.

The test procedure of assemblage CA-1 was simplified insofar as only the composite assemblage test was carried out. Since both assemblages had identical steel members, the initial steel assemblage test was not repeated for CA-1. Composite assemblage CA-1 was tested 28 days after pouring the concrete slab. This time the full gravity loads were applied in the zero drift position and then the lateral load gradually incremented as described for the composite assemblage test of CA-2. This load sequence was possible for CA-1 as the test of CA-2 showed that the struts were able to carry a larger compressive force than originally anticipated.

5. RESULTS OF ASSEMBLAGE TESTS

5.1 Initial Steel Assemblage Test

The experimental lateral load versus drift behavior of the steel frame of CA-2 is shown by the solid line in Fig. 26. The total lateral load is plotted as a function of the lower half-story drift measured at the windward exterior column. The test was terminated at a maximum lateral load of 49 kN (11 kips) before any yielding of the steel members took place. The dashed line in Fig. 26 is a linear elastic prediction curve based on measured material properties.

As mentioned in Art. 4.3 only one initial steel assemblage test was performed. An identical behavior of the steel frame of the second assemblage was anticipcated.

5.2 Composite Assemblage Test CA-1

The experimental lateral load versus drift behavior of composite assemblage CA-1 is shown in Fig. 27. The figure also contains an elastic-plastic prediction curve for the composite assemblage and for the steel assemblage. Location and sequence of formation of plastic hinges are shown for both prediction curves. Plastic hinges adjacent to the columns were assumed to form at the face of a column. The prediction curve for the composite assemblage was obtained by analysis of an equivalent frame having constant beam stiffness and the initial drift characteristic determined by the finite element analysis 4 discussed in Art. 6.4. The moment capacity at the different plastic hinge locations were determined as explained in Chapter 7. Actual

material properties were used. The prediction curve for the steel assemblage is based on the results of the beam test reported in Art. 3.3.

Specific developments which occurred during testing are also indicated in Fig. 27. These are:

Point A: First yielding in top and bottom flange of beam at the leeward column and in the bottom flange at the windward side of the center column (plastic hinge locations 1 and 2).

Point B: Yielding extends into web at hinge locations 1 and 2.

Point C: Spalling of concrete adjacent to the leeward flange of the center column (plastic hinge location 3).

Point D: Spalling of concrete at windward column (plastic hinge location 4). Local buckling of bottom flange and web at plastic hinge location 3. End of test.

The deflections of the assemblage at three stages of the test are shown in Fig. 28. The columns remained nearly straight. The beam deflections became only noticeable at the last load steps.

Figures 29 and 30 show the failure surfaces in the concrete slab at the leeward column face at the end of testing. The same wedge shaped failure surfaces were observed in the composite connection tests described in Part I. The black lines in Figs. 29 and 30 show where cracking in the concrete slab occurred. The numbers indicate the lateral load in kips when a crack was first noticed. Figure 31 shows the

cracking pattern in the negative moment region on the windward side of the center column. The zero load cracks shown in these figures were shrinkage cracks detected before testing.

Figure 32 shows the yielding in the steel beam at plastic hinge location 1 (Fig. 8). A nearly symmetrical extent of yielding in top and bottom flange indicates no composite action at this location. Figure 33 shows the yielding at the windward side of the center column at plastic hinge location 2 (Fig. 8). Start of local buckling of the bottom flange and the web can also be seen.

5.3 Composite Assemblage Test CA-2

Figure 34 shows the experimental lateral load versus drift behavior of composite assemblage CA-2. Also shown are an elastic-plastic prediction curve for the composite assemblage and the steel assemblage. The steel assemblage curve CA-2 is identical with the curve for CA-1 in Fig. 27. The composite assemblage curve CA-2 takes into account the effect of the slab on formed metal deck as discussed in Chapters 6 and 7.

Specific developments which occurred during testing were (Fig. 34):

Point A: Initial slab cracking in negative moment region on windward side of center column.

Point B: Yielding in bottom flange of beam at leeward and center column (plastic hinge locations 1 and 2).

Point C: The windward exterior (west) beam-to-column connection

fractured at a lateral load of 178 kN (40 kips). The fracture started in the heat affected zone of the bottom flange weld of the beam and progressed into the web weld as shown in Fig. 35. No deflection and strain readings could be taken.

Point D: The assemblage stabilized at a lateral load of 149 kN (33.5 kips). Spalling of concrete was observed at the leeward flange of the center and windward column (plastic hinge locations 3 and 4).

Point E: The assemblage was unloaded and the bottom flange re-welded to the column.

Point F: Maximum load after weld repair.

Point G: End of test.

The deflections of the assemblage at three stages of the test are shown in Fig. 36. The deflected shapes of CA-2 are very similar to CA-1. A view of CA-2 after testing is shown in Fig. 37. The remaining inelastic deformations of the slab are well noticeable.

Figures 38 and 39 show the failure surfaces in the concrete slab at the leeward column face. The crushing of the concrete exposed the reinforcement. The slab cracking in the negative moment region on the windward side of the center column is shown in Fig. 40. No shrinkage cracks were found before testing.

Figure 41 shows the yielding on both sides of the center column. Plastic hinge location 2 is shown on the left side; plastic hinge

location 3 on the right side of the column. In Fig. 42 the yielding at the west column is shown (plastic hinge location 2). The repaired bottom flange weld can also be seen.

6. DRIFT ANALYSIS OF ASSEMBLAGES

6.1 Introduction

The drift at service load is an important characteristic and design criteria of multistory frames. In this chapter a finite element model for drift analysis of composite frames is presented. The model is then applied to predict the drift behavior of composite assemblages CA-1 and CA-2.

In Ref. 5 a specialized finite element program for the analysis of composite frames was developed. But this program had certain limitations with respect to boundary and loading conditions. More recently general-purpose finite element programs like SAP IV[10] were developed which are easily available. With program SAP IV it was possible to accurately model the specific boundary conditions of composite assemblages CA-1 and CA-2 and to include slabs with formed steel deck.

A similar application of the finite element method to the analysis of composite floor systems was reported in Ref. 11. This method did not, however, consider cracking of the concrete slab or the flexibility of the shear connection. Those factors are included in this study.

The finite element analysis is limited to the initial drift behavior before any plastification occurs. Therefore, the usual assumptions of linear elastic material behavior can be made. The complete load-drift behavior of the composite assemblages is obtained by an elastic-plastic analysis of an equivalent frame with constant beam

stiffness and the same initial drift behavior as the finite element model. A nonlinear analysis by the finite element method is not attempted because computer costs are excessive.

6.2 Finite Element Model of Composite System

The composite beam and slab system was discretized using the finite element types available in the computer program SAP IV[10]. A number of different discretizations were investigated including the one adopted which represented an optimum in computation time, preparation of input data and accuracy. A schematic view of the selected model is shown in Fig. 43. Only one half of the structure is discretized since the structure is assumed to be symmetric with respect to the beam axis and only load cases symmetrical to this axis are considered.

6.2.1 Slab

The slab (Fig. 43) is represented by a network of quadrilateral thin plate elements with combined bending and membrane stiffness. As alternative methods of discretization of the slab thick shell elements or plane stress membrane elements could be used. The use of thick shell elements results in a very substantial increase in the computation time with only a minimal improvement of the accuracy. This method was therefore discarded in favor of the discretization with thin plate bending elements.

The use of plane stress membrane elements reduces the computational effort, but also neglects the contribution of the slab bending to the story stiffness. The relative importance of the slab bending

depends mainly on the ratio t/d of the slab thickness (t) to the beam depth (d) of the composite system. In the case of composite assemblage CA-1 with a relatively large t/d ratio the slab bending was found to increase the story stiffness about 5%. For composite systems with deeper steel beams a plane stress model for the slab would be satisfactory. There would be a saving in computation time with only a small reduction in accuracy.

Slabs with formed metal deck are modeled by plate bending elements of uniform thickness equal to the slab thickness above the rib. The concrete in the ribs and the metal deck itself are neglected.

6.2.2 Beams and Columns

The steel beams and columns (Fig. 43) are modeled by lines of beam elements. The use of plane stress elements to model web and flanges of the beam shapes complicates the preparation of the input data and is only justified if local stresses are of concern. It does not improve the accuracy of the drift analysis.

6.2.3 Shear Connection

The shear connection (Fig. 43) is modeled by a row of vertical beam elements linking the beam axis to the midsurface of the slab. The task of the linkage elements is twofold: 1) they model the eccentricity of the beam with respect to the slab and 2) they model the load-slip relationship of the shear connectors. In Ref. 12 the load-slip relationship of shear connectors in solid slabs was determined from tests on pushout specimens. The initial tangent stiffness of one stud shear connector, K_c, was found to be

$$K_c = 1.57\, a_c \sqrt{f'_c\, E_c} \qquad \text{units in MPa, N, and mm}$$

$$K_c = 40\, a_c \sqrt{f'_c\, E_c} \qquad \text{units in kips and inches}$$

where a_c = area of a shear connector, f'_c = compressive strength of concrete, E_c = modulus of elasticity of concrete.

A review of pushout tests with slabs on formed steel deck[13,14,15] gave a large scatter of connector stiffnesses. For lack of a conclusive value of the connector stiffness for slabs with formed steel deck the same value as for solid slabs was used. This overestimates the stiffness of composite floor systems with formed steel deck, but is partially compensated by neglecting the slab ribs in the finite element model which has plate elements of uniform thickness.

The leeward column flange is an important element in transmitting forces between concrete slab and steel frame and can be considered as a large shear connector. It is modeled by L-shaped rigid beam elements connected to the column, as shown in Fig. 43.

6.3 Determination of Mesh Size

To determine the optimal mesh size for the analysis of the composite assemblages a convergence study with three different mesh sizes was undertaken. Only one quarter of an assemblage consisting of a column and half of a beam was analyzed. This reduction of the size of the structure was possible because a point of contraflexure could be assumed at midspan under wind loading alone.

Figure 44 shows an elevation and a plan view of the finite element discretization with the intermediate mesh size. Also shown is the applied load at the beam column joint. A moment was applied rather than a horizontal force because the drift due to a moment depends only on the stiffness of the composite beam and not the column.

Figure 45 shows a comparison of the drift obtained by three models with different mesh sizes and the same loading. The drift index is plotted as function of the total number of degrees of freedom of each model. The difference in drift between the intermediate mesh (Point I) and the fine mesh (Point F) is only about 1% even though the number of degrees of freedom was more than doubled. It was therefore concluded that the intermediate mesh is sufficiently accurate for the composite assemblage analyses.

6.4 Drift Prediction for Composite Assemblages CA-1 and CA-2

Figure 46 shows a plan and elevation view of the finite element discretization used for composite assemblages CA-1 and CA-2.

Only one half of an assemblage is discretized for reason of symmetry as explained in Art. 6.2. The model was further simplified by horizontally cutting the assemblage above the slab. This greatly reduces the bandwidth of the stiffness matrix and consequently the computation time and avoids an ill conditioning of the stiffness matrix. The column stress resultants at the cut due to a lateral unit load were determined by analyzing an equivalent frame with constant beam stiffness and the same drift characteristic as the finite element model.

The results of the equivalent frame analysis were then used as load input for the finite element analysis. This lateral load distribution was confirmed by the results of the composite assemblage tests.

The following three parameters were investigated in the drift analysis: 1) cracking of the concrete slab, 2) flexibility of the shear connectors and 3) gap at the leeward column flange.

The cracking of the slab was taken into account by modifying the material properties of the slab elements which are in tension under combined gravity and wind load. The modulus of elasticity of concrete was replaced by an equivalent modulus for the cracked section $E_e = \rho E$, where ρ = reinforcement ratio and E = modulus of elasticity of reinforcement[5].

To show the influence of the flexibility of the shear connection three analyses with different stiffnesses of the connector elements were carried out: 1) very stiff to simulate a rigid shear connection, 2) the stiffness given in Art. 6.2.3 for the actual connector spacing of CA-1 and CA-2, 3) one half of the stiffness of 2 corresponding to a doubling of the connector spacing.

The effect of a gap between the slab and the leeward column flange is shown by comparison of the drift of a model having very stiff and very flexible column flange elements. A gap between slab and column flange may arise from shrinkage of the concrete slab and from negative gravity load moments. The gap at the leeward flange gradually closes under increasing lateral load and affects only the

drift at small loads. The gap at the windward flange is opening up with increasing load.

The results of the drift analyses of CA-1 and CA-2 are given in Table 7. Six different analyses were carried out to show the effect of slab cracking, the connector flexibility and a gap between slab and the leeward column flange. In Figs. 47 and 48 the load-drift curves of CA-1 and CA-2 are plotted for three different cases. The numbers of the load-drift curves correspond to the analyses numbers in Table 7. Analysis 1 assumes no slab cracking and rigid shear connection. Analysis 4 assumes slab cracking and flexible shear connection. And analysis 6 considers slab cracking, flexible shear connection and a gap at the leeward column flanges. The load-drift curve of the steel frame alone is also shown to point out the increase in stiffness due to composite action.

Table 8 shows the relative importance of slab cracking, connector flexibility and a gap at the leeward column flanges. Slab cracking and a gap at the leeward column flange are the most important factors. Slab cracking increases the drift of CA-1 by 14% and the drift of CA-2 by 17% compared with an uncracked slab. A gap between slab and leeward column flange increases the drift of CA-1 and CA-2 by 15%. The flexibility of the shear connectors has only a small influence on the drift behavior. The drift was increased by 2% compared with rigid shear connection. A doubling of the connector spacing also increased the drift only by 2% compared with normal spaced flexible connectors.

6.5 Comparison with Effective Width Method

In the concept of effective width the theoretical stress distribution of the slab is converted into a statically equivalent constant stress distribution of corresponding width. The usefulness of the effective width concept lies in the assumption that the effective width is constant along the span. Even though the effective width is based on an equivalence of stress and is primarily used for strength calculations it can also be used for stiffness calculations. The rules in various codes and specifications for calculating effective width are listed in Ref. 16.

In the case of composite assemblages CA-1 and CA-2 the AISC Specifications[7] give an effective width equal to $\ell/4$, where ℓ is the span of the beam. The recommendations of the European Concrete Committee (CEB) relate the effective width to the distance between points of zero moment (ℓ_e) rather than the span length. The effective width is given equal to $\ell_e/4$. For continuous beams ℓ_e can be taken as $0.7\ \ell$[16].

Table 9 shows the results of the drift analyses of CA-1 and CA-2 by the effective width method. Effective widths of $\ell/4$ = 1.14 m (45 in.) and $\ell_e/4$ = 0.60 m (31.5 in.) were used. The 30% difference between these two values produced only a 4% change of the drift. Also given in Table 9 is the result of the finite element analysis with flexible shear connection and slab cracking. The drift obtained by the finite element method fell in between the two results of the effective width method with a maximum difference of 3%.

The finite element model of CA-1 and CA-2 assumed free edges of the concrete slab. However, the effective width formulas given above assume a continuous slab over several beams. In this case the restrained transverse deformations increase the stiffness of the composite system. A finite element analysis with modified boundary conditions simulating a continuous slab showed a drift decrease of only 0.4% compared with a slab with free edges.

Composite assemblages CA-1 and CA-2 have a relatively small slab width. Increasing the slab width while keeping the span length constant would decrease the drift, but the drift prediction by the effective width method would remain unchanged since the effective width depends on the span length only. Consequently, the effective width method gives a conservative estimate of the drift behavior.

6.6 Application of the Finite Element Model to a Composite System Having Partial Shear Connection

Tests of composite beams with a low degree of partial shear connection showed a significant loss of stiffness compared with complete interaction. In Supplement No. 3 of the AISC Specification[17] this loss of stiffness is taken into account by defining an effective moment of inertia, I_{eff}, for deflection computations:

$$I_{eff} = I_s + \sqrt{\frac{V_h'}{V_h}} (I_{tr} - I_s)$$

where I_s = moment of inertia of steel beam

I_{tr} = moment of inertia of the transformed composite section

V_h = total horizontal shear to be resisted between the point of

maximum moment and points of zero moment for full composite action

V_h' = total allowable horizontal shear of all connectors between the point of maximum moment and points of zero moment.

This relationship overestimates the stiffness of composite beams with full composite action but provides a good approximation for partial shear connection.

This investigation did not include composite assemblages with partial shear connection. Composite assemblages CA-1 and CA-2 were designed for full composite action for ultimate strength reasons. In order to show that the finite element model discussed in Art. 6.2 can also be used to predict the stiffness of composite systems having partial shear connections the beam 1C1 from the test program reported in Ref. 8 was analyzed. The beam had a formed steel deck and a partial shear connection of 30%.

In Fig. 49 the experimental load-deflection curve of beam 1C1 of Ref. 8 in the working load range is shown together with three prediction curves based on 1) complete interaction, 2) effective moment of inertia, I_{eff} and 3) finite element analysis. The finite element prediction comes very close to the I_{eff} prediction and is in good agreement with the test results. Consequently, the finite element model discussed in Art. 6.2 can also be applied to composite systems having partial shear connection.

7. ULTIMATE STRENGTH ANALYSIS OF COMPOSITE ASSEMBLAGES

7.1 Introduction

Figure 50 shows a composite one-story assemblage under combined gravity and wind loads. To determine the ultimate strength of the assemblage the plastic moment of any cross section of the composite beams and columns must be known. The plastic moment of a composite beam section will depend on the sign of the bending moment and the location in the assemblage.

Figure 51 shows a typical bending moment diagram of a one-story assemblage under gravity and wind load. In this case it has been assumed that the wind load is large enough to produce positive bending moments adjacent to the leeward side of the columns. Such a bending moment distribution will determine five regions of different ultimate strength behavior of composite beams[1]:

Region 1 - An interior region under positive bending moment

Region 2 - A positive bending moment region between region 1 and the leeward side of the windward exterior column

Region 3 - A positive bending moment region between region 1 and the leeward side of an interior column

Region 4 - A negative moment region between region 1 and the windward side of an interior column

Region 5 - A negative moment region between region 1 and the windward side of the leeward exterior column.

The ultimate strength behavior in each of these five regions will be discussed in the following articles. The columns are not included in

this discussion, as their ultimate strength behavior is not different from columns of steel assemblages.

7.2 Composite Beam In Interior Positive Moment Region

Region 1 (Fig. 51) does not differ from similar positive moment regions of composite beams subjected only to gravity loads. The ultimate moment capacity is determined by plastification of the steel and by crushing of the concrete over the full slab width[5].

The two possible stress distributions at maximum moment are shown in Fig. 52. The plastic neutral axis is assumed to be in the slab in case a and in the steel beam in case b. In both cases the maximum concrete compressive stress is taken as $0.85\ f'_c$ and the stress in the steel beam is equal to the yield stress f_y[7]. For slabs with formed steel deck the thickness of the compression block can not exceed the slab thickness above the ribs.

7.3 Composite Beam In Negative Moment Region

Figure 53 shows the stress distribution at maximum moment in region 4. Only the reinforcement is assumed to be effective in resisting tensile forces in the slab. The maximum tensile force in the slab is therefore equal to $A_r\ f_{yr}$ where A_r = total area of longitudinal reinforcement in the slab and f_{yr} = yield stress of reinforcement. The maximum stress in the steel beam is assumed to be the yield stress f_y.

In region 5 the full tensile force $A_r f_{yr}$ in the slab cannot be developed because the slab has a free edge at its leeward end and no forces act between the slab and the leeward exterior column. At the leeward limit of region 5 the slab force is zero and the maximum moment of that section is conservatively equal to the plastic moment of the steel beam alone.

7.4 Composite Connection at Exterior Columns

At the windward boundary of region 2 the maximum moment is determined by plastification of the steel beam and crushing of the concrete slab over the column flange width.

Figure 54 shows the assumed stress field if the plastic neutral axis passes through the steel beam. The investigation reported in Part I showed that $1.3 f'_c$ is a lower bound for the maximum compressive stress acting on the slab. The maximum stress can be increased from $0.85 f'_c$ in the span to $1.3 f'_c$ at the connection providing sufficient slab width is present to provide adequate lateral confinement.

In the case of slabs on formed steel deck connection tests (Part I) showed a decrease in ultimate strength compared with solid slabs of equal thickness. The assumed lower bound stress field was modified insofar as the thickness of the compressive zone cannot exceed the slab thickness above the ribs as shown in Fig. 55. The same maximum concrete stress of $1.3 f'_c$ as for solid slabs is assumed.

At the leeward boundary of region 2 the maximum moment reaches the plastic moment capacity of the full composite section (Art. 7.2). In Ref. 5 a method was developed to determine the variation of the plastic moment capacity in region 2 as a function of the shear connection and transverse slab reinforcement.

7.5 Composite Connection at Interior Columns

Figure 56 shows the maximum slab forces of the leeward side of an interior column (region 3). Between the column flange and the slab a maximum force of $1.3\ f_c'\ B_c\ x$ acts as at an exterior column, where B_c = column flange width and x = thickness of the compression zone in the slab. For solid slabs x must be less than or equal to the slab thickness t. For slabs with formed steel deck x must be less than or equal to the thickness above the rib (t-h), where h = rib height of the formed steel deck. Unlike the exterior connection a tension force acts in the longitudinal slab reinforcement. The reinforcement is assumed to have yielded in tension. The maximum tensile force in the slab is therefore equal to $A_r\ f_{yr}$. The stress distribution of the composite section at the leeward column flange is shown in Fig. 57. The resultant maximum slab force is equal to $1.3\ f_c'\ B_c\ x - A_r\ f_{yr}$. An equilibrium condition of the composite section requires that the maximum force in the slab must be less than or equal to the yield force of the steel beam. This implies that

$$1.3\ f_c'\ B_c\ x - A_r\ f_{yr} \leq A_s\ f_y$$

where A_s = cross section area of the steel beam. This relationship

determines the position of the plastic neutral axis, which is shown in the steel beam in Fig. 57.

8. ANALYSIS OF TEST RESULTS

8.1 Ultimate Strength of CA-1 and CA-2

The experimental load-drift curves for composite assemblages CA-1 and CA-2 are shown in Figs. 27 and 34, respectively. Also shown are the prediction curves with numbered circles indicating formation of plastic hinges. The values of the plastic moments were determined according to Chapter 7. The predicted locations and sequence of formation of the plastic hinges were confirmed by the test results.

The experimental and predicted ultimate load capacity of CA-1 and CA-2 are compared in Table 10. Both attained a higher ultimate load than predicted. However, had the flange weld not fractured at 178 kN (40 kips) (Art. 5.3) CA-2 would have attained an even higher ultimate load.

The ultimate strength of the assemblages depends on the moment capacity of the plastic hinges necessary to produce a mechanism. The experimental moment at each location plastic hinge location as a function of the drift is shown in Figs. 58 and 59. Also shown are the predicted plastic moments as dashed horizontal lines. The predicted plastic moment M_{p3} at the leeward side of the center column of CA-1 is only slightly higher than the plastic moment M_{p1} of the steel beam alone as shown in Fig. 58. This comes from the fact that the ultimate longitudinal force in the slab reinforcement is nearly equal to the ultimate slab force at the leeward flange of the center column. The resultant slab force on a cross section near the leeward column flange (Figs. 56 and 57) is therefore nearly zero and the plastic moment of

the steel beam is not increased due to composite action. Only the plastic moment M_{p2} on the windward side of the center column of CA-1 benefits from the composite action. In the case of CA-2 the rebar force is smaller and consequently the plastic moment M_{p3} is greater than the plastic moment of the steel beam as shown in Fig. 59.

In Fig. 59 point A indicates the last load step where strain readings were taken before the weld fracture. Point D shows the reading after weld fracture and point E shows the beginning of reloading after weld repair. The moment M_4 is not shown after weld repair because of the uncertainty of the effect of residual stresses caused by repair welding at the location of M_4 itself.

Table 11 shows the experimental and predicted maximum moment at each plastic hinge location. With the exception of M_4 in assemblage CA-2, all experimental moments attained at least the predicted value. From the shape of the M_4 moment curve in Fig. 59 it can be concluded that M_4 would also have attained the predicted value had no weld fracture occurred. The maximum strength over predicted strength ratios of the composite sections are comparable to those obtained in Ref. 3. The assumption of the concrete stress of 1.3 f_c' in contact with the column flange is therefore confirmed as a lower bound. The plastic hinges M_1 showed a significant increase of their moment capacity due to strain hardening in a zone of high moment gradient.

Compared with the steel assemblage composite assemblage CA-1 had an increase in ultimate strength of 71% and CA-2 an increase of 53%.

8.2 Drift Behavior

8.2.1 Steel Assemblage

Experimental and theoretical load-drift behavior of the initial steel assemblage test of CA-2 are shown in Fig. 26. The experimental and the prediction curve are in very good agreement. The steel assemblage was about 5% more flexible than predicted.

8.2.2 Composite Assemblages CA-1 and CA-2

The complete load-drift behavior of composite assemblages CA-1 and CA-2 are shown in Figs. 27 and 34 together with the prediction curves. The initial slope of the prediction curves is obtained by the relationship[18]

$$S_s = S_f - \frac{\Sigma P}{h}$$

where S_s = second order lateral stiffness

S_f = first order lateral stiffness obtained from the finite element model with flexible shear connection and slab cracking (Analysis 4 in Art. 6.4)

ΣP = sum of the gravity loads

h = story height.

Since gravity loads are applied only to the beams the second order stiffness is only about 2% smaller than the first order stiffness. The experimental curves for CA-1 and CA-2 follow the prediction curves closely up to a lateral load of about 90 kN (20 kips) then the assemblages become more flexible than predicted.

A more detailed analysis of the initial drift behavior of CA-1 is given in Table 12. The experimental drift from 0-45 kN (0-10 kips) was about 20% greater than from 45-90 kN (10-20 kips). This is explained by the formation of a gap at the leeward flange of the columns under gravity load which was closed once the lateral load reached 45 kN (10 kips). The moment curves M_3 and M_4 which change sign at a drift corresponding to a lateral load of about 45 kN (10 kips) confirm this explanation (Fig. 58). The experimental drift from 0-45 kN (0-10 kips) is therefore compared with the result of the finite element model with a gap at the leeward column flange (Analysis 6 in Art. 6.4). The drift from 45-90 kN (10-20 kips) is compared with the finite element model having no gap at the leeward column flange (Analysis 4 in Art. 6.4). Both models predict a slightly too stiff drift behavior.

Table 13 shows the initial drift behavior of CA-2 for the load steps 0-45 kN (0-10 kips) and 45-90 kN (10-20 kips). Since the gravity load of CA-2 was applied at a lateral load level of 45 kN (10 kips) a gap at the leeward column flanges did not form. Therefore, the finite element model without a gap at the leeward column flange (Analysis 4) is used for the drift prediction of both load steps. The drift prediction is in very good agreement with the experimental behavior for the load step 0-45 kN (0-10 kips) while the prediction for the load step 45-90 kN (10-20 kips) is 19% too stiff.

The increase in initial stiffness due to composite action was 46% for CA-1 and 50% for CA-2.

9. SUMMARY AND CONCLUSIONS

Tests of two composite assemblages were performed to investigate the behavior of composite steel-concrete frames under combined gravity and wind loads. The test variable was the slab type of the composite assemblages. A solid slab and a slab with formed steel deck were considered. Gravity loads were applied to the beams of the assemblages and kept constant during testing. The lateral drift was gradually incremented to beyond ultimate load.

The main concern of the composite assemblage tests was the initial drift and the ultimate strength behavior. The experimental load-drift behavior of both assemblages could be closely predicted by an elastic-plastic analysis. The initial stiffness was obtained by a finite element analysis which included the effect of slab cracking, the flexibility of the shear connection and a gap at the leeward column flanges. The plastic moment capacity of the composite beam-to-column connection was determined by using a concrete stress of 1.3 f'_c in contact with the column flange.

Based on the test results and on the drift analysis by the finite element method the following conclusions may be drawn:

1) The load-drift behavior of the composite assemblages was essentially as predicted by an elastic-plastic analysis. The location and sequence of formation of the plastic hinges were as predicted.

2) The plastic moment capacity of the composite beam-to-column connections under positive moment can be conservatively predicted

by using a concrete stress of 1.3 f'_c in contact with the column flange.

3) Slab cracking and a gap at the column flange had the most important influence on the initial drift behavior. The effect of the flexibility of the shear connection was comparable small as long as the shear connection is designed for full composite action.

4) A remarkably good drift prediction was obtained by the effective width method. The distance between points of contraflexure rather than the span length should be used to calculate the effective width.

5) The ultimate strength of the composite assemblage with a solid slab exceeded the ultimate strength of the steel assemblage by about 70%. The ultimate strength of the composite assemblage with a slab on formed steel deck exceeded the ultimate strength of the steel assemblage by about 50%.

6) Both assemblages showed an increase in initial stiffness due to composite action of about 50%.

10. RECOMMENDATIONS FOR FURTHER RESEARCH

Only composite assemblages with symmetrical slabs were considered in the theoretical and experimental part of this study. The drift and ultimate strength behavior of assemblages with a one-sided slab, as they are found in exterior frames of buildings, should be included in a future study.

Composite assemblage CA-2 had a formed steel deck slab with transverse ribs. To include formed steel deck slabs with longitudinal ribs requires additional study.

Both assemblages were designed for full composite action. The effect of a partial shear connection was included in the drift analysis. The ultimate strength analysis should be extended to include partial shear connection.

In the assemblage tests the lateral load was applied directly to the steel columns. In actual frames and in particular if the frame acts together with a shear core or shear walls a part of the lateral load is applied through the slab. This problem requires a three-dimensional analysis of composite frames with eventually additional tests.

Only the static behavior of composite assemblages was studied in this investigation. An extension to dynamic behavior is important from an earthquake point of view. It would require a test program with cyclic loading.

11. ACKNOWLEDGMENTS

The investigation described herein was conducted at Fritz Engineering Laboratory, Lehigh University, Bethlehem, Pa. Dr. Lynn S. Beedle is Director of the Laboratory and Dr. David A. VanHorn is Chairman of the Department of Civil Engineering.

The authors wish to thank the Committee of Structural Steel Producers and the Committee of Steel Plate Producers of the American Iron and Steel Institute for sponsoring this research. The contribution of the AISI Task Force on Project 191 consisting of Dr. W. C. Hansell as Project Supervisor and Prof. E. H. Gaylord, Messrs. A. C. Hauswald, H. S. Lew and W. A. Milek, Jr. is gratefully acknowledged.

The authors gratefully acknowledge the assistance given by Mr. Ken Harpel, Laboratory Superintendant, and his staff in preparing the test setups. The manuscript was carefully typed by Ms. S. Matlock. The photographs were prepared by Mr. R. N. Sopko and the drawings by Mr. J. M. Gera.

12. NOMENCLATURE

A_r = area of the longitudinal reinforcement

A_s = area of the steel beam

B_c = column flange width

E = modulus of elasticity of steel

E_c = modulus of elasticity of concrete

H = lateral load

I_{eff} = effective moment of inertia of a composite section

I_s = moment of inertia of the steel beam

I_{tr} = moment of inertia of the transformed composite section

K_c = initial shear stiffness of a shear connector

M = moment

M_p = plastic moment

P = vertical load

S_f = first order lateral stiffness

S_s = second order lateral stiffness

V_h = total shear to be resisted for full composite action

V_h' = total allowable shear of shear connectors

a_c = area of shear connector

d = depth of steel beam

f_c' = unconfined compressive strength of concrete

f_y = yield stress of steel beam

f_{yr} = yield stress of reinforcement

h = rib height of formed steel deck, story height

ℓ = span length

ℓ_e = distance between points of contraflexure

t = slab thickness

x = thickness of compression zone in the slab

Δ = lateral deflection (drift)

ρ = reinforcement ratio

13. TABLES

	CA-1	CA-2
Height	3.05 m (120 in)	3.05 m (120 in)
Bay width	4.57 m (180 in)	4.57 m (180 in)
Exterior columns	W8x28	W8x28
Center column	W8x48	W8x48
Beams	W10x19	W10x19
Slab type	solid slab	on formed metal deck
Slab width	2.03 m (80 in)	2.03 m (80 in)
Slab thickness	89 mm (3½ in)	102 mm (4 in)
Longitudinal reinforcement:		
top	#3 @ 210 mm (8¼ in)	#3 @ 210 mm (8¼ in)
bottom	#3 @ 210 mm (8¼ in)	
Transverse reinforcement:		
top	#3 @ 152 mm (6 in)	#3 @ 152 mm (6 in)
bottom	#3 @ 305 mm (12 in)	
Stud connectors	64x16 mm (2½x5/8 in)	76x19 mm (3x3/4 in)
Connector spacing	152 mm (6 in)	152 mm (6 in)

Table 1 Characteristics of CA-1 and CA-2

Tension Specimen	Static Yield Stress MPa	(ksi)	Ultimate Stress MPa	(ksi)	Elongation 203 mm (8 in)	Modulus of Elasticity GPa	(ksi)
Flange 1	265	(38.5)	430	(62.4)	30.0%	199	(28900)
Flange 2	240	(34.8)	408	(59.2)	28.8%	207	(30000)
Flange 3	254	(36.9)	430	(62.3)	29.0%	196	(28400)
Flange 4	261	(37.8)	426	(61.8)	29.6%	194	(28200)
Average F	255	(37.0)	423	(61.4)	29.4%	199	(28900)
Web 1	308	(44.6)	453	(65.7)	25.4%	204	(29600)
Web 2	287	(41.6)	435	(63.1)	31.5%	201	(29200)
Web 3	303	(44.0)	448	(65.0)	24.8%	201	(29200)
Average W	299	(43.4)	445	(64.6)	27.2%	202	(29300)

Table 2 Mechanical Properties of W10x19 Beam

Section		d mm (in)	b_f mm (in)	t_f mm (in)	t_w mm (in)	A cm^2 (in^2)	I cm^4 (in^4)
W10x19	Handbook	260 (10.25)	102 (4.02)	10.0 (0.394)	6.35 (0.250)	36.2 (5.61)	4008 (96.3)
	Measured	262 (10.31)	103 (4.05)	10.3 (0.405)	7.09 (0.279)	38.8 (6.01)	4240 (102)
W8x28	Handbook	205 (8.06)	166 (6.54)	11.8 (0.463)	7.24 (0.285)	53.1 (8.23)	4070 (97.8)
	Measured	203 (8.04)	165 (6.50)	11.5 (0.452)	7.26 (0.421)	51.9 (8.04)	3920 (94.2)
W8x48	Handbook	216 (8.50)	206 (8.12)	17.3 (0.683)	10.3 (0.405)	91.0 (14.1)	7660 (184)
	Measured	215 (8.47)	205 (8.09)	17.1 (0.674)	10.7 (0.421)	90.3 (14.0)	7530 (181)

Table 3 Cross-Section Properties of Steel Members

Bar Size	Static Yield Stress MPa (ksi)	Ultimate Stress MPa (ksi)	Elongation	Modulus of Elasticity GPa (ksi)
#3	336 (48.8)	504 (73.2)	15%	192 (27900)

Table 4 Mechanical Properties of Reinforcing Bars

Age	Curing	Compressive Strength MPa (psi)	Splitting Tensile Strength MPa (psi)	Modulus of Elasticity GPa (ksi)
7 days	TF1	16.5 (2390)		
	TF2	15.6 (2260)		
	Average	16.0 (2320)		
28 days	TF3	20.5 (2970)		
	TF4	20.4 (2960)		
	Average	20.5 (2970)		21.4 (3110)
28 days	MR1	19.6 (2850)		
	MR2	18.4 (2670)		
	Average	19.0 (2760)		20.6 (2990)
28 days	MR3		2.19 (318)	
	MR4		2.47 (358)	
	Average		2.33 (338)	

TF = Test Floor Curing

MR = Moist Room Curing

Table 5 Concrete Properties of CA-1

Age	Curing	Compressive Strength MPa (psi)	Splitting Tensile Strength MPa (psi)	Modulus of Elasticity GPa (ksi)
7 days	TF1	15.6 (2260)		
	TF2	13.9 (2020)		
	Average	14.8 (2140)		
28 days	TF3	21.1 (3060)		
	TF4	20.3 (2940)		
	Average	20.7 (3000)		21.5 (3120)
28 days	MR1	21.0 (3040)		
	MR2	20.5 (2970)		
	Average	20.7 (3010)		21.5 (3120)
28 days	MR3		2.45 (356)	
	MR4		3.11 (451)	
	Average		2.78 (403)	

TF = Test Floor Curing

MR = Moist Room Curing

Table 6 Concrete Properties of CA-2

Analysis No.	Slab Cracking	Shear Connection	Gap at Leeward Flange	Drift Δ for a Lateral Load of 100 kN (22.5 kips) CA-1 mm (in.)	CA-2 mm (in.)
1	No	Rigid	No	72.4(.285)	71.6(.282)
2	No	Flexible	No	78.2(.308)	76.1(.299)
3	Yes	Rigid	No	86.0(.338)	86.9(.342)
4	Yes	Flexible	No	88.9(.350)	88.6(.349)
5	Yes	Flexible, Double Conn. Spacing	No	91.3(.359)	90.2(.355)
6	Yes	Flexible	Yes	102.3(.403)	101.9(.401)

Table 7 Results of Drift Analyses of CA-1 and CA-2

Parameter	No. of Compared Analyses	Increase in Drift CA-1	CA-2
Flexible Shear Connection	3 and 4	3%	2%
Doubling of Conn. Spacing	4 and 5	3%	2%
Slab Cracking	2 and 4	14%	17%
Gap at Leeward Column Flanges	4 and 6	15%	15%

Table 8 Effect of Several Parameters on Initial Drift Behavior of CA-1 and CA-2

	Drift Δ for a Lateral Load of 100 kN (22.5 kips)	
	CA-1 mm (in.)	CA-2 mm (in.)
$B_{eff} = \ell/4$ = 1.14 m (45 in.)	88.8 (.350)	85.7 (.337)
$B_{eff} = \ell_e/4$ = 0.80 m (31.5 in.)	91.7 (.361)	89.1 (.351)
% Difference	3.3%	4%
Finite Element Analysis 4	88.9 (.350)	88.6 (.349)
% Difference with B_{eff} = 1.14 m (45 in.)	0.1%	3.3%
% Difference with B_{eff} = 0.80 m (31.5 in.)	3.1%	0.6%

Table 9 Drift of CA-1 and CA-2 by Effective Width Method

	Ultimate Load Capacity	
	CA-1 kN (kips)	CA-2 kN (kips)
Experiment	193 (43.4)	178 (40.0)
Predicted	172 (38.7)	173 (38.9)
% Difference	12.2%	2.9%

Table 10 Ultimate Load Capacity of CA-1 and CA-2

		Ultimate Moments at Plastic Hinge Locations			
		M_1 kNm kip-in	M_2 kNm kip-in	M_3 kNm kip-in	M_4 kNm kip-in
CA-1	Experiment	119 (1050)	172 (1520)	122 (1080)	163 (1440)
	Predicted	98.8 (875)	156 (1380)	101 (895)	150 (1324)
	% Difference	20%	10.4%	20.7%	8.8%
CA-2	Experiment	124 (1100)	156 (1380)	124 (1100)	132 (1170)
	Predicted	98.8 (875)	141 (1250)	120 (1060)	146 (1290)
	% Difference	28%	10.4%	3.7%	-9%

Table 11 Ultimate Moments at Plastic Hinge Locations

CA-1	Drift Δ for Lateral Load Step			
	0-45 kN (0-10 kips)		45-90 kN (10-20 kips)	
	mm	(in.)	mm	(in.)
Experiment	5.26	(.207)	4.14	(.163)
Prediction without gap at col. flange			4.02	(.158)
Prediction with gap at col. flange	4.61	(.182)		
% Difference	12%		3%	

Table 12 Initial Drift Behavior of CA-1

CA-2	Drift Δ for Lateral Load Step			
	0-45 kN (0-10 kips)		45-90 kN (10-20 kips)	
	mm	(in.)	mm	(in.)
Experiment	4.22	(.166)	4.93	(.194)
Prediction without gap at col. flange	4.00	(.158)	4.00	(.158)
% Difference	5%		19%	

Table 13 Initial Drift Behavior of CA-2

14. FIGURES

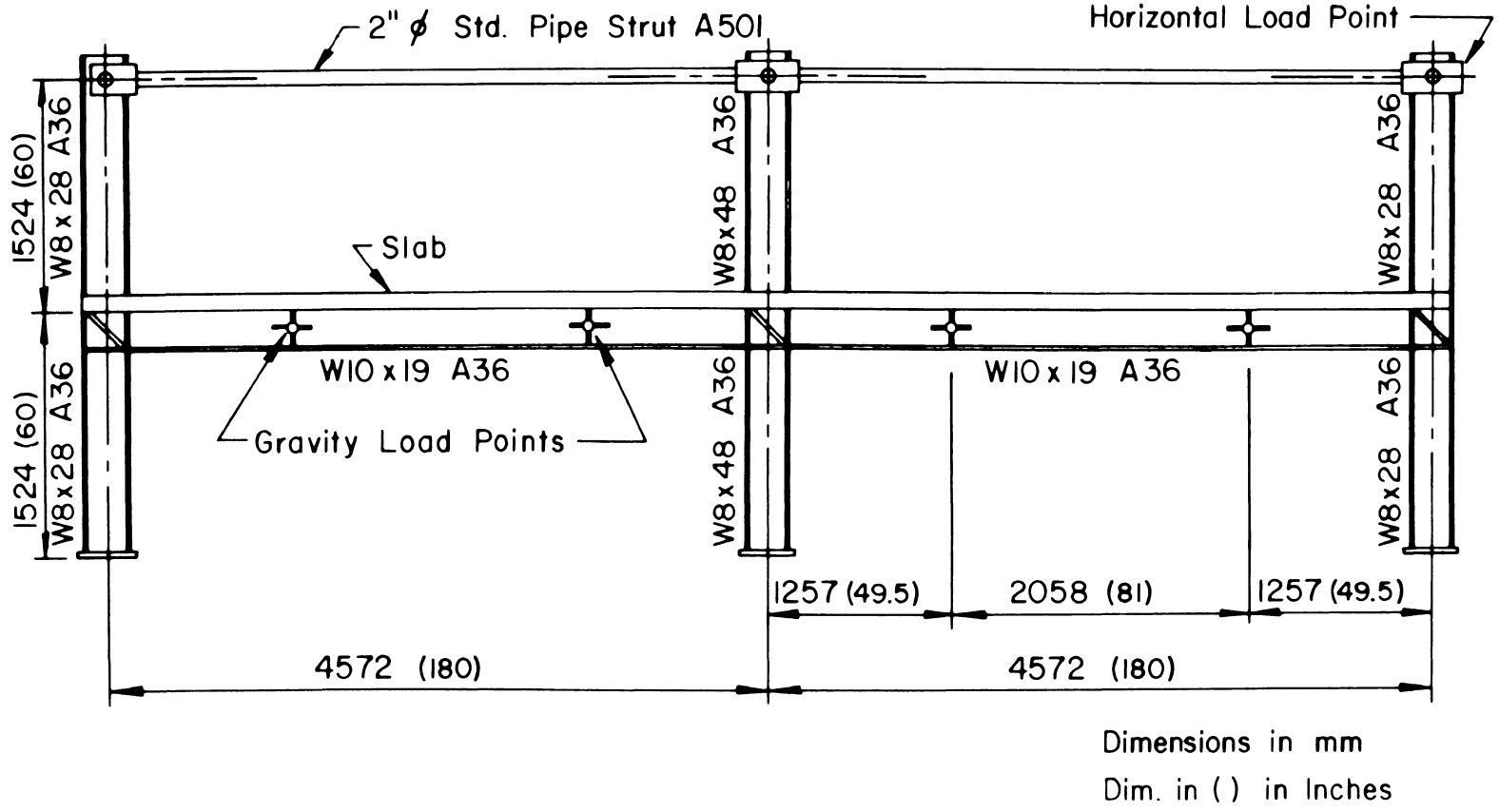

Fig. 1 Elevation View of CA-1 and CA-2

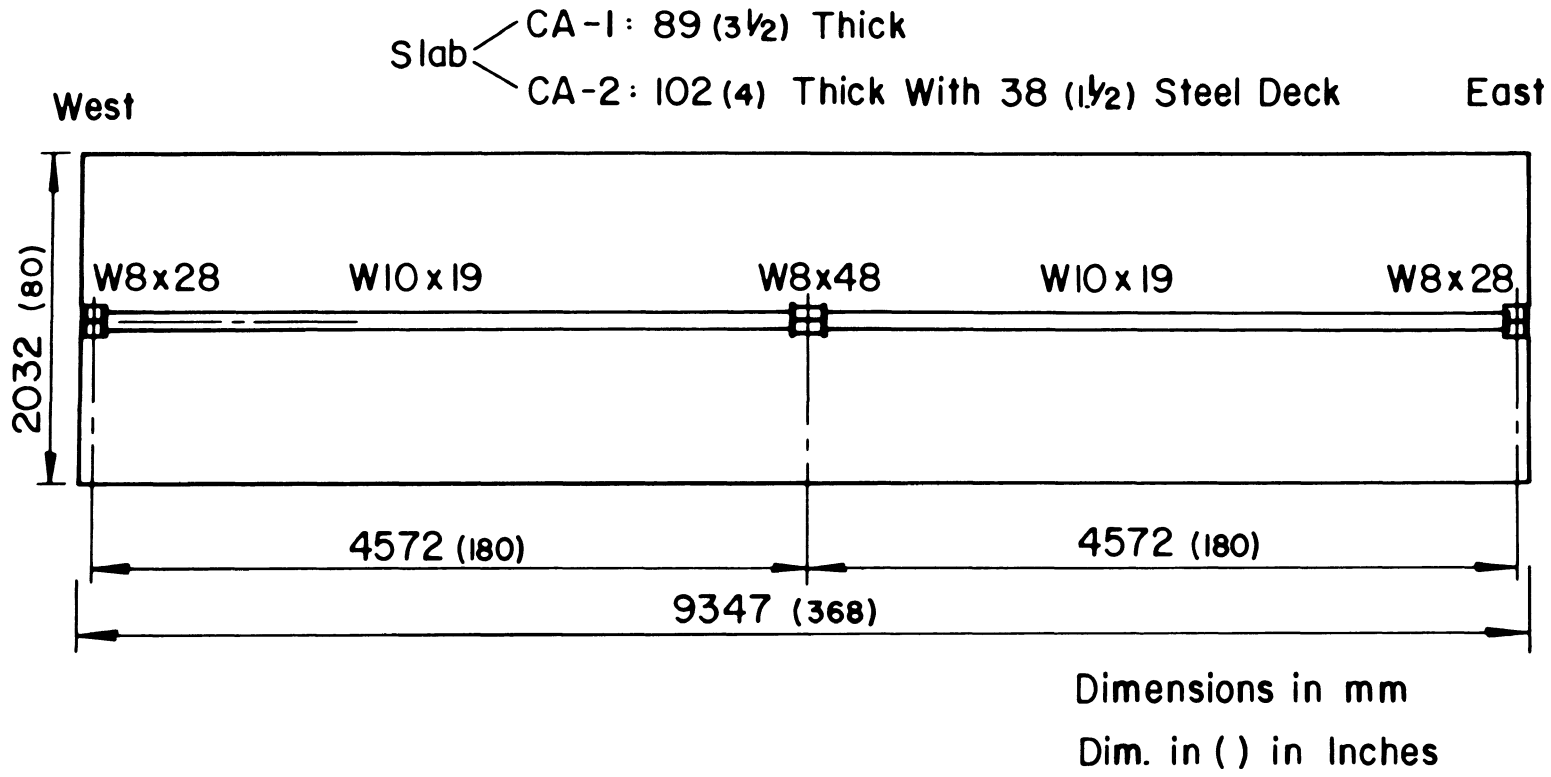

Fig. 2 Plan View of CA-1 and CA-2

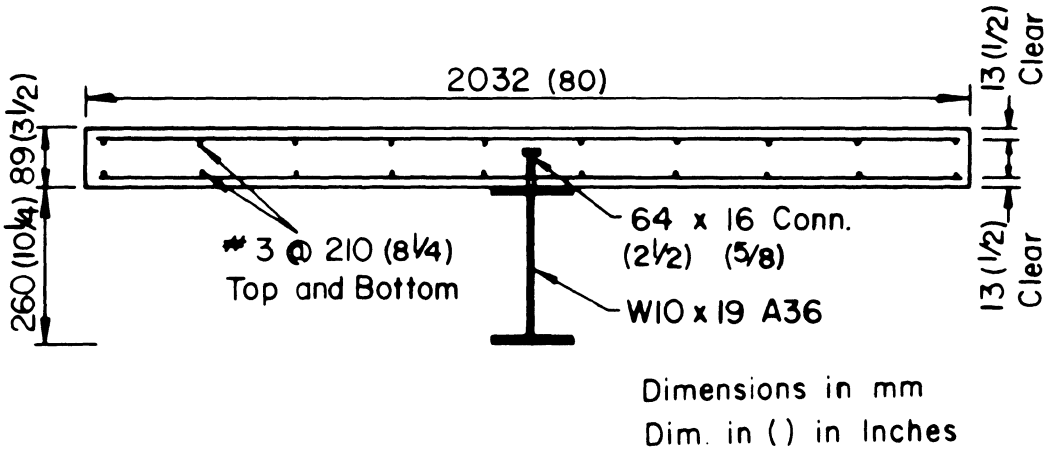

Fig. 3 Section of Beam CA-1

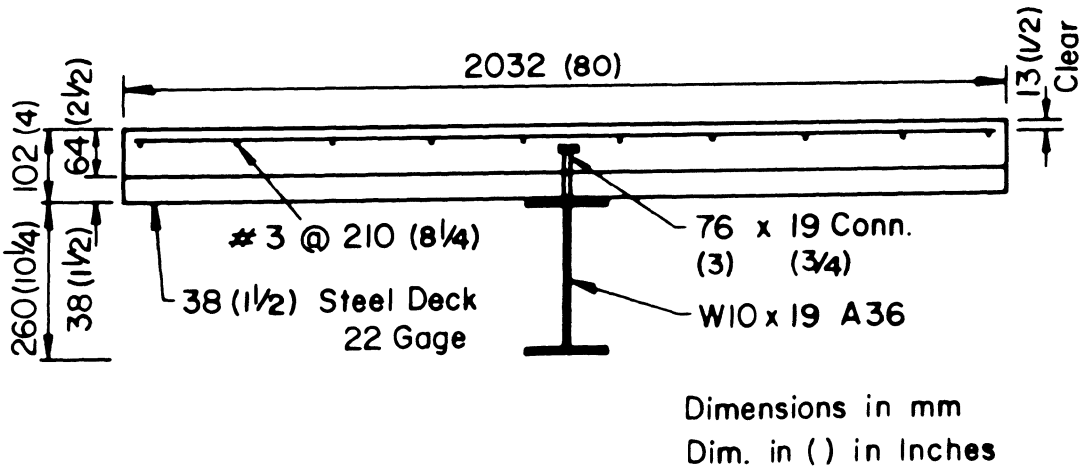

Fig. 4 Section of Beam CA-2

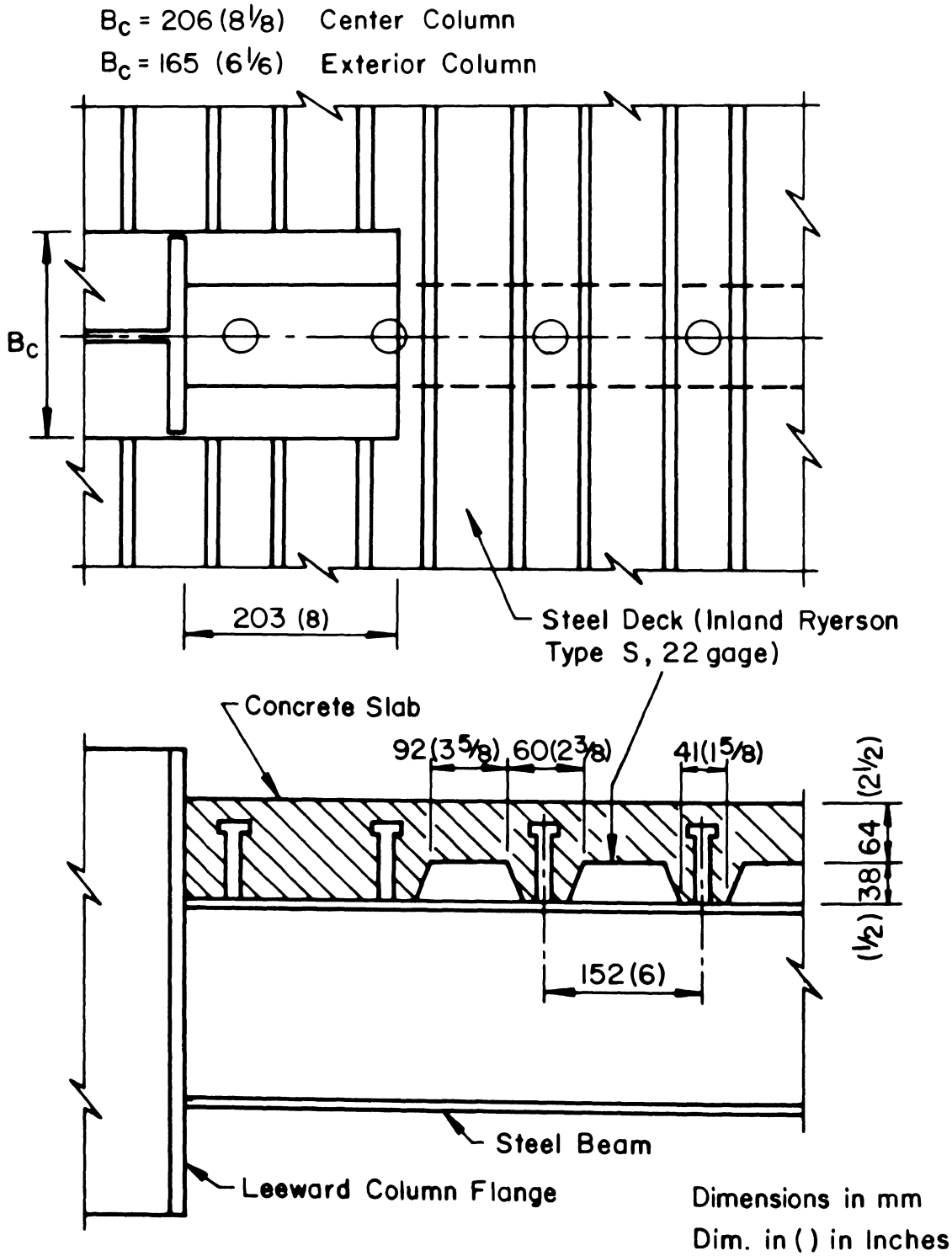

Fig. 5 Plan and Elevation View of Leeward Beam-to-Column Connection of CA-2

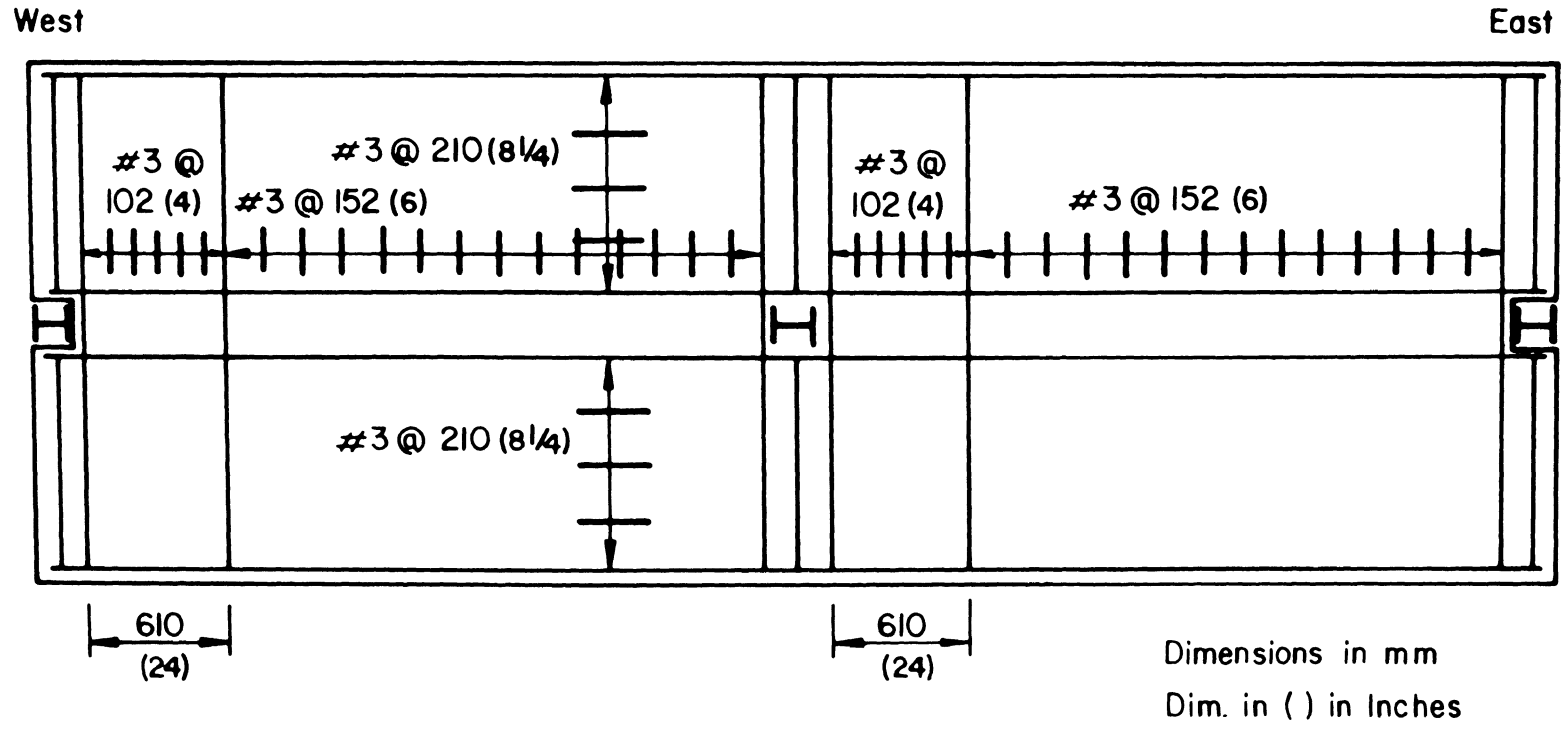

Fig. 6 Top Layer of Reinforcement of CA-1 and CA-2

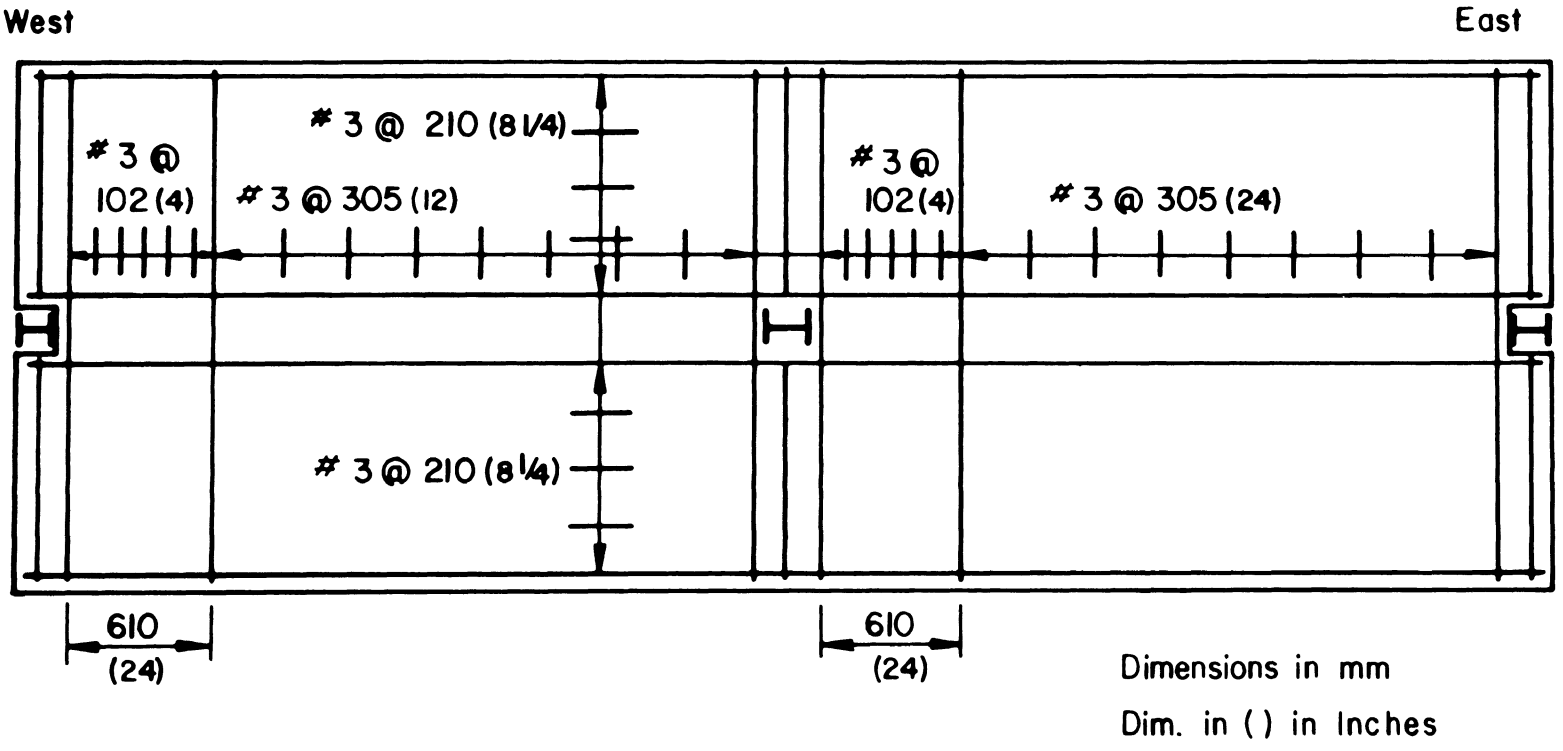

Fig. 7 Bottom Layer of Reinforcement of CA-1

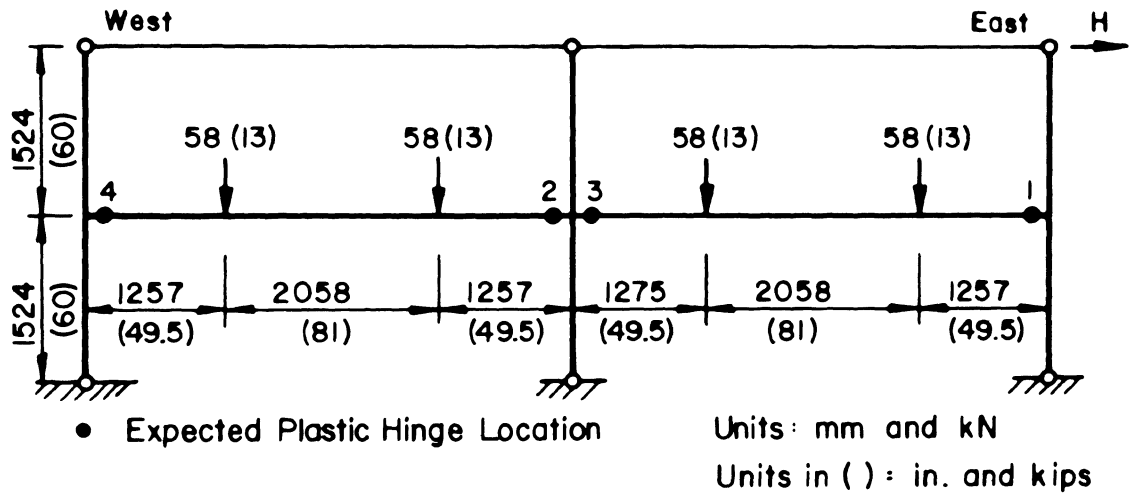

Fig. 8 Statical System of CA-1 and CA-2

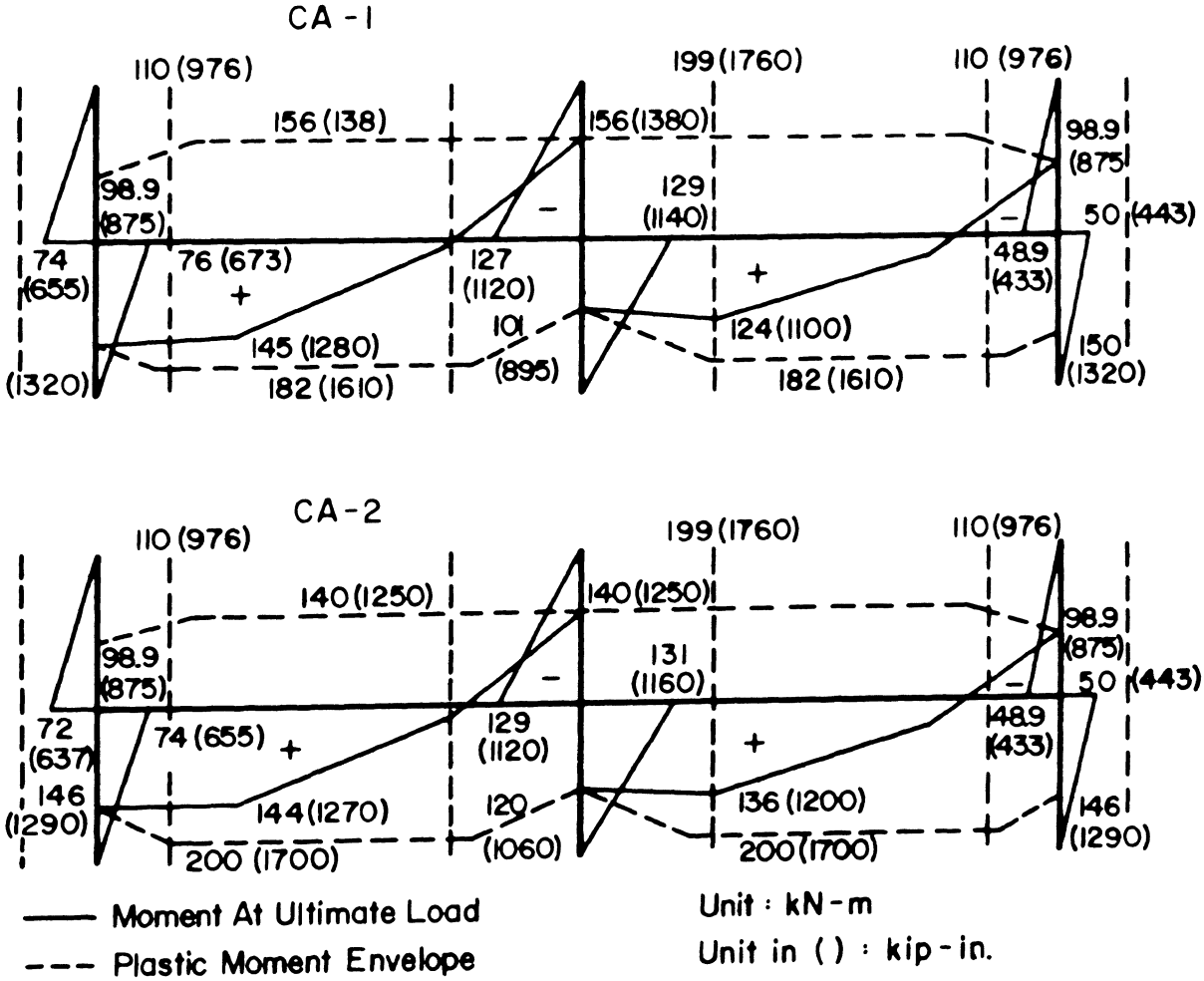

Fig. 9 Moment Diagrams at the Predicted Ultimate Load and Plastic Moment Envelopes of CA-1 and CA-2

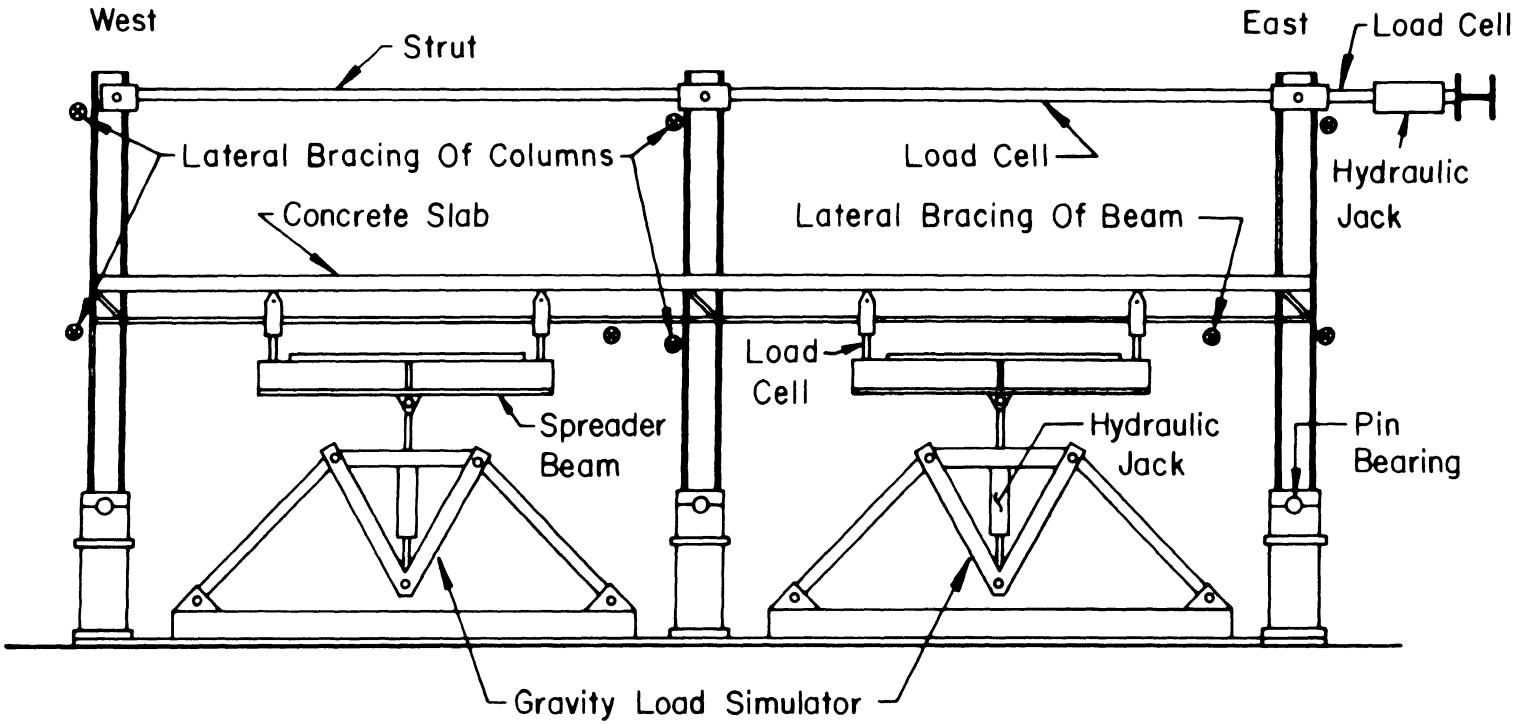

Fig. 10 Schematic Elevation View of Test Setup

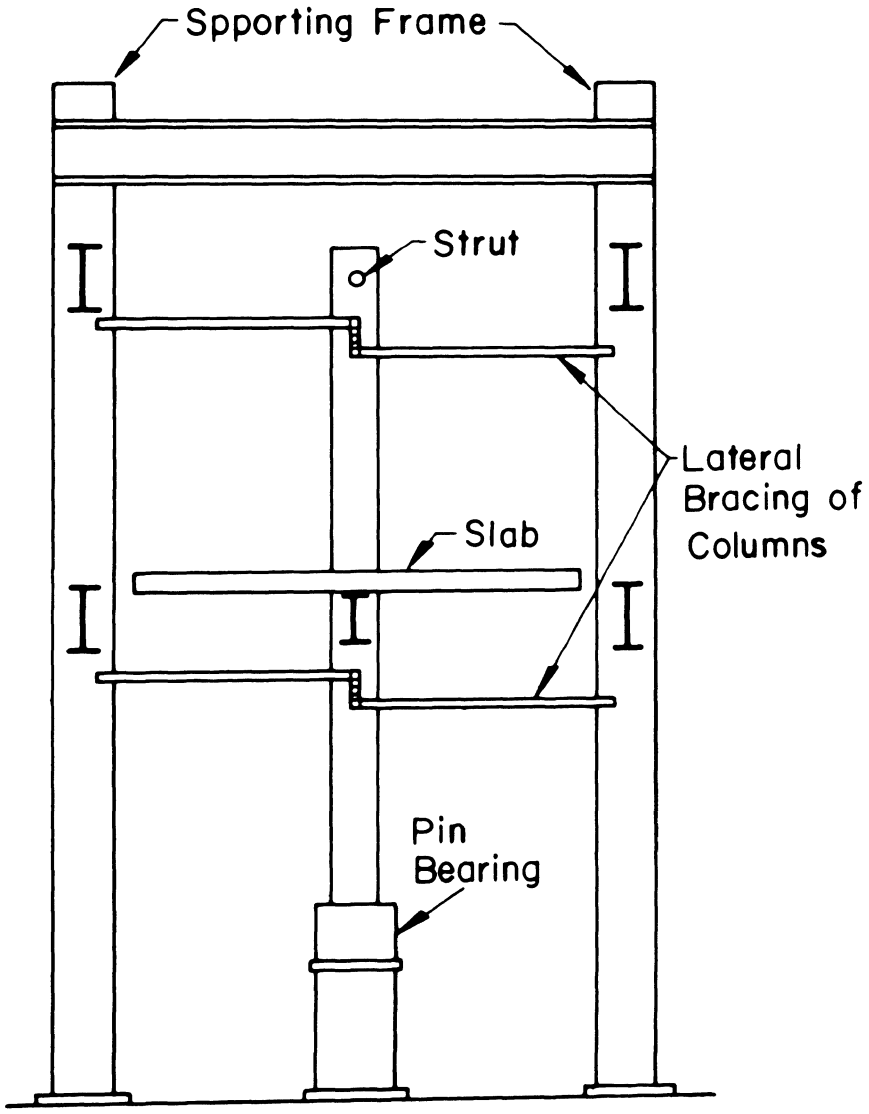

Fig. 11 Schematic Section View of Test Setup

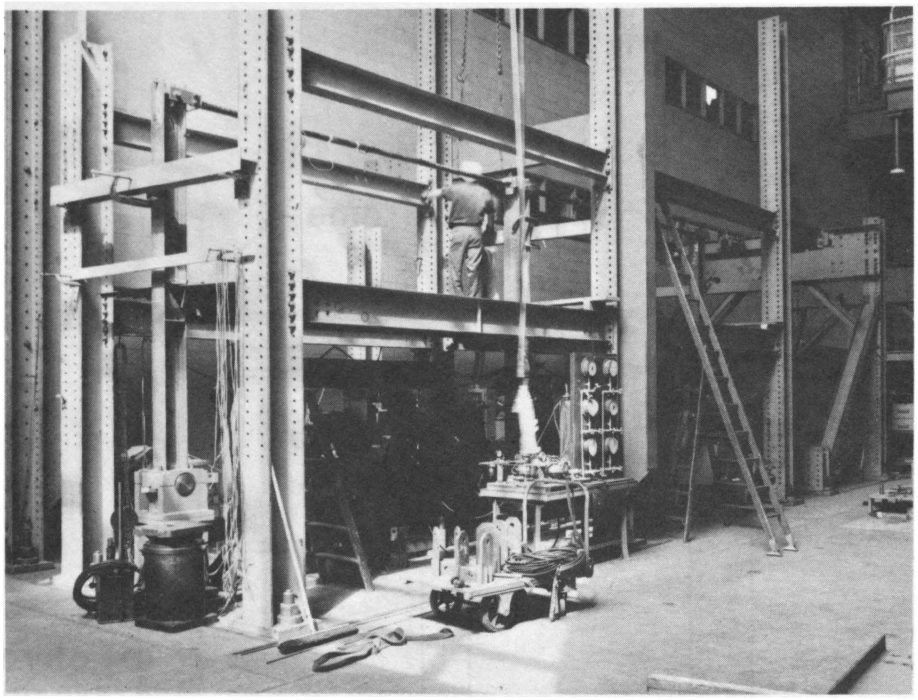

Fig. 12 Steel Frame of CA-2 Ready for Welding

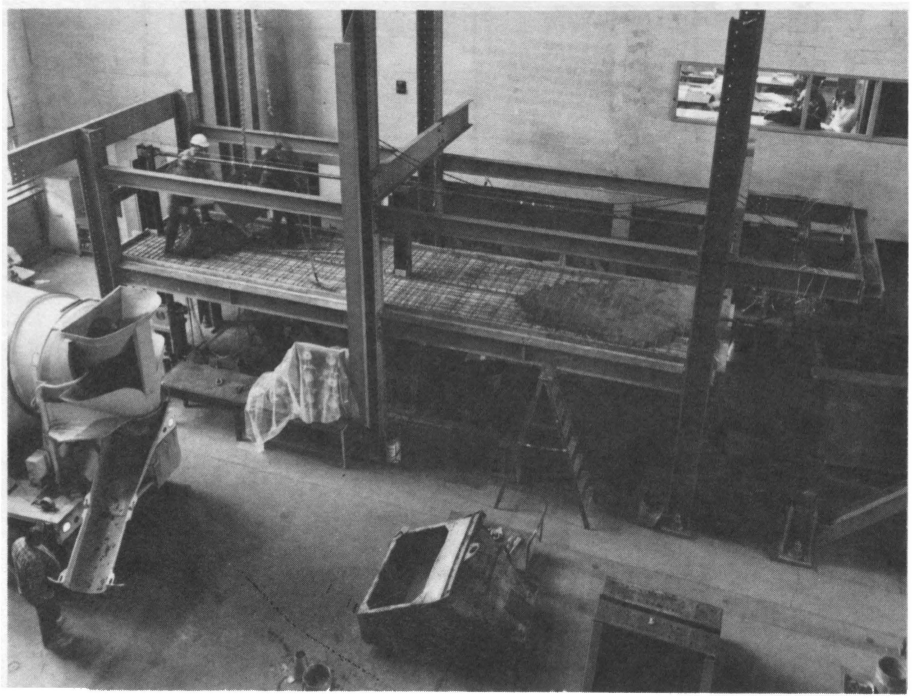

Fig. 13 Pouring of the Slab of CA-1

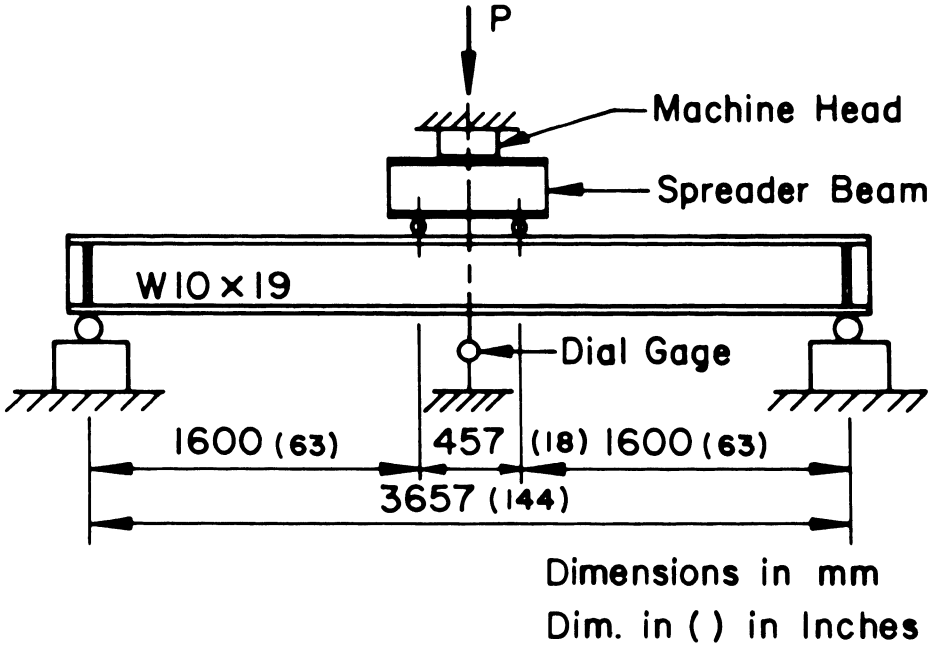

Fig. 14 Test Setup of Beam Test

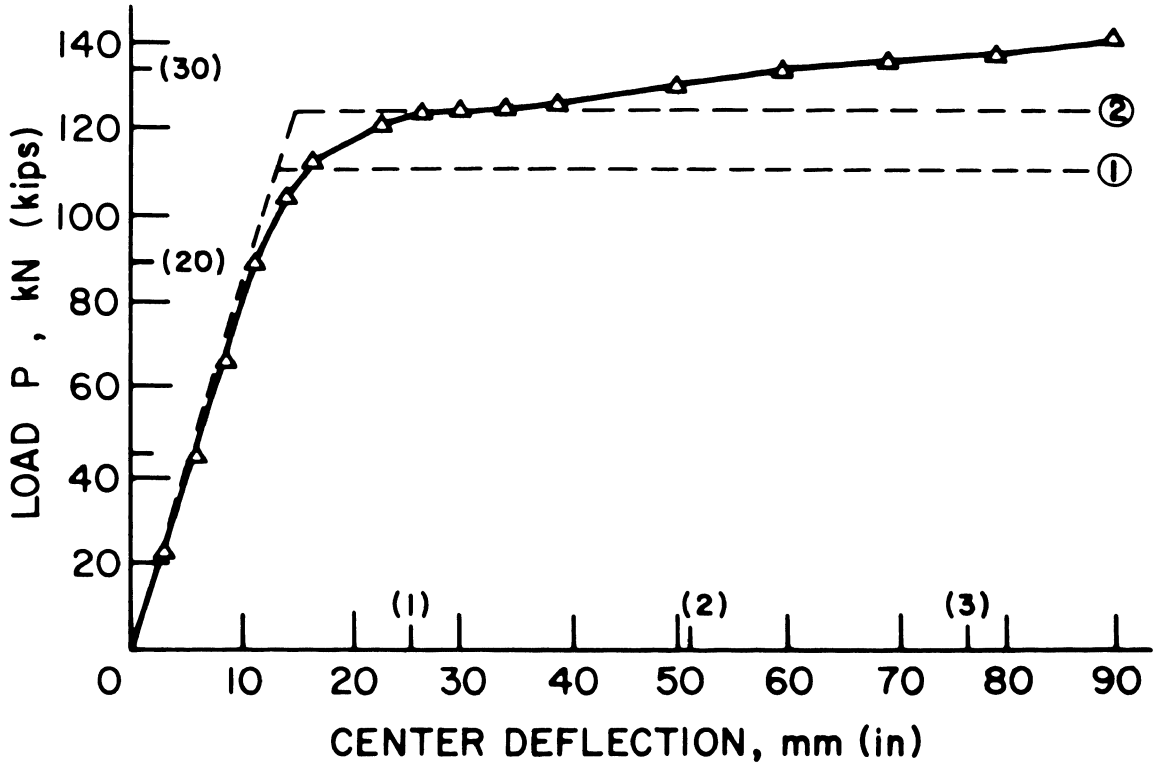

Fig. 15 Load-Deflection Curves of Beam Test

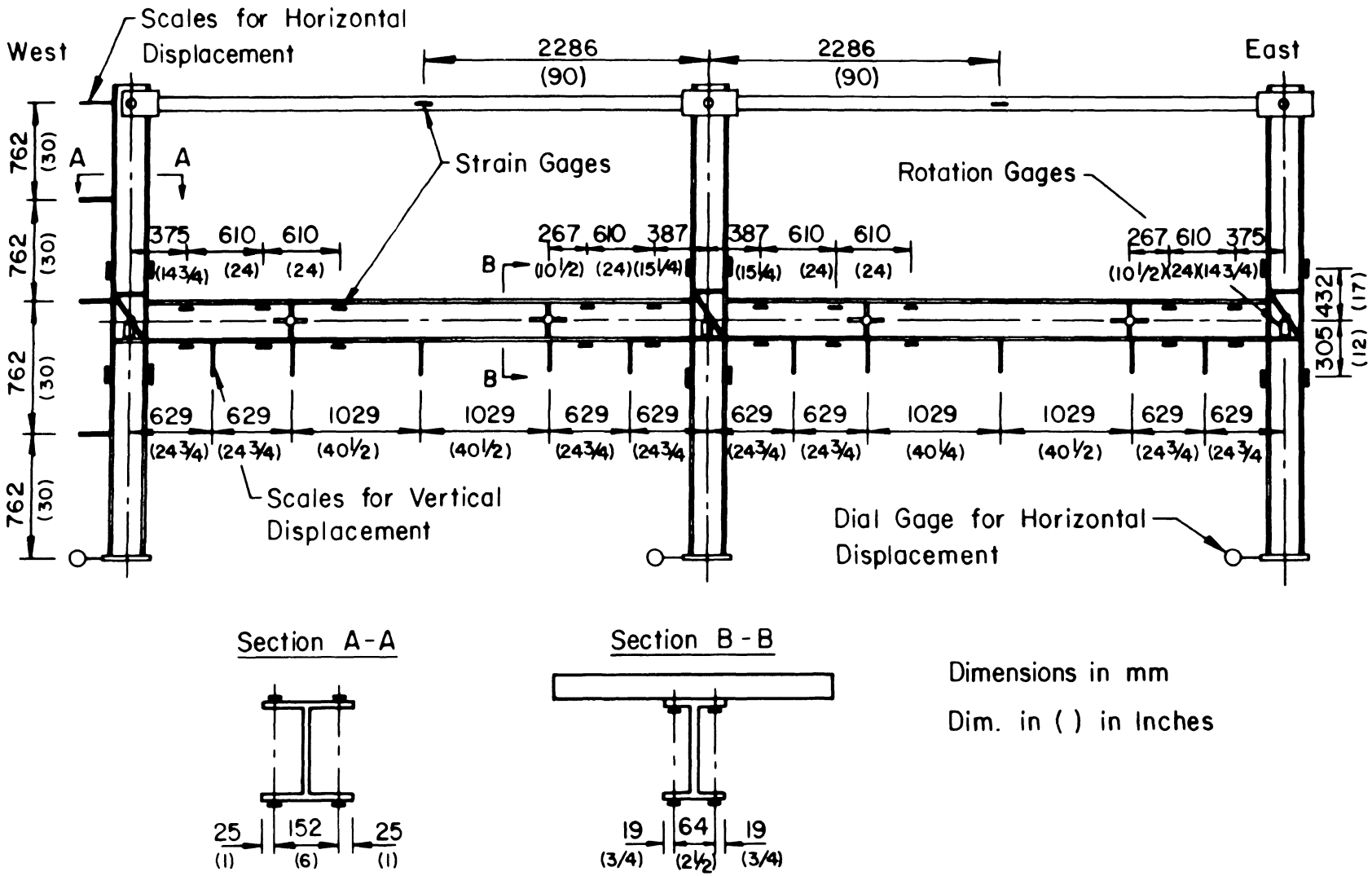

Fig. 16 Instrumentation of Steel Frame of CA-1 and CA-2

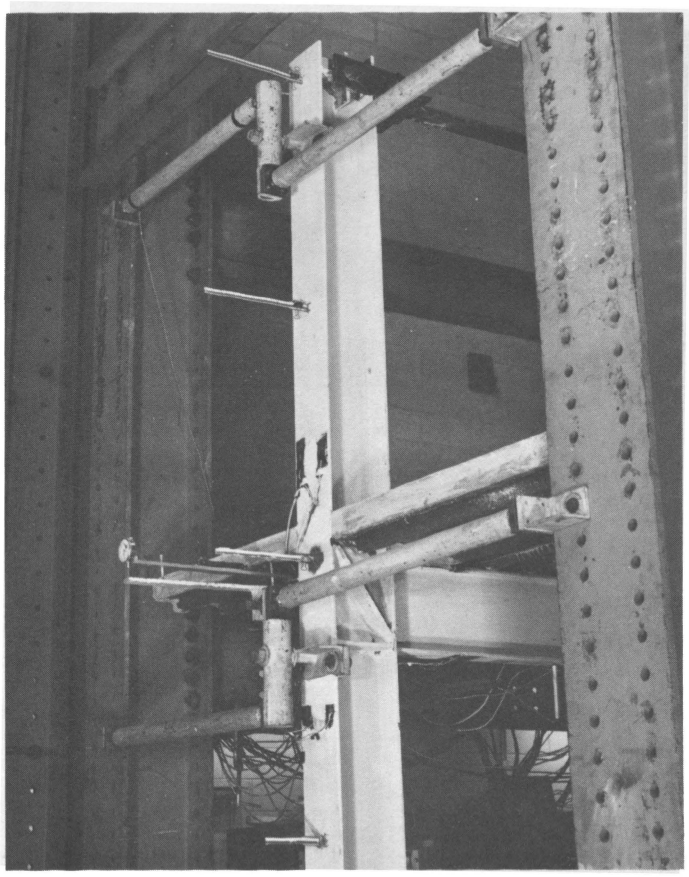

Fig. 17 View of West End of CA-2 Showing Scales for Deflection Readings and Column Bracing (Ref. 9)

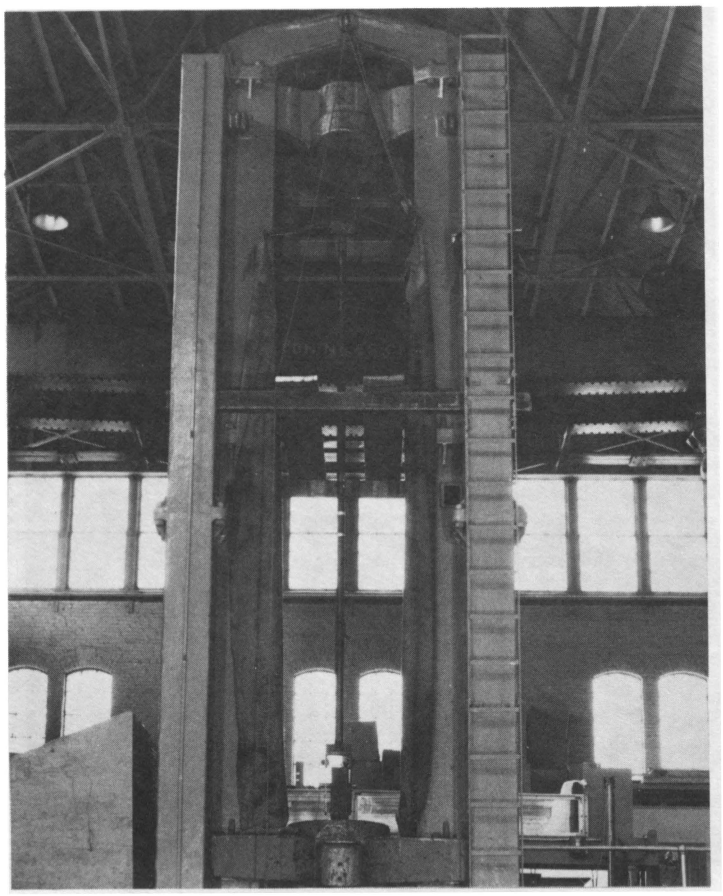

Fig. 18 Calibration of Top Strut in Testing Machine

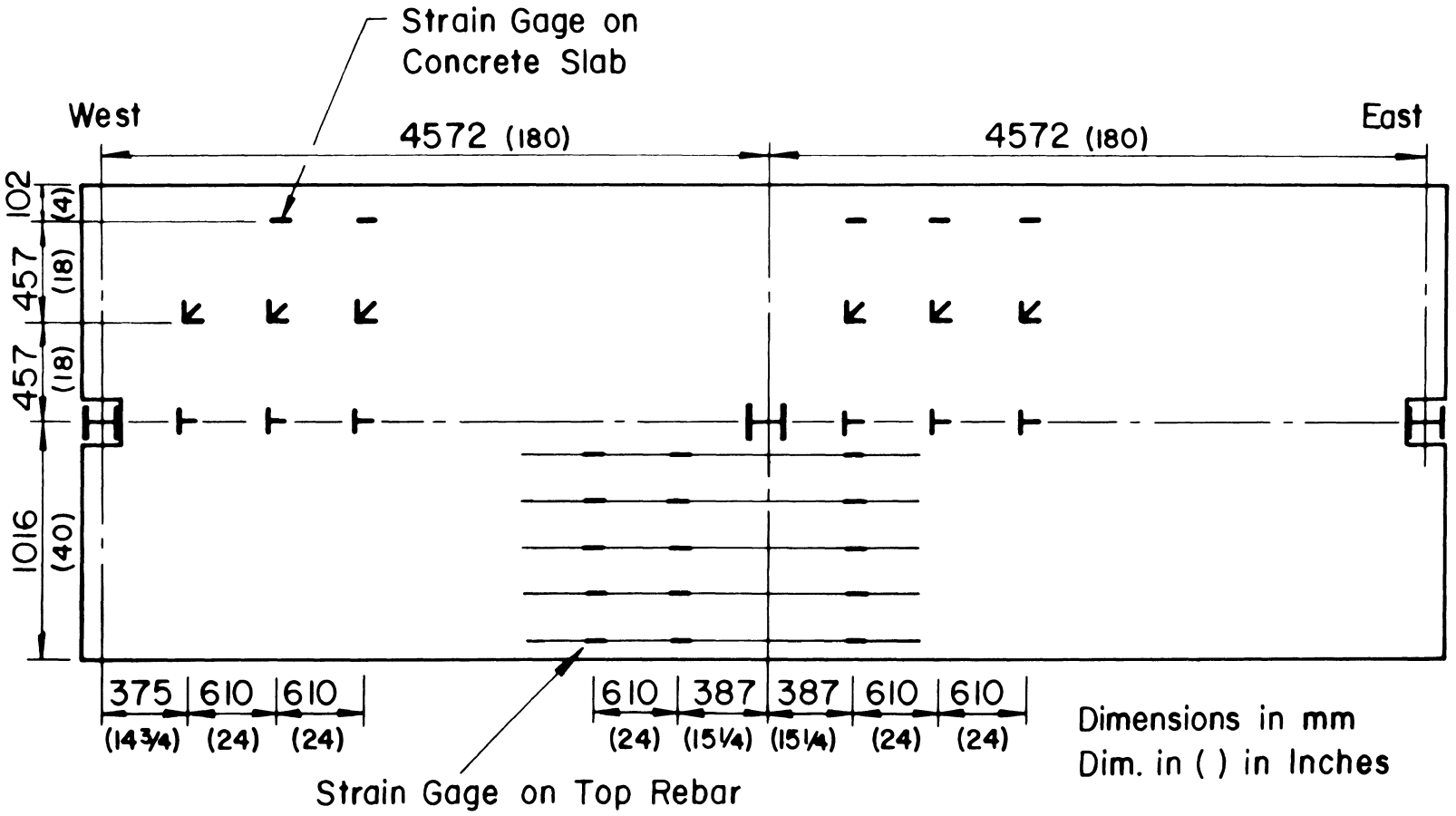

Fig. 19 Slab Instrumentation of CA-1 and CA-2

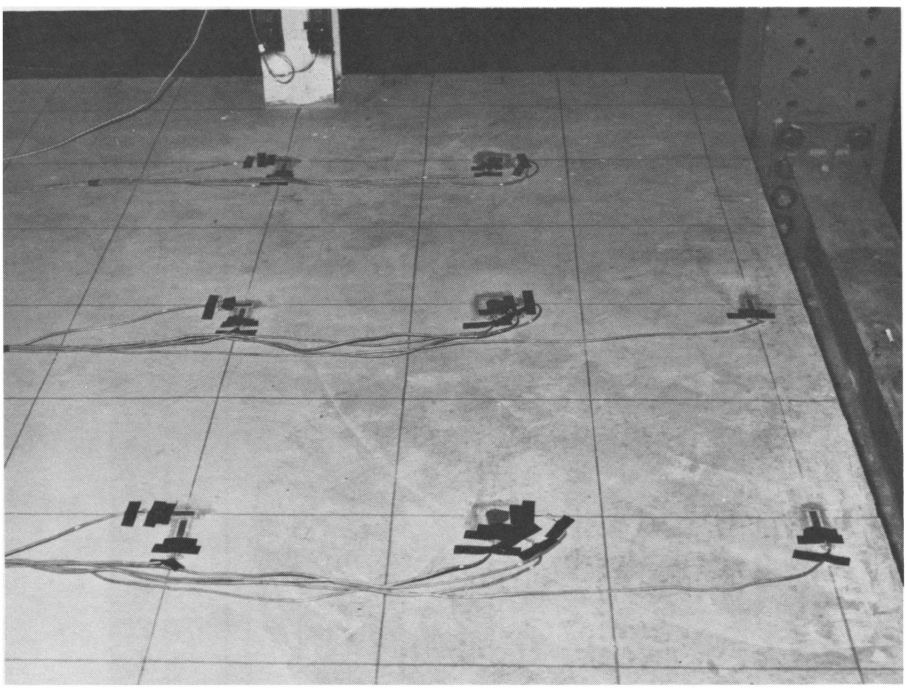

Fig. 20 Instrumentation of the Slab

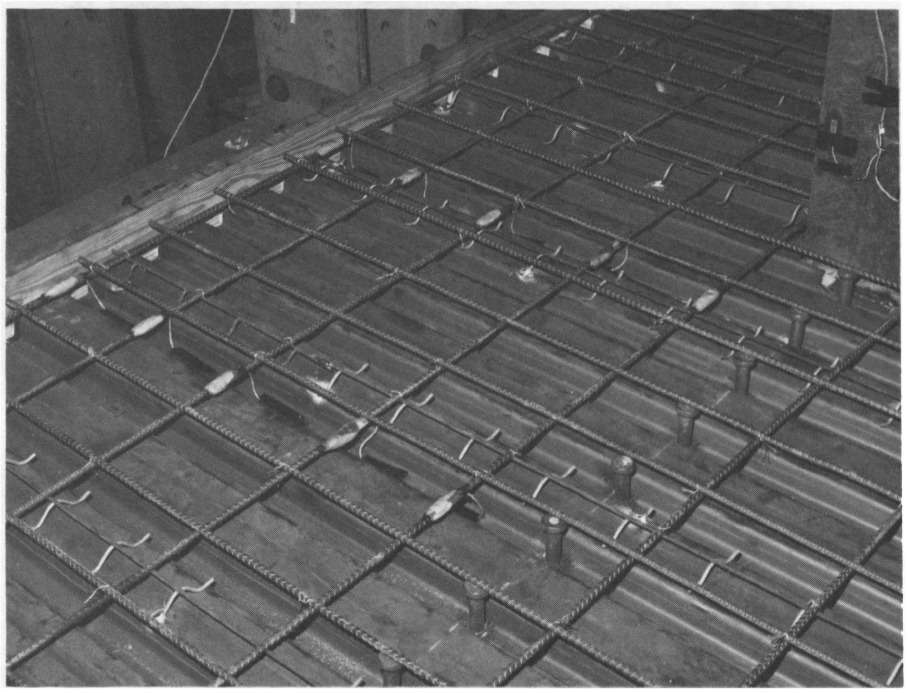

Fig. 21 Instrumentation of the Reinforcement of CA-2

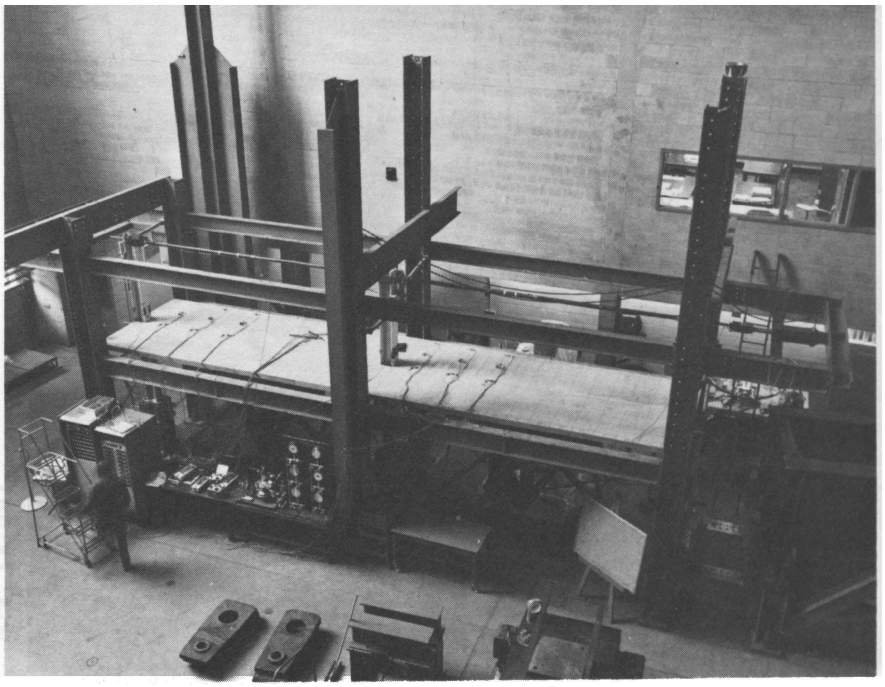

Fig. 22 Overall View of the Test Setup

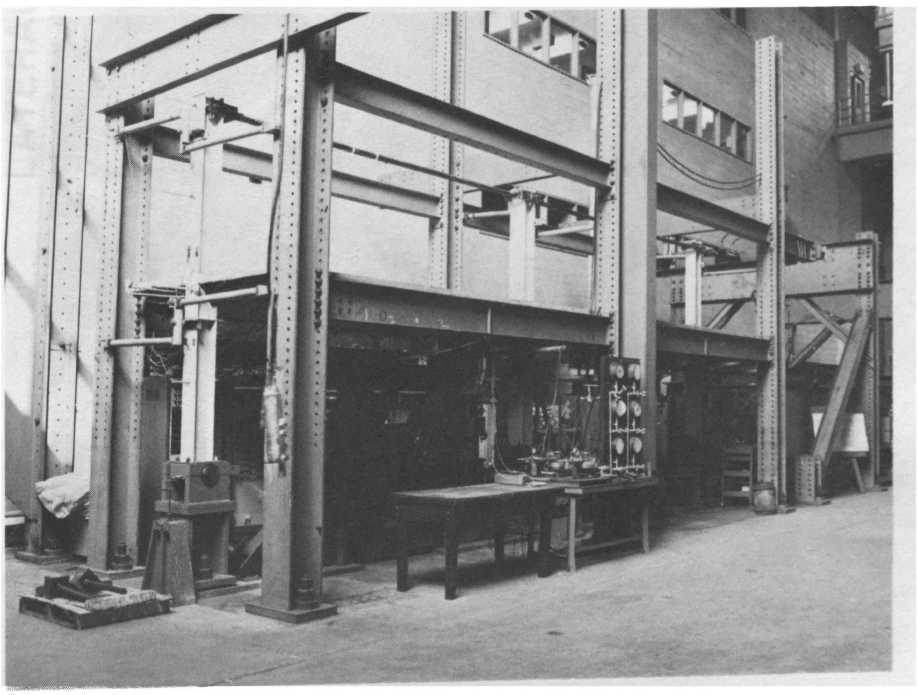

Fig. 23 Overall View of the Test Setup

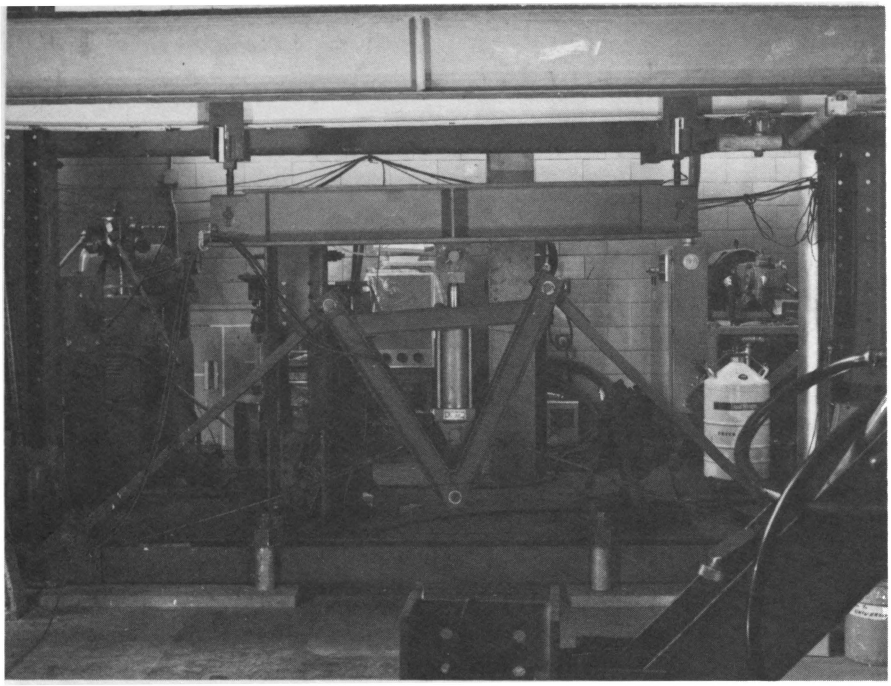

Fig. 24 View of Gravity Load Simulator During Test (Ref. 9)

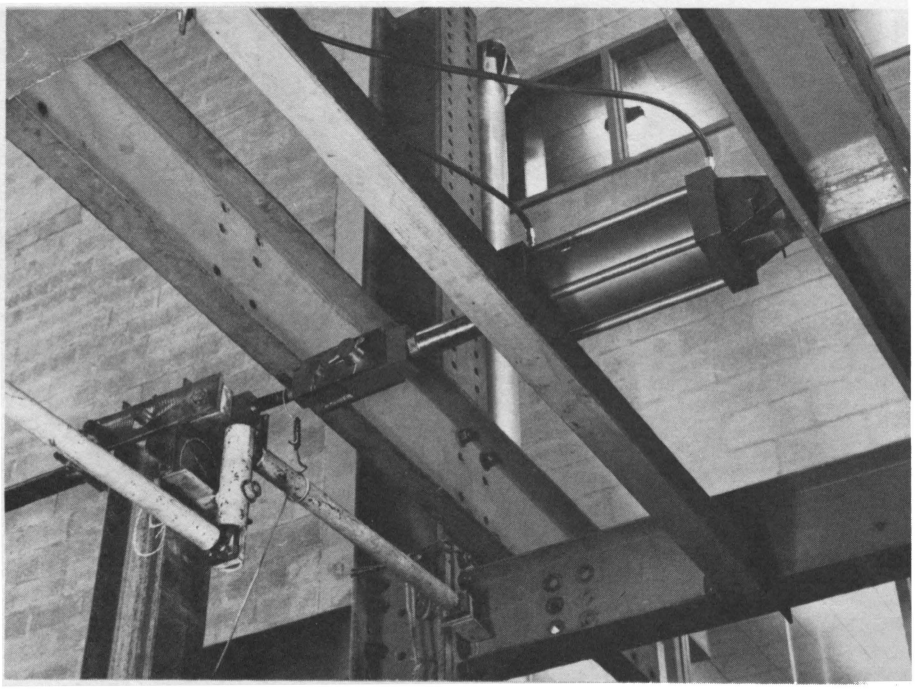

Fig. 25 Hydraulic Jack Used to Apply Horizontal Load

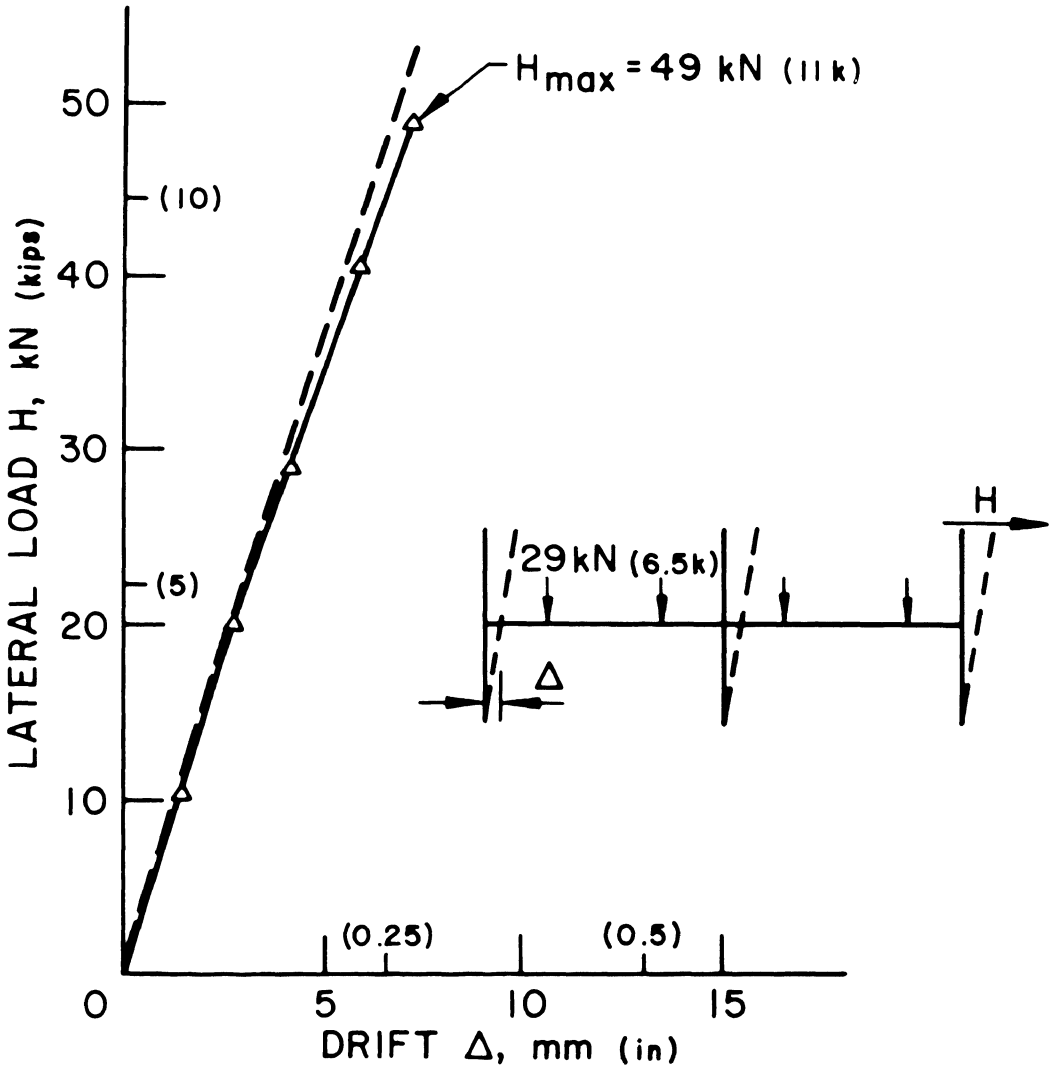

Fig. 26 Lateral Load vs. Drift Behavior of Steel Assemblage CA-2 (Behavior of CA-1 Assumed to be Identical)

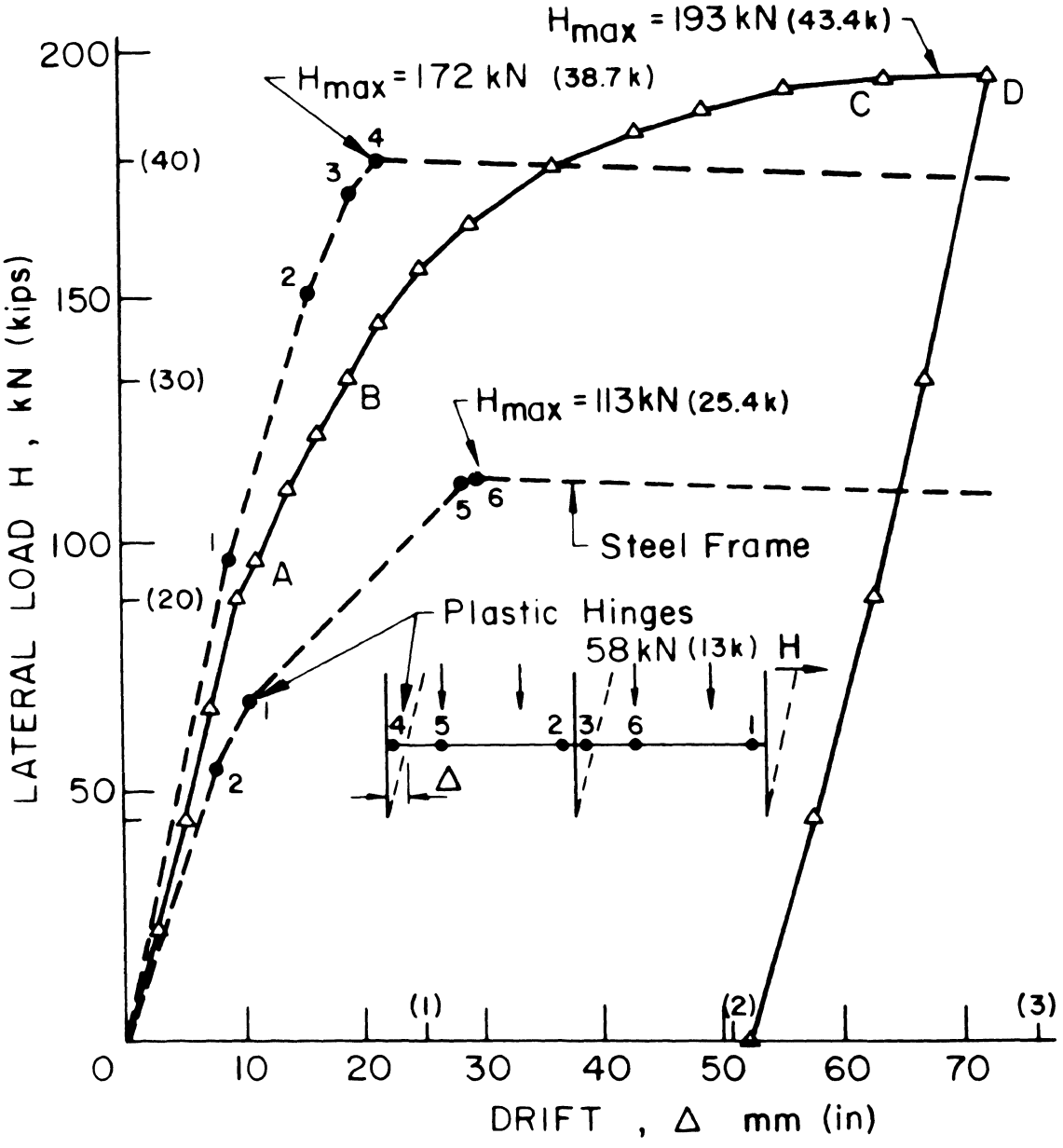

Fig. 27 Load-Drift Behavior of CA-1

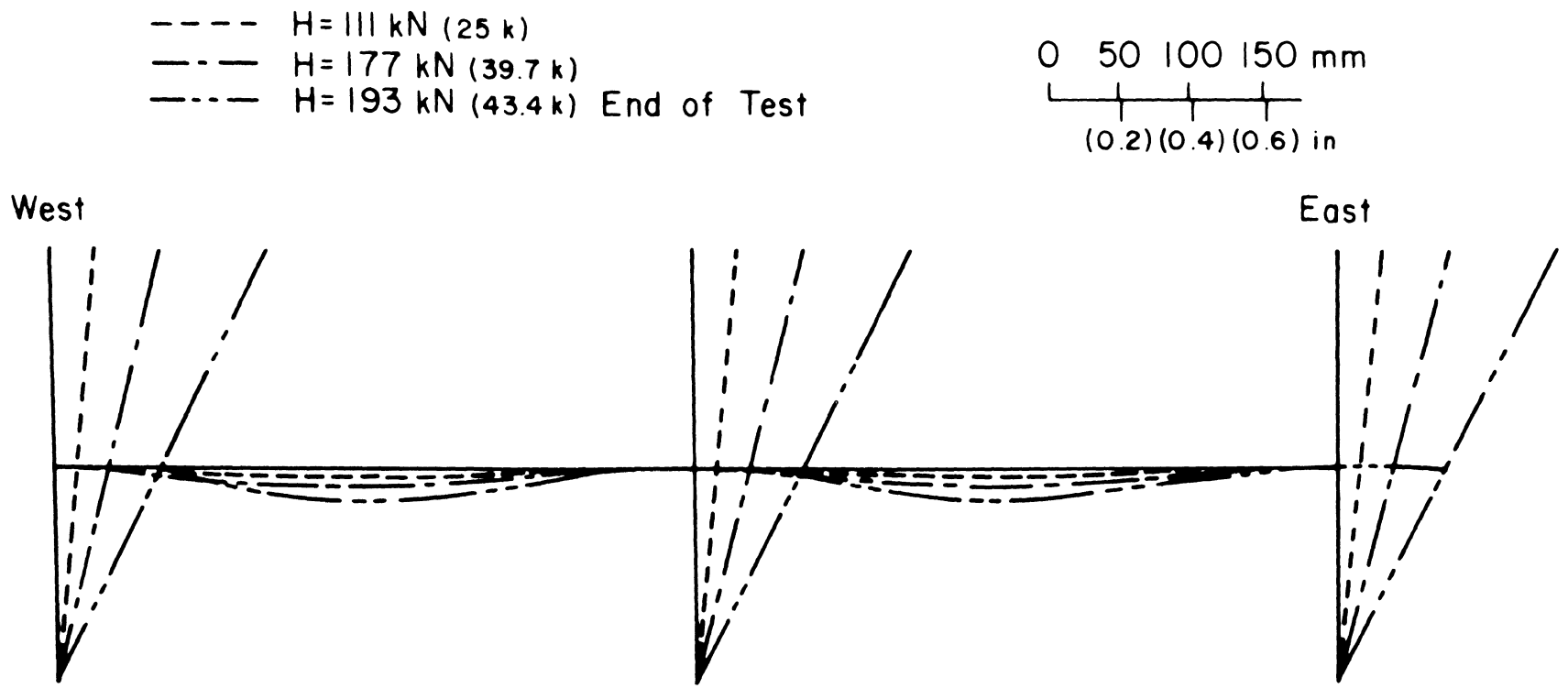

Fig. 28 Deflections of Composite Assemblage CA-1

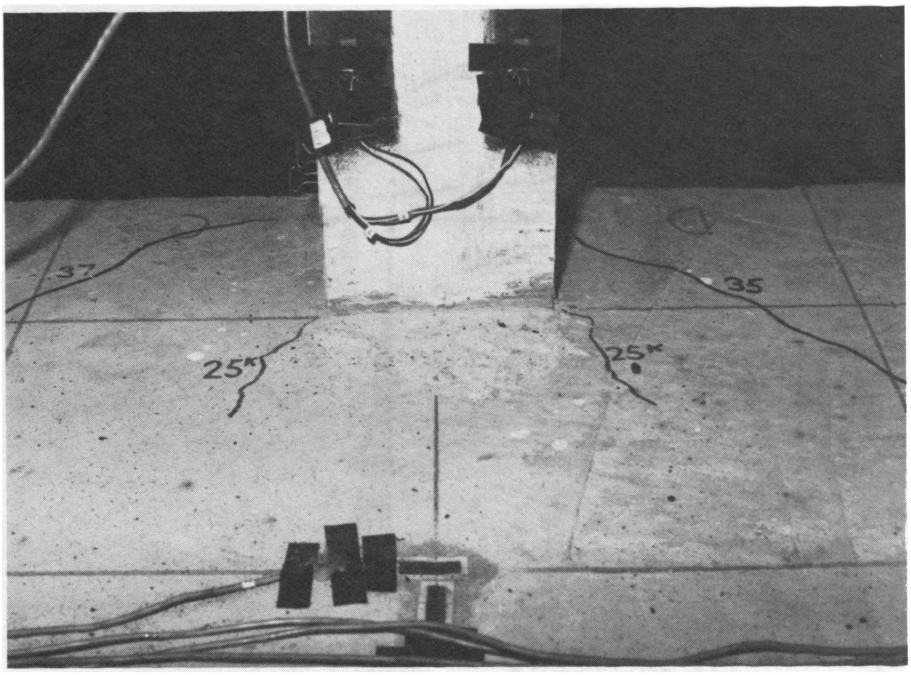

Fig. 29 Failure Surface on Leeward Side of West Column of CA-1

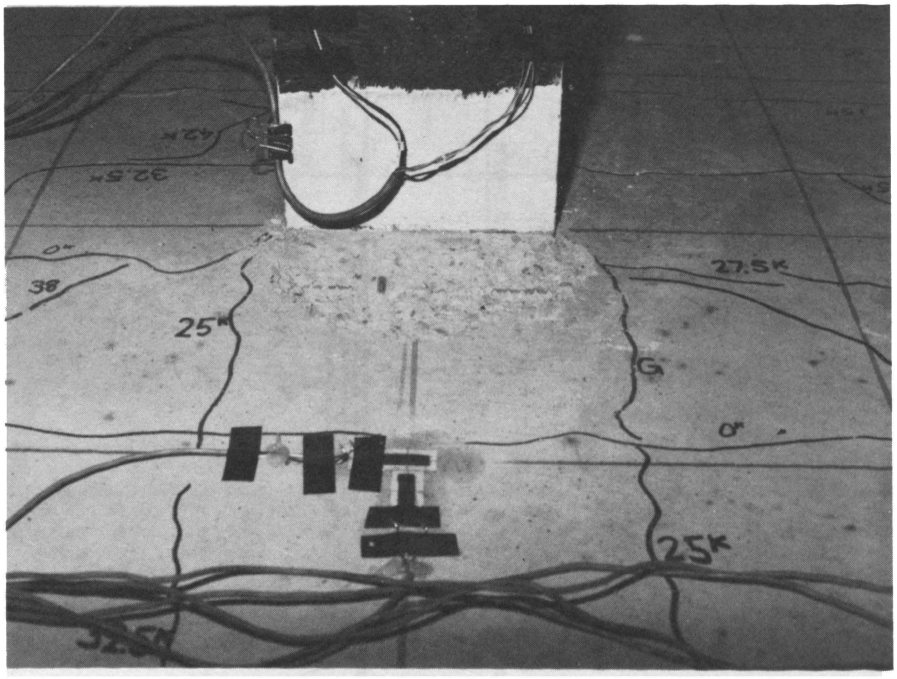

Fig. 30 Failure Surface on Leeward Side of Center Column of CA-1

Fig. 31 Slab Cracking on Windward Side of Center Column of CA-1

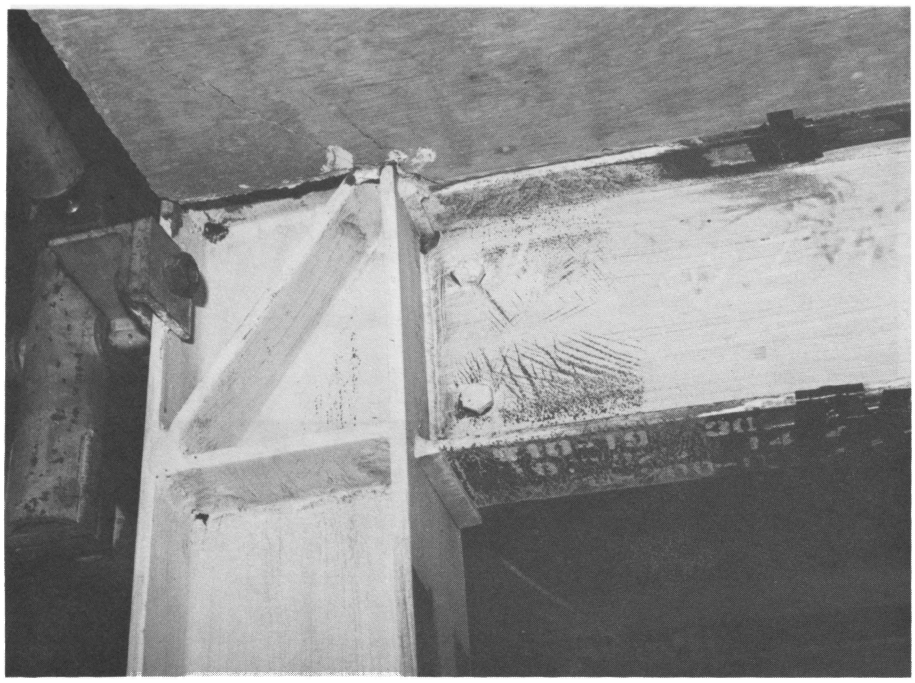

Fig. 32 Extent of Yielding at Plastic Hinge Location 1 of CA-1

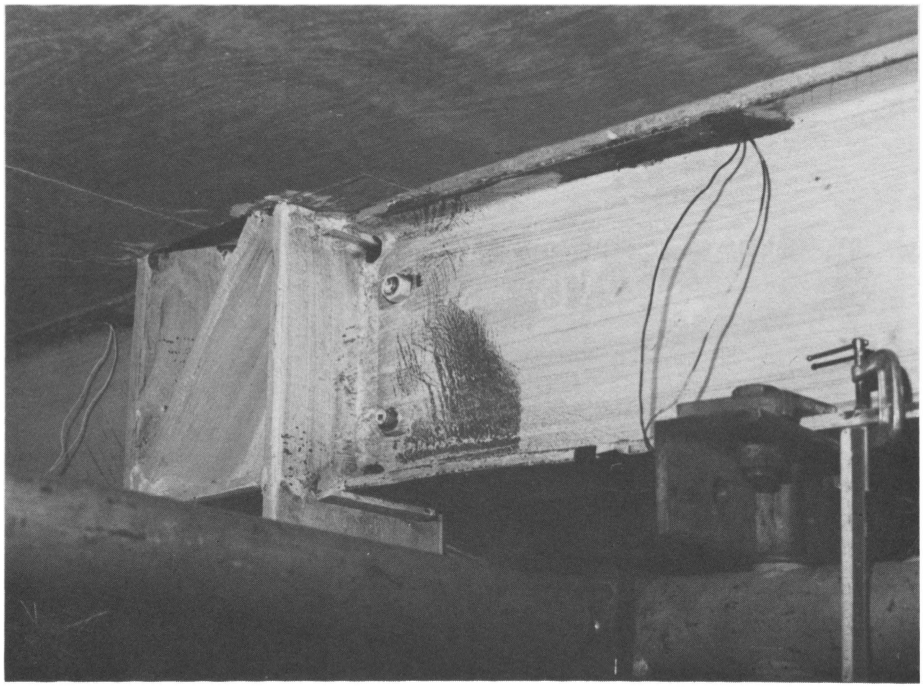

Fig. 33 Extent of Yielding at Plastic Hinge Location 2 of CA-1

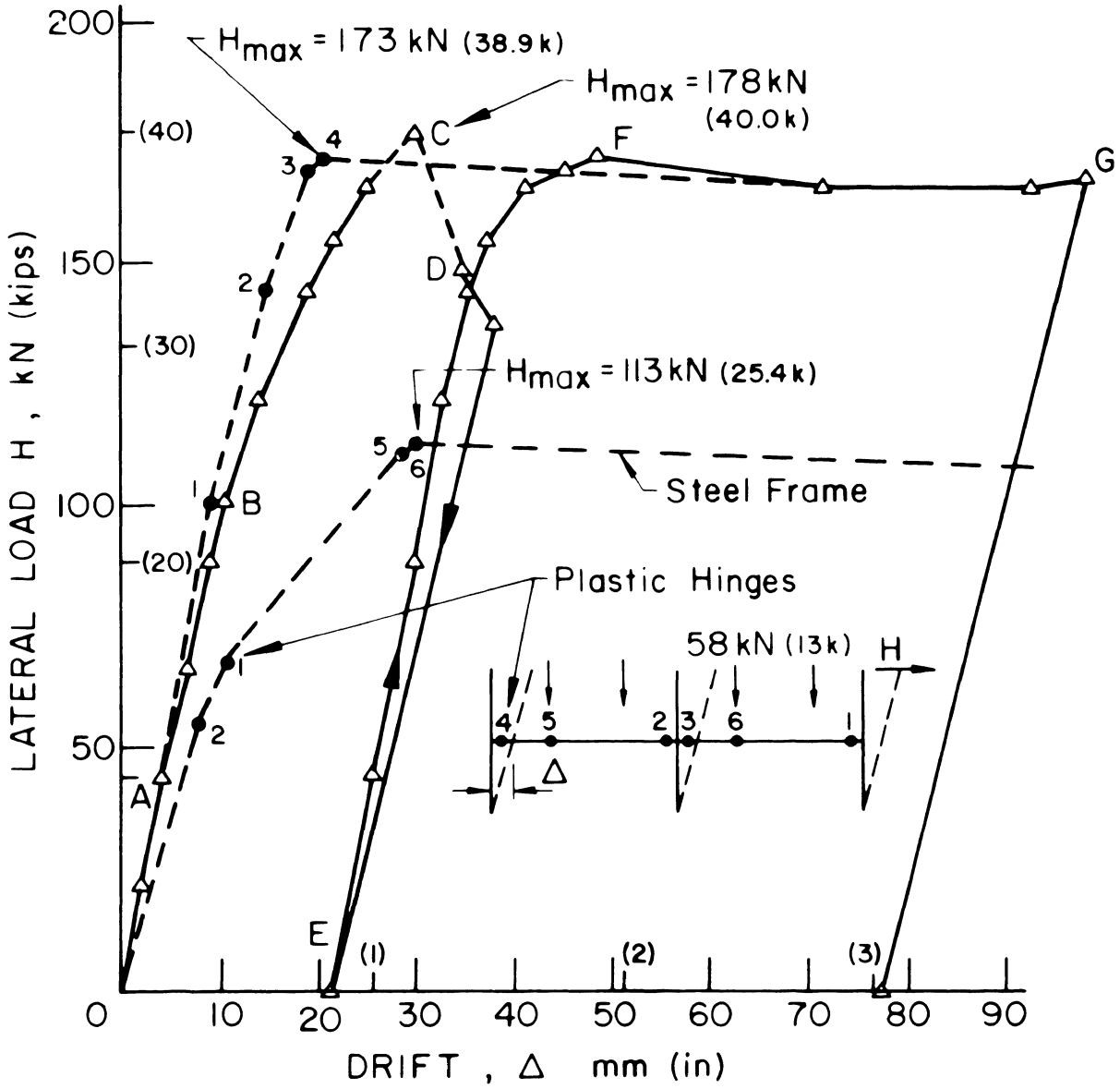

Fig. 34 Load-Drift Behavior of CA-2

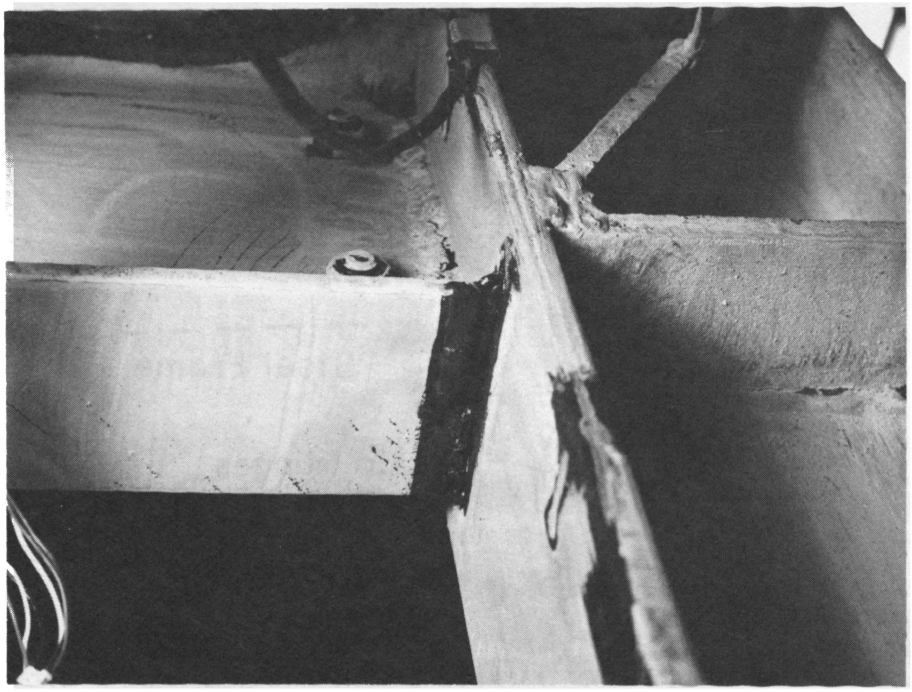

Fig. 35 Weld Fracture at West Column of CA-2

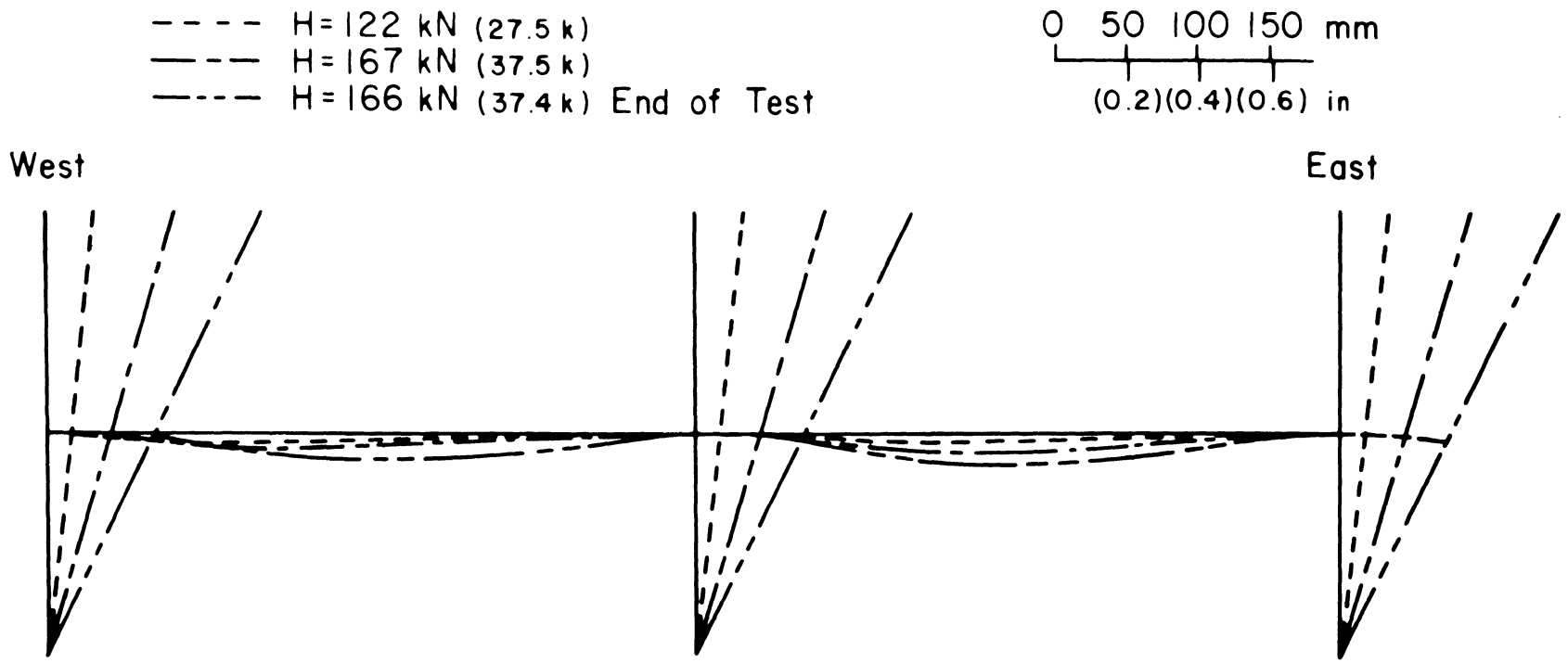

Fig. 36 Deflections of Composite Assemblage CA-2

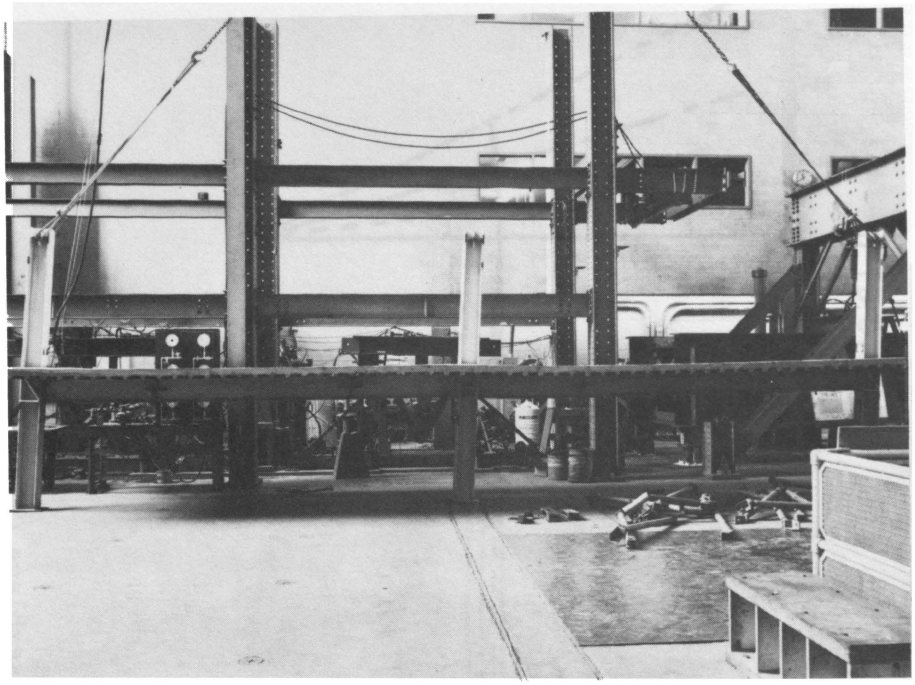

Fig. 37 View of CA-2 After Testing

Fig. 38 Failure Surface on Leeward Side of West Column of CA-2

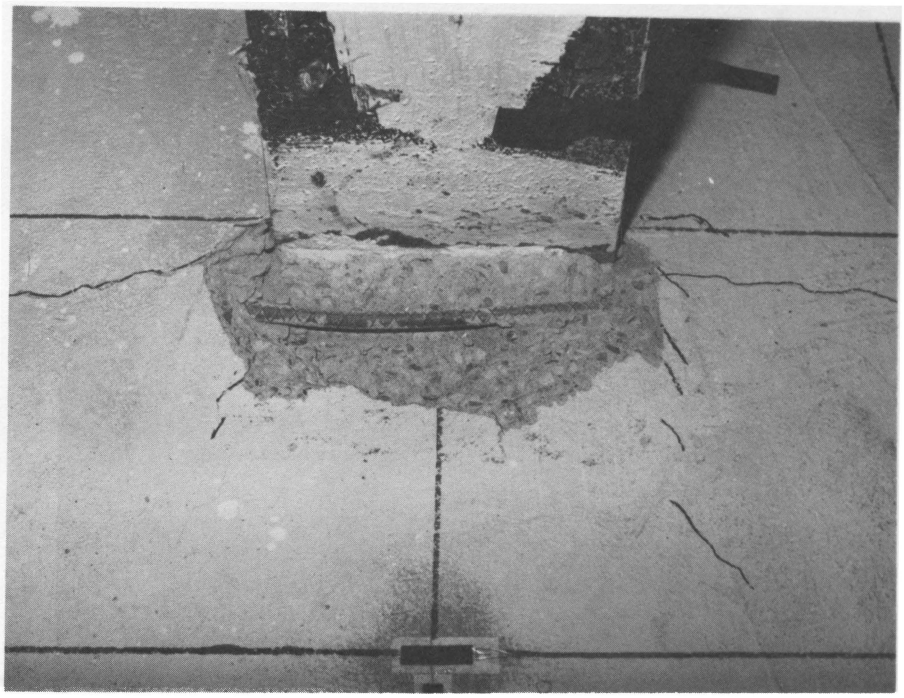

Fig. 39 Failure Surface on Leeward Side of Center Column of CA-2

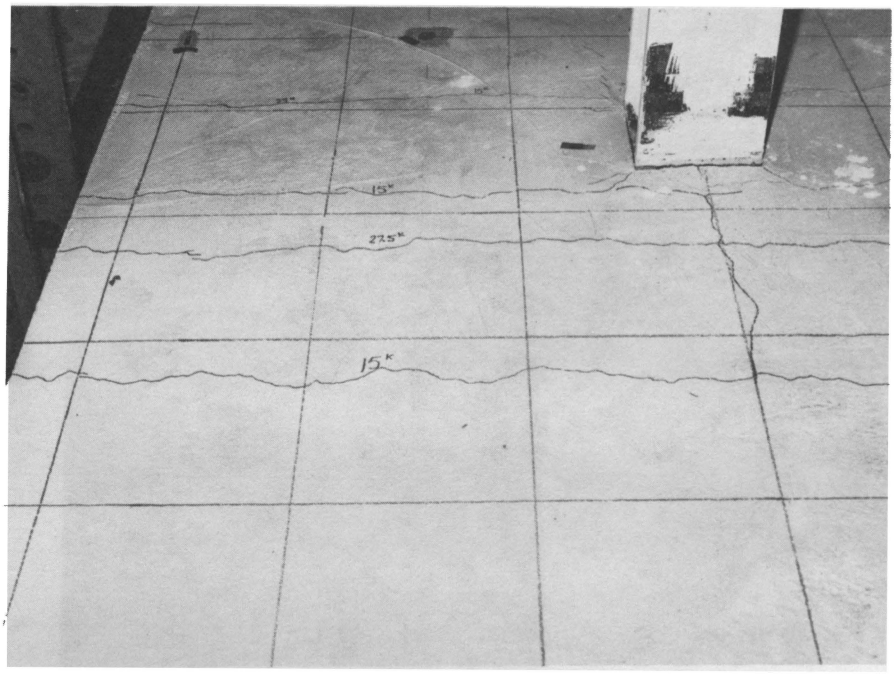

Fig. 40 Slab Cracking on Windward Side of Center Column of CA-2

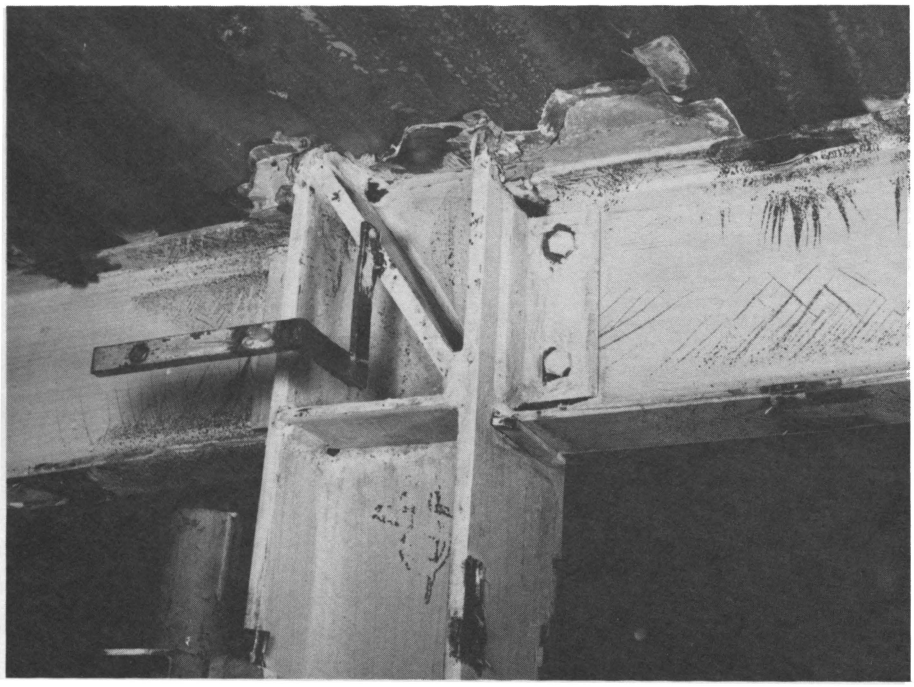

Fig. 41 Extent of Yielding at the Center Column of CA-2

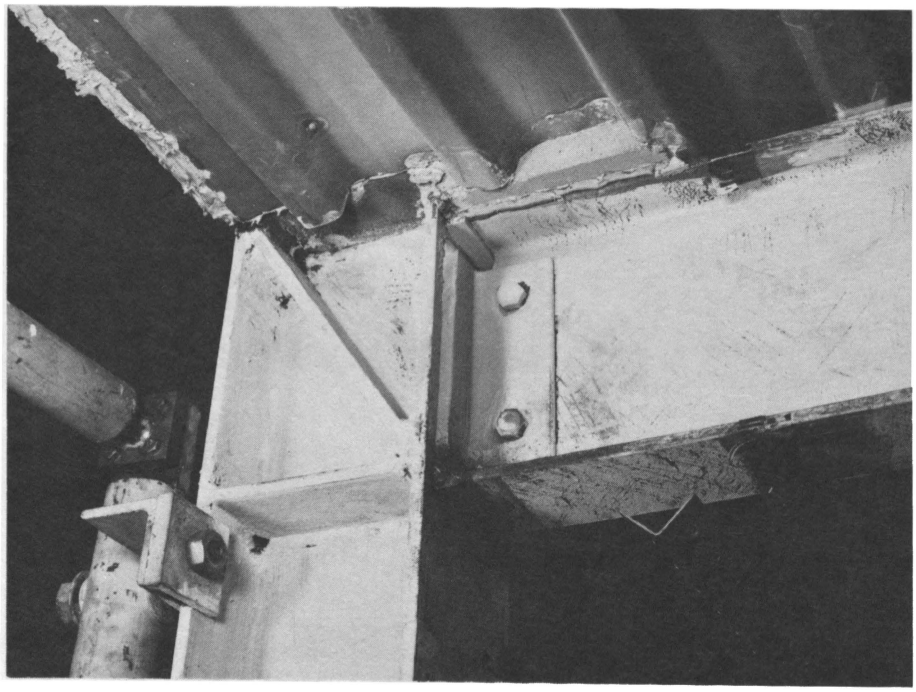

Fig. 42 Extent of Yielding at the West Column of CA-2

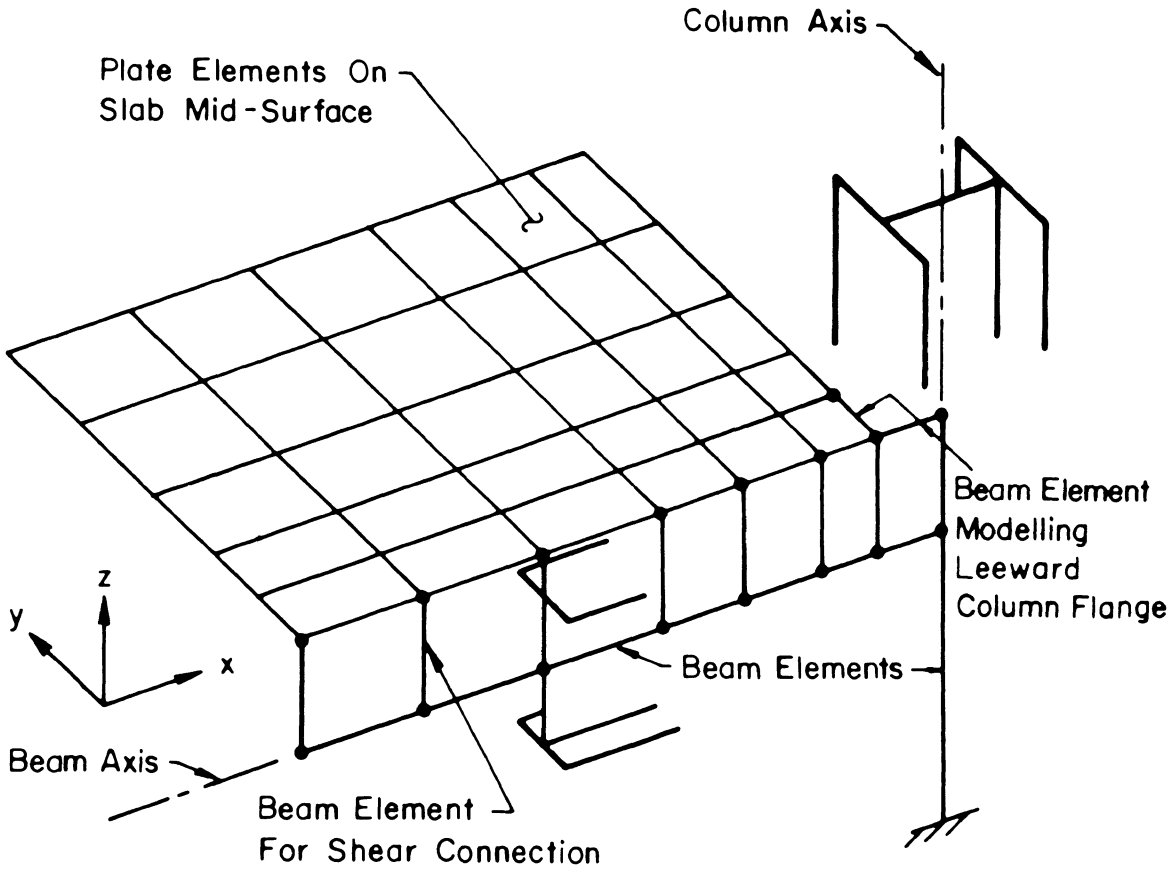

Fig. 43 Finite Element Model of Composite System

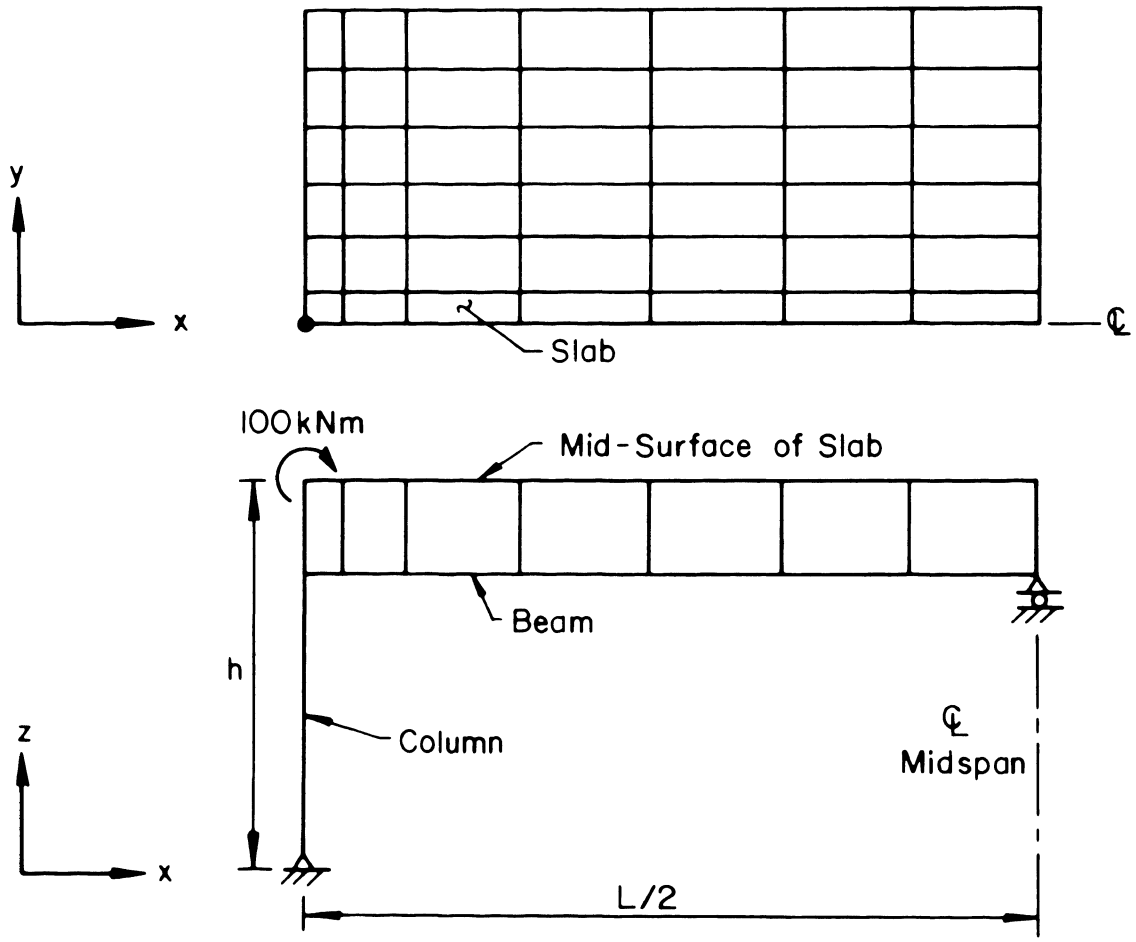

Fig. 44 Plan and Elevation View of Finite Element Discretization

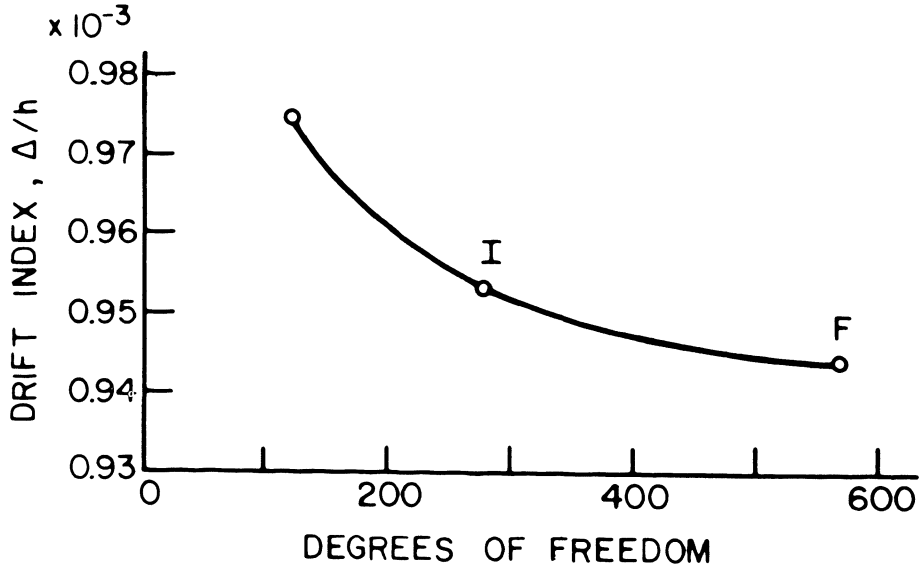

Fig. 45 Plot of Drift Index vs. Degrees of Freedom

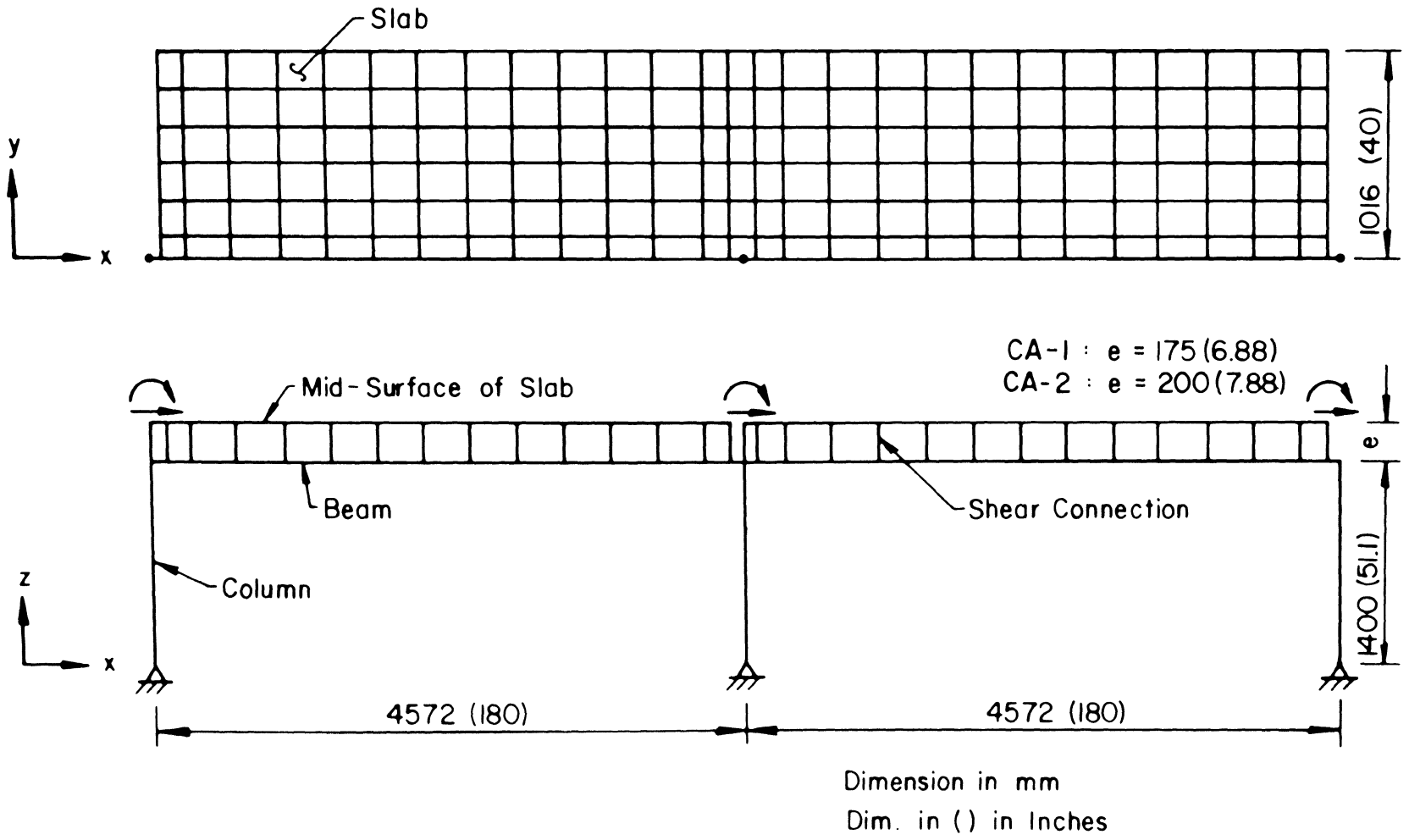

Fig. 46 Plan and Elevation View of Finite Element Discretization of CA-1 and CA-2

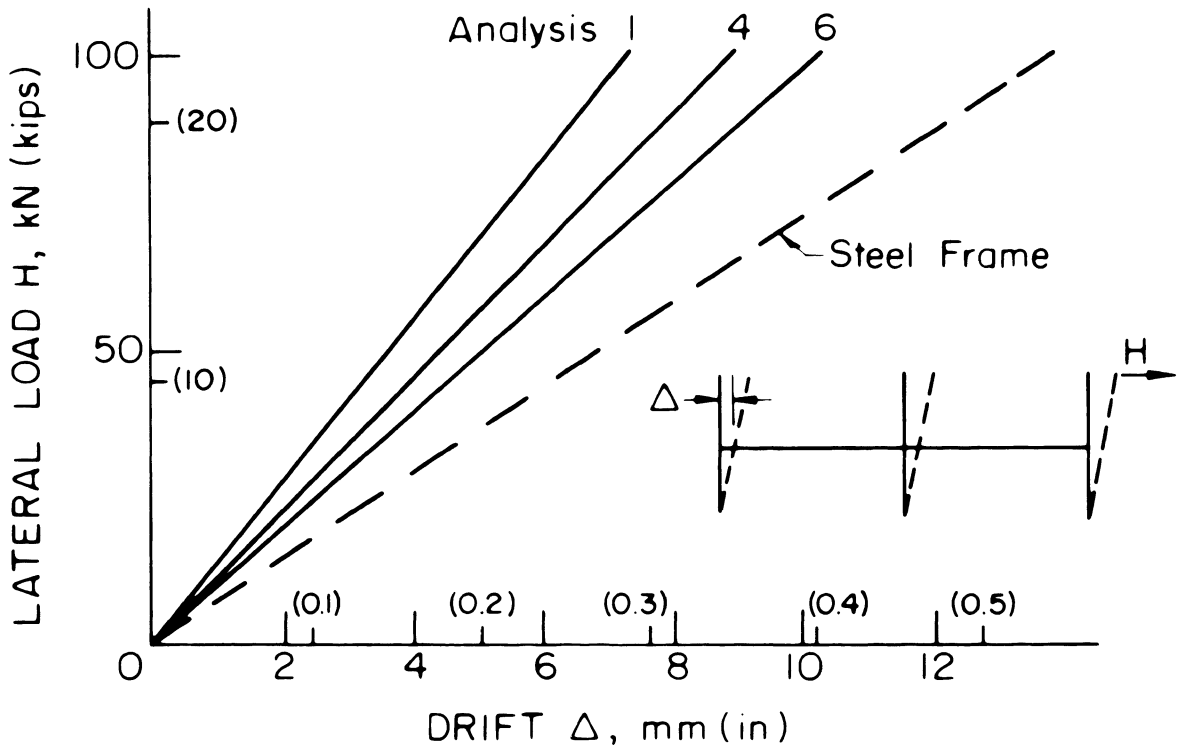

Fig. 47 Drift Predictions for CA-1

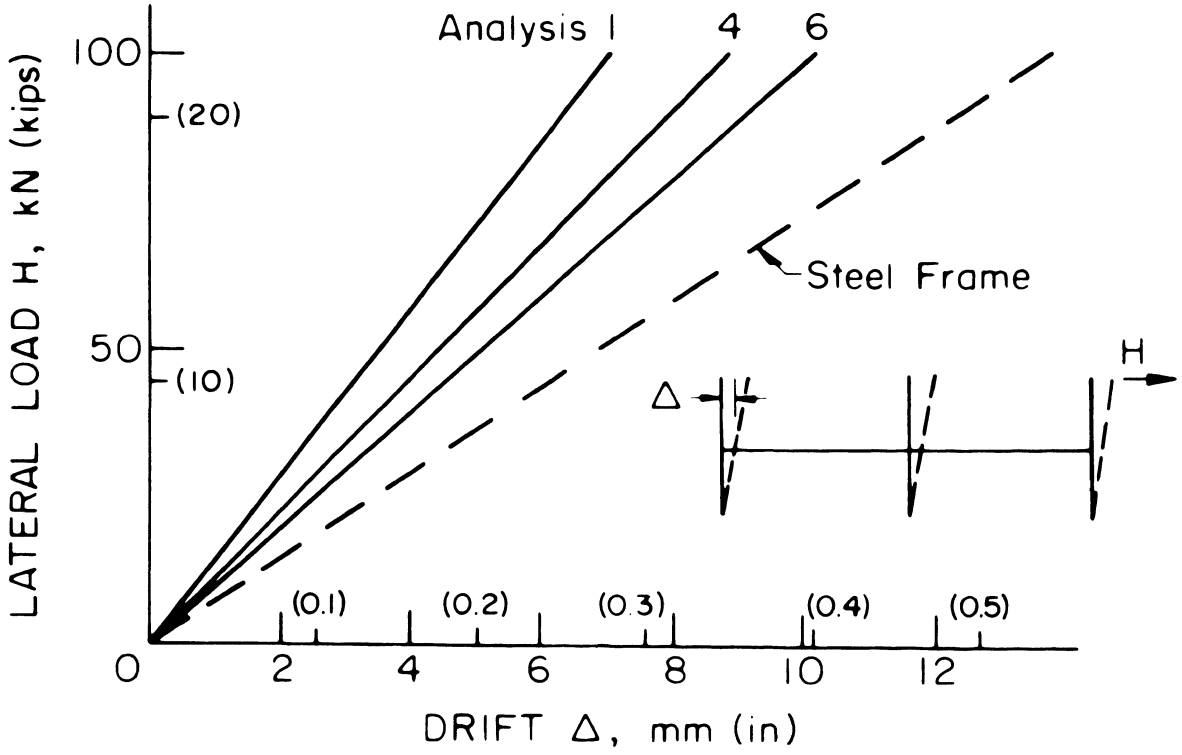

Fig. 48 Drift Predictions for CA-2

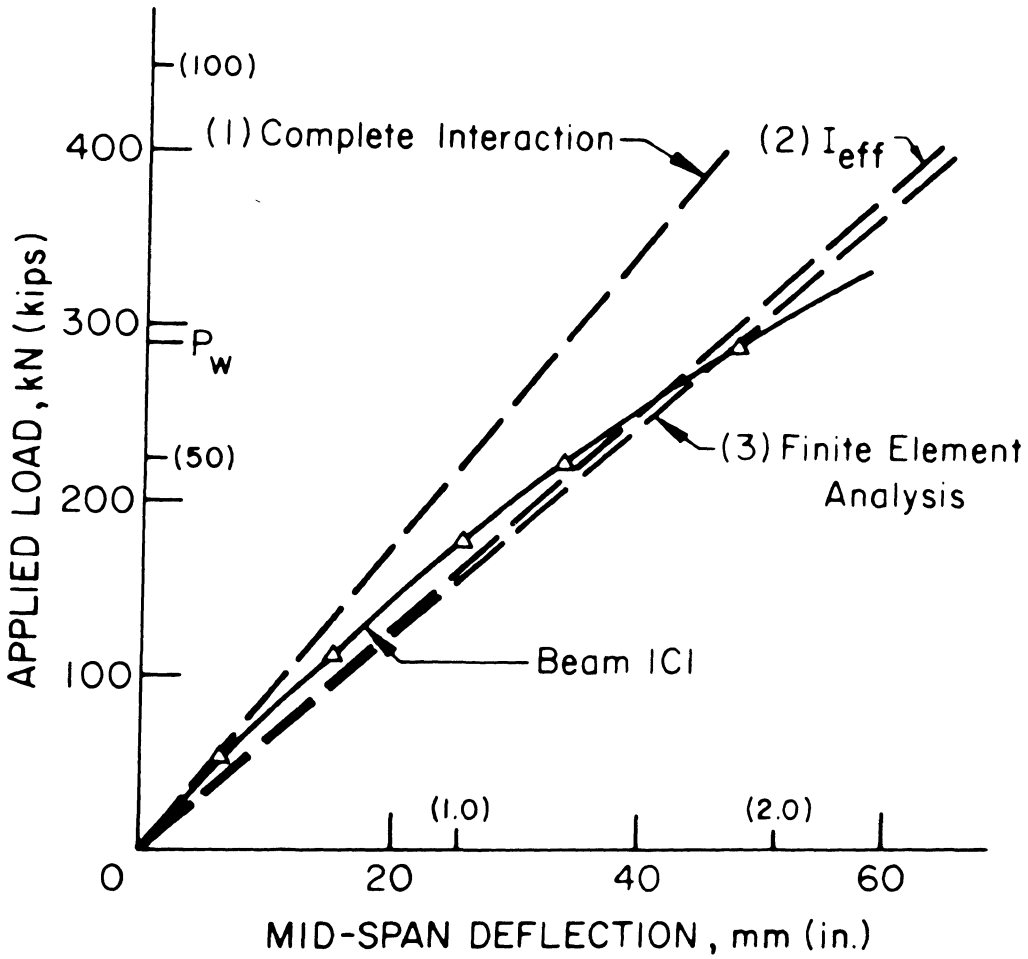

Fig. 49 Load-Deflection Curves of Beam 1C1 in Working Load Range (Ref. 8)

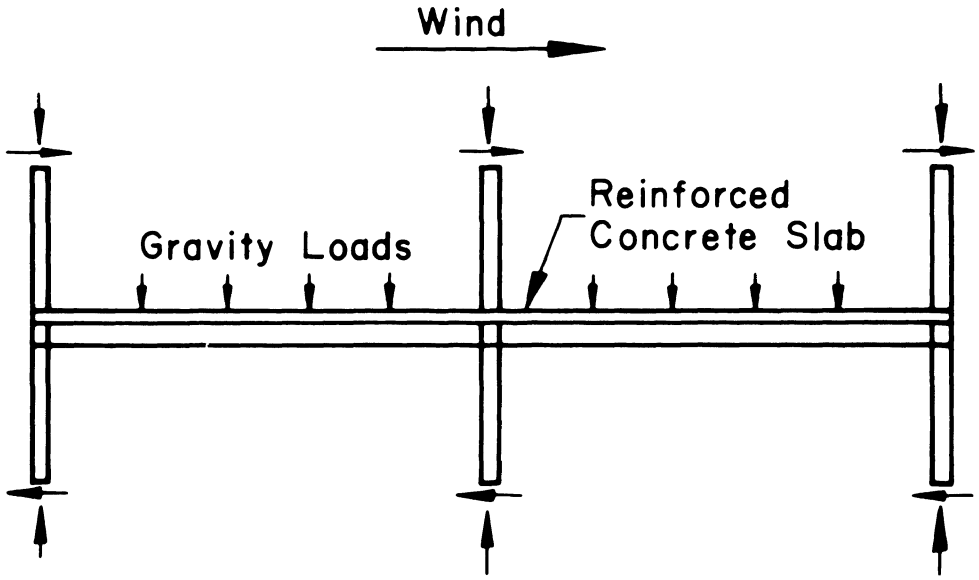

Fig. 50 Composite One-Story Assemblage Under Combined Gravity and Wind Loads

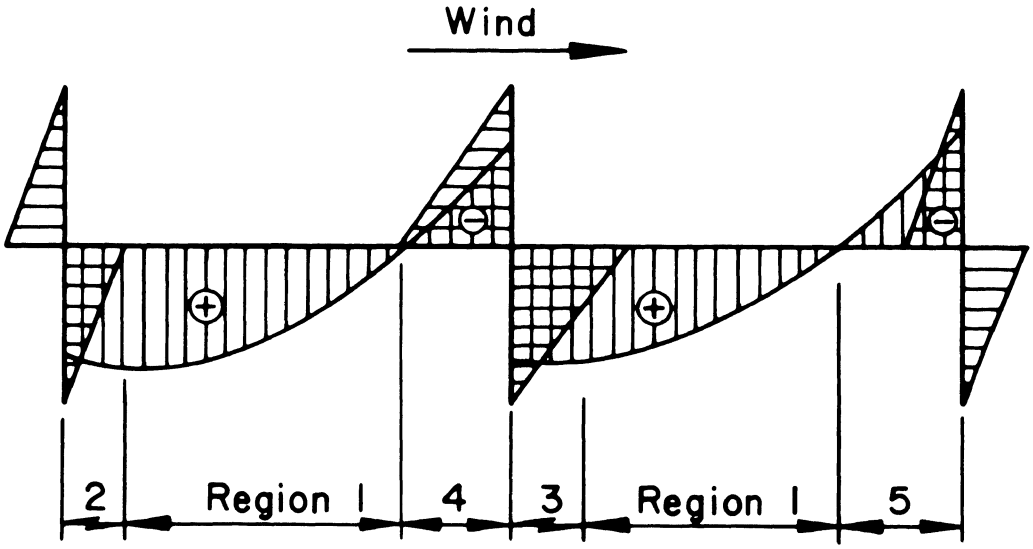

Fig. 51 Bending Moment Diagram Under Combined Gravity and Wind Load

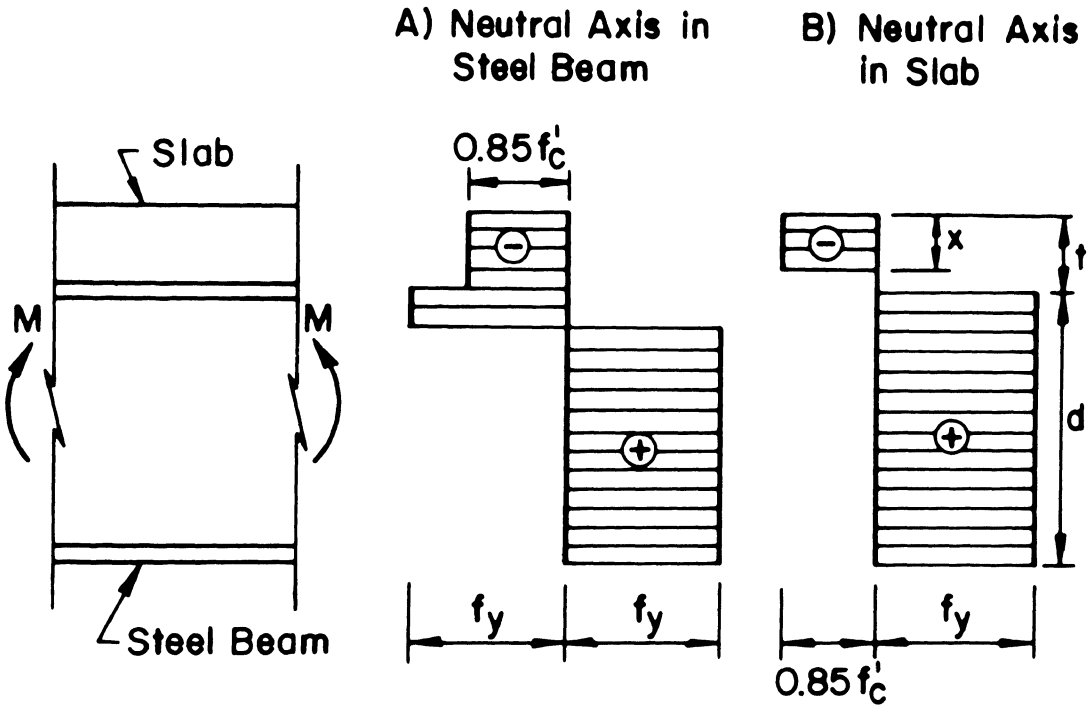

Fig. 52 Maximum Stress Field in Composite Beam Under Positive Moment

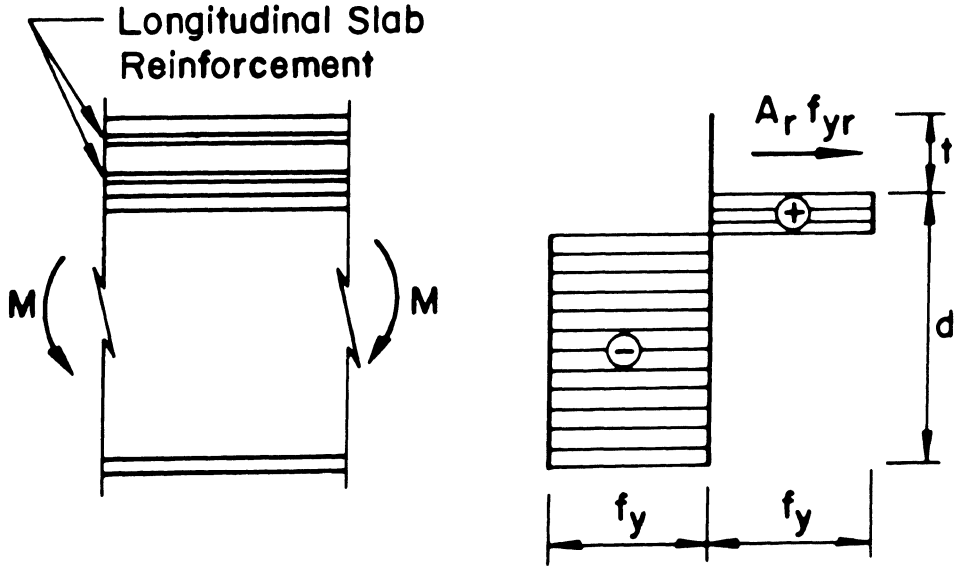

Fig. 53 Maximum Stress Field in Composite Beam Under Negative Moment

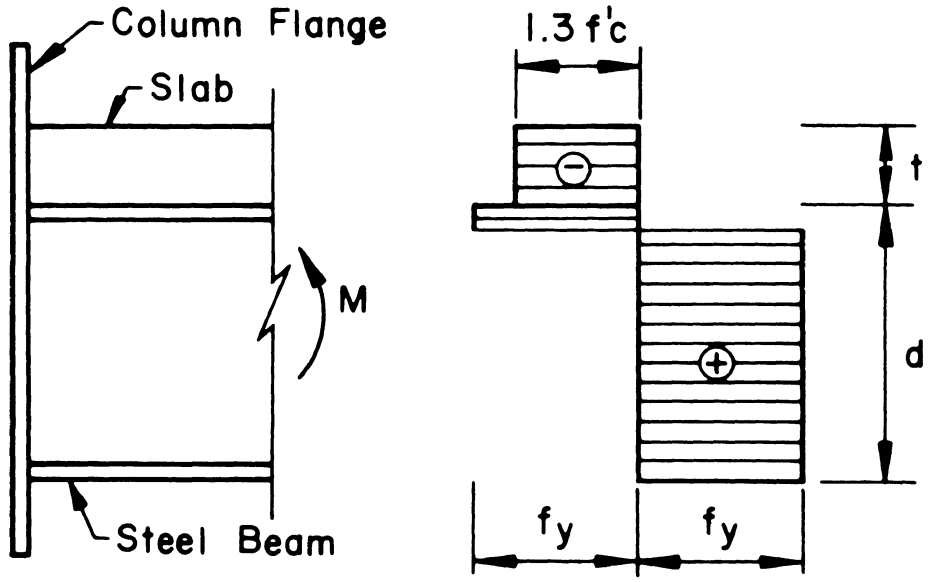

Fig. 54 Maximum Stress Field at Exterior Column for Solid Slab

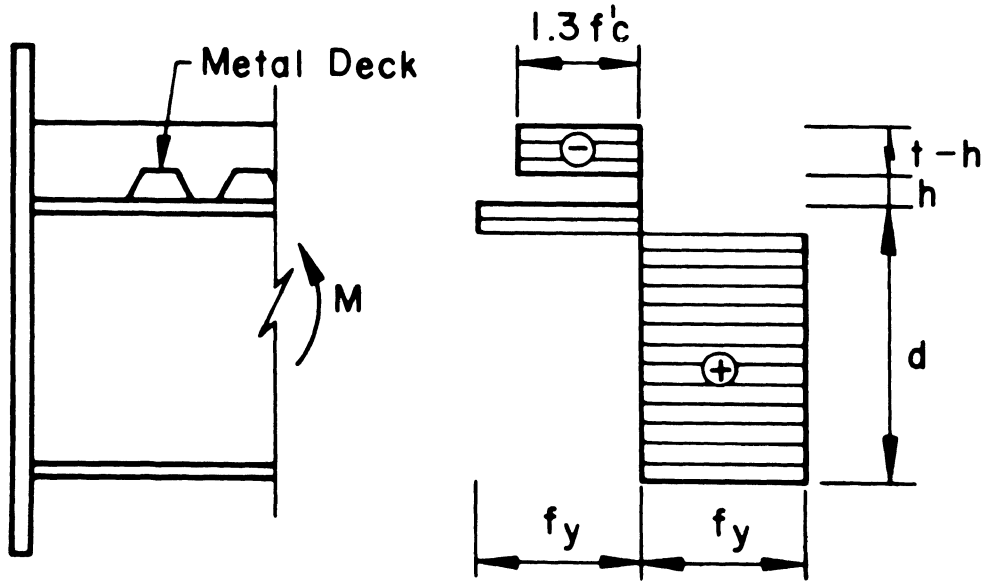

Fig. 55 Maximum Stress Field at Exterior Column for Slab with Metal Deck

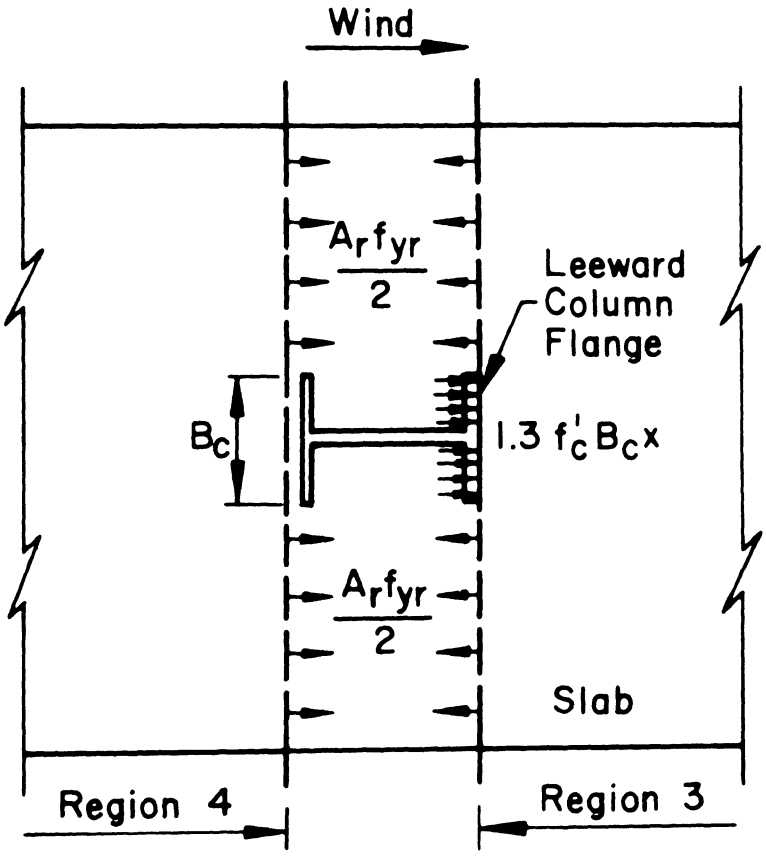

Fig. 56 Maximum Slab Forces at Interior Column

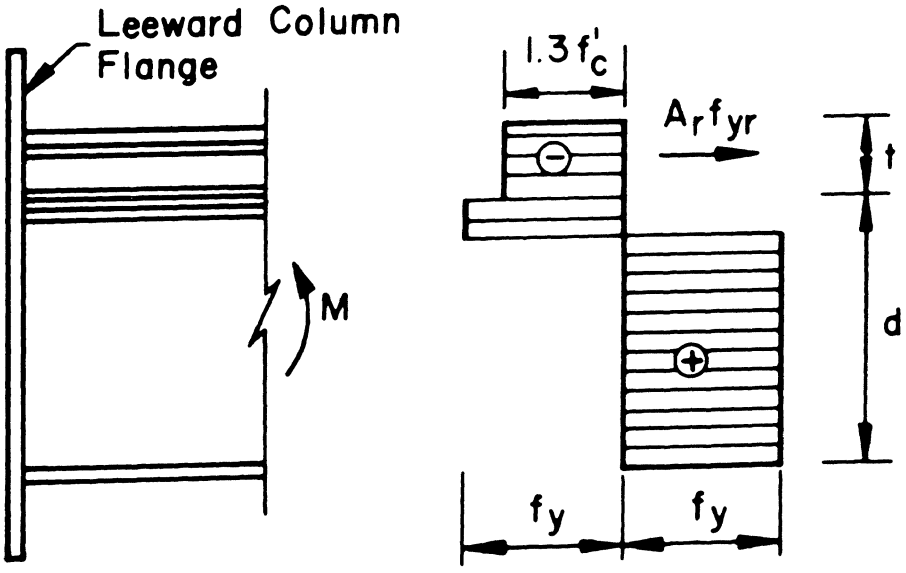

Fig. 57 Maximum Stress Field at Interior Column for Solid Slab

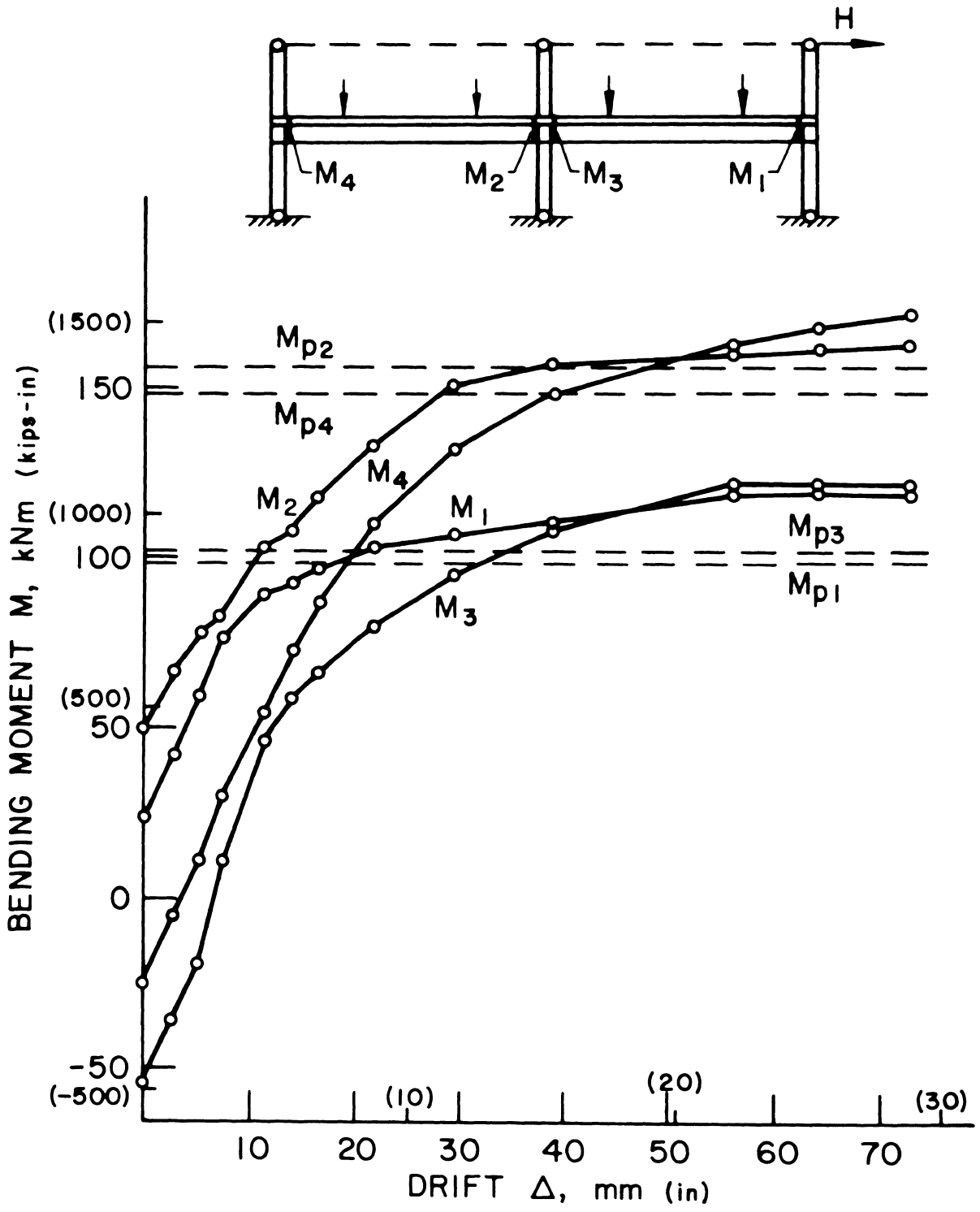

Fig. 58 Experimental Moments at Plastic Hinge Locations of CA-1

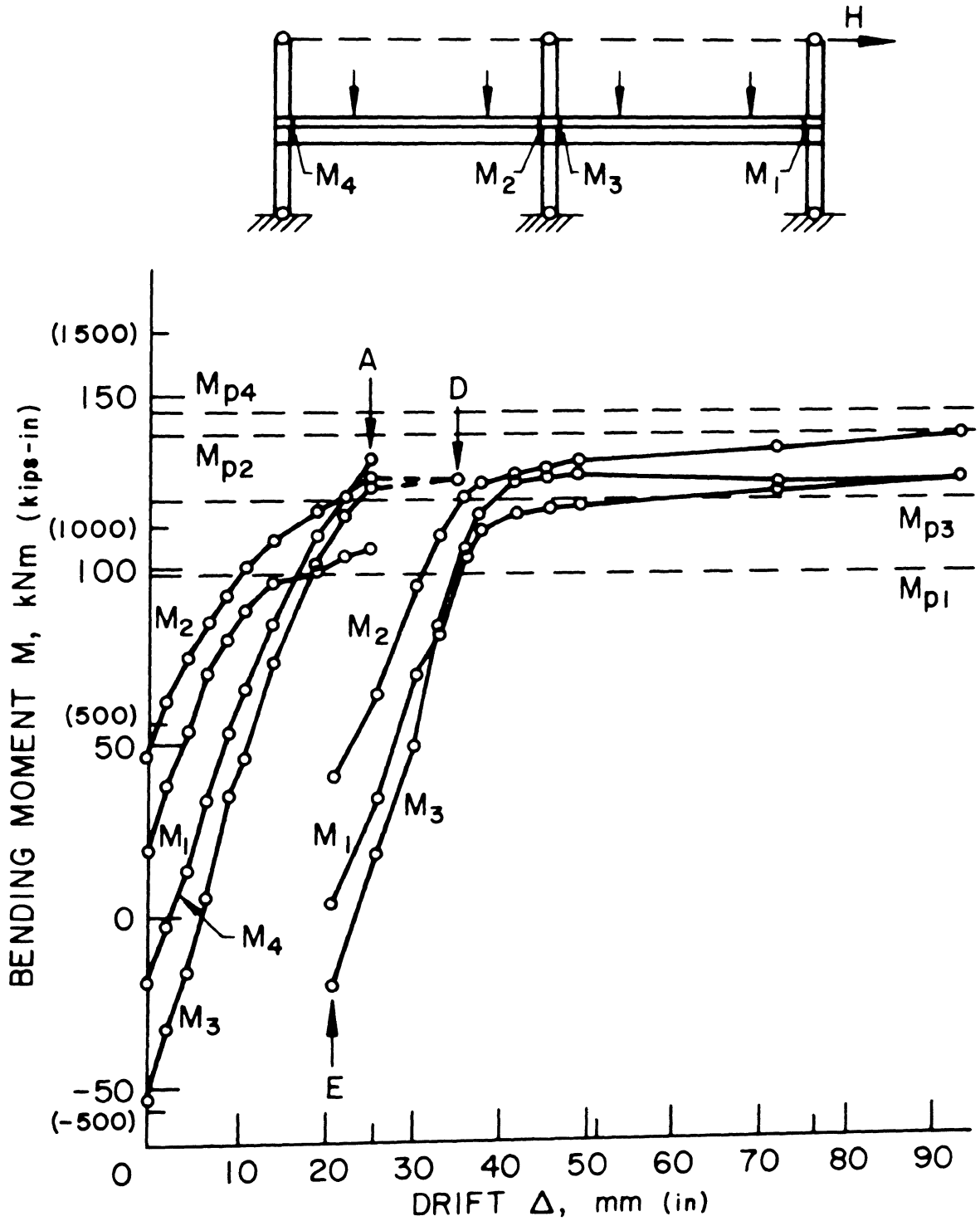

Fig. 59 Experimental Moments at Plastic Hinge Locations of CA-2

15. REFERENCES

1. Daniels, J. H., Kroll, G. D. and Fisher, J. W., BEHAVIOR OF COMPOSITE BEAM-TO-COLUMN JOINTS, Journal of the Structural Division, ASCE, Vol. 96, No. ST3, March 1970.

2. Ansourian, P. and Roderick, J. W., COMPOSITE CONNECTIONS TO EXTERNAL COLUMNS, Journal of the Structural Division, ASCE, Vol. 102, No. ST8, August 1976.

3. Daniels, J. H., PLASTIC ANALYSIS OF ONE-STORY ASSEMBLAGES, AISI Bulletin No. 23, March 1973.

4. Kim, S. W. and Daniels, J. H., EXPERIMENTS ON UNBRACED ONE-STORY ASSEMBLAGES, AISI Bulletin No. 23, March 1973.

5. duPlessis, D. P., THE INTERACTION OF FLOORS AND FRAMES IN MULTISTORY BUILDINGS, A dissertation presented to the Graduate Committee of Lehigh University, Bethlehem, Pa., in partial fulfillment of the requirements for the degree of Doctor of Philosophy, 1974.

6. Leonhardt, F., PRESTRESSED CONCRETE, DESIGN AND CONSTRUCTION, W. Ernst, Berlin, 1964.

7. AISC, SPECIFICATION FOR THE DESIGN, FABRICATION AND ERECTION OF STRUCTURAL STEEL FOR BUILDINGS, American Institute of Steel Construction, New York, 1969.

8. Grant, J. A., Fisher, J. W. and Slutter, R. G., COMPOSITE BEAMS WITH FORMED STEEL DECK, Engineering Journal, American Institute of Steel Construction, First Quarter, 1977.

9. Yarimci, E., Yura, J. A. and Lu, L. W. TECHNIQUES FOR TESTING STRUCTURES PERMITTED TO SWAY, Proceedings, Society for Experimental Stress Analysis, Vol. XXIV, No. 2, 1967.

10. Bathe, K. J., Wilson, E. L., and Peterson, F. E.,
SAP IV - A STRUCTURAL ANALYSIS PROGRAM FOR STATIC AND DYNAMIC RESPONSE OF LINEAR SYSTEMS, Earthquake Engineering Research Center Report No. EERC 73-11, University of California, Berkeley, California, June 1973.

11. Ansourian, P.,
AN APPLICATION OF THE METHOD OF FINITE ELEMENTS TO THE ANALYSIS OF COMPOSITE FLOOR SYSTEMS, Proceedings of the Institution of Civil Engineers, London, Part 2, Vol. 59, December 1975.

12. Ollgaard, J. G.,
THE STRENGTH OF STUD SHEAR CONNECTORS IN NORMAL AND LIGHTWEIGHT CONCRETE, Fritz Engineering Laboratory Report No. 360.4, Lehigh University, May 1960.

13. Robinson, H.,
TESTS ON COMPOSITE BEAMS WITH CELLULAR DECK, Journal of the Structural Division, ASCE, Vol. 93, No. ST4, August 1967.

14. Fisher, J. W., Kim, S. W. and Slutter, R. G.
TESTS OF LIGHTWEIGHT CONCRETE COMPOSITE BEAMS AND PUSHOUT SPECIMENS WITH CELLULAR STEEL DECK, Fritz Engineering Laboratory Report No. 200.67.438.1, Lehigh University, July 1967.

15. Slutter, R. G.,
TESTS OF LIGHTWEIGHT CONCRETE MEMBERS WITH METAL DECKING, Fritz Engineering Laboratory Report No. 200.68.458.1, Lehigh University, March 1969.

16. Iyengar, S. H. et al.,
MIXED CONSTRUCTION, Planning and Design of Tall Buildings, Vol. SB, Structural Design of Tall Steel Buildings, Chapter A41, Joint Committee on Tall Buildings, 1975 (to be published).

17. AISC,
SUPPLEMENT NO. 3 TO THE SPECIFICATION FOR THE DESIGN, FABRICATION AND ERECTION OF STRUCTURAL STEEL FOR BUILDINGS, American Institute of Steel Construction, New York, 1974.

18. Cheong-Siat-Moy, F. and Lu, L. W.,
STIFFNESS AND STRENGTH DESIGN OF MULTISTORY FRAMES, International Association for Bridge and Structural Engineering, Vol. 36-II, Zürich, 1976.

BULLETINS
Steel Research for Construction

*No. 1 Current Paving Practices on Orthotropic Bridge Decks-*Battele Memorial Institute, October, 1965*

No. 2 Strength of Three New Types of Composite Beams-*A. A. Toprac, October, 1965*

No. 3 Research on and Paving Practices For Wearing Surfaces on Orthotropic Steel Bridge Decks, Supplement to Bulletin 1-*Battelle Memorial Institute, August, 1966*

No. 4 Protection of Steel Storage Tanks and Pipe Underground-*Batelle Memorial Institute, May, 1967*

No. 5 Fatigue Strength of Shear Connectors-*R. G. Slutter and J.W. Fisher, October,1967*

No. 6 Paving Practices for Wearing Surfaces on Orthotropic Steel Bridge Decks, Supplement to Bulletins 1 and 3-*Battelle Memorial Institute, January, 1968*

*No. 7 Report on Investigation of Orthotropic Plate Bridges-*D. Allan Firmage, February, 1968*

No. 8 Deformation and Energy Absorption Capacity of Steel Structures in the Inelastic Range-*T. V. Galambos,March, 1968*

No. 9 The Dynamic Behavior of Steel Frame and Truss Buildings-*Dixon Rea, J.G. Bouwkamp and R. W. Clough, April, 1968*

No. 10 Structural Behavior of Small-Scale Steel Models-*Massachusetts Institute of Technology, April,1968*

No. 11 Response of Steel Framest to Earthquake Forces-Single Degree of Freedom Systems-*M. J. Kaldjian and W. R. S. Fan, November, 1968*

No. 12 Response of Multistory Steel Frames to Earthquake Forces-*Subhash C. Goel, November, 1968*

No. 13 Behavior of Steel Building Connections Subjected to Inelastic Strain Reversals-*E. P. Popov and R.B. Pinkney, November, 1968*

No. 14 Behavior of Steel Building Connections Subjected to Inelastic Strain Reversals-Experimental Data-*E P. Popov and R. B. Pindney, November,1968*

No. 15 Tentative Criteria for Load Factor Design of Steel Highway Bridges-*George S. Vincent, March, 1969*

No. 16 Strength of Plate Girders with Longitudinal Stiffeners-*Lehigh University, April, 1969*

No. 17 Fatigue Strength of Plate Girders-*Lehigh University, April, 1969*

No. 18 Interior Corrosion of Structural Steel Closed Sections-*February, 1970*

No. 19 Criteria for the Deflection of Steel Bridges-*R. N. Wright and W. H. Walker, November, 1971*

No. 20 Addendum Report on Paving Practices for Wearing Surfaces on Orthotropic Steel Bridge Decks-*Battelle Memorial Institute, October, 1971*

No. 21 Cyclic Loading of Full-Sized Steel Connections-*E. P. Popov and R. M. Stephen, February, 1972*

No. 22 Seismic Behavior of Multistory Braced Steel Frames-*S. C. Goel and R. D. Handon, April,1972*

No. 23 Plastic Subassemblage Analysis and Tests for Rigid High-Rise Steel Frames-*Lehigh University, March,1973*

No. 24 Reversed and Repeated Load Tests of Full-Scale Steel Frames-*L. W. Carpenter and L. W. Lu, April, 1973*

No. 25 Deflection of Buried Pipes-*R.K. Watkins and A.B. Smith, April, 1974*

No. 26 Seismic Behavior of Staggered Truss Framing Systems-*University of Michigan, April,1974*

No. 27 Proposed Criteria for Load and Resistance Factor Design of Steel Building Structures-*Washington University, January, 1979*

No. 28 Plastic Analysis and Tests for Rigid High-Rise Composite Frames-*Lehigh University, April,1979*

* Out of Print